DEEP INELASTIC MUON SCATTERING AT 270 GEV

By

Phillip F. Schewe

A DISSERTATION

Submitted to
Michigan State University
in partial fulfillment of the requirements
for the degree of

DOCTOR OF PHILOSOPHY

Department of Physics

1978

G113003

ABSTRACT

DEEP INELASTIC MUON SCATTERING AT 270 GEV

By

Phillip F. Schewe

The nucleon structure function νW_2 for deep inelastic muon scattering at 270 GeV has been measured in an experiment performed at Fermi National Accelerator Laboratory. A large violation of Bjorken scale invariance has been observed out to q^2=150 $(GeV/c)^2$, greatly extending previous deep inelastic results.

The data reported here is based on a flux of 1.5×10^{10} positively charged muons incident on an iron target/calorimeter. The energy of the scattered muon is measured in a spectrometer consisting of iron toroid magnets and wire spark chambers.

The values of νW_2 measured in this experiment for high q^2 and fixed x lie systematically above the values predicted by a particular formulation of quantum chromodynamics (QCD). The data also lies above the values for νW_2 obtained by extrapolating previous deep inelastic data to higher q^2. The possibility that this rise in νW_2 is due a threshold-like behavior in W^2 (the hadron final state mass squared) is studied by calculating the scale breaking parameter $b(x)=\partial \ln(\nu W_2)/\partial \ln(q^2)$, and by fitting the data to various functions of W^2.

ACKNOWLEGMENTS

Fermilab Experiment 319, on which this dissertation is based, was conducted by a large group Michigan State physicists: R.C. Ball, D. Bauer, C. Chang, K.W. Chen, S. Hansen, J.Kiley , I. Kostoulas, A. Kotlewski, L. Litt, and myself. All of these people have been of some help to me during the running and analysis phases of E319. In particular, I have worked very closely with, and received much help from, Bob Ball, Jim Kiley, and Dan Bauer.

It is a pleasure to mention the help and friendship of Sten Hansen, now working at Fermilab. His electrical troubleshooting abilities and his good humor helped keep the experiment going on many occasions.

Keith Thorne was very helpful in preparing a myriad of fits to the data. He is patient, thorough, and resourseful.

I have had several useful conversations about theoretical and experimental aspects of our experiment with Professors Wayne Repko, Lawrence Litt, William Francis, K.W. Chen (thesis advisor), and Eliot Lehman. Mr. Francis has been very forthcoming with the (as yet unpublished) results of the complementary muon experiment E398.

The crew and staff of the neutrino department at Fermilab deserve special thanks. During the running of the experiment we were in almost continuous contact with them, and their response to the needs of our experiment was always quick and courteous.

Finally I would like to thank the administrative and typing assistance of Mr. Mehdi Ghods, Candy Gronseth, and Delores Sullivan.

TABLE OF CONTENTS

		Page
List of Tables		vi
List of Figures		viii
1.	Deep Inelastic Lepton Scattering	1
1.1	Introduction to Lepton Scattering	1
1.2	Deep Inelastic Muon Scattering and Related Physics	2
1.3	The Quark-Parton Model	8
1.4	Bjorken Scale Invariance	11
1.5	Gluons and Scale Breaking	15
1.6	QCD	21
1.7	Experiment 319	27
2.	The Apparatus and Data Taking	29
2.1	Fermilab Muon Beam Line	29
2.2	Tuning the Muon Beam	31
2.3	The E319 Apparatus	34
2.4	Target/Calorimeter	34
2.5	Proportional Chambers	40
2.6	Spectrometer	40
2.7	Trigger Logic	48
2.8	Computer	54
2.9	Running Conditions	55
3.	Analysis of the Data	61
3.1	Alignment	61
3.2	Calibration of the Spectrometer	67
3.3	Data Analysis	77
3.4	Resolution	97
3.5	Acceptance	99
3.6	Data Distributions	99
4.	Monte Carlo	122
4.1	Monte Carlo Philosophy	122
4.2	The Beam	124

4.3 Interaction in the Target 124
Coulomb Multiple Scattering 125
Energy Loss 125
Fermi Motion 125
Cross Section 126
Conversion to Iron 126
Radiative Corrections 127
Dependence on $R=\sigma_S/\sigma_T$ 127
Wide Angle Bremsstrahlung 129

4.4 Ray Tracing 131
4.5 MCP Distributions 131
4.6 Data/MCP Comparison: Extracting $F_2(x,q^2)$ 131
4.7 Systematic errors in $F_2(x,q^2)$ 142

5. Results and Conclusions 151

5.1 Summary of the Data Sample 151
5.2 Normalization of F_2 154
5.3 Parameterizing Scale Breaking 157
5.4 F_2 versus x 160
5.5 QCD Predictions 162
5.6 $F_2(x,q^2)$ Compared to QCD 167
5.7 Moments 180
5.8 Fits to the Data 182
5.9 Speculations on Scaling Violations 184
5.10 Summary and Conclusions 190

Appendix A $F_2(x,q^2)$ for Various Values of x and q^2 191

References 199

LIST OF TABLES

		Page
2.1	Magnet currents in Neutrino Hall	30
2.2	Calibration of the 1E4 Dipoles	35
2.3	N1 Muon Beam Line Magnet Settings at 270 GeV	36
2.4	Z Positions for Elements in the E319 Apparatus	38
2.5	Target/Calorimeter Density	41
2.6	Proportional Chamber System	41
2.7	Spark Chamber Properties	45
2.8	Iron Toroid Magnets	46
2.9	Trigger Types and Notation	50
2.10	Primary Data Tape Format	56
2.11	Scaler Averages for a Single Run	58
2.12	E319 Data Runs	60
3.1	Final E319 Alignment Constants in cm.	68
3.2	CCM (Chicago Cyclotron Magnet) Calibration Runs	72
3.3	Apertures in E398 Walls	72
3.4	Calibration of the Spectrometer Using the CCM	78
3.5	Calibration of the Spectrometer Using Monte Carlo Data	78
3.6	Beam Tape Format	82
3.7	Digitizer Clock Counts	83
3.8	Track Finding Cuts	86
3.9	Secondary Tape Format	98

3.10	(a) % Resolution σ as a Function of $y=\nu/E_0$	101
	(b) % Resolution σ as a Function of ω	102
	(c) % Resolution σ as a Function of q^2	102
4.1	Summary of Main Monte Carlo Features	123
4.2	Monte Carlo (E_0+.4%)/Monte Carlo (E_0)	143
4.3	Monte Carlo (E'+1%)/Monte Carlo (E')	144
4.4	Monte Carlo (θ+.4%)/Monte Carlo (θ)	145
4.5	Radiative Corrections (off)/Radiative Corrections (on)	147
4.6	Wide Angle Bremsstrahlung (off)/Wide Angle Bremsstrahlung (on)	148
4.7	Monte Carlo (R=0)/Monte Carlo (R=.25)	149
5.1	Single-Muon Analysis Cuts	152
5.2	Data/Monte Carlo Comparison Results	153
5.3	Various Fits to the Combined b(x) Data	159
5.4	E319 Values for $b(x)=\partial(\ln F_2)/\partial(\ln q^2)$	164
5.5	Moments	183
5.6	Power Law Fit to $F_2(x,q^2)$ in Various q^2 Regions	183
5.7	Fits to F_2	185
A.1	$F_2(x,q^2)$ Versus q^2 for fixed x Regions	192
A.2	$F_2(x,q^2)$ Versus x for fixed q^2 Regions	195

LIST OF FIGURES

		Page
1.1	Feynman Diagram for Deep Inelastic Scattering and Associated Kinematic Variables	3
1.2	Other Kinds of Lepton-Hadron Scattering	7
1.3	Incoherent Scattering from a Single Parton with Momentum xP	14
1.4	Quark Structure Function	14
1.5	Nucleon Structure Function	14
1.6	SLAC-MIT Data (ref. 10) Showing Approximate Scaling in the Modified Scaling Variable $\omega'=2m\nu/(q^2+m^2)$	16
1.7	Deep Inelastic Scattering Without Gluons: $F_2(\text{quark}) \simeq \delta(x/z-1)$	18
1.8	Gluon Correction Terms: $F_2(\text{quark})\simeq\delta(x/z-1)+g^2a(x/z)\ln(\frac{q^2}{q_o^2})$	18
1.9	Nonzero σ_S and $P_\perp$ related to Gluon Bremsstrahlung	19
1.10	μ - Fe Scale Violations	20
1.11	Constituents of the Quark in QCD Renormalization	25
1.12	Gluon Pair Production of Quarks	25
1.13	Kinematic Region of E319	28
2.1	Properties of the Primary Proton Beam	30
2.2	Schematic of Muon Beam and Beam Detectors	32
2.3	Proportional Chambers and Beam Counters	33
2.4	Magnetic Field in 1E4 Dipoles	35
2.5	E319 Apparatus	37
2.6	The Details of a Corner of a Spark Chamber	43
2.7	Trigger Banks	49

			Page
2.8	Fast Logic for the Full Trigger		51
2.9	Trigger Bank Logic		52
2.10	Gate Logic		53
3.1	Aligning PC2, PC1, and the Front Spark Chambers		64
3.2	Conventions for Spark Chamber Coordinate Axes		64
3.3	Layout of E398 and E319 Apparatus During the Spectrometer Calibration		70
3.4	Spectrometer Calibration	(a) 250 GeV	74
		(b) 200 GeV	75
		(c) 150 GeV	75
		(d) 100 GeV	76
		(e) 50 GeV	76
3.5	Flow Chart of the Analysis Program VOREP		80
3.6	Joining Spectometer and Beam Tracks		88
3.7	A High q^2 event		91
3.8	Idealized Momentum Reconstruction		92
3.9	Percentage Acceptance: ω vs. q^2		103
3.10	Percentage Acceptance: q^2 vs. ν		104
3.11	ν Acceptance		105
3.12	Θ Acceptance		105
3.13	Acceptance in q^2		106
3.14	ω Acceptance		107
3.15	Acceptance in $y=\nu/E_0$ and Ratio=E'/E_0		108
3.16	Acceptance in $x=q^2/2m\nu$		109
3.17	Acceptance in $W^2=2m\nu+m^2-q^2$		110
3.18	Data Distribution: ZMIN (a) before cuts (b) after cuts		111
3.19	Data Distribution: q^2		112

		Page
3.20	Data Distributions: W^2	112
3.21	Data Distributions: $P_\perp$	113
3.22	Data Distributions: χ^2	113
3.23	Data Distributions: E'	114
3.24	Data Distributions: E_o	114
3.25	Data Distributions: Θ_{beam}	115
3.26	Data Distributions: $\Theta_{scatter}$	115
3.27	Data Distributions: x_{beam}	116
3.28	Data Distributions: y_{beam}	116
3.29	Data Distributions: R(WSC 5)	117
3.30	Data Distributions: R(WSC 1)	117
3.31	Data Distributions: R_{beam}	118
3.32	Data Distributions: RMAG	118
3.33	Data Distributions: ω	
3.34	Data Distributions: $x_{Bjorken}$	119
3.35	Consistency of Several Kinematic Variables for Randomly Chosen Runs	120
4.1	The Effect of $R=\sigma_S/\sigma_T$ on the Cross Section	128
4.2	Radiative Correction Diagrams	130
4.3	The "Effective Radiator" Method	130
4.4	Contributions to the Radiative Corrections in the (E_o,E') Plane	130
4.5	Monte Carlo Distributions: ZMIN (a) before cuts (b) after cuts	132
4.6	Monte Carlo Distributions: q^2	133
4.7	Monte Carlo Distributions: W^2	133
4.8	Monte Carlo Distributions: $P_\perp$	134

		Page
4.9	Monte Carlo Distribution: χ^2	134
4.10	Monte Carlo Distribution: E'	135
4.11	Monte Carlo Distribution: E_o	135
4.12	Monte Carlo Distribution: Θ_{beam}	136
4.13	Monte Carlo Distribution: $\Theta_{scatter}$	136
4.14	Monte Carlo Distribution: x_{beam}	137
4.15	Monte Carlo Distribution: y_{beam}	137
4.16	Monte Carlo Distribution: R(WSC 5)	138
4.17	Monte Carlo Distribution: R(WSC 1)	138
4.18	Monte Carlo Distribution: R_{beam}	139
4.19	Monte Carlo Distribution: RMAG	139
4.20	Monte Carlo Distribution: ω	139
4.21	Monte Carlo Distribution: $x_{Bjorken}$	140
4.22	Contours of Constant Systematic Error in F_2 in the x-q^2 Plane	150
5.1	Corrected Yield vs. Flux	156
5.2	The Scaling Violation Parameter b(x)	158
5.3	F_2 vs.x	161
5.4	E319 b(x)	163
5.5	QCD Predictions for F_2 and for Quark Densities	168
5.6	Measured F_2 versus x for Fixed q^2	169
5.7	Measured F_2 versus q^2 for Fixed x	176
5.8	First Moments of F_2 for μ-p, μ-d, and μ-Fe Scattering	181
5.9	A Fit to F_2 Using a Linear Rise Above W^2=80	186

CHAPTER I

DEEP INELASTIC LEPTON SCATTERING

1.1 Introduction to Lepton Scattering

Since the time of Rutherford, physicists have probed the structure of matter, and the behavior of physical forces, by performing scattering experiments. It is convenient to describe the relative probability for a particular scattering reaction to take place in terms of a "cross section." This geometrical equivalent is intuitively useful: the larger the cross section, the greater will be the equivalent profile which the target particle presents to the incoming projectile particle, and therefore the more probable the interaction.

Rutherford expressed the differential cross section for the scattering of an alpha particle from a nucleon target in terms of the scattering angle θ (solid angle Ω), the energy of the incident particle, E_0, and the atomic number of the target nucleus, Z:

$$\frac{d\sigma}{d\Omega} = \frac{Z^2 e^4}{4E_0^2 \sin^4 \theta/2} \qquad (1)$$

For the case of an electron scattering from a nucleus the electron's spin must be considered. If we also account for the effects of relativity and nucleus recoil, the formula in (1) becomes:

$$\frac{d\sigma}{d\Omega} = \frac{Z^2e^4\cos^2\theta/2}{4E_0^2\sin^4\theta/2}\{1+\frac{2E_0}{m}\sin^2\theta/2\}^{-1} \qquad (2)$$

This is the so-called "Mott scattering" of an electron with spin from a spinless point-like nucleus with mass m.[1]

Finally one must also account for the proton's spin, and the proton's structure (it is not a point-like object). The "Rosenbluth formula" describes the scattering of an electron from a proton with structure:[2]

$$\frac{d\sigma}{d\Omega} = (\frac{d\sigma}{d\Omega})_{Mott}\{\frac{G_E^2+q^2G_M^2/4m^2}{1+q^2/4m^2}+\frac{q^2}{4m^2}2G_m^2\tan^2\theta/2\} \qquad (3)$$

In this formula, G_E is a form factor which describes the scattering of the electron by the proton's charge (which is distributed in some way throughout the proton), while G_M is a form factor for scattering from the proton's magnetic moment. m is the mass of the proton and q^2 is the momentum transfer squared.

The evolution of equations (1) - (3) shows how new concepts, such as relativity or spin, can be incorporated into the basic scattering cross section formula. The next development to be discussed is the situation in which the lepton-proton interaction is inelastic.

1.2 Deep Inelastic Muon Scattering and Related Physics

The Feynman diagram and associated kinematic relations for inelastic muon-proton scattering are shown in Figure 1.1. The matrix element squared can be given in terms of a current-current interaction:[2]

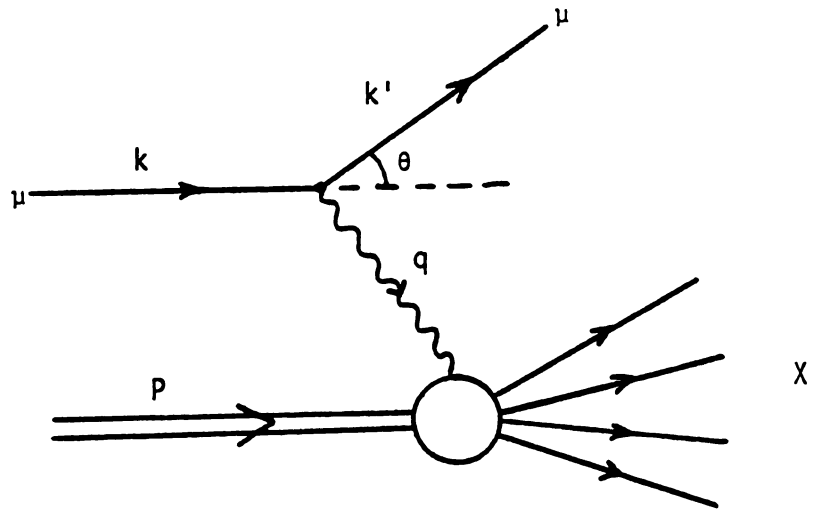

P=(m,0,0,0)= proton at rest in lab frame

$k=(E_0,0,0,E_0)$= incident muon

$k'=(E',0,E'\sin\theta,E'\cos\theta)$= scattered muon

$q=(\nu,0,-E'\sin\theta,E_0-E'\cos\theta)$= virtual photon

$\nu=q.P/m = E_0-E'$ = energy transfer

$q^2=(k-k')^2 = 4E_0E'\sin^2\theta/2$= momentum transfer squared

$W^2= M_x^2 = 2m\nu+m^2-q^2$ =hadron final state mass squared

$x=1/\omega = q^2/2m\nu$ = Bjorken scaling variable

elastic scattering: $2m\nu/q^2=\omega = 1$

inelastic scattering: $2m\nu/q^2 = \omega= 1/x>1$

Figure 1.1 Feynman diagram for deep inelastic scattering and associated kinematic relations

$$|M|^2 = [(\bar{k}'\gamma_\nu k)^*(\bar{k}'\gamma_\mu k)]\ (\frac{4\pi e^2}{q^2})^2\ [\sum_x <p|J_\nu(-q)|x>$$

$$\cdot <x|J_\mu(q)|p> 2\pi\delta((\underline{p}+q)^2-W^2)] \tag{4}$$

$$= L_{\mu\nu}\ (\frac{4\pi e^2}{q^2})^2\ W_{\mu\nu} \tag{5}$$

The first bracket represents the lepton part of the matrix element and is known from quantum electrodynamics. This is the advantage of using a lepton beam to probe the structure of the nucleon; since the muon does not interact strongly, its contribution can be calculated exactly leaving only the hadronic part to be measured:

$$L_{\mu\nu} = (\bar{k}'\gamma_\nu k)^*(\bar{k}'\gamma_\mu k) = 2(k'_\mu k_\nu + k_\nu k'_\mu - \delta_{\mu\nu} k\cdot k') \tag{6}$$

The second bracket in equation (4), representing a summation over all hadron final states, can be simplified using gauge and Lorentz invariance:[2]

$$W_{\mu\nu} = \sum_x <p|J_\nu(-q)|x><x|J_\mu(q)|p>\ 2\pi\delta((p+q)^2-W^2) \tag{7a}$$

$$= (p_\mu - q_\mu \frac{p\cdot q}{q^2})(p_\nu - q_\nu \frac{p\cdot q}{q^2})\ W_2(q^2,\nu)$$

$$- m^2(\delta_{\mu\nu} - \frac{q_\mu q_\nu}{q^2})\ W_1(q^2,\nu) \tag{7b}$$

W_1 and W_2 are structure functions roughly analogous to G_M and G_E in the elastic case, equation (3). They are functions of the two Lorentz

invariants ν and q^2. Although I will return later to equation (7a) while discussing the formulation of quantum chromodynamics, I will now just utilize (7b), which can be used to give an expression for the scattering cross section analogous to the Rosenbluth formula. This expression, for small scattering angles, is given by:

$$\frac{d^2\sigma}{dE'd\Omega}(q^2,\nu) = \frac{\alpha^2\cos^2\theta/2}{4E_0^2\sin^4\theta/2}[W_2(q^2,\nu) + 2\tan^2\theta/2\ W_1(q^2,\nu)] \tag{8}$$

This cross section can also be expressed in terms of equivalent absorption cross sections for the scattering of transversely polarized (σ_T) and longitudinally polarized photons (σ_s):

$$\frac{d^2\sigma}{dE'd\Omega} = \Gamma(\sigma_T + \varepsilon\sigma_s) \tag{9}$$

$\Gamma(q^2,\nu) = \frac{\alpha}{4\pi^2}\frac{k}{q^2}\frac{E'}{E}(\frac{2}{1-\varepsilon})$ = effective flux of virtual photons

$\varepsilon = [1 + 2(1+\nu^2/q^2)\tan^2\theta/2]^{-1}$ = virtual photon polarization

$k = (W^2 - m^2)/2m$

The conversion between W_1 and W_2, and σ_s and σ_T is given by:

$$W_1 = \frac{k}{4\pi^2\alpha}\sigma_T$$

$$W_2 = \frac{k}{4\pi^2\alpha}\frac{q^2}{q^2+\nu^2}(\sigma_T+\sigma_s) \tag{10}$$

The ratio $R(q^2,\nu) = \sigma_s/\sigma_T$ is a more useful function than W_1.

With a little algebra, equation (8) becomes:

$$\frac{d^2\sigma}{dE'd\Omega}(q^2,\nu) = \frac{\alpha^2\cos^2\theta/2}{4E_0^2\sin^4\theta/2}\frac{\nu W_2}{\nu}\left[1 + 2\tan^2\theta/2\ \left(\frac{1+\nu^2/q^2}{1+R}\right)\right] \qquad (11)$$

Present data[34] give R= constant = .25±.10 although there are indications that R may vary with q^2 and ν. In the quark-parton model, a measurement of $\nu W_2(q^2,\nu)$ and its moments can be used to find the momentum distributions of individual quarks within the nucleon.

There are other interactions which also probe the structure of hadrons. Besides $\mu p \to \mu X$, which I have been describing, the reaction $ep \to eX$ should be entirely equivalent from muon-electron unversality.[3] The annihilation process $e^+e^- \to X$ is similar to the ep interaction, only turned on its side, as shown in Figures 1.2a and 1.2b. In the annihilation case, $q^2 > 0$ is timelike, whereas for inelastic ep scattering, $q^2 < 0$. Figure 1.2c shows neutrino scattering where the hadron's weak current is probed by an intermediate vector boson W. The scattering cross sections analogous to equation (11) for the annihilation and neutrino scattering respectively, are given by:[4]

$$\frac{d^2\sigma}{dE'd\Omega}(e^+e^- \to X) = \frac{2\alpha^2}{q^4}m^2\sqrt{\nu^2/q^2 - 1}$$

$$\left\{2W_1^{e^+e^-} + \frac{2m}{q^2}\left(1 - \frac{q^2}{\nu^2}\right)\frac{\nu W_2^{e^+e^-}}{2m}\sin^2\theta/2\right\} \qquad (12)$$

$$\frac{d^2\sigma}{dxdy}(\overset{(-)}{\nu}p \to \mu X) = \frac{G^2}{2\pi}s\left[F_2(1-y) + F_1xy^2 \pm y(1-y/2)xF_3\right] \qquad (13)$$

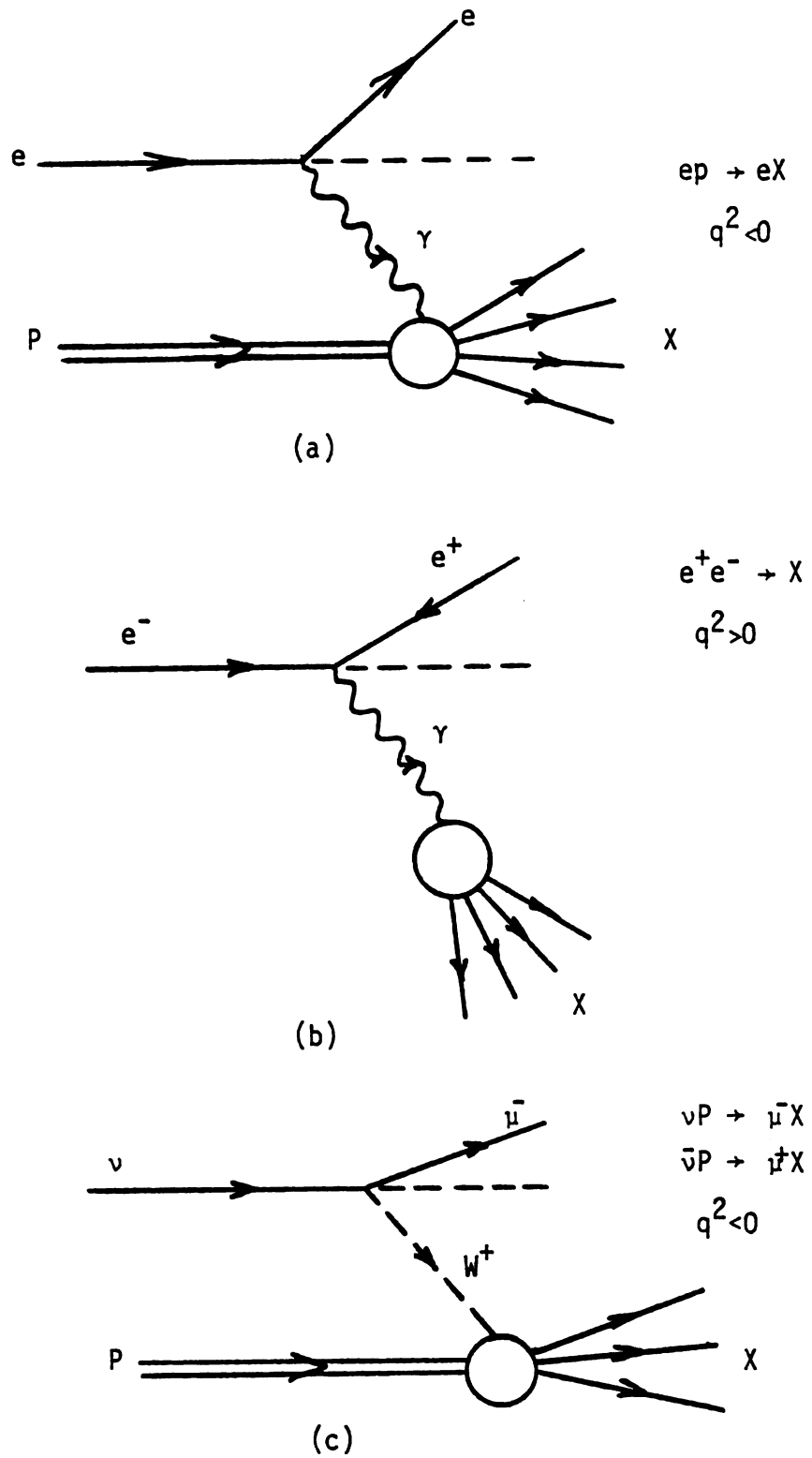

Figure 1.2 Other kinds of lepton-hadron scattering

In the above expression m=proton mass, $y=\nu/E_0$, and F_3 is a third structure function necessitated by the violation of parity in the weak interaction.

From crossing symmetry, we can relate the inelastic and annihilation structure functions:

$$W_1^{e^-e^+}(q^2,\nu) = - W_1^{ep}(q^2,-\nu)$$
$$\nu W_2^{e^+e^-}(q^2,\nu) = - \nu W_2^{ep}(q^2,-\nu) \qquad (14)$$

The reactions $\mu p \to \mu h X$ (with certain final state hadrons being measured), $ep \to eX$ (with polarized beam and target), $\nu p \to \nu p$ (weak neutral current), and $pp \to \mu\mu X$ (massive lepton pair produced) also help to measure hadronic structure. All of these interactions can profitably be studied, and related, using the language of the quark-parton model.

1.3 The Quark-Parton Model

The identification of the hypothesized (charged) pointlike constituents of nucleons, known as partons[5], with quarks, appears to be nearly complete,[6,2] and I will use the words interchangeably. With this identification comes the best features of both theories; the ability to classify the hierachy of observed particles as well as making dynamical predictions about interactions. The standard quark-parton model of the proton is one where three "valence" quarks are accompanied by a "sea" of quark-antiquark pairs.[7] In addition there are perhaps an infinite number of neutral vector gluons around to mediate the interactions between quarks, and, presumably, to bind them within the proton.

In studying how the partons are distributed within the proton, it is useful to consider a single parton, carrying a fraction x of the proton's total momentum P. The remaining partons (and gluons) together carry the rest of the momentum.

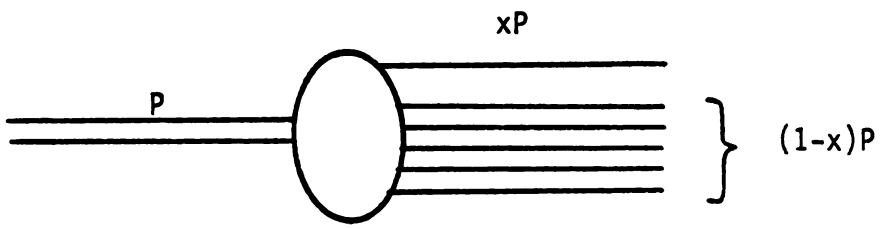

Quark density functions $q_i(x)$ can be defined such that $q_i(x)dx$ is the number of quarks of type i with momentum between xP and (x+dx)P. i can be any of the quark flavors (u,d,s,c) or antiquarks.

$$q_i(x) = q_i^{valence}(x) + q_i^{sea}(x) \tag{15}$$

The total momentum carried by i-type quarks is the density times x, integrated over x from zero to one: $\int_0^1 xq_i(x)dx$.

In the next section, I will show that the structure function νW_2, as used in equation (11), is the sum of scattering contributions from all the quarks in the proton weighted by their quark charge e_i:

$$\nu W_2 = \sum_i e_i^2 xq_i(x) \tag{16}$$

Using this equation, and the above convention for quarks in the proton, several predictions can be made (sum rules, cross sections, etc.). The agreement between theory and data tends to be good, but not perfect.

For describing scattering from neutrons as well as protons, it is convenient to define $u=u_p=d_n$ and $d=d_p=u_n$. Then, the structure functions for the nucleons become[8]:

$$\frac{1}{x}\nu W_2^{\mu p} = \frac{4}{9}(u+\bar{u}) + \frac{1}{9}(d+\bar{d}) + \frac{4}{9}(c+\bar{c}) + \frac{1}{9}(s+\bar{s}) \tag{17a}$$

$$\frac{1}{x}\nu W_2^{\mu n} = \frac{4}{9}(d+\bar{d}) + \frac{1}{9}(u+\bar{u}) + \frac{4}{9}(c+\bar{c}) + \frac{1}{9}(s+\bar{s}) \tag{17b}$$

If we neglect charm and set $\theta_{cabibbo}=0$ for the moment, the neutrino structure functions are[6]:

$$\frac{1}{x}\nu W_2^{\nu p} = 2(d+\bar{u}) \tag{18}$$

$$\frac{1}{x}\nu W_2^{\nu n} = 2(u+\bar{d}) \tag{19}$$

Some simple sum rules can be formulated[6]:

$$\text{no. of u quarks in the proton} = \int_0^{'} dx(u-\bar{u}) = \int_0^{'} dx u_{valence} = 2 \tag{20}$$

$$\text{no. of d quarks in the proton} = \int_0^{'} dx(d-\bar{d}) = \int_0^{'} dx d_{valence} = 1 \tag{21}$$

$$\int_0^{'} \frac{dx}{x}(\nu W_2^{\nu n} - \nu W_2^{\nu p}) = 2 \tag{22}$$

$$\frac{\nu W_2^{ep} - \nu W_2^{en}}{\nu W_2^{\nu p} - \nu W_2^{\nu n}} \simeq \frac{\frac{5}{9}(u+\bar{u}+\bar{d}+d) + \frac{2}{9}(s+\bar{s})}{2(u+\bar{u}+d+\bar{d})} \gtrsim \frac{5}{18} \tag{23}$$

$$\int \frac{dx}{x}(\nu W_2^{ep} - \nu W_2^{en}) = \frac{1}{3}\int dx(u+\bar{u}-d-\bar{d})$$

$$= \frac{1}{3}\int dx(u_{valence} - d_{valence}) = \frac{1}{3} \qquad (24)$$

1.4 Bjorken Scale Invariance

One of the most important applications of the parton model has been in deep inelastic scattering. First, because the lepton part of the scattering matrix element is known from QED, the structure of the nucleon can be measured directly. Secondly, since the muon does not interact strongly, it need not scatter coherently off all the constituents in the nucleon, but can concentrate its transverse momentum transfer on a single parton; in this way, relatively higher q^2 is attainable than in a hadron-hadron collision with the same center-of-mass energy. Equivalently, for large enough q^2 (large compared to the proton mass squared), the virtual photon's wavelength is so small that the photon begins to resolve structure at the level of individual partons, and no longer scatters from the nucleon as a whole. The contributions from two-photon exchanges has been shown to be small[9] so that the impulse approximation of a single photon, scattering incoherently, is generally assumed when discussing inelastic scattering.

Bjorken and Paschos built up their parton theory of inelastic scattering using a reference frame where the proton has infinite momentum[5]. In this frame the constituent partons share the proton's longitudinal momentum while their motion within the proton is slowed down by Lorentz time dilation. The muon discovers the proton in a particular virtual state and scatters off a single parton, as in

Figure 1.3. The time of interaction in the proton-muon center-of-mass system is:

$$\tau = 1/q_0 = 4E_0/(2m\nu - q^2) \tag{25}$$

The lifetime of the virtual state is given by:

$$T = \frac{[(xP)^2+\mu_1^2]^{1/2}}{[(1-x)^2P^2+\mu_2^2]^{1/2} - [P^2+m^2]^{1/2}} \tag{26}$$

Where μ_1 is the mass of the struck parton and μ_2 is the mass of the remaining partons. For large enough q^2, τ is much smaller than T, and the interaction is indeed highly incoherent. Bjorken and Paschos therefore claimed that there would be no time for the partons to interact among themselves during the interaction. This, and the assumption that partons are pointlike, led them to assert that the muon-parton interaction is elastic. The structure function for μp would be the sum of contributions from all possible muon-quark interactions[16].

The contribution from each quark is a delta function, affirming the elastic nature of the quark-muon interaction (Figure 1.4). The quark structure function is also weighted by the quark's charge squared, and its momentum:

$$W_2^i(\nu,q^2) = e_i^2 x_i \ \delta(\nu x_i - q^2/2m) \tag{27}$$

$$\nu W_2^i(\nu,q^2) = e_i^2 x_i \ \delta(x - q^2/2m\nu) \tag{28}$$

i = quark type

νW_2 for the whole nucleon is the sum of the convolutions of the quark structure functions (28) with the quark density functions (15):

$$\nu W_2^{\mu p}(q^2,\nu) = \sum_i \int_0^1 dx q_i(x) e_i^2 x\delta(x-q^2/2m\nu) \tag{29}$$

$$= \sum_i x e_i^2 q_i(x) = F_2(x) \tag{30}$$

The assumptions that there are no quark-quark interactions during the muon scattering (which would alter the quark density functions and give them a q^2 dependence), and that the quarks are pointlike (making the quark-muon interaction elastic), have resulted in the phenomenon of "Bjorken scale invariance." As $q^2 \to \infty$ and $\nu \to \infty$, the structure functions $\nu W_2(q^2,\nu)$ and $mW_1(q^2,\nu)$ no longer depend on the Lorentz invariants q^2 and ν independently, but only on their ratio $x=1/\omega=q^2/2m\nu$ which remains finite. This is seen in equations (29) and (30). Furthermore, in this quark-parton formulation of the inelastic scattering process, W_1 and W_2 are linked through the "Callen-Gross" relation[2]:

$$F_2(x) = 2xF_1(x) = 2xmW_1 \tag{31}$$

Besides making the scattering behavior apparently simpler, the result of depending only on the dimensionless quantity x, for large enough q^2 and ν, is to remove any mass or energy scale from the deep inelastic process.

In Figures 1.4 and 1.5 are shown the structure functions for quarks and protons respectively. Figure 1.5 (for q^2 held constant) shows some bumps at high x which correspond to the excitation of low-lying nucleon resonances. One would expect a flat distribution for

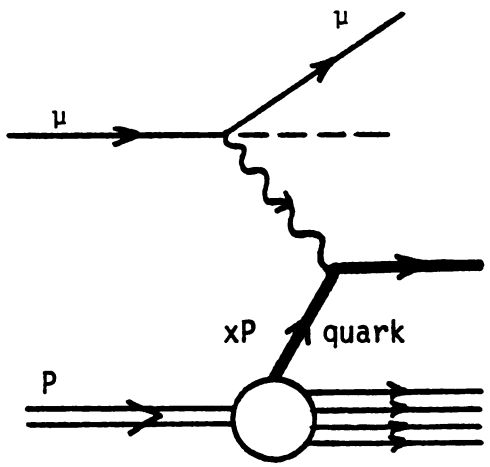

Figure 1.3
Incoherent scattering from a single parton with momentum xP

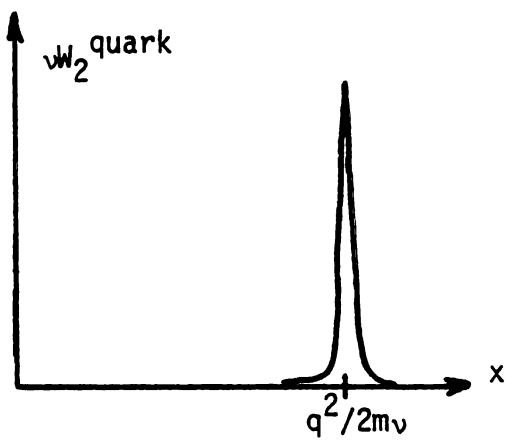

Figure 1.4
Quark structure function

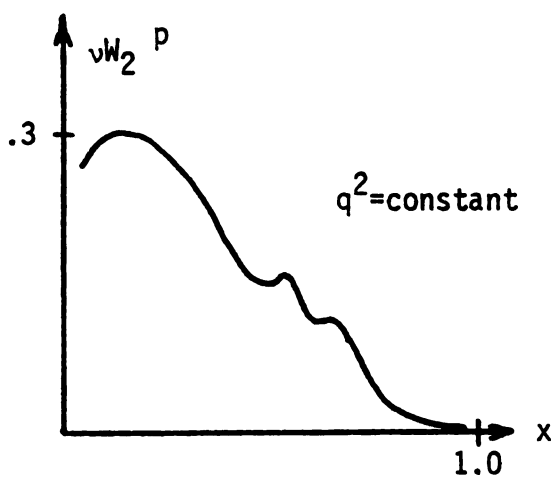

Figure 1.5
Nucleon structure function

νW_2 as a function of q^2 when x is held constant: this is the characteristic prediction of scale invariance.

Early experimental work by the SLAC-MIT group appeared to vindicate the scaling hypothesis[10]; this data is shown in Figure 1.6. At first it was puzzling why scaling should set in so early. For some values of ω, νW_2 flattens out (after an initial rise) at q^2 as low as $1(GeV/c)^2$. This "precocious scaling" is now believed to be a result of the relatively light parton masses (~100 MeV), and does not represent a premature attainment of an asymptotic condition for q^2 and ν.[11]

1.5 Gluons and Scale Breaking

Performing integrations over the quark density functions, using existing data and the sum rules devised in the quark-parton model, one finds that between thirty and fifty percent of the nucleon's momentum is carried by neutral partons other than the fractionally charged quarks[2]. These particles are the massless vector gluons which carry the color force between quarks.

In quantum electrodynamics (QED) the interactions of electrons with its electromagnetic field results in the radiation of photons, renormalizing the electron's mass and charge. Analogously, the radiation of gluons "dresses" the quarks and alters their density in the nucleon as probed by the incoming photon. Figure 1.7 shows again the scattering diagram for the deep inelastic process with no gluons present; the muon scatters off a single parton with momentum fraction z. The quark structure function in this case is a delta function (27); $F_2^{Quark} \simeq \delta(x/z - 1)$, where $x=q^2/2m\nu$.

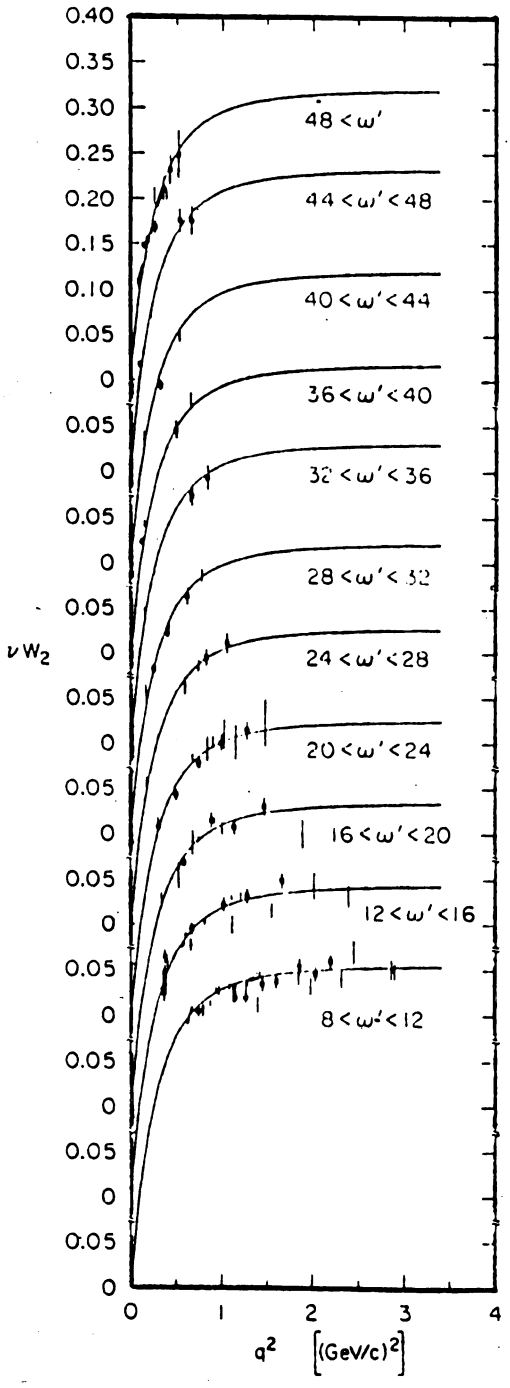

Figure 1.6 SLAC-MIT data (ref. 10) showing approximate scaling in the modified scaling variable $\omega'=2m\nu/(q^2+m^2)$

In Figure 1.8, the supposed effects of gluons are illustrated. Gluon bremsstrahlung is possible on the leading or trailing legs of the quark current (1.8 a, b); vertex corrections are also possible (1.8 d). At small x ($x \lesssim .2$), quark-antiquark pair production can occur (1.8 c). The effects shown in Figure 1.8 all depend on the size of the structure being probed; the quark density functions therefore regain a q^2 dependence. The new terms depend logarithmically on q^2:[12]

$$F_2^{quark} = F_2^{quark}(x,q^2) \simeq \delta(\frac{x}{z} - 1) + g^2\, a(\frac{x}{z}) \ell n(q^2/q_0^2) \qquad (32)$$

where g is the quark-gluon coupling constant (analogous to α, the electron-photon coupling constant in QED), q_0^2 is a reference q^2, and a is a function of the ratio x/z to be discussed in the next section.[13]

Besides possibly accounting for violations of scaling, as in equation (32), gluon bremsstrahlung may be responsible for the high $P_\perp$ scattering observed in hadron-hadron collisions. In inelastic collisions, the quantity $R=\sigma_L/\sigma_T$ should be zero since $\sigma_L=0$ for spin 1/2 quarks from helicity conservation. Figure 1.9 shows how the emission of a gluon can impart a transverse momentum to a single quark such that the photon now has a polarization component which is longitudinal with respect to the quark. H. D. Politzer[12] computes this effect in QCD:

$$R = \sigma_L/\sigma_T = \frac{4\langle P_\perp^2\rangle}{Q^2} \simeq \frac{1-x}{2\log Q^2/\Lambda^2} \simeq \frac{1-x}{2\log 4Q^2} \qquad (33)$$

Therefore $$\langle P_\perp^2\rangle \simeq \frac{(1-x)Q^2}{8\log 4Q^2} \qquad (34)$$

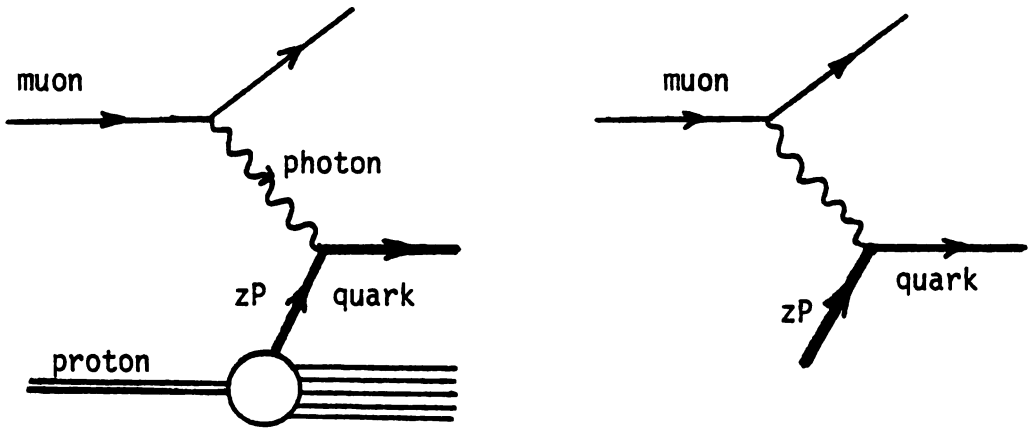

Figure 1.7 Deep inelastic scattering without gluons: $F_2^{quark} \simeq \delta(x/z-1)$

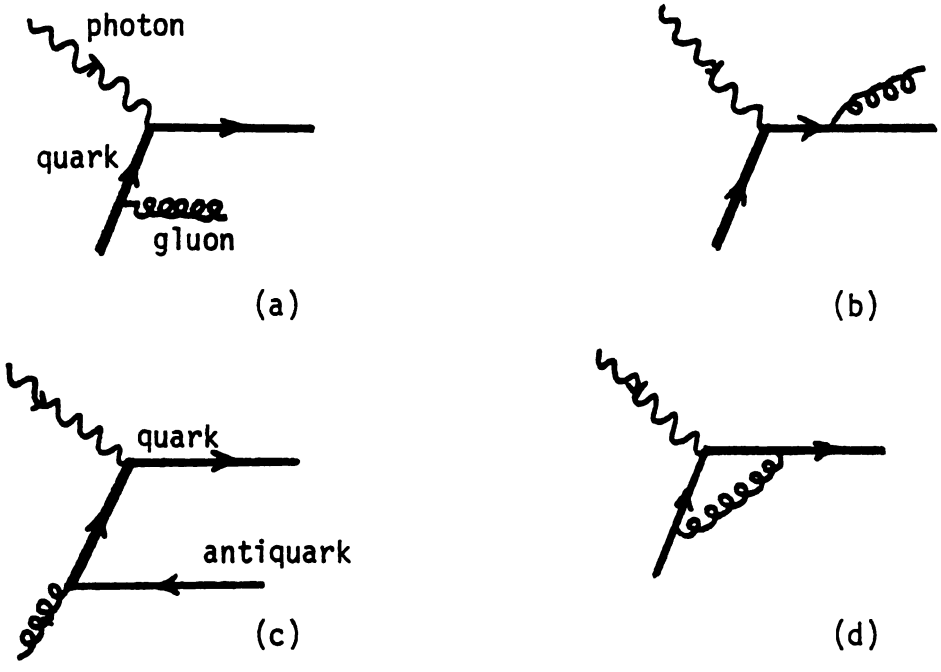

Figure 1.8 Gluon correction terms: $F_2^{quark} \simeq \delta(x/z-1)+g^2a(x/z)\ln(q^2/q_0^2)$

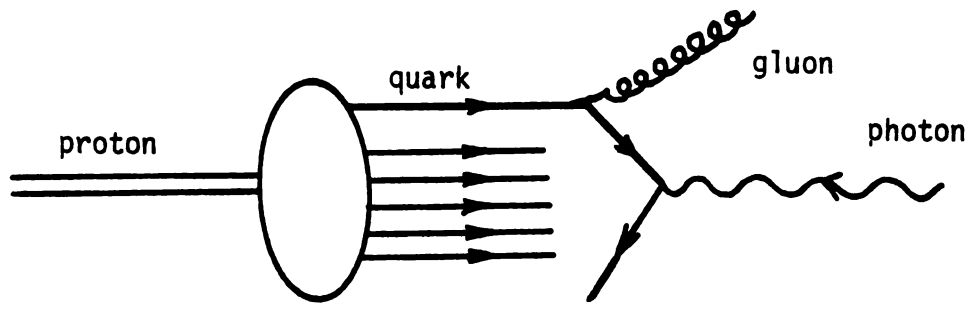

Figure 1.9 Nonzero σ_s and $p_\perp$ related to gluon bremsstrahlung

Thus the gluon-bremsstrahlung induced "Fermi motion" within the nucleon contributes a scale violating term to the cross section, provides for a nonzero value of R, and could help explain Drell-Yan processes.[25]

After the initial success of the scaling hypothesis at SLAC[10], several experiments were conducted at higher values of q^2 and ν. The results of these experiments indicated that scaling is indeed violated, that is, that the structure function F_2 does possess a q^2 dependence for fixed x. μ-Fe [14], e-p [15], μ-d [16], and μ-p [17] data show scale breaking effects. Similar results in neutrino scattering are summarized by Perkins, Schreiner, and Scott.[18] Figure 1.10 shows the μ-Fe results. In this figure, the ratio [Data events]/[Monte Carlo events] (which is proportional to F_2) is plotted versus q^2 for constant $\omega=1/x$. A definite q^2 dependence is present.

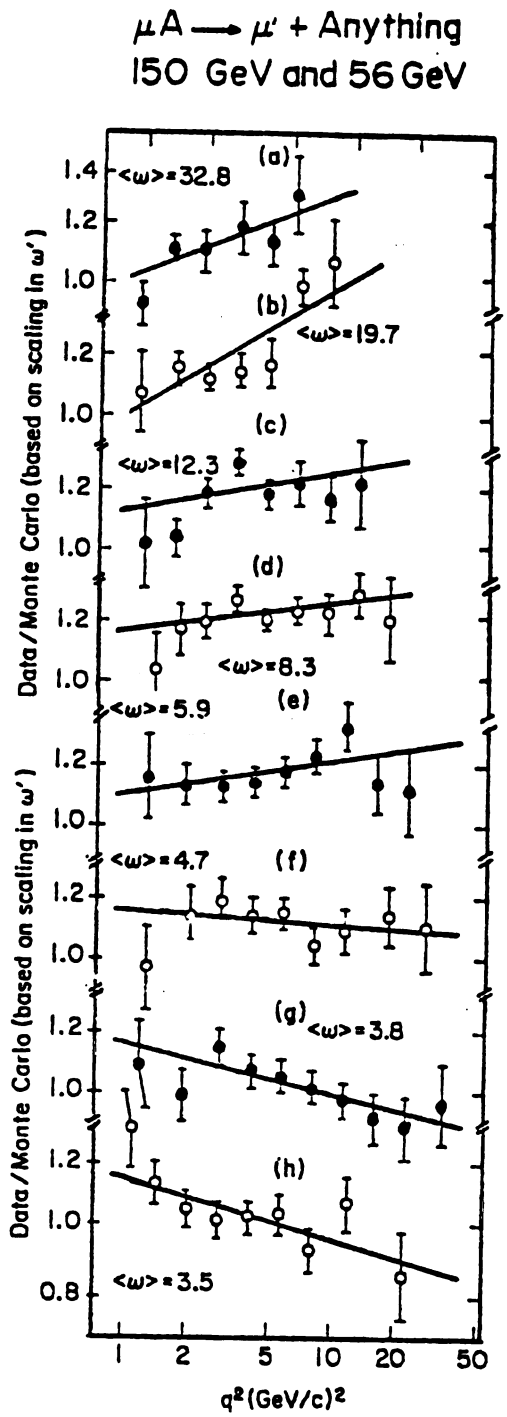

Figure 1.10 μ-Fe scale violation results

At first an effort was made to recover scaling by defining new scaling variables. Indeed, by using the variable $\omega'=\omega+m^2/q^2$ some of the scale-breaking tendencies apparently disappear.[19] But the violations persisted to even higher values of q^2 ($\simeq 40(GeV/c)^2$), and the breaking of scaling is now reasonably established.

The demise of scaling has been an important development in the study of constituent theories of the nucleon. The field theory which seeks to explain how these violations come about is known as quantum-chromo-dynamics (QCD). It is a gauge theory of gluon-quark interactions and calculates the gluon radiative correction terms illustrated in Figure 1.8. It is thought by some that QCD will be the field theory which can explain the strong interaction and possibly unite it with the weak and electromagnetic interaction as well.[20]

1.6 QCD

Equation (7a) expressed the tensor for the hadron part of the deep inelastic matrix element ($|f\rangle$ = final state).

$$W_{\mu\nu} = \sum_X \langle p|J_\mu(-q)|f\rangle\langle f|J_\nu(q)|p\rangle 2\pi\delta(P+q-x) \tag{35}$$

But since $$\delta(P+q-P_f)= \int d^4x\, e^{i(P+q-P_f)\cdot x} \tag{36}$$

and $$\langle p|J_\mu(-q) = \langle p|e^{-iqx}J_\mu(0)\, e^{iqx} \tag{37}$$

then $$W_{\mu\nu} = \frac{1}{4\pi}\int d^4q\, e^{iq\cdot x}\langle p|J_\mu(x)J_\nu(0)|p\rangle \tag{38}$$

The commutation of the two currents is $[J_\mu(x), J_\nu(0)] = J_\mu(x)J_\nu(0) - J_\nu(0)J_\mu(x)$. The integral over the second term is zero from momentum conservation,[2] so that (38) can be rewritten:

$$W_{\mu\nu} = \frac{1}{4\pi} \int d^4x \, e^{iq\cdot x} \langle p|[J_\mu(x), J_\nu(0)]|p\rangle \qquad (39)$$

In other words, $W_{\mu\nu}$ is equivalent to the Fourier transform of the one-nucleon expectation value of the current commutator.

A lot of theoretical work has been devoted to the study of equation (39).[20] The right hand side of (39) can be expanded using Wilson's operator product expansion.[21] The operators in this expansion are characterized by a spin n (tensor rank) and by their "twist" (dimensionality minus two).[22] Pursuing this technique, one arrives at an expression for the moments of F_2 but not F_2 itself. The n^{th} moment is described in terms of spin-n operators only:[23]

$$M(n,q^2) = \int d\xi \, \xi^{n-2} \, E_n(\xi,q^2) F_2(\xi,q^2) \qquad n=2,4,6,... \qquad (40)$$

$$E_n(\xi,q^2) = (1 - m^4\xi^4/q^4)(1 + q^2/\nu^2)\left(1 + 3 \, \frac{(n+1)m\nu\xi - (n+2)q^2}{(n+2)(n+3)(\nu^2+q^2)}\right) \qquad (41)$$

In these expressions, a new scaling variable is introduced to account for the mass of the target proton and differs from x only at small q^2:[24]

$$\xi = \frac{1}{m}\left(\sqrt{\nu^2+q^2} - \nu\right)$$

For larger q^2 ($\simeq 10(\mathrm{GeV/c})^2$) a simpler formula for the moments can be used

$$\tilde{M}(n,q^2) = \int_0^1 dx\ x^{n-2} F_2(x,q^2) \tag{42}$$

In expanding (39) and in formulating the moments, there are two approximations which are conventional in QCD. Firstly, for a reference $q_0^2 \lesssim 3\ (\mathrm{GeV/c})^2$ one need only keep the "leading contributions" from twist 2 operators. Secondly, for $q^2 > 3$, the running coupling constant $\alpha_s(q^2) = g^2/4\pi$ is less than 0.3 so that only the lowest order perturbation term need be kept. This leads to the QCD operator expansion for the deep inelastic structure function moments:[22]

$$M(n,q^2) = \sum_{k=0}^{f} e_k^2\ [e^{-s\lambda(n)}]_\beta^k\ A^\beta(n,q_0^2) \tag{43}$$

In this expression, k=0,..2f (quark flavors), e_k=quark charge (k=0 corresponds to gluons so that e_0=0), $s = \ell n\left[\frac{\ell n q^2/\Lambda^2}{\ell n q^2/q_0^2}\right]$, and $\lambda(n)$ is the color matrix of gluons. By comparing this expression for $q^2=q_0^2$,

$$M(n,q_0^2) = \sum_i e_i^2\ A^i(n,q_0^2) \qquad i=1,\ldots,f \tag{44}$$

with the parton model expression for $F_2(x,q_0^2)$ (16):

$$F_2(x,q_0^2) = \sum_i e_i^2\ x\ q_i(x) \qquad i=1,\ldots,f \tag{45}$$

one can interpret $A^i(n,q_0^2)$ as the moment of the quark density function $q_i(x)$ at $q^2=q_0^2$. Note that gluons do not contribute to either (44) or (45) (since $e_{gluon}=0$), but this is true only at the renormalization point $q^2=q_0^2$. Equation (43) shows how the gluon (k=0) and quark (k=1,...f) contributions to $M(n,q^2)$ are mixed together by the non-diagonal matrix $\lambda(n)$ for $q^2 > q_0^2$. The method for computing the gluon distribution function, and the expression for the elements in the λ matrix, are given in reference [22]. The method for finding quark density functions will be described in chapter five at which time a QCD prediction for $F_2(x,q^2)$ will be compared with the present deep inelastic data.

Figure 1.11 shows how the interdependence of gluon and quark densities comes about. Radiated gluons can split into quark-antiquark pairs of "sea" quarks which in turn can radiate gluons. In QCD, the virtual photon in deep inelastic scattering probes this complex system and not just a single bare quark. In equation (32) I indicated that the result of gluon-quark interactions was to introduce a scale-breaking term $g^2a(z/x)\ell nq^2/q_0^2$. A typical diagram is shown in Figure 1.12 where the muon scatters from a sea quark with momentum zP which was pair produced from a parent parton (a gluon in this case) with momentum xP. At small values of x this scattering from a sea quark will exceed that of valence quarks. Altarelli[13] gives a detailed account of how such diagrams arise in QCD and how the quark and gluon densities are effected by the logarithmic q^2 term:

$$\frac{dq_i(z,t)}{dt} = \frac{\alpha_s(t)}{2\pi} \int_z^1 \frac{dx}{x} [q_i(x,t)\ P_{qq}(z/x) + G(x,t)P_{qG}(z/x)] \qquad (46)$$

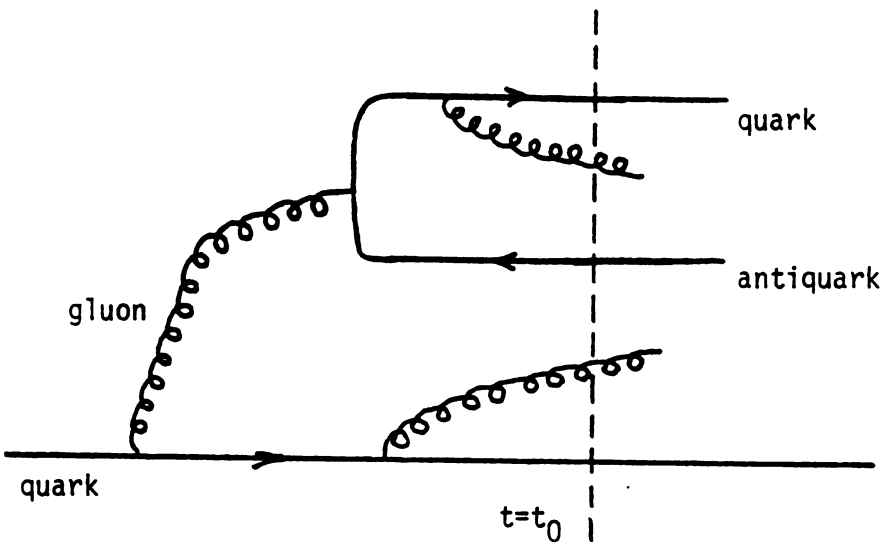

Figure 1.11 Constituents of the quark in QCD renormalization

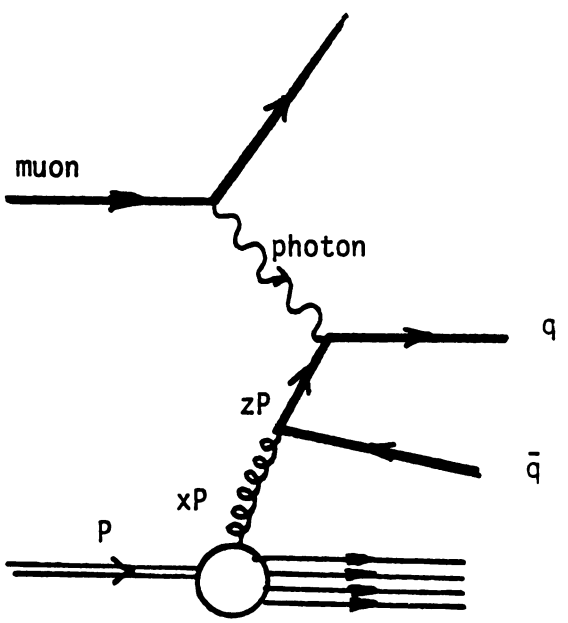

Figure 1.12 Gluon pair production of quarks

$$\frac{dG(z,t)}{dt} = \frac{\alpha_s(x)}{2\pi} \int_z^1 \frac{dx}{x} \left[\sum_i^{2f} q_g(x,t) P_{Gq}(z/x) + G(x,t) P_{GG}(z/x) \right] \qquad (47)$$

where $t = \ell n q^2/q_0^2$, f = number of quark flavors, and q_i and G are the quark and gluon densities. The function $P_{qq}(z/x)$ is the probability that a quark with momentum zP is contained in a quark with momentum xP, $P_{qG}(z/x)$ is the probability that a quark with momentum zP is to be found within a gluon with momentum xP (Figure 1.12). There are also terms for gluons within quarks and for gluons inside gluons: unlike photons in QED, gluons in QCD can interact with other gluons. Equations (46) and (47) show how the quark and gluon densities observed at momentum zP (gluon densities are measured indirectly[22]) are a function of parent quark and gluon densities at momentum xP (where there is an integration over x from z to one). Except for the gluon-gluon interaction (gluons carry color while photons do not carry charge), this heirarchy of partons within partons is similar to QED where electrons are said to be made from electrons and photons.[26,27] The level of this hierarchy at which the virtual photon probes is determined by $t=\ell n q^2/q_0^2$.

The use of perturbation theory in QCD is made possible by asymptotic freedom. The running gluon-quark coupling constant is a logarithmically decreasing function of q^2:

$$\alpha_s(k) = g^2/4\pi = \frac{12\pi}{(33-2f)\ell n(q^2/\Lambda^2)} \qquad (48)$$

where Λ is a mass parameter believed to be about $0.5(\text{GeV/c})^2$.[23]

At larger q^2, the level of hadronic structure being explored is smaller. At these smaller inter-quark distances, the coupling constant α, and therefore the strength of the interaction, is smaller. The principle of asymptotic freedom ($\alpha \to 0$ as $q^2 \to \infty$) is related to the current theories of quark confinement, theories which hypothesize that the "strong" interaction (color force) increases at larger quark-quark separations; and decreases at small separations.[14,26]

1.7 Experiment 319

The purpose of Experiment 319 was to extend the study of scale invariance to higher kinematic limits with better statistics, and to observe certain multimuon final states. This dissertation is a report of the 270 GeV μ^+ data (single muon in the final state) recorded during E319. The structure function $\nu W_2 = F_2(x,q^2)$ is plotted versus q^2 and x and compared to results of previous deep inelastic tests of Bjorken scale invariance. The observed νW_2 is also compared with a QCD prediction which uses some of these previous results as input.

So far, the kinematic region for comparison of deep inelastic data to theory has been roughly $0 \leq q^2 \leq 40(\text{GeV/c})^2$ and $0 \leq \nu \leq 130\,\text{GeV}$.[9,13,14,15,16] Experiment 319, which our group performed at Fermilab in 1976 significantly expands this region, as shown in Figure 1.13.

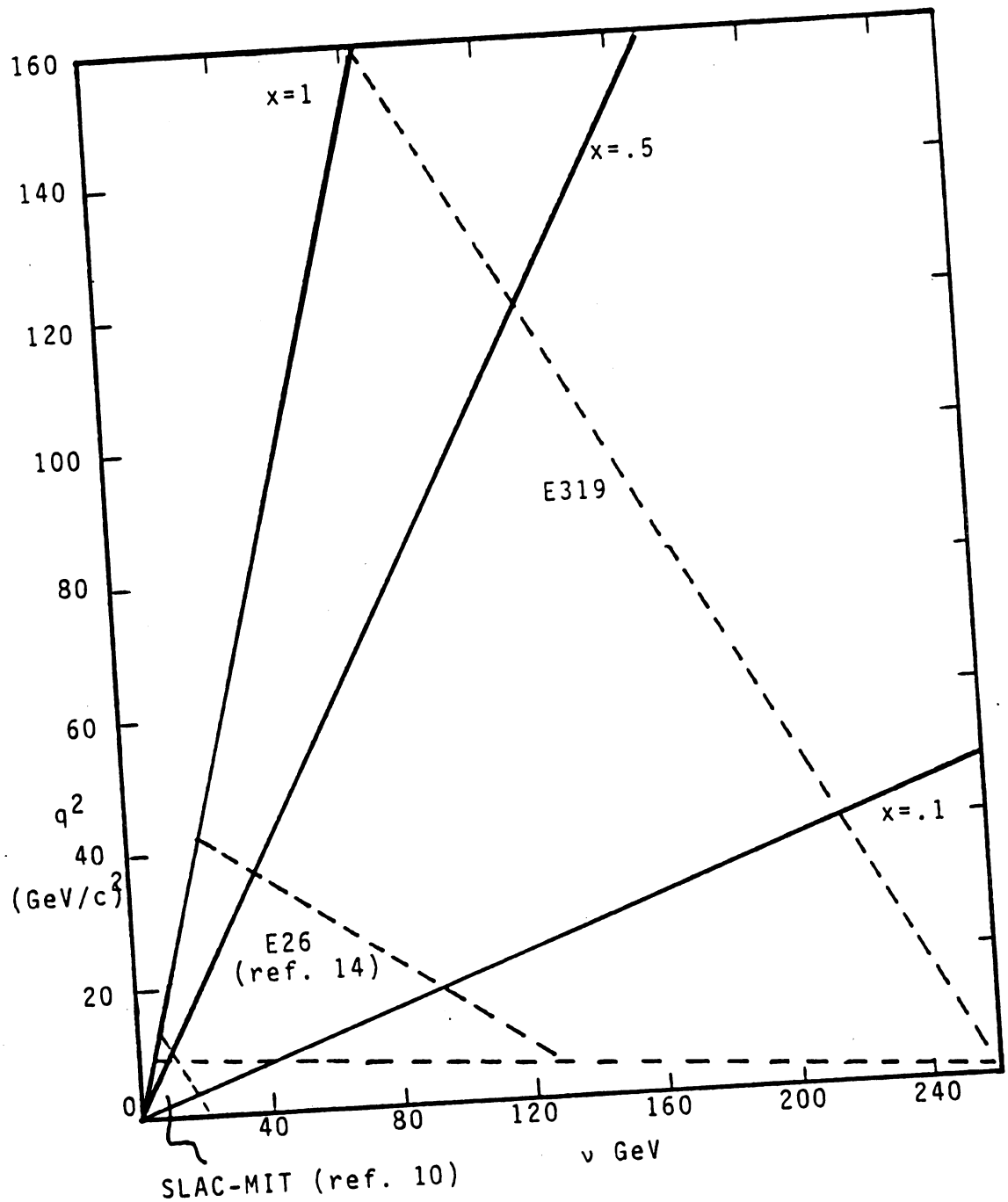

Figure 1.13 Kinematic region of E319

CHAPTER II

THE APPARATUS AND DATA TAKING

2.1 Fermilab Muon Beam Line

The external proton beam at the Fermi National Accelerator Laboratory can be divided and directed toward three principal experimental areas: the proton area, the neutrino area, and the meson lab. Since the neutrino area (of which the muon lab is a part) requires such high intensities for producing secondary beams (muon and neutrinos), it frequently receives the largest share of the main ring's protons.

The proton beam is steered into the neutrino hall where it is focused onto a cylindrical solid aluminum production target 0.75" in diameter and 12" long. This target, and the magnets which bend and focus the proton beam and the beam of produced particles, are mounted on a train car on railroad tracks. The "triplet train," containing three sets of extra focusing quadruples, is the configuration designed for muon experiments. The magnets and their currents used during the 270 GeV μ^+ running are listed in Table 2.1. After striking the production target, the unscattered proton beam is deposited in a beam dump while the production products, mostly pions with about ten percent kaons, travel down a 300 m pipe and are allowed to decay. The secondary decay products, mostly muons and neutrinos, are then used in specially designed experiments.

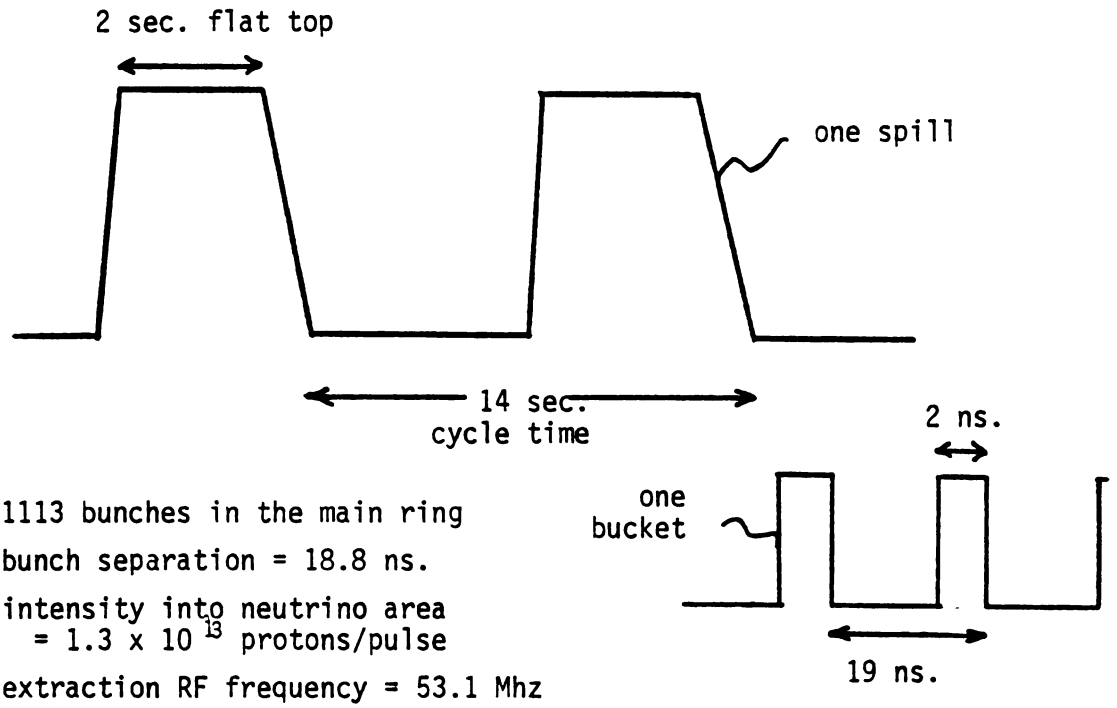

Figure 2.1 Properties of the primary proton beam

Table 2.1 Magnet currents in Neutrino Hall

Magnet	Setting(amps)	Reading(amps)
OUT	290	281-284
OVT	15	15.5
OHT	121	117.5
OFT1	96.2	92.5
OFT2	95.6	92.4
ODT	2777	2690
OPT	3102	2978
OPT3	3177	3060

At the end of the decay pipe the charged particles are swept out into the N1 beam line. If a pure muon beam is desired, the remaining hadrons in the beam can be absorbed using polyethylene inserted into the gap of the bending magnets. During E319, 60' of CH_2 was in place, so that the effective hadron contamination in the muon beam was roughly 10^{-6}. The energy-selected muon beam is then brought into the muon lab via a series of bending, pitching, and focusing magnets. Figure 2.2 shows the N1 muon beam line leading into the muon lab.

2.2 Tuning the Muon Beam

Figure 2.3 shows the last leg of the muon's journey into the muon lab along with the proportional chambers and scintillation counters used to define the beam trajectory and momentum. 1F3 and 1D3 in enclosure 103 are sets of quadrupole magnets used to focus the beam on the face of the E319 target.

In enclosure 104 the 1E4 magnets steer the muon beam through its final bend (28.7 mr) and are used for finding the energy of each beam muon. In Figure 2.3 HA and HB are beam hodoscopes, arrays of 3/4" wide scintillator counters which help to locate the position of each muon. The beam counters B_1, B_2, and B_3 define a preliminary beam trigger. Besides the beam hodoscopes, several proportional chambers were used to accurately establish a linear trajectory before and after the bending magnets; these are located in enclosure 104 and in the muon lab. We also had the help of several E398 (the Chicago-Harvard-Illinois-Oxford μ-p experiment upstream of our apparatus) chambers for this purpose. These are labelled by plane orientation (x or y).

The magnetic field in the 1E4 bending magnets was calibrated using an NMR probe, a gaussmeter, and a very accurate pole-face magnet. The

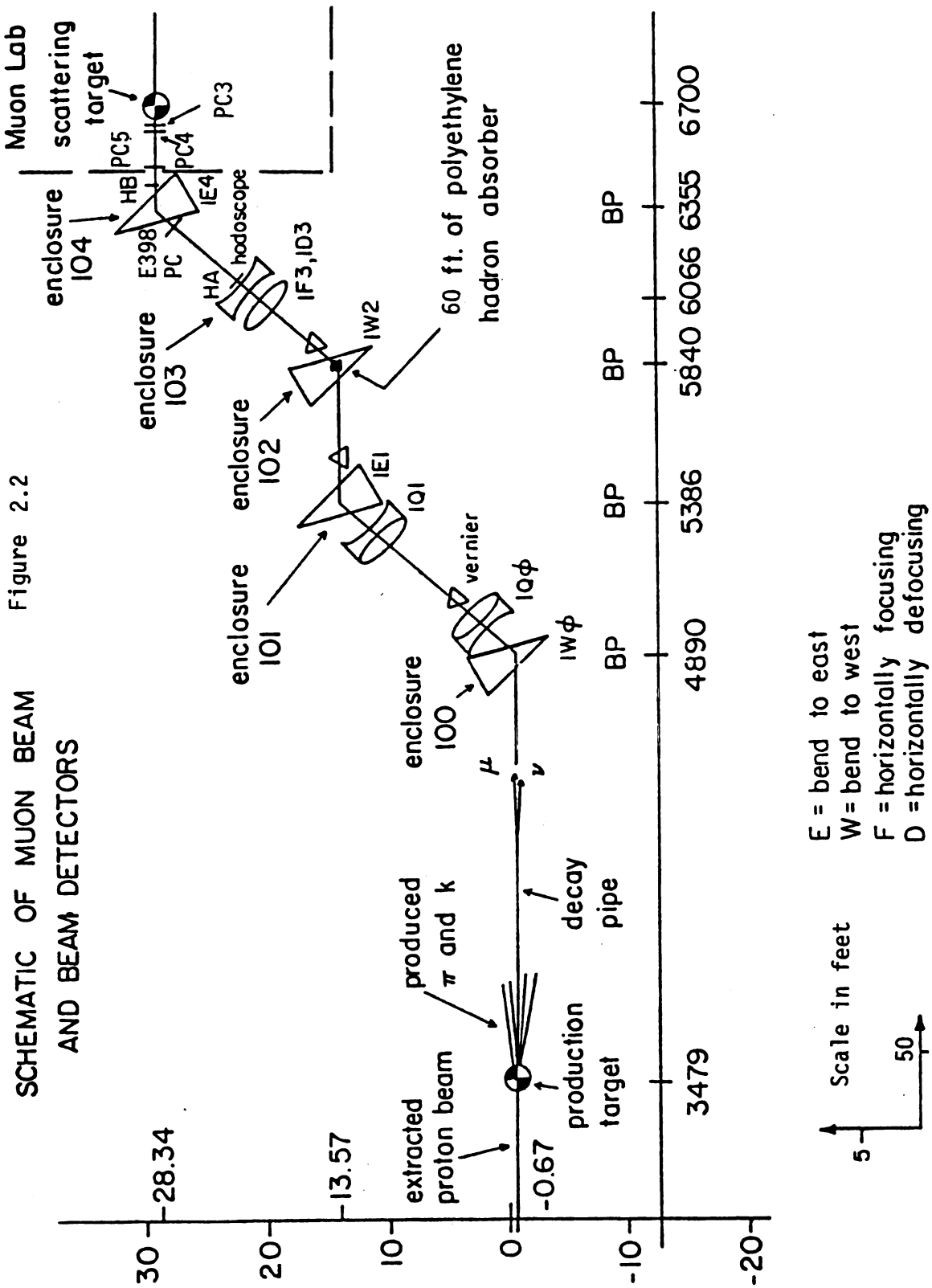
SCHEMATIC OF MUON BEAM AND BEAM DETECTORS
Figure 2.2
Muon Lab
scattering target
PC5
PC4
PC3
HB
IE4
hodoscope
enclosure 104
E398 PC
HA
IF3,ID3
enclosure 103
IW2
60 ft. of polyethylene hadron absorber
enclosure 102
IE1
ID1
enclosure 101
vernier
IQφ
IWφ
enclosure 100
μ
ν
produced π and k
extracted proton beam
production target
decay pipe
28.34
13.57
-0.67
BP
3479
4890
5386
5840
6066
6355
6700
30
20
10
0
-10
-20
Scale in feet
5
50
E = bend to east
W = bend to west
F = horizontally focusing
D = horizontally defocusing

Figure 2.3 Proportional Chambers and Beam Counters

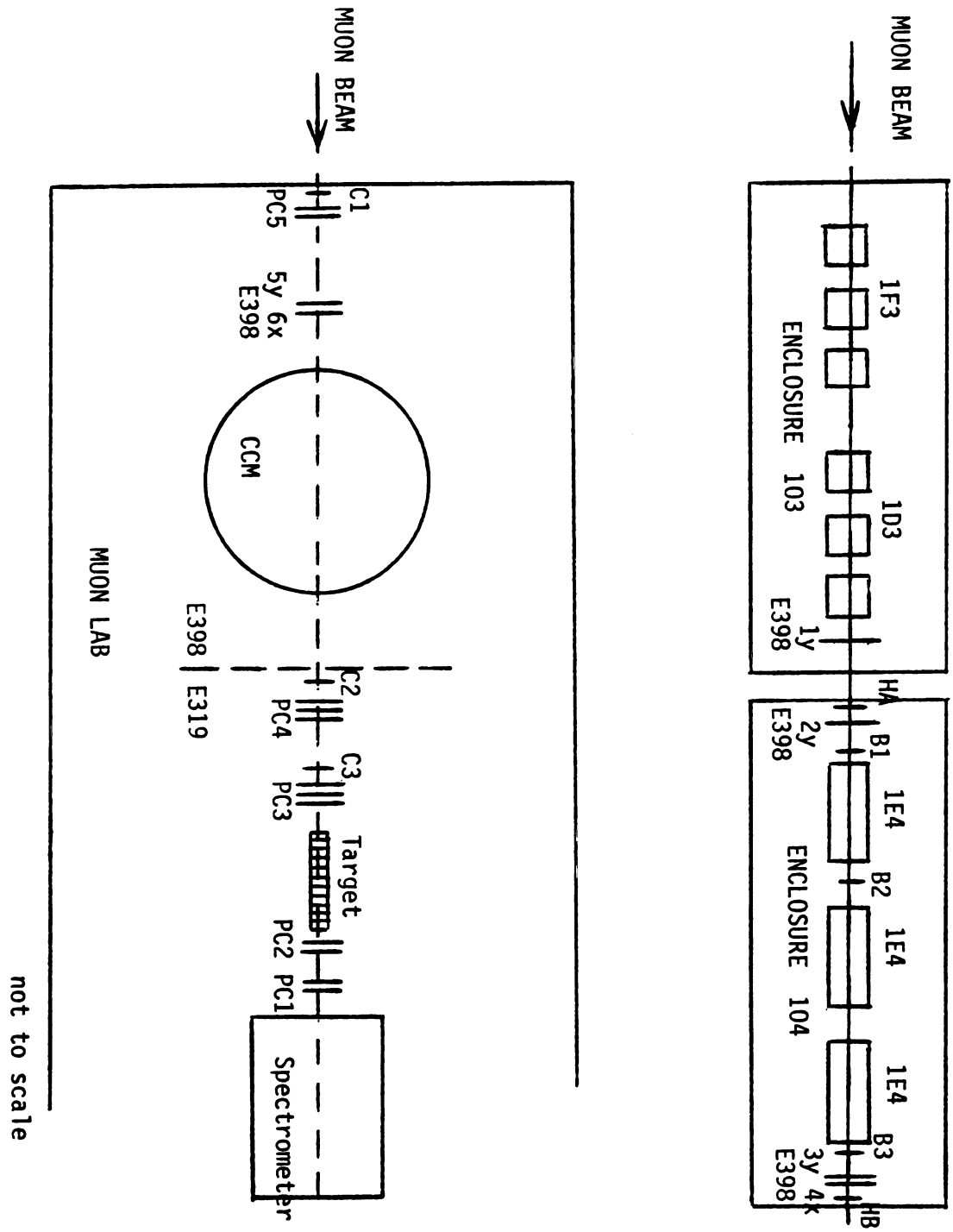

measurement of the field as a function of the longitudinal coordinate (along the beam axis) is shown in Figure 2.4. This gives the effective length of the magnet. Table 2.2 gives a fit to the magnet field as a function of magnet current. The momentum spread of the beam at enclosure 104 is about 2% while the measurement uncertainty in E_0, the energy of individual beam muons, is about 0.4%.

After enclosure 104, the muons travel straight into the muon lab, through the E398 apparatus (shutters are opened in the E398 hadron shield), and into the E319 target where the spot size is an oval about 15 cm wide (east-west) and about 12 cm high (up-down). The intensity, energy, and focus of the beam could be controlled from a console located in the muon lab, from which the currents for all of the muon beam line magnets could be adjusted. These currents, both the settings and the measured values, are listed in Table 2.3. These currents were used for a majority of the 270 GeV μ^+ runs although there were some variations.

2.3 The E319 Apparatus

The B counters (3.5" diameter) and the C counters (7.5" diameter) shown in Figure 2.3 act as a beam trigger. The proprotional chambers PC5, PC4, and PC3 record the coordinates of the muon's trajectory up to the E319 target. Following the target is the rest of the E319 apparatus which serves to detect scattered muons and measure their momenta. A complete layout is shown in Figure 2.5, while the z coordinate of each apparatus element is listed in Table 2.4.

2.4 Target/Calorimeter

During the principal 270 GeV μ^+ running, the target-calorimeter consisted of 110 sandwiches each comprising a 20" x 20" x $1\frac{7}{8}$" slab of

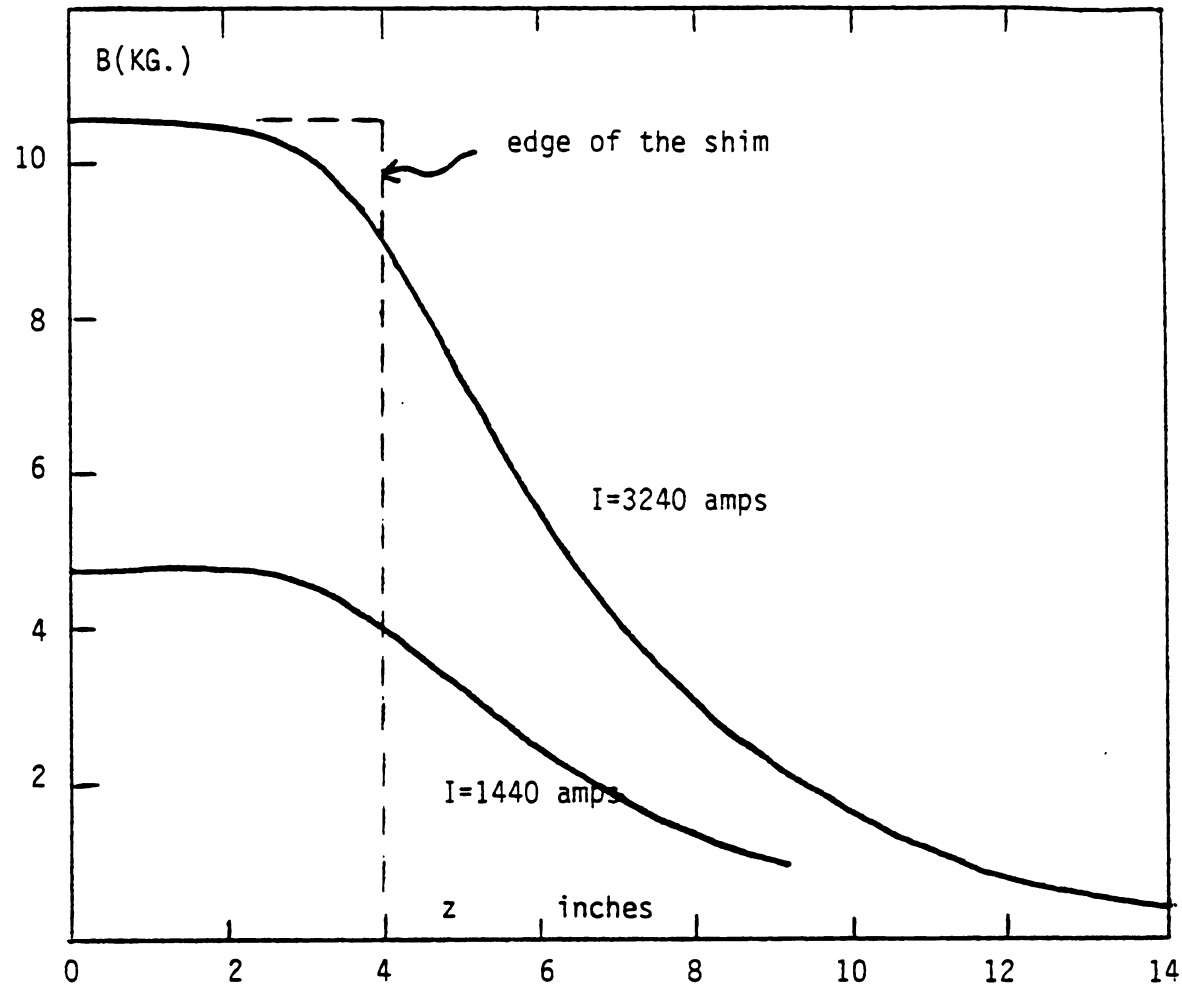

Figure 2.4 Magnetic field in 1E4 dipoles

Table 2.2 Calibration of the 1E4 dipoles

$B(KG) = aI^2 + bI + c$ I=current(amps)

	Runs before 8/23/76	Runs after 8/23/76
a	$(-.5964 \pm .6656) \times 10^{-8}$	$(-.1714 \pm .6134) \times 10^{-8}$
b	$.32892 \times 10^{-2} \pm .3015 \times 10^{-4}$	$.33635 \times 10^{-2} \pm .2658 \times 10^{-4}$
c	$-.03107 \pm .0273$	$-.032787 \pm .0273$
χ^2/dof	0.10	0.10

Table 2.3 N1 muon beam line magnet settings at 270 GeV μ^+

Magnet	Type	Setting(amps)	Reading(amps)
1W01	bend	0	4630
1W02	bend	4332	4190-4180
1W03	bend	4832	4630
1V0	pitch	25	106.25
1F0	focus	370	361.5
1D0	focus	370	353-350
1Q1	focus	4175	4000
1E1	bend	3862	3715-3720
1V1	pitch	120	8.125
1W2	bend	3712	3540
1F3	focus	940	918.747
1D3	focus	980	955
1E41	bend	4319.98	4237.48
1E42	bend	0	4234-4230

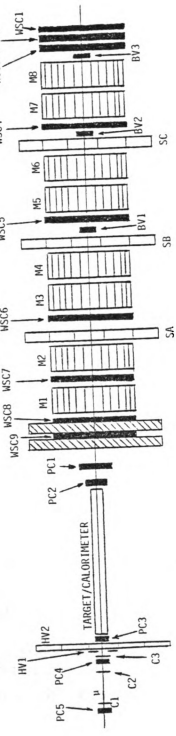

Figure 2.5 E319 Apparatus

Table 2.4 z positions for elements in the E319 apparatus

Distances, in cm., are measured from the muon lab zero reference stud

E319 PC's	1. 649.765		Trigger Banks	SA	1148.9
	2. 625.318			SA'	1170.7
	3. -235.346			SB	1427.8
	4. -517.764			SB'	1449.9
	5. -3685.54			SC	1710.5
				SC'	1731.9
E398 PC's	1. -15512.95				
	2. -8512.305				
	3. -6393.487		Beam Veto	I	1464.8
	4. -6393.487			II	1746.7
	5. -3294.281			III	1972.2
	6. -3294.281				
E319 target	upstream end -166		Halo Veto	I	-480
	downstream end +572			II	-400
	total length 738				

Magnets	position	length
	1. 1911.193	78.90
	2. 1822.770	77.95
	3. 1655.128	78.74
	4. 1565.593	78.58
	5. 1370.330	79.06
	6. 1282.700	78.03
	7. 1092.678	78.98
	8. 978.555	78.98

WSC's	1. 2190.433	
	2. 2086.29	
	3. 1988.03	
	4. 1761.49	
	5. 1478.92	
	6. 1201.42	
	7. 1035.37	
	8. 922.02	
	9. 848.68	

Hadron Shield	upstream piece 61.6 cm. thick	front edge: z=736
	downstream piece 37.5 cm. thick	front edge: z=870
	84" high x 145" wide	

iron followed by a 20" x 20" x $\frac{3}{8}$" scintillator counter. The effective density of the target is calculated in Table 2.5. When a muon interacts in the iron, the resultant hadronic shower deposited a characteristic amount of energy in the scintillators, which were observed by RCA 6342 A phototubes (gain = $.4 \times 10^6$). These signals were digitized by LRS 2249-A analog-to-digital converters and used to determine the energy of the hadronic shower, in addition to finding the interaction vertex. Calibration of the calorimeter was achieved by directing beams of hadrons (90% pions and 10% protons) at fixed energy into the target and then measuring the total digitized signal. Also, by using a standard light pulse from a light-emitting diode attached to the face of each scintillator, the effect of a single minimum-ionizing muon could be simulated. The following results for an optimum voltage of 1400 V were observed: signal/noise = 26.4, anode current = 62 mA, and anode charge = 18 pC. The construction and calibration specifications are given in greater detail in the dissertation of D. Bauer.[28]

The use of the calorimeter for finding hadron energy has been a disappointment so far. It was feared that the electrical noise from spark chamber firings had disrupted the ADC gate pulse. This resulted in an apparent discrepancy between the hadron energy as found by the calorimeter and that found using the spectrometer. Since these two measurements are redundant, it has been possible to proceed with the data analysis without the benefit of the calorimeter. Recently though, the calorimeter mystery has been solved; the problem was in the way ADC pedestals (digitized signal for zero input) were being assigned, and not a faulty gate signal. This means that calorimeter results will appear in all future analyses of the data, but not in this dissertation.

2.5 Proportional Chambers

The proportional chambers, on loan from Cornell University, were used to observe the incident beam track and, downstream of the target, to determine the scattered muon's trajectory before entering the spectrometer. Each wire was monitored continuously and its status (fired or not fired) sent to a latch where it could later be read by the computer and stored on tape. The PC latches were cleared by a PC reset pulse while a second pulse, the PC strobe, enabled the latches only during the brief instant following an "interesting" event, as defined by a fast pre-trigger. Some features of the proportional chambers are described in Table 2.6. Construction details can be found in the thesis of Y. Watanabe.[29]

2.6 Spectrometer

HADRON SHIELD

Before entering the spectrometer the muon must pass through the hadron shield, two slabs of iron used to protect the forward wire spark chambers from the hadron shower particles which frequently emerge from the rear of the target. These slabs were 61.6 cm and 37.5 cm thick and covered the whole face of the spectrometer. The presence of hadrons in the spark chambers remained a slight problem, although not nearly as bad as in the previous muon experiment, E26.

WIRE SPARK CHAMBERS

The E319 spectrometer consists mainly of trigger banks to signal a scattering event, toroid magnets for deflecting the muon, and spark chambers for recording the muon's trajectory. Each spark chamber module consists of two pairs of planes; one set of planes (x-y)

Table 2.5 Target/calorimeter density

The E319 calorimeter consists of 110 Fe-scintillator sandwiches

Fe	110 x $1\frac{7}{8}$" = 523.9cm x 7.87 gm/cm^3	=4123.09 gm/cm^2
Scint.	110 x $\frac{3}{8}$" = 104.8cm x 1.032 gm/cm^3	= 108.15 gm/cm^2
Vinyl	110 x 2 x .015" = 8.4cm x 1.39 gm/cm^3	= 11.68 gm/cm^2
Al.foil	110 x 4 x .006" = 2.64cm x 2.70 gm/cm^3	= 7.13 gm/cm^2
Air	110 x $\frac{3}{8}$" = 104.8cm x .0012 gm/cm^3	= .13 gm/cm^2
		4250 gm/cm^2

effective density=4250gm/cm^2 /738cm

= 5.759 gm/cm^3

no. targets/cm^2 = 5.759gm/cm^3 x 738cm x 6.022x10^{23}atoms/mole x 56 targets/atom /55.85gm/mole

= 2.5 x 10^{27} target nucleons/cm^2 (the target is not entirely iron)

Table 2.6 Proportional Chamber system

PC	Planes	Active area in cm.
1	x y	38.4x38.4
2	x y	32 x 32
3	u v w	19 cm diameter
4	u v w	19 cm diameter
5	x y	19 x 19

wire spacing = 2.0 mm.

PC reset pulse = 10-15 ns.

PC Strobe pulse = 90-100 ns.

Gas mixture
.263 % Freon 13B1
20.0 % Isobutane
3.92 % Methylal
balance = Argon

Typical voltage = 5 kv.

covered with wires placed at right angles, and another set of orthogonal wire planes (u-v) oriented at 45° to the first pair, mounted immediately behind them in the same external aluminum frame. Each plane of wires was placed at a large voltage difference with respect to its mate. An event trigger would cause a spark breakdown in a polished brass spark gap which in turn caused a spark discharge between the two orthogonal wire planes along the path of ions left in the wake of an ionizing high energy particle. The wire in each plane nearest the spark carried the current to one edge of the chamber (the other edge was damped) where an acoustic wave was induced in a magnetostrictive wire lying in a trough running the whole length of the chamber. This wire was encased in a plastic catheter which was filled with Argon to diminish corrosion. The catheter was mounted in a long narrow aluminum channel known as a "wand." This is positioned beneath the current-carrying wires of the chamber itself. The acoustic wave, induced by the passage of the current at 90°, propagated toward the end of the wand where it was detected by a small pick-up coil and amplifier assembly. The signals from as many as eight sparks can be detected in this way. The train of pulses from each wand is sent along to a discriminator and digitized by comparing the time of arrival with an accurate clock signal. Knowing the physical distance between the fiducial wires at either side of the chamber (giving fiducial pulses), one can calculate the spatial coordinate of each spark in each wire plane. The digitized signals from each plane (x,y,u,v) and each chamber (1-9) are recorded on magnetic tape. There are thus 36 planes of spark chamber information, a complete record of the muon's passage through the spectrometer. A view of one corner of a spark chamber is shown in Figure 2.6 while general properties of the chambers

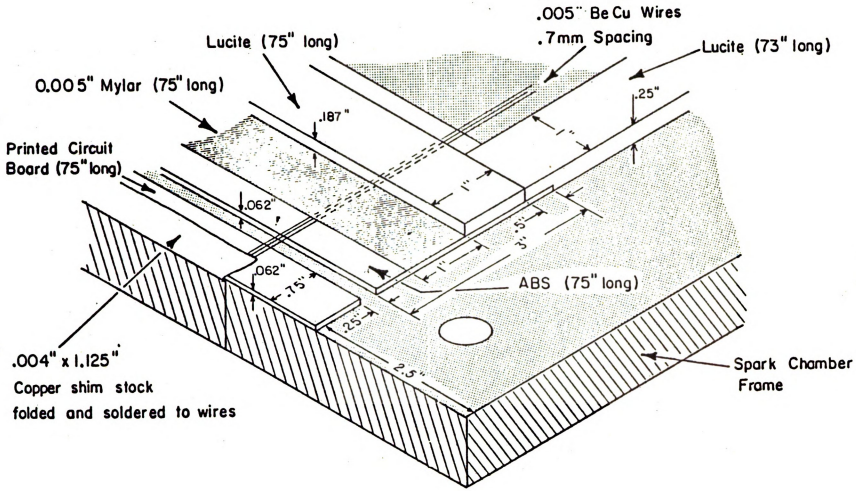

Figure 2.6 The Details of a Corner of a Spark Chamber

are listed in Table 2.7. For construction details, and diagrams of the associated amplifier and discriminator circuits, see the dissertation of C. Chang.[30]

IRON TOROID MAGNETS

The analyzing magnets were wire-wound iron toroids. Made of four sections welded together at the outer edge, these magnets were run in saturation with an average field of about 17 Kg. This field, applied over the length of the magnet (80 cm), imparts a transverse momentum bend of about 0.4 GeV/c. The general features of these magnets are listed in Table 2.8. Construction details and the methods for precise field measurements are given in the thesis of S. Herb.[31]

VETO COUNTERS

Halo particles, mostly muons in the beam at a radius larger than about 9 cm, were kept from triggering the apparatus by placing halo veto counters in front of the target. Muons in the beam at large radius tend to have a larger beam angle relative to the beam axis, they often miss the active area of the beam proportional chambers, and they have often suffered energy loss by interacting in magnets and beam pipes along the way. Such muons are unsuitable for studying deep inelastic scattering. A large counter array similar to the horizontally oriented trigger banks is placed directly in front of the target, and rejects muons at large radius. A smaller counter, 15" square with a 7.5" diameter hole in the middle is directly in front of the first halo veto. This counter lets in good beam particles, but vetos muons which pass just outside the useful beam area. The tubes used in all these counters were Amperex 56 AVP's.

Table 2.7 Spark Chamber properties

- each module has 2 pairs of orthogonal wire planes at 45 degrees relative to each other
- 25 mil Al plates 80" x 80" outer dimension
- active area = 73" x 73"
- Be-Cu wires .005" in diameter
- wire spacing = .7mm.
- distance between fiducial wires = 184.15 cm for ch's 1,2,3,4,5
  = 182.88 cm for ch's 6,7,8,9

-high voltage for each chamber module:

chamber	1	2	3	4	5	6	7	8	9
voltage(kV)	8.6	8.4	8.4	7.6	7.2	8.6	7.6	7.8	7.4

- triggering process:

NIM trigger → thyratron → spark gap → spark breakdown between wire planes in chamber

- from onset of trigger signal to spark gap break down = 220 ns.
- recovery time of charging capacitor in spark gap box = 40 ms.
- memory time = 1 μsec (a clearing field sweeps out stale ions)
- gas mixture: Ne-He 78-80 %, Ar 2-3 %, Alcohol .7 SCFH @ 80°F } gas purified in "Berkeley" purifier and recirculated
- Ar in wand catheters, N_2 in spark gaps

Table 2.8 Iron toroid magnets

- 172.7 cm outer diameter, 30.5 cm inner diameter
- about 80 cm long
- saturation current = 35 A, 450 turns
- average field = $\frac{\int B(r)\,dr}{\int dr}$ = 17.09 KG magnet 1,3,5,7
  = 17.27 KG magnet 2,4,6,8
- residual "degaussed" field = 200 gauss
- each magnet = 7.87 gm/cm^3 x 80 cm = 629.6 gm/cm^2
- spectrometer = 8 magnets x 629.6 = 5036 gm/cm^2
- field measured using (i) B-H curve was measured for a smaller toroid of the same type, and scaled up
  (ii) B(r) measured directly using a coil wound around one slab of the toroid; coil passed through the center of the toroid and small holes drilled in the body of the toroid slab
- radial dependence of the field known to within 1 %

$$B(r) = A/r + C + Dr + Fr^2 \qquad \begin{matrix} B(KG) \\ r(cm) \end{matrix}$$

magnet	A	C	D	F
1,3,5,7	12.20	19.92	-.08357	.0004346
2,4,6,8	12.07	19.71	-.0827	.0004301

The muons which are not scattered into the magnetized region of the spectrometer continue on down the beam axis through the holes in the toroid magnets. To add additional protection against an accidental triggering of the apparatus by such a muon, beam veto counters (12.5" diameter) were positioned in the beam region behind magnets 4, 6, and 8. These counters, called BV_1, BV_2, and BV_3 respectively, vetoed the trigger whenever a signal resulted from the coincidence of BV_3 with BV_1 or BV_2. The use of these counters significantly reduced the accidental trigger rate. On the other hand, a good event (a successful muon scatter into the spectrometer) might be vetoed if a shower hadron, not in the original beam, were to exit the end of the target, survive the hadron shield, and then penetrate the veto counters. To give further protection against such "punch-through" particles, the toroid holes were filled with concrete plugs which should allow through only unscattered beam muons.

TRIGGER BANKS

The principal type of trigger used in E319 consists of a beam muon scattering in the target and proceeding into the spectrometer where it will register as a "good" event if it passes through the three trigger banks (counter arrays) located behind magnets 2, 4, and 6. In order to do this the angle of scatter must have been large enough for the muon to have missed the holes in the toroid magnets and also to have avoided the beam veto counters.

Trigger banks SA', SB', SC' are arrays of vertical scintillation counters observed at either end by 56 AVP phototubes. Each of the five scintillation counters is 14.25" wide by $\frac{3}{8}$" thick, and overlaps with the other counters by $\frac{1}{4}$". Immediately in front of these is another set of

arrays. SA, SB, SC are mounted in the horizontal position. Since these arrays have a square hole in the middle, correction counters with round holes were added to restore full azimuthal symmetry. The dimensions and layout of the trigger banks are shown in Figure 2.7.

2.7 Trigger Logic

The essential components of the trigger were a beam trigger and a halo veto before the target, and a trigger bank signal and beam veto after the target. The notation used to describe the various triggers is given in Table 2.9. Not all of these triggers actually resulted in data being recorded and the spark chambers being fired, but scaler readings were kept and latch information maintained for each coincidence signal.

Figure 2.8 shows the main trigger circuit. The electronic modules such as disciminators, gate generators, and logic units sat in powered crates which could be gated (or enabled) for the length of the whole spill ("spill gated") or only during that fraction of the spill when the computer was actually ready to record data ("event gated"). The distinction between these two types of gating is indicated in the figure along with the various delay times in nanoseconds. Figure 2.9 shows the logic circuits for the trigger banks in greater detail. Figure 2.10 is the logic diagram for the actual formulation of the trigger and for generating various gates. Below is a description of how a trigger comes about.

(1) The Fermilab T2 timing signal enters the delay pulser (refer to Figure 2.10) which in turn puts out several timing signals. If the computer is not occupied and there is no "pinger veto" signal present indicating the onset of a sharp pulse of neutrinos for the bubble

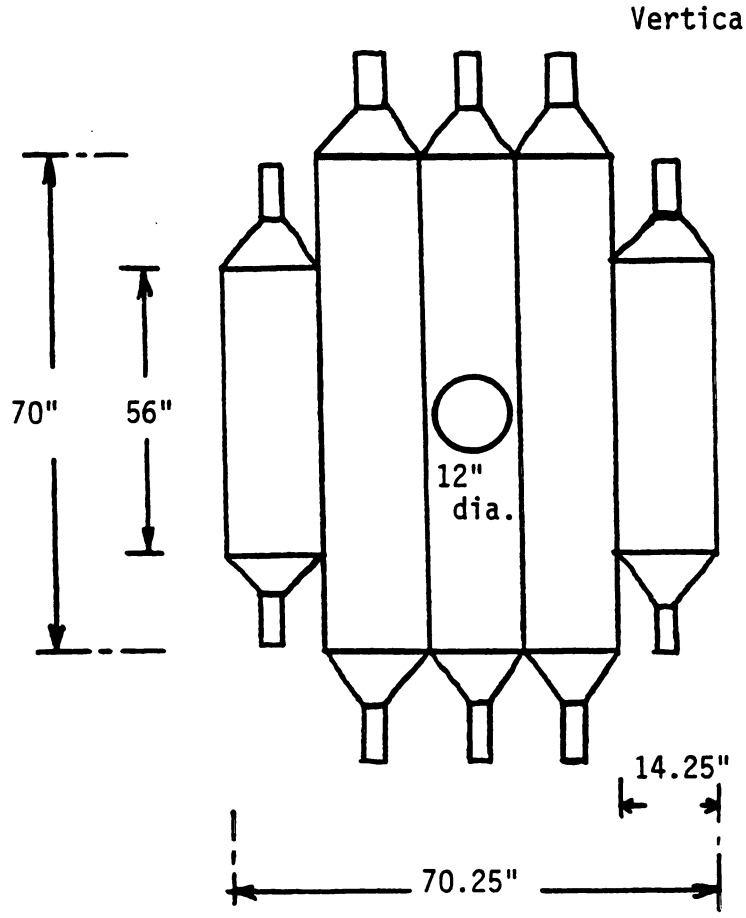

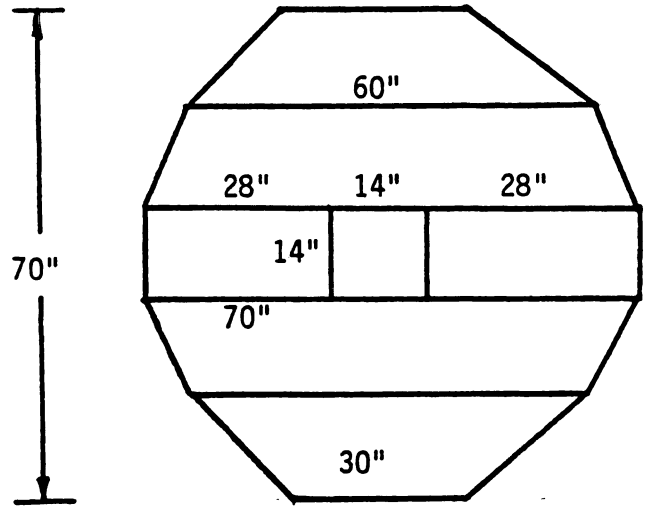

Figure 2.7 Trigger Banks

Table 2.9 Trigger types and notation

evg = event gated

spg = spill gated

SA, SB, SC = horizontal trigger counter arrays

SA', SB', SC' = vertical trigger counter arrays

$S = (SA+SA') \cdot (SB+SB") \cdot (SC+SC')$

$HV = HV_I + HV_{II}$ = halo veto

$C = C_1 \cdot C_2 \cdot C_3$

$B = B_{104} \cdot C \cdot \overline{HV}$ = Beam trigger

SD = any 2 or more counters in SA and SA', and in SB and SB'
= "dimuon trigger"

SL = hits in outer lying counters = "large angle" trigger

SS = hits in inner lying counters = "small angle" trigger

Π = pion trigger for calorimeter calibration = $B_{evg} \cdot \bar{S}_{nv}$

$B_{evg} \cdot S \cdot \overline{BV}$ = single muon trigger

$B_{evg} \cdot SD \cdot \overline{BV}$ = full dimuon trigger

$B_{evg} \cdot P$ = pulser trigger

operating trigger for E319 at 270 GeV =

$$B_{evg} \cdot S \cdot \overline{BV} + B_{evg} \cdot SD \cdot \overline{BV} + B_{evg} \cdot P$$

$B_{104} = B_1 \cdot B_2 \cdot B_3$

$BV = (BV_1 + BV_2) \cdot BV_3$ = Beam Veto

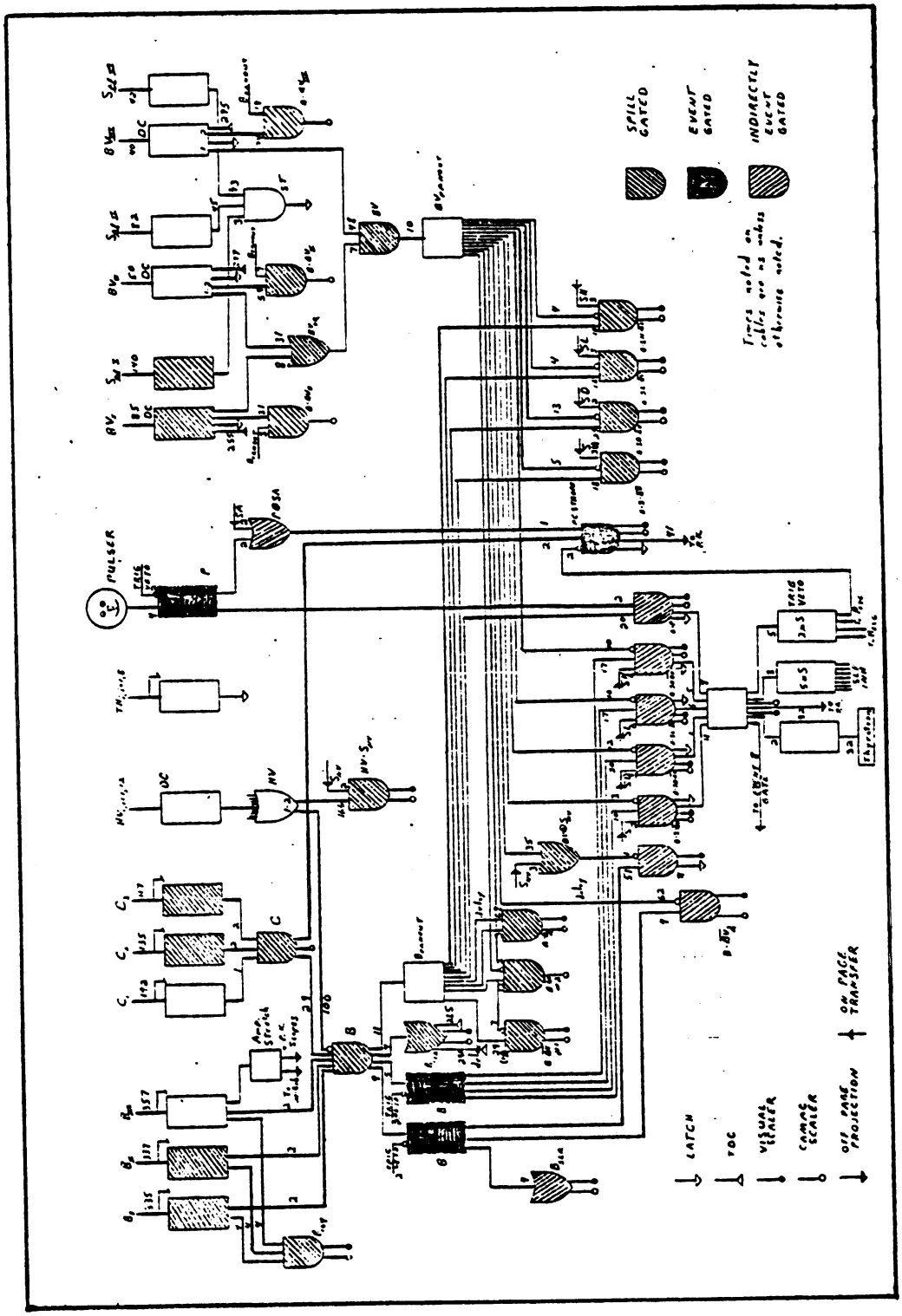

Figure 2.8 Fast logic for the full trigger

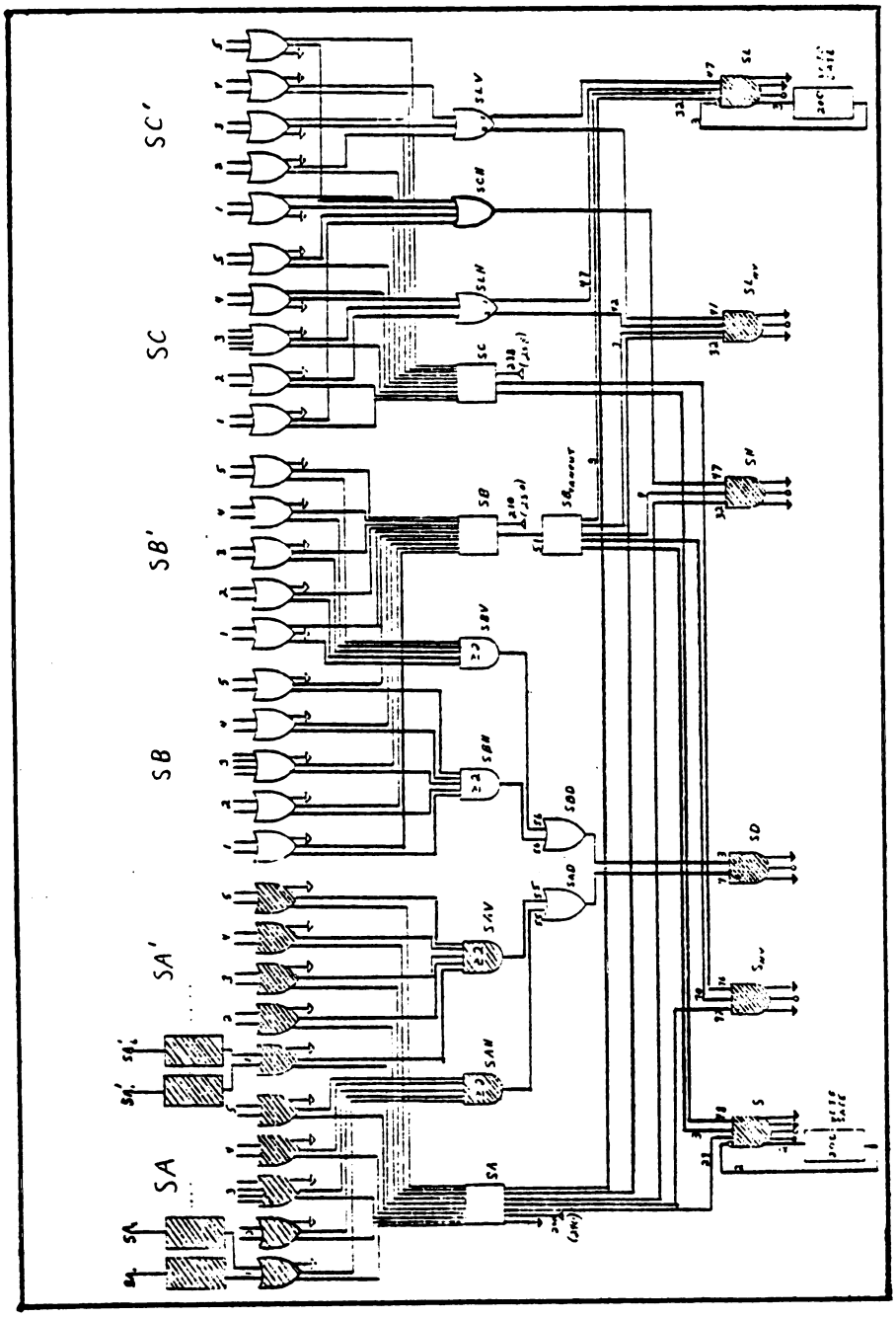

Figure 2.9 Trigger bank logic

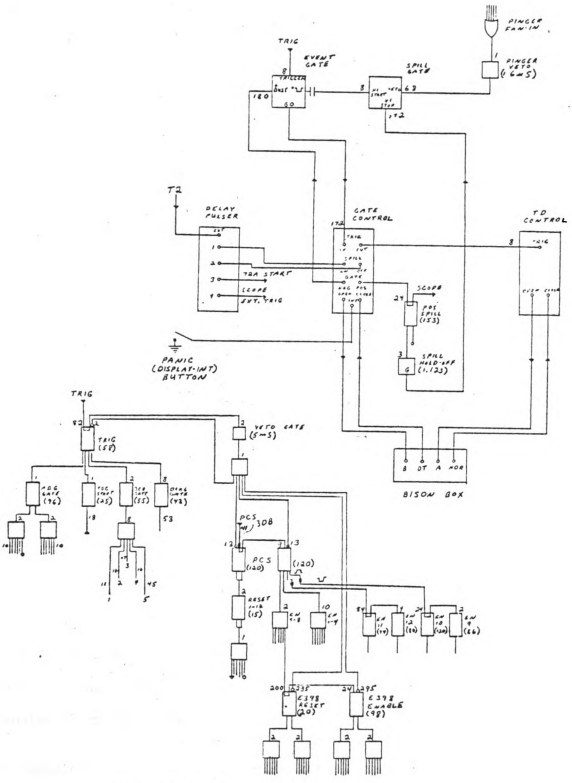

Figure 2.10 Gate logic

chamber, the spill gate is turned on and stays on for the duration of the spill, about two seconds. This enables all spill-gated modules.

(2) A successful scattering event will generate a NIM-level trigger. An early quick trigger, $B \cdot (SA + P)$, has already cleared and enabled the proportional chamber latches. Now the more thorough NIM trigger, $B \cdot S \cdot \overline{BV} + B \cdot SD \cdot \overline{BV} + B \cdot P$, is formed in the gate control box. This signal fires the spark chambers, begins the time-digitizer clocks, starts the process of latching counter and scaler information, and generates a TTL-level trigger for other specialized tasks.

(3) Now the event gate is turned off, vetoing any new-arriving information. The computer begins to read all of the latched data and other information modules via a branch driver and the CAMAC data acquisition system. This takes about 10 msec, during which time the event gate remains off. Of course, the scalers which monitor the incident muon flux are also gated off; it's as if the entire experiment was turned off while the computer was busy. Actually it is the spark chamber recovery time, about 40 msec, which establishes the amount of dead time and not the computer.

(4) When the built-in dead time counter has elapsed, and the computer and spark chambers are ready again, the interrupt is lifted and the event gate is turned on. The experiment is "active" again. Events continue to be recorded until the end of the spill, signalled by another Fermilab timing pulse, and the spill gate is turned off.

2.8 Computer

The computer used for the on-line superintending of the experiment was a PDP11-45 with a 32K memory. This computer was interfaced to the CAMAC hardware via a BDØ11 branch driver . For a 2 second spill and

a deadtime of 40 msec, it was possible to handle as many as 50 triggers per spill. The block of data for each event was stored on disc, and when time allowed, was written onto nine-track magnetic tape. Approximately 10^4 triggers could be written onto a single tape. There were 768 words per event and 4 events per buffer. The data block format for each event is shown in Table 2.10.

Logging data is not the only function of the on-line software. The computer accumulated run information continuously. When time allowed, between spills for instance, this information could be displayed on a CRT or printed out on paper. Many of these accumulated diagnostics were regularly printed as part of the end-of-run procedure. The information available concerned all aspects of the apparatus: spark chamber spark distributions for each wand, histograms are made of fiducial positions and behavior, and the number of sparks on each wand; hit distributions and hit multiplicities for all proportional counter planes; DCR latch information giving hit information for each counter in all the trigger banks; calorimeter counter pulse heights and the equivalent number of ionizing particles; and an event display which showed a plan view of the whole apparatus with the appropriate sparks displayed.

2.9 Running Conditions

The majority of running time during E319 was devoted to 270 GeV muons. The trigger rate was sufficiently high that some care had to be taken in optimizing the shape of the main ring acceleration cycle. Although a high trigger rate was desirable, each trigger was followed by a 40 msec deadtime (while the spark chambers recovered) during which time the incident muons on the target, including those that scattered,

Table 2.10 Primary data tape format

Words	Contents	# words used
1-15	I.D. block	15
16-87	24-bit scalers	72
88-179	E319 PC's	92
180-215	E398 PC's	36
216-220	DCR's	5 packed
221-228	TDC's	8 packed
229-456	ADC's	228 packed
457-464	unused	8
465-761	WSC digitizers	297
762-768	unused	7
		768 words/event

were ignored. We can define the number of event-gated triggers per spill as T_{evg}. If we define T_{spg} as the number of spill--gated triggers per spill, f as the duration of the spill, and d (40 msec) as the dead-time then

$$T_{evg} = \frac{T_{spg}}{1 + \frac{T_{spg} * d}{f}} \tag{49}$$

The optimum trigger rate was achieved with a flat top (length of spill) of 2 seconds with a main ring cycle time of 14 seconds.

There were several important indicators of the quality and consistency of each run (a "run" was usually a full tape's worth of data--10,000 events--or a fraction thereof). These quantities, for a typical run, are shown in Table 2.11. They were recorded by hand from visual scalers in the lab, as well as written on magnetic tape along with the other data for each event. Some of these scalers, or ratios of scalers, need some explanation.

BDERR is the number of branch driver errors, caused by malfunction of the CAMAC reading process or by the computer itself. We took data primarily during the summer of 1976, which was very hot. The number of branch driver errors rose almost linearly with the outside temperature.

The effective incident flux of muons was given by $B_{evg} \cdot \overline{BV}_{delay}$ and not by B_{evg} itself. Remember that $BV=(BV_1+BV_2)\cdot BV_3$ is the beam veto signal. BV_{delay} is BV delayed by 60 ns. which is approximately 3 r.f. buckets. In magnitude it should be the same as BV since the number of muons in any r.f. bucket should be a constant. There are two main

Table 2.11 Scaler averages for a single run

Scaler	Interpretation	Average per run
$B\cdot S\cdot\overline{BV}_{evg}$ + $B\cdot SD\cdot\overline{BV}_{evg}$ + $B\cdot P$	standard trigger	7838
BDERR	branch driver errors	111.6
$B\cdot\overline{BV}_{delay}$	effective incident flux	7.831×10^{7} μ's
$B\cdot S\cdot\overline{BV}_{evg}$	single muon trigger	7383
$B\cdot SD\cdot\overline{BV}_{evg}$	dimuon trigger	865
$B\cdot P_{evg}$	pulser trigger	376.7
$\frac{B\cdot S\cdot\overline{BV}_{evg}}{B_{evg}}$	event rate	$.90536 \times 10^{-4}$
$HV\cdot S_{nv}/B_{spg}$	halo	102.53%
B_{spg}/SEM	μ / p yield	5.44×10^{-8}
B_{spg}/no. of spills	incident μ's per spill	$.50272 \times 10^{6}$
B_{evg}/B_{spg}	dead time	46.56 %
$B_{spg}/B_{spg}(104)$	beam tune	68.38 %
average flux x #targets/cm^2	average luminosity per run	2.0×10^{35} cm^{-2}

reasons why B_{evg} itself (the normal beam trigger) overestimates the usable incident flux:

(i) BV has a non-zero accidental rate; that is, occasionaly, BV=1 and $\overline{BV}$=0 even when there was no muon through the beam veto counters. This would kill an otherwise good event. We correct for this by substracting an appropriate amount of flux.

(ii) A second muon coming in the same bucket as one which scattered successfully will fire the beam veto and kill the good event.

$\overline{BV}_{delay}$ simulates both of these problems and can be used to correct the effective flux accordingly:

$$B\cdot\overline{BV}_{delay} = B - B\cdot BV_{delay} = B - \text{corrections for (i) and (ii)} \quad (50)$$

The halo is defined as the coincidence of a halo veto signal with a spill gated signal from the trigger bank divided by the number of muons in the beam proper (B spill-gated).

The μ/p yield is an indication of how well the whole muon beam line is tuned. For a given number of protons incident on the neutrino area production target, we tuned the magnets (Table 2.3) for maximum muon yield. SEM is just the Fermilab record of the number of protons sent to our experiment for producing muons.

Dead time is the fraction of the muon beam which was actually used. Many of the muons in the beam passed unused because the computer was busy recording data (when the event gate was turned off). This dead time is related to, but not the same as, the "dead time" due to spark chamber recovery time.

The beam tune is just the ratio of beam muons into the target, B_{spg}, divided by the number of muons which were in the beam as of enclosure 104 ($B_{104}=B_1 \cdot B_2 \cdot B_3$). This ratio gives an indication of how well focused or parallel the beam was by the time it reached our target.

There were several modes of running other than 270 GeV positive muons during E319. In order to check interference effects we used a 270 GeV μ^- beam. A sample was taken at 150 GeV as a possible check of energy dependent scaling effect or multimuon production. Another 270 GeV μ^+ sample was taken with two thirds of the iron target removed; it was hoped that this would facilitate the study of possible rate effects in the full-target 270 GeV μ^+ sample. Various calibration runs were made for the calorimeter and the spectrometer.

The following table is a summary of running modes in E319

Table 2.12 E319 Data Runs

Type of Running	Triggers	Incident Flux
270 GeV μ^+	1.47×10^6	1.473×10^{10} μ's
270 GeV μ^-	0.39×10^6	0.365×10^{10} μ's
270 GeV μ^+ (1/3 target)	0.14×10^6	0.418×10^{10} μ's
150 GeV μ^+	0.29×10^6	0.162×10^{10} μ's

CHAPTER III

ANALYSIS OF THE DATA

3.1 Alignment

The alignment of the apparatus elements produces, in effect, a system of absolute spatial coordinates for all proportional chambers (PC's) and wire spark chambers (WSC's) relative to the toroid magnets and the nominal beam axis. The establishment of such a coordinate system is crucial to the determination of the scattered muon's momentum. Any accidental offset, rotation, or physical defect in the chambers which would give an inaccurate representation of the muon's coordinate at any of the chambers before, after, or between the toroid magnets, must be corrected for.

E319 run number 130 was made with the target removed and the toroid magnets shut off. Beam muons could therefore travel the entire length of the E319 apparatus in straight lines, except for some Coulomb multiple scattering in the toroid iron. The sparks registering in all the chambers were fit to a straight line. The residue $\Delta x = x_{fitted} - x_{observed}$ is then histogrammed for each chamber. These "window" distributions show how much a particular chamber is misaligned. The intrinsic measurement error of the spark chambers is 0.1 cm. An additional error is expected due to multiple scattering and is proportional to the amount of iron traversed by the muon. These errors

are symmetrical about the straight-line trajectory the muon would otherwise follow. If the chamber is misaligned the mean of the window histogram will be nonzero. This nonzero mean is used as an alignment shift for each PC plane and each WSC wand (x,y,u,v planes in the WSC's). The alignment is run again with the new parameters; this process is iterated until the residues become acceptably small.

The alignment procedure consists of several steps. First, the alignment of PC's 3 and 4 (the beam chambers upstream of the target position) is fixed. These chambers serve as the anchor for all subsequent alignments. Although the other beam proportional chamber, PC5, would ordinarily have been used to help locate the beam track, it was not utilized during the alignment since the heavy iron shutter in the E398 apparatus had been accidentally left in place. Due to multiple scattering in this iron (about six feet thick), and the great distances involved, PC5 could not really contribute effective beam information.

For run 130, only events with a single beam muon (about 80%) were kept. The muon beam track, established in PC3 and PC5, was extrapolated into the "hadron" proportional chambers, PC1 and PC2, downstream of the target position, and into the four forward spark chambers (WSC 9,8,7,6). The rear spark chambers (WSC 5,4,3,2,1) could not be aligned with the rest since their center regions were deadened in exactly the central region where the beam passed through.

In addition to having only one beam track, each acceptable event had to have sparks present in all four views (x,y,u,v) in at least three out of the front four spark chambers, and with residues smaller than 2.0 cm. In the case of multiple sparks in a single view, the one with the smallest residue was chosen. New alignment constants were

derived from the window (residue) histograms made for each wand, and the alignment process was begun again. The iterations were stopped when the mean of each window histogram (the amount by which the alignment would have been shifted in the next iteration) was smaller than .001 cm. In this way the hadron PC's and the front spark chambers were aligned relative to PC3 and PC4. The layout of this part of the apparatus is shown in Figure 3.1.

Each spark chamber module has four views. This built-in redundancy is desirable in reconstructing the proper trajectory of the muon in three dimensional space. Therefore, it is important that in minimizing the "window" residues of all wands in a particular view, all the y wands for instance, that the internal relations among the four views of a single chamber module are not distorted. The following "match" residues were histogrammed for each chamber:

$$\Delta x_{match} = \frac{u-v}{\sqrt{2}} - x \qquad \Delta u_{match} = \frac{y+x}{\sqrt{2}} - u$$

$$\Delta y_{match} = \frac{u+v}{\sqrt{2}} - y \qquad \Delta v_{match} = \frac{y-x}{\sqrt{2}} - v \tag{50}$$

The coordinate axes, as they are used in E319, are shown in Figure 3.2. In this figure, one is looking downstream at a single spark chamber module.

To determine how well the overall alignment was progressing, the spark positions were fit to a straight line and the resulting chi-squared was histogrammed. As the alignment converges, the window and match distributions should become more nearly centered along with a decreasing average χ^2 per degree of freedom. The best indication of

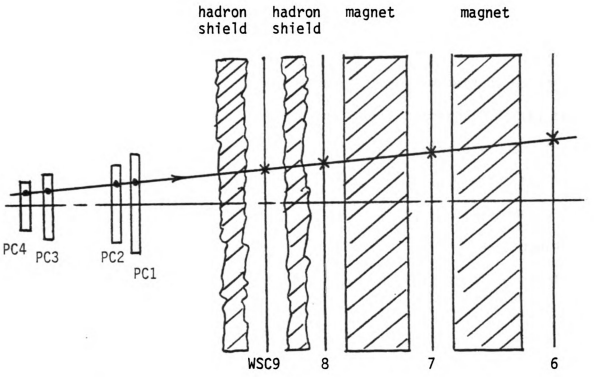

Figure 3.1 Aligning PC2,PC1, and the front spark chambers

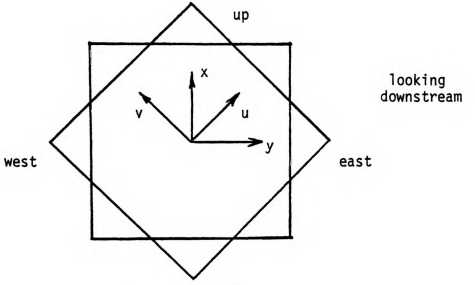

Figure 3.2 Conventions for spark chamber coordinate axes

a good alignment is the number of good events being found; previously misaligned chambers would gradually contribute true spark positions increasing the chances for acceptance of the event.

The rear spark chambers were aligned by the same method, using instead straight lines found in the front spark chambers (9,8,7,6) to find expected spark positions in back (5,4,3,2,1). The data used for this part of the alignment consisted of runs 113-120, in which the muon beam was purposely defocused by turning off the quadrupole magnets in enclosure 103, sending a broad beam into the face of the spectrometer rather than down the nominal beam line. The trigger for these events was $S \cdot \overline{BV}$ (a muon through the trigger bank but not through the beam veto).

As mentioned above, one of the main problems encountered in the alignment procedure is the broadening of the window distributions due to multiple scattering. This problem was partially overcome by using high statistics, 10,000 events. We also tried to avoid multiple scattering by triggering only on muons traveling through the "bat wings" of the chambers, the eight triangular regions which stick out beyond the extent of the toroid magnets. But statistics were so low in these runs that they could not be used for alignment.

A second, and more serious problem is that of the relative alignment of wands within a single chamber module. Centering the window distributions in each of the four views within 0.1 mm. can leave the match distributions off-center by as much as 3 mm. This is remedied by displacing the x and y wands by an amount $\Delta x = a+bz$ and $\Delta y = c+dz$ respectively, where z is the distance along the beam axis and a,b,c, and d

are to be found by minimizing the following expression:

$$\chi^2 = \sum_{WSC=1}^{9} \left(\frac{u+v}{\sqrt{2}} - y\right)^2 + \left(\frac{u-v}{\sqrt{2}} - x\right)^2 + \left(\frac{y+az+b-x-cz-d}{\sqrt{2}} - u\right)^2 + \left(\frac{y+az+b+x+cz+d}{\sqrt{2}} - v\right)^2 \qquad (51)$$

This shift in the x and y views will leave all of the window distributions unchanged while it centers the match distributions.

The remaining chambers, E319 PC5 and the E398 proportional chambers in enclosure 104, were aligned using beam tracks from a regular data run (no. 363).

At this point, the chamber planes are aligned relative to each other. It remains to establish the relation between this coordinate system and that of the toroid magnets and the beam axis. This is done by observing the reconstructed momenta for monoenergetic muons in the four azimuthal quadrants. Any misalignment, such as a rotation, displacement, or tilt, which remains between the chamber system, and the longitudinal axis of the toroids (oriented along the nominal beam axis), will result in an asymmetry in reconstructed momentum in the various quadrants.

Several calibration runs using muons of fixed energy were used for this purpose. By introducing an overall shift and rotation in the four views which kept the relative alignment intact, the momentum asymmetry can be reduced and the chi-squared for the muon's fitted track through the spectrometer can be lowered. The final asymmetry in reconstructed momentum was 2.53%, which is within the statistical error of the

measurement. This final (absolute) alignment was accomplished by these shifts:

$$\Delta x = 3.0 \text{ cm.} \qquad \Delta y = 1.3 \text{ cm.}$$

$$\Delta\theta_x = -.01 \text{ mr.} \qquad \Delta\theta_y = 0.0 \text{ mr.}$$

A complete list of alignment constants is given in Table 3.1. These numbers represent the amount by which the spatial coordinate of each proportional chamber plane or spark chamber wand must be displaced from the raw data coordinate to give an accurate representation of the muon's true trajectory.

3.2 Calibration of the Spectrometer

The calibration of the spectrometer is actually equivalent to a calibration of the analysis computer program which reads chamber and magnet information, and calculates from this the muon's incident energy, its scattering angle, and its outgoing energy (E_0,θ, E'). Calibration is achieved by analyzing muon beams of known fixed energy, and adjusting the computer program until the reconstructed momentum nearly equals the known momentum. This calibration can be checked using a monte carlo (simulated) beam of muons which are analyzed in the same way as the data.

Several runs were taken with small toroid magnets (inner diameter = 1.5", outer diameter = 18") placed along the beam axis in order to deflect the beam muons outward so as to fall into the active area of the spectrometer; otherwise these muons would have travelled down the beam axis and through the field-free holes in the large spectrometer toroid magnets. One set of the small toroids, with a combined length

Table 3.1 Final E319 Alignment Constants in cm.

Wands

		x	y	u	v
WSC	1	.211	.742	.953	.521
	2	.324	.557	.508	.148
	3	.111	.611	.663	.391
	4	.341	.606	.375	.136
	5	.034	.190	.429	.189
	6	.140	.069	.036	-.142
	7	-.124	.057	.144	.122
	8	-.020	.206	.255	.316
	9	-.034	1.122	.590	.327

		x	y
E319 PC	1	0.637	0.688
	2	1.073	-0.115
	3	0.438	0.324
	4	-0.090	1.284
	5	0.151	1.918

E398 PC	1	0.0
	2	0.054
	3	0.476
	4	0.0
	5	-0.435
	6	0.0

of 48" along the beam axis, was placed between PC3 and PC4. Another set (total length of 97") was placed just downstream of PC5 but upstream of the E398 Cyclotron Magnet. It was hoped that beam muons could be sprayed out in a conical, azimuthally symmetric pattern into the spectrometer. Unfortunately the muons were not bent out far enough or in sufficient quantities to make this type of calibration useful. In addition, the energy lost by the muons in the small toroids themselves was often difficult to measure, making a momentum determination unreliable.

Instead of the small toroid magnets, the large Chicago Cyclotron Magnet (CCM) was used to steer muons outward from the beam axis into the face of the E319 spectrometer. This large magnet, which was once the cyclotron magnet at the University of Chicago, was the main analyzing magnet of the E398 apparatus just upstream of E319. Figure 3.3 shows the layout of the CCM and various walls within the E398 area in relation to E319.

Calibration data was taken at several incident muon energies: 250,200,150,100, and 50 GeV, and at several CCM current settings. These runs are summarized in Table 3.2. In this way the spectrometer could be calibrated in a wide range of energies (the expected kinematic range of the experiment and at several radial positions outward in the spark chambers. For these runs, the target was removed to decrease Coulomb multiple scattering and energy loss.

Since the beam was purposely steered outside the active area of the E319 beam proportional chambers, in order for the muons to enter the spectrometer, a modified method was used for finding the beam energy. E398 PC planes 1 and 2 (upstream of the enclosure 104 bending magnets) and planes 3 and 5 (downstream) were used to define straight lines

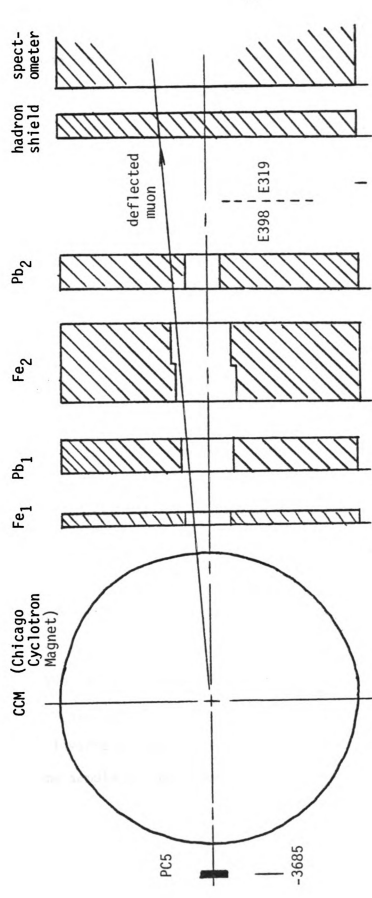

Numbers are coordinates in Muon Lab reference system (distances in cm)
This drawing is not to scale.

Figure 3.3 Layout of E398 and E319 apparatus during the spectrometer calibration

before and after the bend respectively. Unfortunately the PC-reset for these chambers was not working correctly for these runs, and the resultant chamber hit information corresponded to random muons in the beam. The beam energy for any of the calibration runs can therefore be established for the whole run, as an average over random muons in the beam, but not on an event-by-event basis.

After being brought into the muon lab and deflected in the CCM, the muon passes through several iron and lead walls in the E398 apparatus before coming into the E319 spectrometer. Each of these walls has an aperture for admitting the normally-unbent muon beam. Some dimensions for these apertures are given in Table 3.3. After being deflected in the CCM field, some muons missed the apertures and passed through the walls, thereby losing energy, perhaps as much as a few GeV. Finally the muon's energy in the E319 spectrometer is analyzed using the computer program VOREP which is discussed in section 3.4.

The ability of the spectrometer to determine a muon's energy is limited by the Coulomb multiple scattering in the iron toroids. In the analysis process, it is the radius of curvature of the muon's trajectory through the magnetic field of the toroids which is of importance. A distribution of the radii of curvature for a sample of monoenergetic muons sent into the spectrometer would have a gaussian shape due to multiple scattering. Since the reconstructed muon energy is proportional to the inverse of the radius of curvature, the distribution of E' for the same sample of muons would be nearly gaussian with a high-energy tail.

Table 3.2 CCM (Chicago Cyclotron Magnet) calibration runs

RUN	E_0	Tape	Events	1E4 Current	CCM Current	Date	Shutter
467	150	297	5177	2306.2	4000	8/31/76	UP
468	150	298	5265	2306.5	3500	"	UP
469	150	298	5178	2306.5	4500	"	UP
470	200	299	10065	3072.5	4200	"	UP
471	250	300	7630	3840	4875	"	UP
472	100	300	2596	1538.7	2400	"	UP
473	100	301	9963	1538.7	2400	"	UP
474	50	302	9994	770	1200	"	UP
475	250	303	10023	3841.2	4500	9/1/76	DOWN
476	150	304	5407	2306.2	4500	"	DOWN
477	150	304	4746	2306.2	3500	"	DOWN
478	25	305	1217	392.5	600	"	DOWN

Table 3.3 Apertures in E398 walls

Fe_1 20cm thick, all muons through this aperture, z=-1320cm

Pb_1 41.3cm thick, aperture: 40.6cm wide x 38.2cm high, z=-1224cm

Fe_2 (Rochester cyclotron magnet iron used for hadron filter)
aperture: 160.6cm thick x 90.6 cm high x 90.6 cm wide
upstream edge: z=-892.5cm

PB_2 2 slabs of Fe: 1.27cm thick, aperture: 15.9cm wide x 13.4cm high

Pb: 20.98cm thick, aperture: 19cm x 19cm, upstream edge: z=-605 cm

The following procedure was performed for each fixed incident energy:

(1) For each event, the radius of curvature k is found. E'=A/k (where A is a proportionality constant) is immediately corrected for energy loss in the hadron shield. Energy loss in iron is computed using a fit to the CERN energy-loss table.[33]

(2) Using the sparks found in WSC 9 and 7 (8 and 9 are too close together), a line can be extrapolated back upstream into the E398 apparatus. If the extrapolated trajectory is found to pass through one of the lead or iron walls (Table 3.3) the muon's energy is corrected accordingly.

(3) After all corrections have been made to E', the quantity 1/E' is histogrammed.

(4) After chi-squared, radius, and angle cuts are made, the final 1/E' histogram is fit to a gaussian function.

(5) The calibrated value of E' is taken to be the inverse of the fitted peak position of the 1/E' distribution. The resolution of the spectrometer for this E' is the value of sigma (standard deviation) for the 1/E' distribution. Figures 3.4(a-e) show the histograms of the quantity 1000/E' for the five incident energies. Table 3.4 shows the results of the calibration using the CCM magnet.

The runs using the CCM to deflect the muon beam are better than the small-toroid calibration runs, but they too involve calculating the energy loss of muons in iron and lead walls, and the extrapolation of tracks over great distances. As the final step in the calibration process, the monte carlo program MCP (to be described in chapter four)

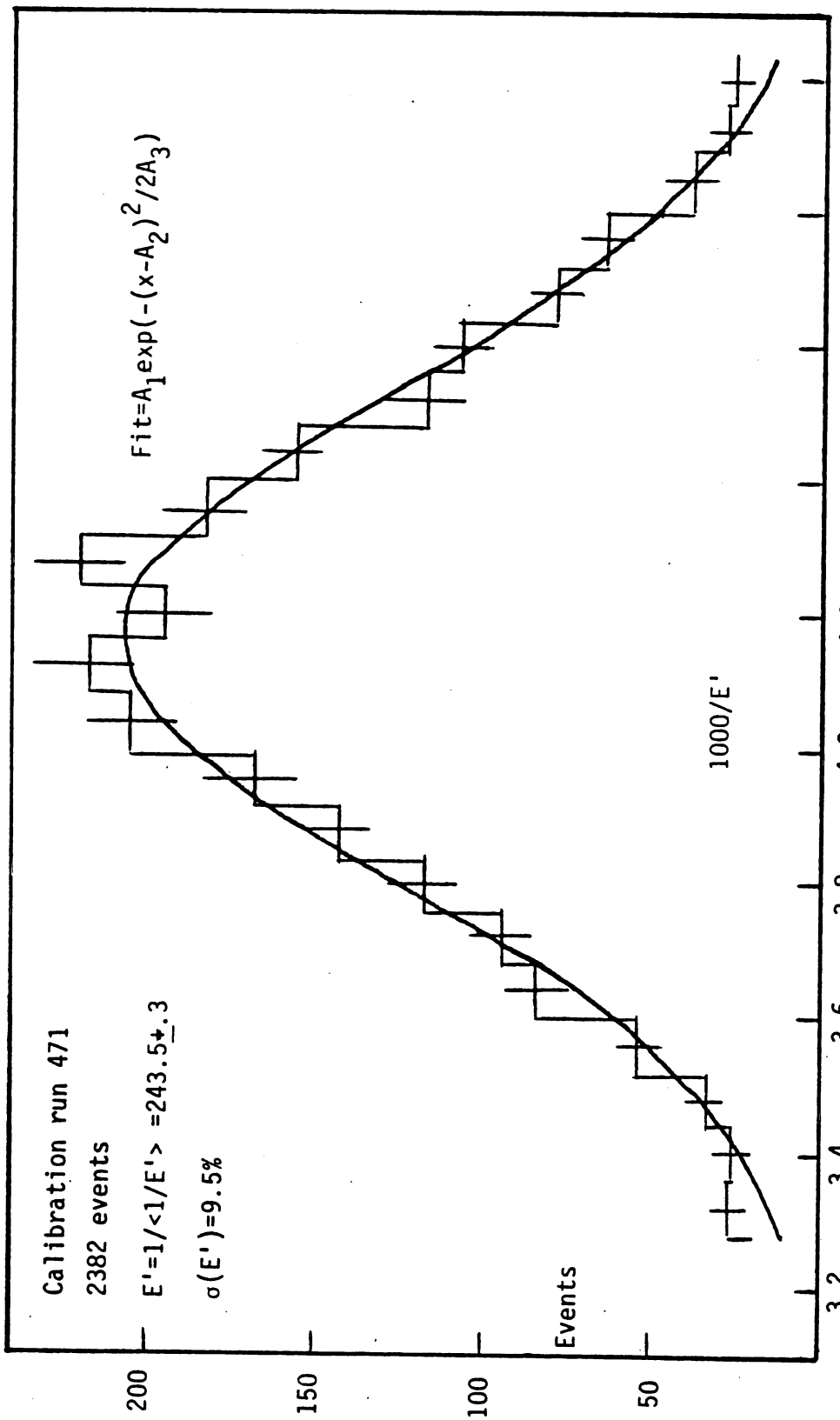

Figure 3.4 (a) Spectrometer calibration

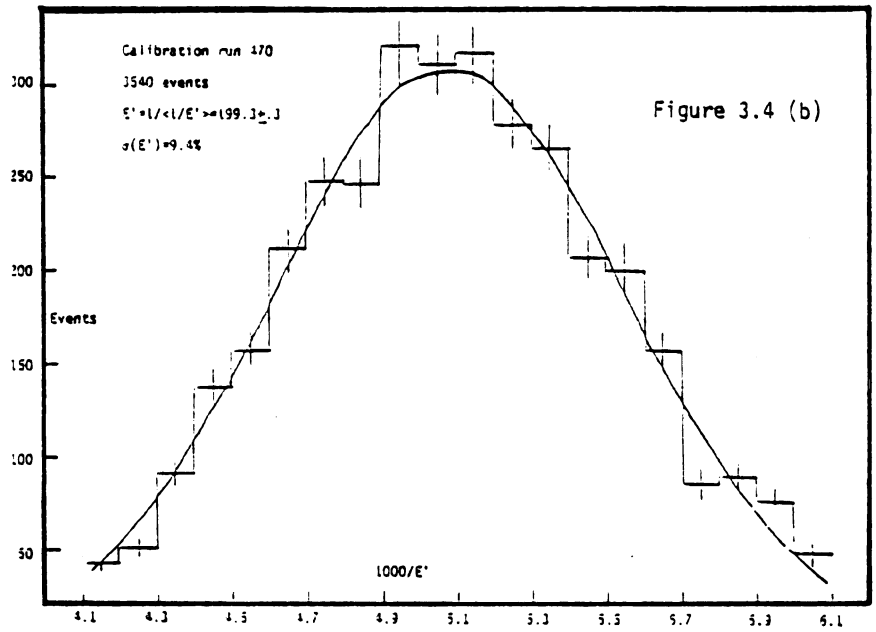

Figure 3.4 (b)

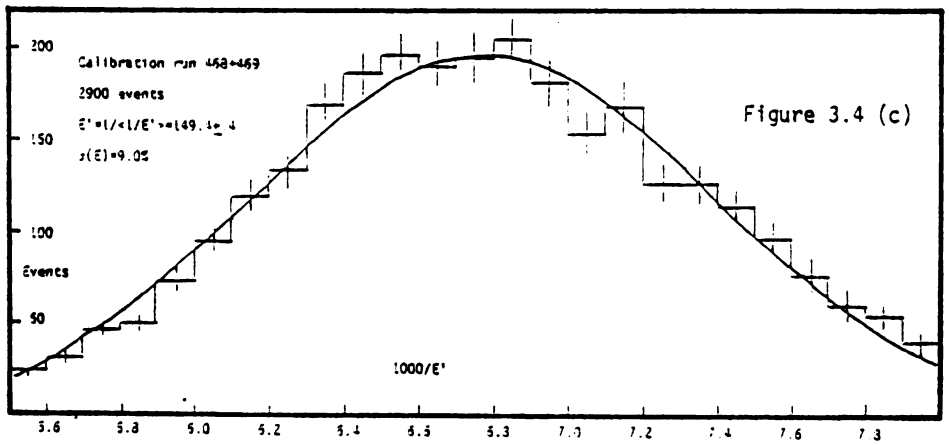

Figure 3.4 (c)

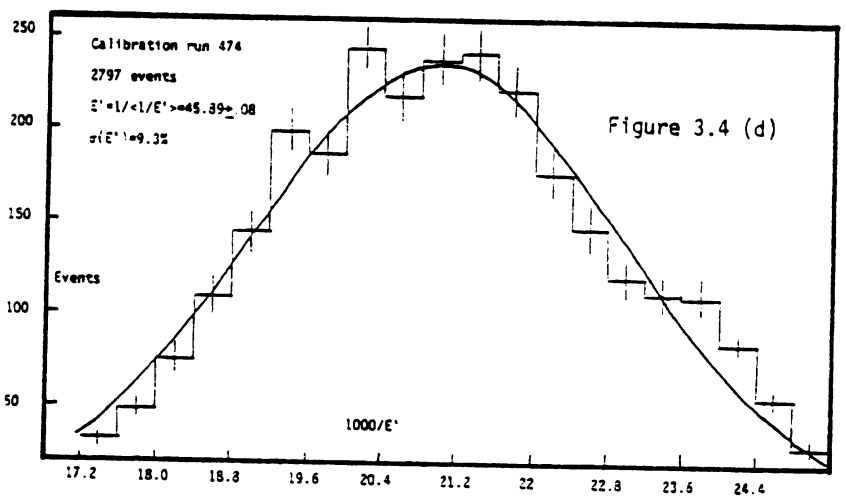

Figure 3.4 (d)

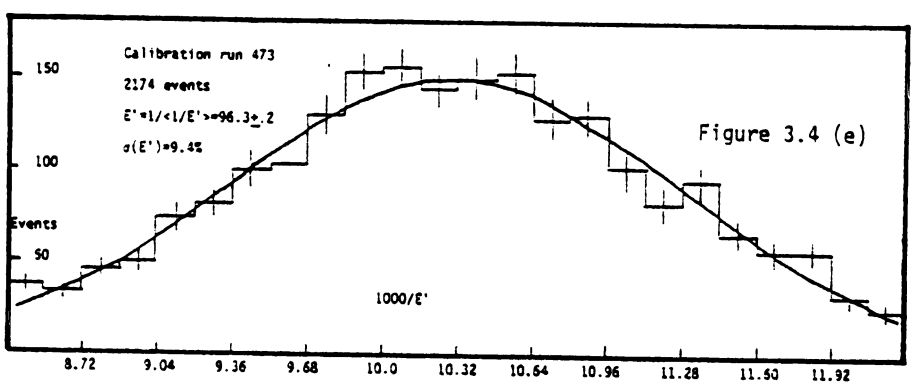

Figure 3.4 (e)

was used to generate muons at the same incident energies as the calibration data. These simulated calibration runs were analyzed just like real data. For these particular monte carlo runs, the simulated multiple scattering in the toroids was "turned off" to give us a sharper value of the peak in the reconstructed 1/E' distribution. The monte carlo calibration of the spectrometer took up where the actual calibration left off. It consisted of the following steps:

(1) Analyze simulated runs at E'=250,200,150,100, and 50 GeV, and at θ=20,25,35 mr., where θ is the angle of incidence into the spectrometer.

(2) Fit the momentum and plot E'(incident) vs. E' (reconstructed).

(3) Fit this plot to a straight line and use the fit parameters to adjust the energy-loss subroutine in VOREP (the analysis program).

(4) Analyze the same monte carlo runs over again with the newly adjusted analysis programs and continue iterating until the incident and reconstructed energies are sufficiently close.

Table 3.5 shows the final results of the monte carlo calibration. The incident and reconstructed energies agree to within 1%. Incidentally, the value of σ in Table 3.5 can be thought of as the "intrinsic" resolution of the momentum reconstruction program. It is the resolution of the spectrometer if there were no Coulomb multiple scattering.

3.3 Data Analysis

The principal computer program for doing single-muon data analysis is called VOREP: View Oriented Reconstruction Program. This program reads the primary data tape, finds beam and spectrometer tracks for

Table 3.4 Calibration of the Spectrometer using the CCM

RUN NO.	NOMINAL ENERGY	E_0 GeV	$1/\langle 1/E' \rangle$ GeV	$\sigma(E')$	EVENTS	$(E_0-E')/E_0$
471	250	248.4±1.0	243.5±.3	9.5%	3488	2.0%
470	200	200.3±0.5	199.3±.3	9.4%	5528	0.5%
468	150	149.5±0.4	149.3±.2	8.9%	3098	0.13%
469	150	149.1±0.4	148.6±.3	9.1%	2954	0.35%
comb	150	149.4±0.4	149.0±.2	9.0%	6052	0.25%
473	100	98.9±0.24	96.3±0.2	9.4%	6055	2.6%
474	50	47.56±.14	45.89±.08	9.3%	2665	3.5%

Table 3.5

Calibration of the Spectrometer using Monte Carlo Data

E(MC)	E(reconstructed)	$\sigma(E)$	EVENTS	(E(MC)-E(RE))/E(MC)
250	251.83±.17	1.8%	699	-0.7%
200	201.36±.21	1.6%	228	-0.7%
150	150.91±.08	1.4%	631	-0.6%
100	100.56±.08	1.2%	223	-0.6%
50	49.51±.04	1.2%	274	+1.0%

each event, fits the trajectory in a multiparameter fit to get the outgoing energy and scattering angle, and then writes the results on an output tape which can be scanned separately. Figure 3.5 shows the flow of the analysis process and the names of some of the major subroutines. I will now describe each of these steps in detail.

INITIALIZATION

Several input files are required by VOREP. These include a fiducial file for finding sparks in the wire chambers, and a pedestal file and peaks file for processing the calorimeter ADC information. When all the preparations are complete, the analysis can begin. The first buffer on the data tape is read. It contains two events worth of information, each of length 768 words. All of the packed words, such as the scalers and ADC blocks, are decoded and loaded into special arrays.

FINDING BEAM TRACKS

If the PC-reset bit indicates that the proportional chamber information latched corresponds to the actual muon which caused the trigger, and not just a random beam muon, then the latches for PC3, PC4, and PC5 (the "beam" PC's) are decoded. The hits in each plane (u,v, or w) of each chamber are found and converted into spatial coordinates. Clusters of hits on neighboring wires are averaged over. Then a three-way match is sought among the hits in the three planes. If no three-way matches are found, all two-way matches are formed. The window size for finding such matches is 0.5 cm.

Next, the fired wires which have been matched to other wires within the individual chamber are compared to the matched wires in the other

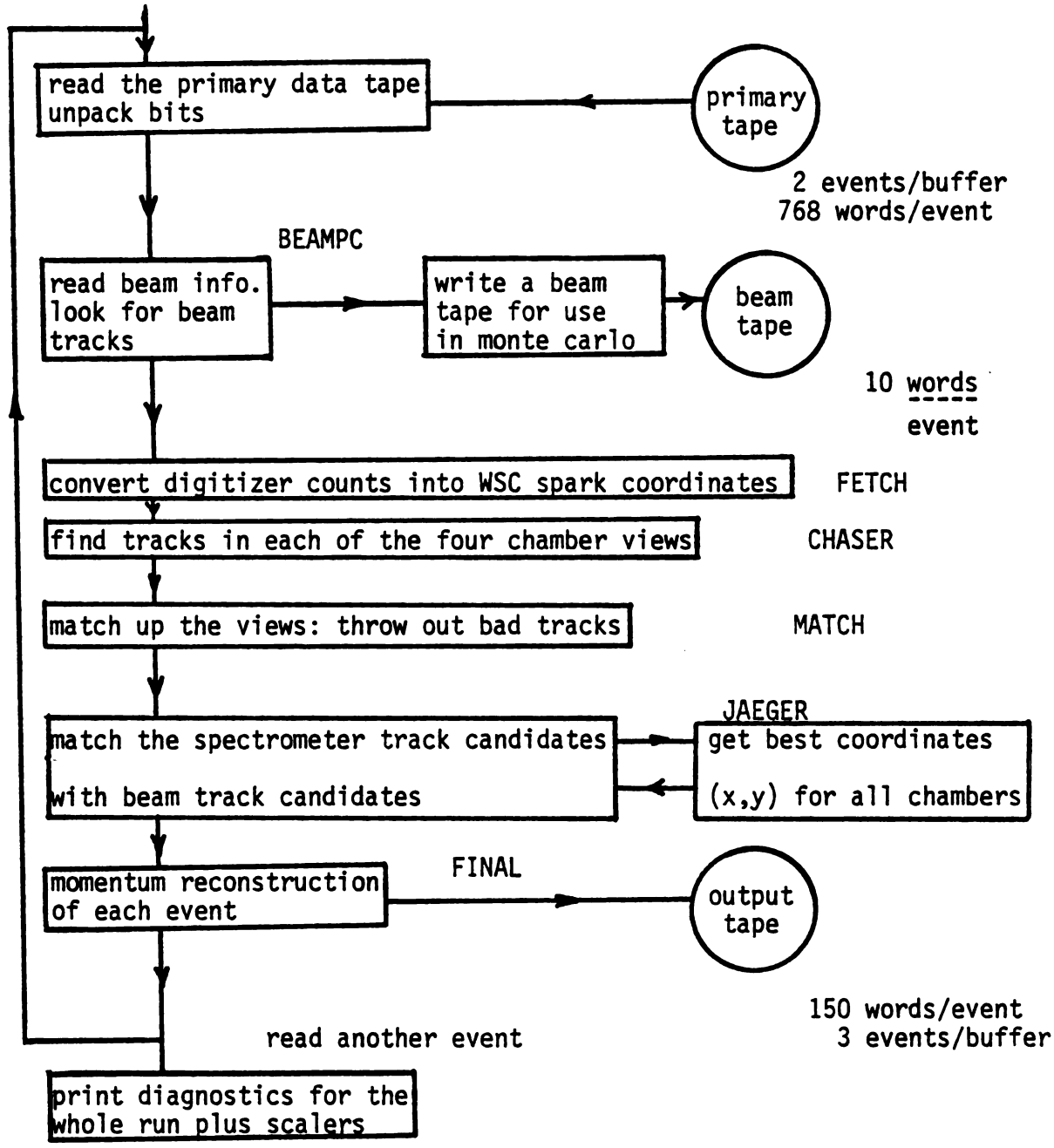

Figure 3.5 Flow chart of the analysis program VOREP

beam chambers. Tracks with a 3-3-3 match (a match of 3 in PC3, PC4, and PC5) are examined first, followed by lesser combinations. In each case the extrapolated track candidate must proceed through the target, must make an angle of less than 0.25 mr. with respect to the beam axis, and must have a chi-squared (for a straight line fit) of less than 12.5. The measurement error in the beam PC's is 0.1 cm. This beam information in conjunction with the E398 PC's, and the known magnetic field in enclosure 104, allows a measurement of the energy of the beam muon, E_0. Each acceptable beam track is stored in an array. If the pulser flag is on, each track is also written onto a separate beam file which is used to generate monte carlo events. The format of this tape is given in Table 3.6.

Interaction vertex candidates are formulated on the following basis: whenever four successive calorimeter counters give a reading of ten or more equivalent particles (ten times minimum ionizing), the first counter is deemed a potential vertex. Whenever no such vertex is found, three dummy vertices are assigned at the center of each third of the target. The total number of beam-vertex candidates is the number of beam tracks times the number of vertex candidates.

FINDING SPARKS IN THE WIRE CHAMBERS

The information from each of the four wands for each spark chamber module consists of eight words. These contain the digitizer clock counts corresponding to the arrival of as many as eight wand pulses (including fiducials). The fiducial file read in at the beginning of the analysis run contains the expected position, in terms of digitizer counts, of the two fiducials for each wand, for that run. Such a thorough record of fiducial positions was found to be necessary because

Table 3.6 Beam Tape Format

Word	Contents
1	run number
2	trigger number
3	θ_x (beam)
4	θ_y (beam)
5	x intercept (z=0)
6	y intercept (z=0)
7	$\chi^2(x)$ straight line fit to beam track
8	$\chi^2(y)$
9	DCR packed with information on trigger type and PC reset
10	E_0 (measured)

of a large temperature dependence. On a hot day, the wands could expand and change the effective position of the fiducials.

The train of spark positions, in terms of digitizer counts, is examined one by one. If the spark is within ±10 counts of the nominal second fiducial, it becomes the new second fiducial. Likewise, if it is within ±10 counts of the first fiducial, it becomes the new position for the first fiducial. If the spark position puts it outside either of the two fiducials, it is rejected. All other digitizer count readings are interpreted as real sparks which correspond to the passage of an ionizing muon through the chamber. The digitizer counts for these sparks are converted into real spatial coordinates (x,y,u,v). Table 3.7 shows a "wand dump," one of the on-line diagnostic displays which was written out during the run. This table shows the digitizer

Table 3.7 Digitizer Clock Counts

WAND DUMP EVENT NUMBER 9480

WAND

1	0	0	0	0	0	776	4402	7676
2	0	0	0	0	0	801	3354	7697
3	0	0	0	0	0	800	4789	7741
4	0	0	0	0	616	5023	5075	7831
5	0	0	0	0	0	815	4000	7755
6	0	0	0	0	0	802	5199	7739
7	0	0	0	0	0	781	3745	7716
8	0	0	0	0	774	3479	3626	7721
9	0	0	0	0	0	779	4445	7713
10	0	0	0	0	0	054	3303	7855
11	0	0	0	0	0	790	4777	7730
12	0	0	0	0	0	779	5042	7717
13	0	0	0	0	0	784	4049	7721
14	0	0	0	0	0	789	5187	7723
15	0	0	0	0	0	704	3746	7720
16	0	0	0	0	0	781	3453	7725
17	0	0	0	0	0	785	4474	7730
18	0	0	0	0	0	810	3404	7749
19	0	0	0	0	0	797	4740	7735
20	0	0	0	0	0	804	5057	7741
21	0	0	0	0	509	4172	4207	7768
22	0	0	0	0	0	0	0	736
23	0	0	0	0	1015	4292	4494	8228
24	791	3234	3278	3327	3413	3508	3550	4028
25	0	0	0	0	603	4130	4234	4395
26	0	0	0	594	3423	3766	3930	4176
27	0	0	0	638	4357	4552	4608	7807
28	0	0	0	521	4312	4360	4792	7691
29	0	0	0	0	0	0	0	4187
30	0	0	0	0	0	0	790	7674
31	0	0	0	0	586	3811	4022	7745
32	0	0	0	580	3514	3894	3951	7743
33	0	0	0	560	4186	4654	5086	7736
34	0	0	2744	3516	3758	3932	4038	7764
35	0	0	0	518	3846	4254	4438	7674
36	0	0	602	4392	4456	4604	4796	7764

SPILL:- 427 6:30:13 16/7/76

counts for all 36 wands (4 wands times 9 spark chambers). For most wands, the first and last numbers correspond to the two fiducials, while those in between should represent real sparks. A "clean" event with only one muon would then leave only a single spark in each chamber. For this particular event, extra sparks seem to be present in the upstream end of the spectrometer (wands 21-36) where particles from the hadronic shower can still sometimes be found. Wands 22, 29, and 30 appear to have been defective since they do not give any clear evidence of a spark. Near the rear of the spectrometer, the extra sparks seem to have died away. Wand 24 has an overflow of sparks (perhaps an edge breakdown problem).

As can be seen from the wand dump, the number of digitizer counts from one fiducial to the other is about 7000. The physical distance between fiducials is about 184 cm. and the wire spacing is .07 cm. Therefore one finds that:

$$\begin{aligned} 7000 \text{ counts}/184 \text{ cm.} &= 38 \text{ counts/cm.} = 3.8 \text{ counts/mm} \\ &= 5.43 \text{ counts/wire spacing} \end{aligned} \tag{52}$$

$$184 \text{ cm.}/.07 \text{ cm./wire} = 2629 \text{ wires} \tag{53}$$

In real time, the distance between fiducials (the real time duration of the whole pulse train) is about 350 μs.

$$\text{pulse velocity} = 184 \text{ cm.}/350 \text{ μs.} = .53 \text{ cm./μs.} = 5.3\times10^{5} \text{cm./sec} \tag{54}$$

$$350 \text{ μs.}/2629 \text{ wires} = .13 \text{ μs./wire} = 130 \text{ ns./wire} \tag{55}$$

That is, if each wire carried a current (caused by a spark at that wire), the time between each wire would be 130 ns. The width of each individual pulse was measured to be about 300 ns. This means that sparks at neighboring wires could just possibly be resolvable.

Once the sparks have been assigned coordinates, the only cut imposed at this time is that there be sparks in at least two views in at least two of the last three chambers. This insures that we can conduct a hunt for muon tracks.

FINDING TRACKS IN EACH VIEW

For each of the four views (x,y,u,v) track finding begins at the back of the spectrometer by forming all possible straight lines in WSC's 1, 2, and 3 (which sit behind the last toroid magnet). Taking into account the bending power of the toroids, sparks are sought in WSC4 and WSC5. At this point, a track candidate having the right polarity (curving "in" toward the axis rather than "out"), and having passed the cuts described in Table 3.8, will consist of sparks in the rear five spark chambers. Sparks in the front four spark chambers will be sought after the track candidates in the back have been matched to give three dimensional tracks. As many as 20 tracks can be retained.

MATCHING TRACKS FROM DIFFERENT VIEWS

A "matched" track is a three dimensional combination of tracks from all four views. The match residuals $\Delta x = x - \frac{u+v}{\sqrt{2}}$ for each of the five rear spark chambers are examined for three views at a time. Firstly, the residual must be smaller than 0.5 cm for the match to be successful. Secondly, matches which result in a location within a magnet hole are rejected. A trivial requirement is that the tracks

Table 3.8 Track finding cuts

1. maximum tangent at the back = TANTMAX = 125 mr.
   this corresponds to an energy cut of about 25 GeV.

2. the extrapolated trajectory in the magnetic region (i.e., at the "bend points") cannot be outside XBMAX = 100 cm.

3. to be included in a track candidate, a spark must be within the allowable window for that chamber. The windows for chambers 1...9 = (.50, .30, .60, 1.0, 3.5, 3.5, 4.0, 3.5, 3.5 cm.). The window size for the hadron proportional chambers was 3.5 cm.

4. tracks which cross the beam axis between bend points cannot also have an extrapolated position XB at the bend point of greater than the inner radius of the toroid=15.24 cm.

5. a cut is made on the change in tangent over a two-toroid bending region. Tracks with $\Delta TAN \geq 50$ mr. are cut: this also is equivalent to a cut in E'.

6. a cut on events that are obviously bending out: TAN < -25 mr. for x > 0 and $\Delta TAN > 0$. Tracks bending out only slightly will be retained

7. reject tracks which are coincident with previous tracks, or are subsets of other tracks.

8. for the same number of sparks, two tracks must have at least two sparks not in common.

9. rank the tracks according to the number of sparks. No more than 20 tracks will be allowed.

10. there must be tracks in at least 2 views for the event to be studied further.

being matched have the same polarity. Whenever two views are being taken as reference (e.g. x and u), the match to a third view (in this case, y or v) must be successful in at least five out of the possible 2x5=10 matches. The maximum number of matched tracks allowed is 20. For each matched track candidate which is accepted, the contributions from the four views are converted into (x,y) coordinate pairs for each chamber.

JOINING SPECTROMETER AND BEAM TRACKS

The last step in the identification of the true muon trajectory is to join a beam track with a spectrometer track (sparks in WSC 1-5) and then to add in the contributions from the forward spark chambers (WSC 6-9). The geometrical layout for this process is shown in Figure 3.6.

All possible combinations of a spectrometer track with a beam track are formed. For each combination, the resultant curvature in the spectrometer is checked to see if the track corresponds to spurious low-energy particles or to halo muons. The best match-up of a beam-vertex candidate with a spectrometer track is kept for momentum reconstruction. The following two criteria were used to arrive at the best combination:

(1) In Figure 3.6, θ_{23} is the angle of bend from the front to the back of the spectrometer. In what amounts to an E' cut of about 25 GeV, we require that $\cos\theta_{23} > 0.75$.

(2) As defined in the figure, θ_2 is the angle observed in the front chambers of the trajectory into the spectrometer, while θ_1 is the same angle found by extrapolating the spectrometer track candidate (sparks in the rear five chambers) towards

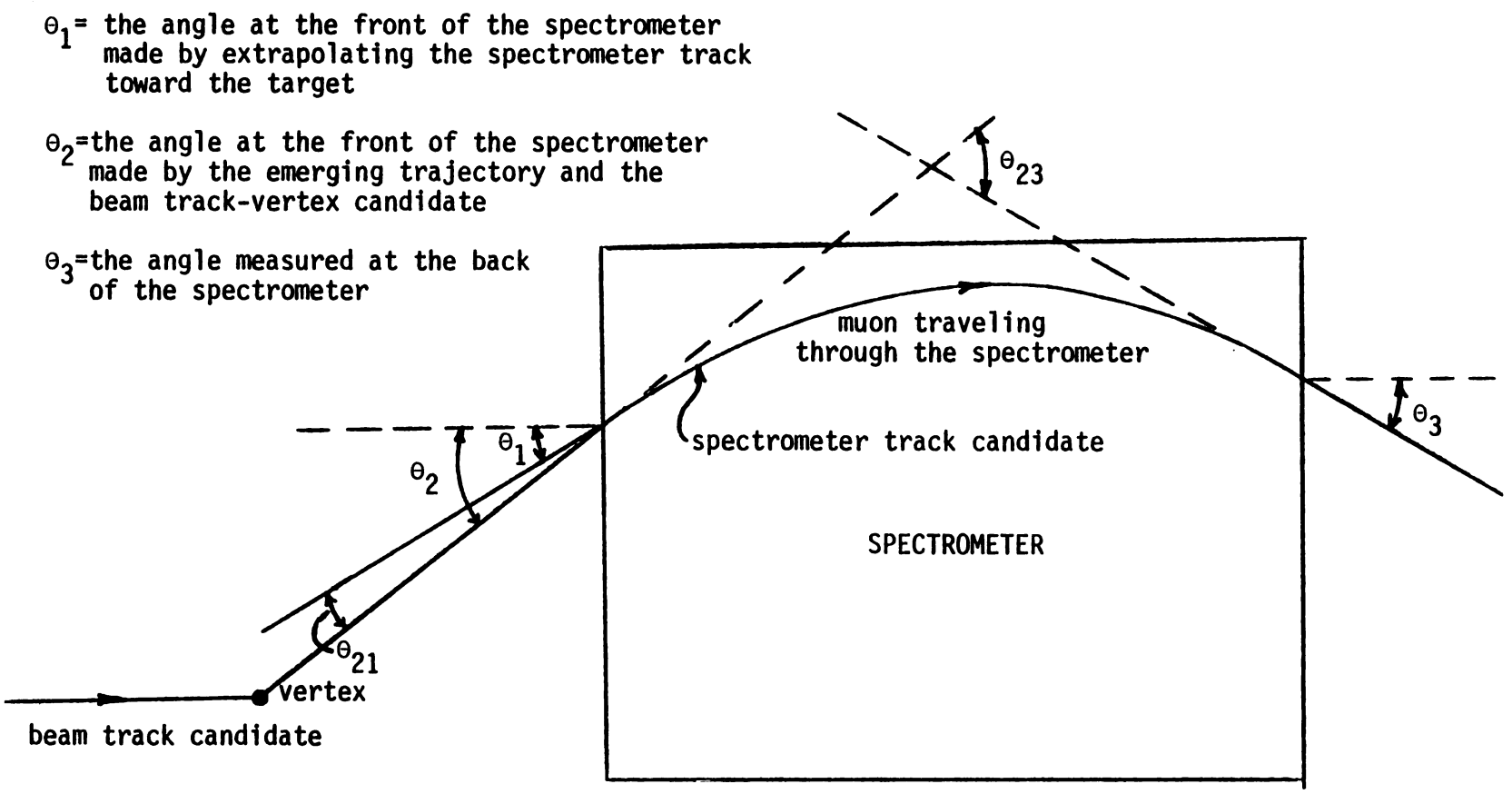

Figure 3.6 Joining spectrometer and beam tracks

the front of the spectrometer and into the target. θ_{12} is the difference of these two angles, or equivalently the difference between the predicted and observed angles in the front. If the beam-spectrometer track combination under consideration is the true one, the only reason θ_{12} would be nonzero is the uncertainty in θ_2 due to Coulomb multiple scattering in the process of extrapolating the trajectory from back-to-front. Recall the formulas for multiple scattering, and for magnetic deflection in a magnet of length L:

$$\Theta \text{ (multiple scattering)} = \langle\Theta^2\rangle^{1/2} = \frac{.015}{E}\sqrt{\frac{L}{1.77}} \tag{52}$$

$$\Theta \text{ (bend)} = \frac{.03}{E}\int B\cdot dl \simeq \theta_{23} \tag{53}$$

$$\Theta \text{ (mult. scatt.)} = \frac{.015\sqrt{L/1.77}}{.03\int B\cdot dl}\,\theta_{23} = \text{constant} \times \theta_{23} \tag{54}$$

We impose the cut $\sin\theta_{12}/\sin\theta_{23} < 12.5$. This is essentially a halo cut. By dividing by the factor $\sin\theta_{23}$, which is proportional to the multiple scattering, we can measure the departure of the measured angle θ_1 from the predicted angle θ_2, for reasons other than multiple scattering (e.g., that the muon did not originate in the target, but is instead a halo muon).

Next, the hit positions in PC2, PC1, and the front two spark chambers WSC9, and WSC8 were filled in using the newly accepted beam-vertex-spectrometer track. These chambers did not contribute directly to the track selection process because of the errors introduced in extrapolating the spectrometer track all the way forward toward the

target. These forward chambers were beset with the extra hits associated with the hadron shower particles, and were also the poorest performing chambers. Nevertheless, when carefully selected, the sparks in the forward chambers were useful in the momentum determination during the multiparameter fit, where every additional point along the muon's trajectory contributed to a better fit. Figure 3.7 shows a schematic of the E319 apparatus and a high q^2 event taking place. The rear five chambers contribute sparks while the front chambers are less effective. One can see in this figure a beam track entering and the interaction near the end of the target. The vertical lines near the target indicate ADC information on the shower pulse height at each counter.

MOMENTUM RECONSTRUCTION

At this point in the analysis, a complete muon trajectory has been formulated: beam track, interaction vertex, and the curving path of the scattered muon as it bends through the magnetized regions of the spectrometer. Knowing the spark coordinates (x,y) of chambers before, after, and interspersed within the spectrometer, and knowing the magnetic field in the toroids, we can find the scattered muon's energy, E', its scattering angle, θ, and its interaction vertex. Along with the incident energy E_0 measured separately in enclosure 104, these parameters specify all the kinematics of the deep inelastic scattering reaction.

I shall begin my description of the momentum-angle reconstruction process by pretending that there is no Coulomb multiple scattering in the spectrometer. This idealized spectrometer, including several chambers and magnets, is shown in Figure 3.8. The incident muon enters

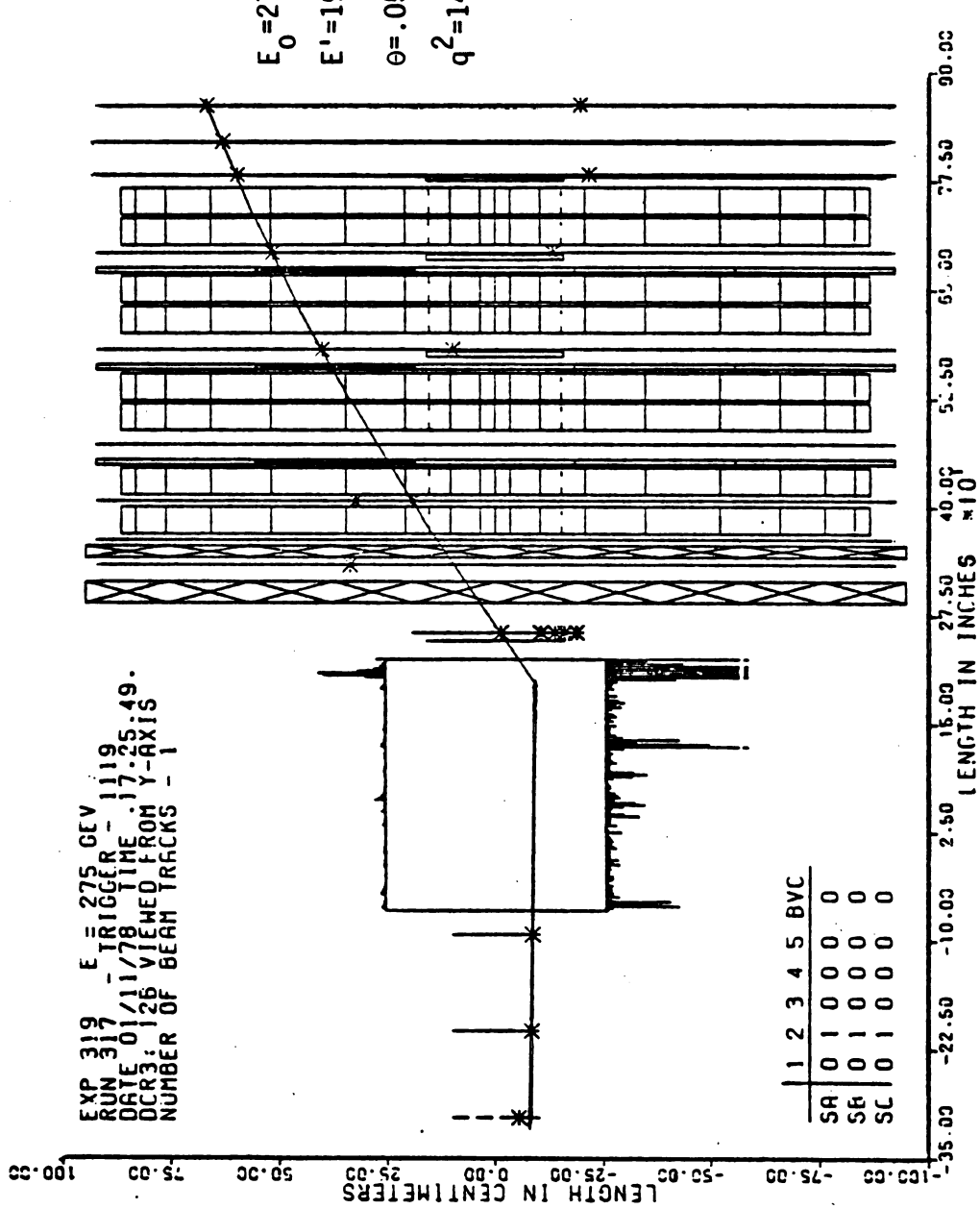

Figure 3.7 A high q^2 event

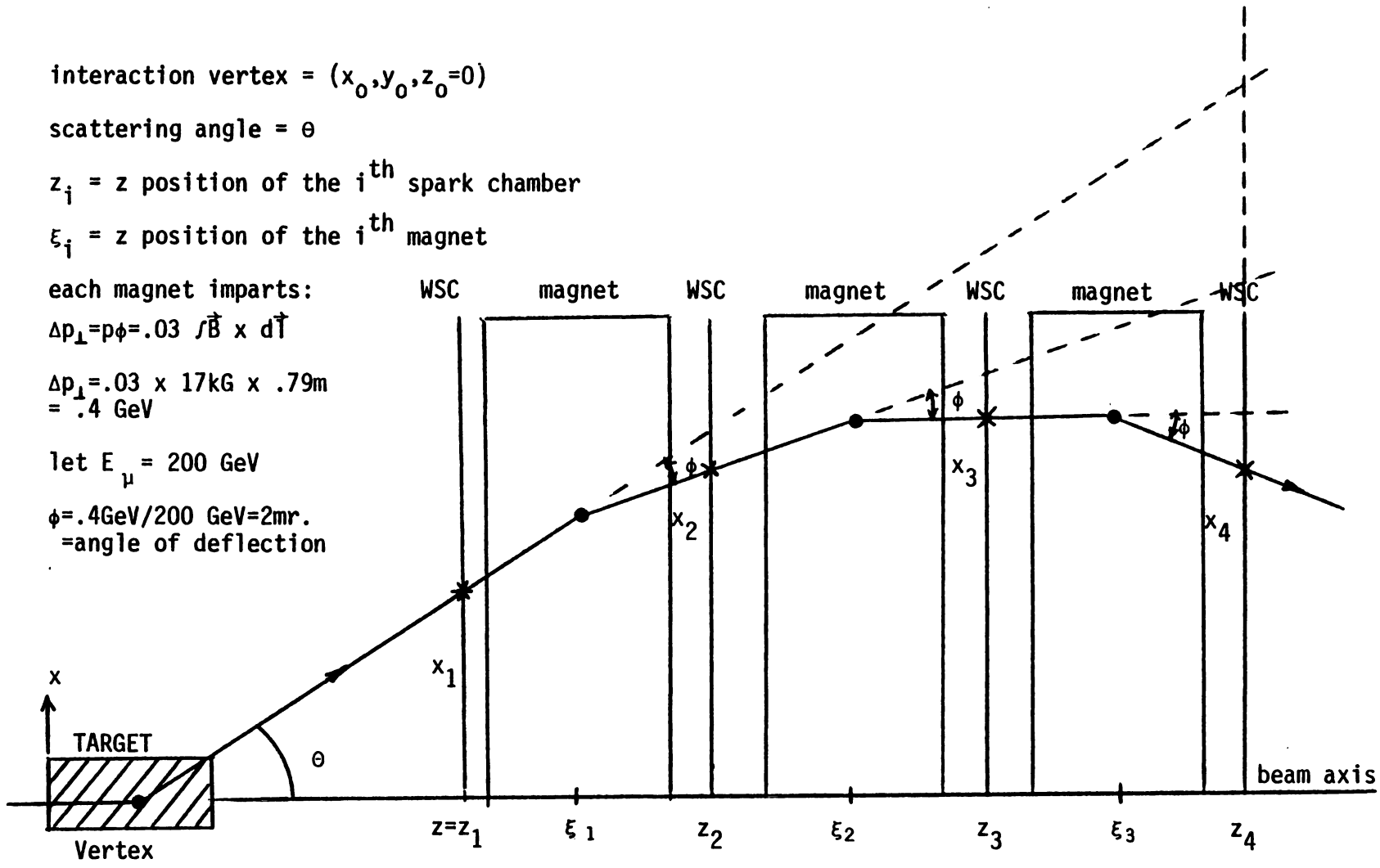

Figure 3.8 Idealized momentum reconstruction

from the left, interacts at the point $(x_o, y_o, z_o=0)$, and scatters through an angle θ. After entering the spectrometer, it bends through an angle ϕ at the center of the magnet (the impulse approximation). The muon proceeds in this way through the spectrometer; bending through an angle ϕ at each magnet, and registering its path in the wire spark chambers along the way. The spark position (transverse coordinate x) at the first chamber $(z=z_1)$ is easy to compute:

$$x_1 = x_o + z_1\,\theta \qquad (\theta<<1) \tag{55}$$

The muon is then bent in the first magnet $(z=\xi_1)$. Its position in the second chamber is

$$x_2 = x_o + z_2\,\theta - \phi(z_2 - \xi_1) \tag{56}$$

Similarly:

$$x_3 = x_o + z_3\,\theta - \phi(z_3 - \xi_1) - \phi(z_3 - \xi_2) \tag{57}$$

For the n^{th} chamber, the coordinate will be:

$$x_n = x_o + z_n\,\theta - \phi \sum_{\substack{i \\ (z_n > \xi_i)}} (z_n - \xi_i) \tag{58}$$

Now use the formula for ϕ found in Figure 3.7:

$$x_n = x_o + z_n\,\theta - \left[\frac{.03}{p} \int \vec{B} \times \vec{dl}\right] \sum_i (z_n - \xi_i) \tag{59}$$

Since we know all the z's, ξ's, $\vec{B}$, and the spark positions measured at each chamber, we ought to be able to invert the n equation (59) to get

p, $\theta(\theta_x,\theta_y)$, and (x_o,y_o). Unfortunately, we really do not know $\vec{B}$; the field in the toroids has a complex radial dependence. Also, in real life the muon undergoes continuous energy loss and multiple scattering. Equation (59) is just too simple.

The nonlinear multiparameter fit which is used in VOREP proceeds like this: (i) guess the initial values of p, x_o, y_o, θ_x, and θ_y (these variables, on which everything depends, are called $\alpha_1,\alpha_2,\alpha_3,\alpha_4,\alpha_5$); (ii) predict the spark positions in all chambers using a modified version of equation (59); (iii) in order to test the quality of the fit so far, define a chi-squared function which depends on the residues $\delta x = x_{predicted} - x_{observed}$, and with proper allowance for multiple scattering and energy loss; (iv) minimize the χ^2 with respect to the five variables α_i; (v) solve for new values of the α_i and make new spark predictions. Keep iterating until the values for the α_i (i.e., $x_o,y_o,\theta_x,\theta_y,p$) change by an arbitrarily small amount.

The following expression is <u>not</u> a good expression for χ^2:

$$\chi^2 = \sum_i \left[\left(\frac{\delta x_i}{\sigma_i}\right)^2 + \left(\frac{\delta y_i}{\sigma_i}\right)\right] \qquad \begin{array}{l} i = \text{summation over chambers} \\ \text{downstream of the target} \end{array} \qquad (60)$$

where δx_i=x residual at the i^{th} chamber and σ is the measurement error at that chamber. Because of multiple scattering in the toroids, spark predictions in some chambers (the back chambers for instance) will be worse than for others. Therefore, any expression for χ^2 should contain error terms which are correlated among all the chambers:

$$\chi^2 = \sum_{\substack{i,j \\ i\leq j}} V_{ij}^{-1} (\delta x_i \delta x_j + \delta y_i \delta y_j) \qquad (61)$$

In this expression the simple measurement error σ_i has been replaced by an error matrix Y_{ij} which properly weights the correlation terms involving errors in chamber i and chamber j.

The error in a measurement of a spark coordinate made at $z=z_1$ due to multiple scattering in a piece of iron of length L, at $z=\xi$, is given by:

$$\Delta x = \Theta_{ms} (z_1 - \xi)$$

where $$\Theta_{ms} = \langle\Theta_{ms}^2\rangle^{1/2} = \frac{.015}{p}\sqrt{\frac{L}{1.77}} \qquad (62)$$

A typical correlation term would look like

$$\delta x_i \delta x_j = \Delta x_i \Delta x_j = \Theta_{ms} \cdot (z_i - \xi) \cdot \Theta_{ms} \cdot (z_j - \xi) \qquad (63)$$

The full expression for Y_{ij} will contain a summation over all magnets which are upstream of both the i^{th} and j^{th} spark chamber. The inherent measurement error of the chamber (σ_i = 0.1 cm) must also be included:

$$Y_{ij} = \langle\Theta_{ms}\rangle^2 \sum_{m=1}^{8} (z_i - \xi_m)(z_j - \xi_m) + \delta_{ij}\sigma_i^2 \qquad (64)$$

where $z_i > \xi_m$, $z_j > \xi_m$, and $\langle\Theta_{ms}\rangle^2 = (.015/p)^2\, L/1.77 \tilde{=} 1.1\times10^{-2}/p^2(\text{GeV})^2$.

Equation (59) turns out to be extremely complicated when multiple scattering and energy loss in iron, and the radial dependence of the magnetic field are introduced. Instead, the prediction of spark positions will be made using an expansion in powers of p^{-1}. As mentioned earlier, the quantity we actually deal with in the

reconstruction process is the radius of curvature k, which is related to the momentum: $k=(qB_0/3327.4)/p$, (qB_0=constant). The coordinate x and slope $x' = dx/dz$ at each chamber is calculated in powers of k:

$$x = c_0 + c_1 k + c_2 k^2$$

$$x' = c_0' + c_1' k + c_2' k^2 \qquad (65)$$

where $c_0, c_1, c_2, c_0', c_1'$, and c_2' are coefficients of the expansion and which depend on the $\alpha_i(x_0, y_0, \theta_x, \theta_y, p)$. There are similar expressions at each chamber for the y coordinates.

Using our initial guesses for the α_i, we can predict (x, x', y, y') at the front of the spectrometer. Since we know the behavior of muons in an azimuthal magnetic field, we can trace the muon's trajectory toward the back of the spectrometer. This provides us with a set of predicted sparks and launches the iterative procedure described above. We finally arrive at values for $x_0, y_0, \theta_x, \theta_y$, and $p=E'$

We make a special effort to discover and correct for wrong sparks during the fitting process. By observing the residue $\delta x = x_{predicted} - x_{observed}$ for all the chambers, the sign of one of the residues will sometimes be opposite that of all the other chambers. If, in addition, the size of the residue is larger than a prescribed window, then we conclude that this spark was found erroneously (that it does not lie on the muon's true trajectory), and it is removed. The fit is then repeated. Usually the deletion of the bad spark significantly improves the χ^2 for the overall fit, and gives a more reliable estimate for E' and θ.

The last function of the analysis program is to write a secondary file containing the results of the spark selection, the momentum fit, and other useful information. The format for this file is shown in Table 3.9.

3.4 Resolution

The reconstruction program described above is limited in its ability to find E_0, E', and θ by the nature of the apparatus used in E319. Since we used a nuclear target (iron) the Fermi motion of the nucleons in each iron nucleus has the effect of smearing the actual value of E_0 in the nucleon rest system by as much as 13%. Furthermore, by using an iron spectrometer, multiple scattering limits resolution in E' to about 9%. The resolution in θ is about 1%. The spectrometer calibration showed that the resolution in E' was relatively constant, about 9%, for an E' range of 50 up to 250 GeV. For E' below about 30 GeV, energy losses become more important and the calibration begins to break down. Above about 250 GeV the calibration again becomes suspect; the scattered muon's trajectory is relatively "stiff" and unbending, and this makes a reliable momentum reconstruction more difficult.

The uncertainties in E_0, E', and θ can result in rather large resolutions in derivative quantities such as ν, q^2, and ω. Using a large sample of monte carlo events, made to simulate real data, we can see how big the resolution is. For each monte carlo event, the values of E_0, E', and θ are known for the nucleon rest system (without Fermi motion this frame would be the same as the lab frame); these I shall call the "physics" values of those variables. We also know the values of E_0, E', and θ via the reconstruction process (just like for real data). A histogram of the quantity $[\nu_{physics}-\nu_{reconstructed}]/\nu_{physics}$

Table 3.9 Secondary tape format (energies in Gev, distance in cm.)

WORD	CONTENT
1	run number x 100000 + trigger number
2	E (hadron) from calorimeter
3	spill number
4-17	measured x in all chambers (PC5...WSC1)
18-31	measured y in all chambers (PC5...WSC1)
32-42	fitted x in most chambers (PC2...WSC1)
43-53	fitted y in most chambers (PC2...WSC1)
54-56	(p_x,p_y,p_z) beam muon
57-58	(x,y) beam track at z=0
59-61	(p_x,p_y,p_z) scattered muon
62-63	(x,y) scattered track at z=0
64	χ^2 (spectrometer track fit)
65	degrees of freedom for spectrometer track
66	ZADC
67	Monte Carlo event weight (=1 for data)
68-71	(x,y,θ_x,θ_y) at WSC 8
72	PBACK (E' at the back of the spectrometer)
73	χ^2/DOF for the track in the rear seven WSC's
74	packed word: number of fired wires in PC1,2
75	packed word: number of fired wires in WSC1-9
76	coordinates of PC5-1, WSC9-1 contributing to the beam track and the scattered track
77	number of spectrometer tracks
78	number of beam tracks
79-90	DCR's and TDC's
91-150	packed 16 bit ADC's

will have a Guassian shape, indicative of the Guassian processes causing the uncertainties (e.g., Coulomb multiple scattering). The standard deviation (square root of the variance) of this distribution is taken to be the "resolution" of the apparatus in the variable ν; the same for the other kinematical quantities. Table 3.10 shows the resolutions of ν, ω, q^2, and $x=q^2/2m\nu$ for several values of $y=\nu/E_0$, and also for q^2 and ω.

3.5 Acceptance

The most striking feature of this apparatus, from an acceptance standpoint, is the bias against low-angle scattering. The field-free regions in the toroid magnet holes and the beam veto counters cause such events to be rejected. Muons which scatter at very large angles (>100 mr.) and which pass outside the physical extent of the toroids (87 cm. outer radius) are also lost. The acceptance of the apparatus, as a function of one or more kinematic variables, is defined to be the number of accepted monte carlo events (events successfully reaching the rear of the spectrometer and passing other nominal cuts) in a certain kinematic range, divided by the total number of monte carlo events generated in that range. Figure 3.9 shows the acceptance in the ω-q^2 plane while Figure 3.10 shows the acceptance in the q^2-ν plane. Figures 3.11-3.17 show the acceptances in single kinematic variables.

3.6 Data Distributions

The data sample studied in this dissertation consists of approximately 126,000 fully accepted and reconstructed data events, with a like number of monte carlo events. Figure 3.18 through 3.34 show

histograms of this data for several important kinematic and reconstruction parameters. The analogous histograms for the monte carlo events will appear in chapter four. An overall comparison of data to monte carlo distributions, including averages of all important kinematic quantities, will be given in chapter five.

Several of the quantities histogrammed need explanation:

--ZMIN is the z position at which the distance-of-closest-approach between spectrometer track and beam track occurs. It is taken to be the z coordinate of the interaction vertex.

--χ^2 is the chi-squared per degree of freedom of the entire spectrometer track for the multiparameter reconstruction fit.

--(x_{beam}, y_{beam}) are the coordinates of the beam muon extrapolated to $z=0$.

--The radius of the muon's trajectory in WSC5, WSC1, and at the face of the front magnet (RMAG) is given in cm.

Finally consistency plots of several important variable are shown in Figure 3.35. These plots show the average value of the particular variable plotted for randomly chosen runs from throughout the running period.

Table 3.10(a) (%) Resolution σ as a Function of $y=\nu/E_o$

	$\sigma(\nu)$	$\sigma(\omega)$	$\sigma(q^2)$	$\sigma(x=1/\omega)$
all y	21.4	37.3	22.7	35.9
0<y<.1	--	99.9	27.9	35.5
.1<y<.2	48.6	55.5	21.7	36.6
.2<y<.3	30.4	40.6	20.5	41.9
.3<y<.4	22.0	34.1	19.9	37.6
.4<y<.5	18.5	31.5	20.9	32.9
.5<y<.6	17.2	30.6	22.1	31.5
.6<y<.7	16.9	30.8	22.1	31.1
.7<y<.8	16.3	33.7	27.7	33.6
.8<y<.9	15.5	36.2	28.8	36.2

Table 3.10 (b)

(%) Resolution σ as a Function of ω

ω	$\langle\omega\rangle$	$\sigma(\omega)$	$\sigma(q^2)$
$1<\omega< 2$	3.160	42.8	23.9
$2<\omega< 3$	3.400	33.2	15.8
$3<\omega< 4$	3.600	35.2	16.7
$4<\omega< 8$	5.400	37.4	17.7
$8<\omega<16$	9.960	35.9	20.3
$16<\omega<32$	20.600	33.9	26.4
$32<\omega<64$	34.000	37.3	37.7

Table 3.10 (c)

(%) Resolution σ as a Function of q^2

q^2	$\langle q^2\rangle$	$\sigma(x=1/\omega)$
$0<q^2< 10$	8.222	45.5
$10<q^2< 20$	14.780	36.4
$20<q^2< 30$	25.000	30.1
$30<q^2< 50$	38.760	26.7
$50<q^2< 80$	61.480	24.6
$80<q^2<150$	91.060	32.2

Percentage Acceptance: ω vs q^2

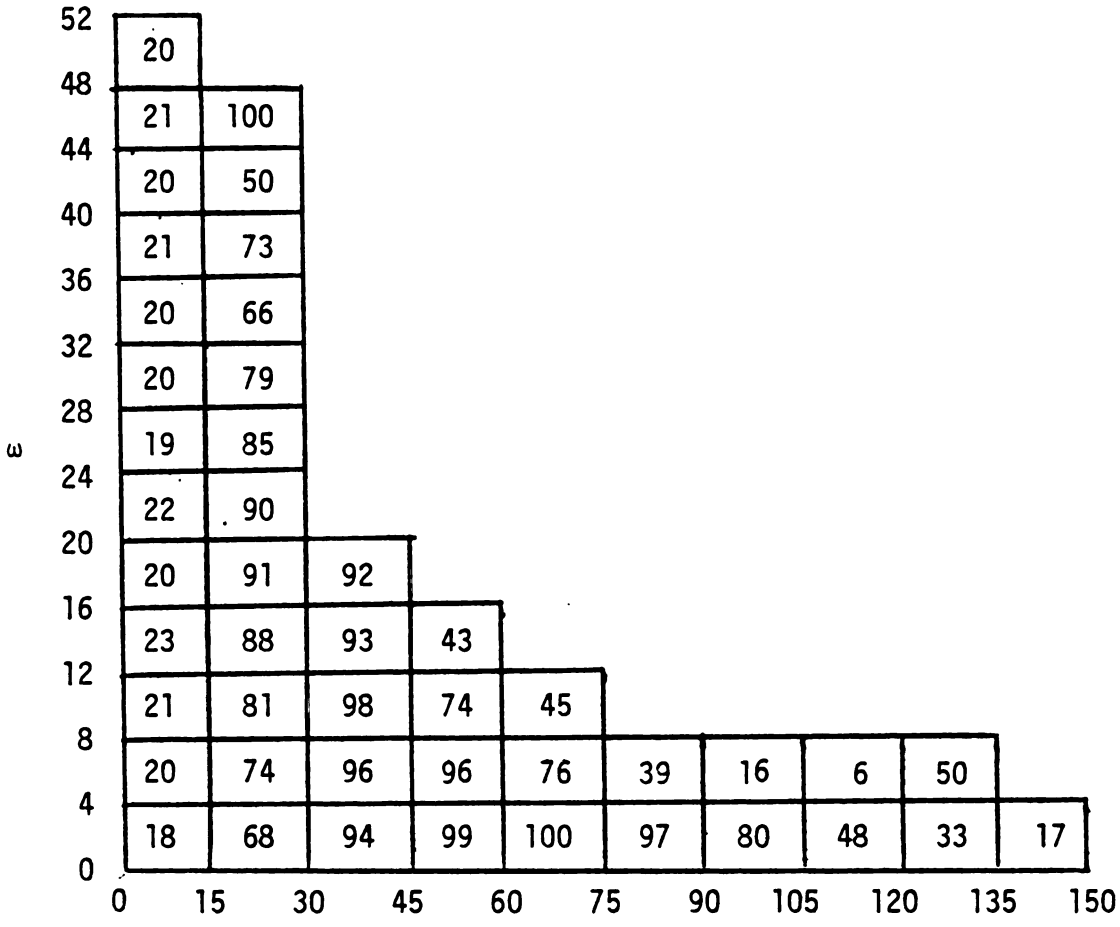

Figure 3.9

Percentage Acceptance: q^2 vs. ν

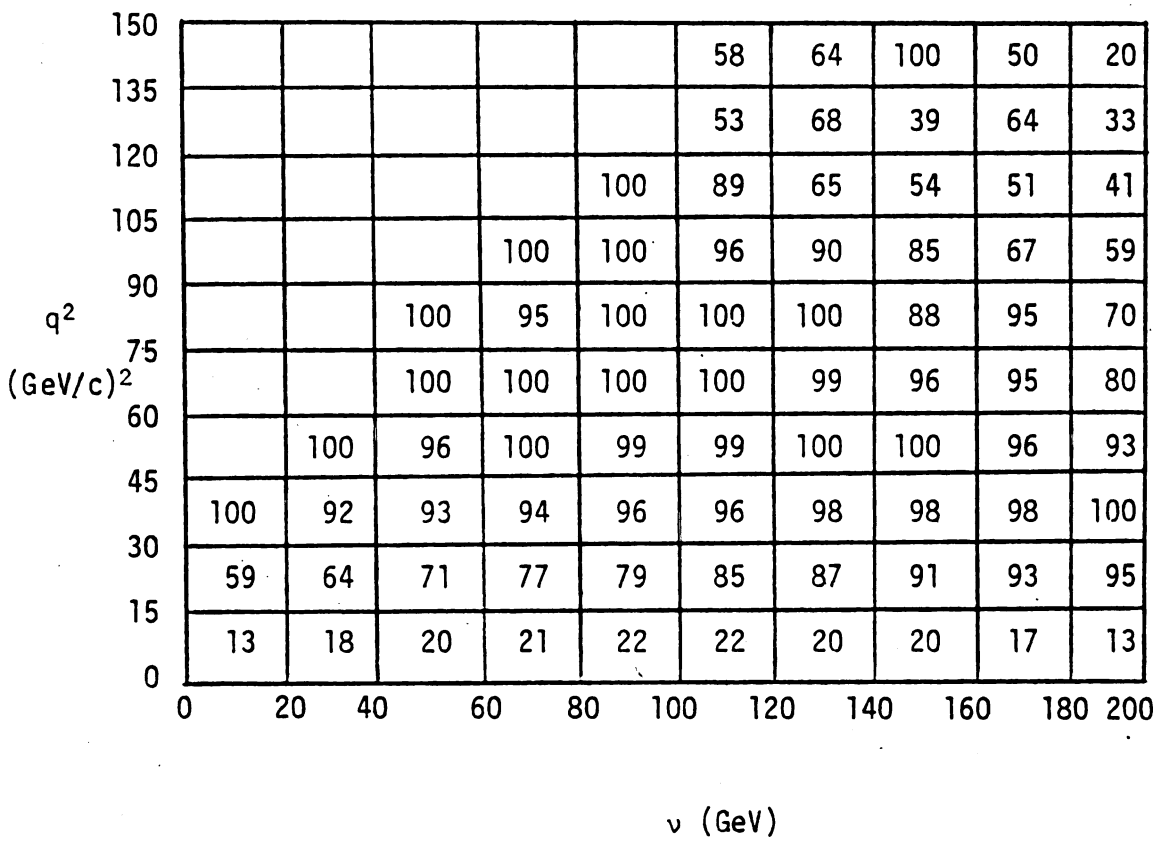

					58	64	100	50	20
					53	68	39	64	33
				100	89	65	54	51	41
			100	100	96	90	85	67	59
		100	95	100	100	100	88	95	70
		100	100	100	100	99	96	95	80
	100	96	100	99	99	100	100	96	93
100	92	93	94	96	96	98	98	98	100
59	64	71	77	79	85	87	91	93	95
13	18	20	21	22	22	20	20	17	13

Figure 3.10

Figure 3.11

Figure 3.12

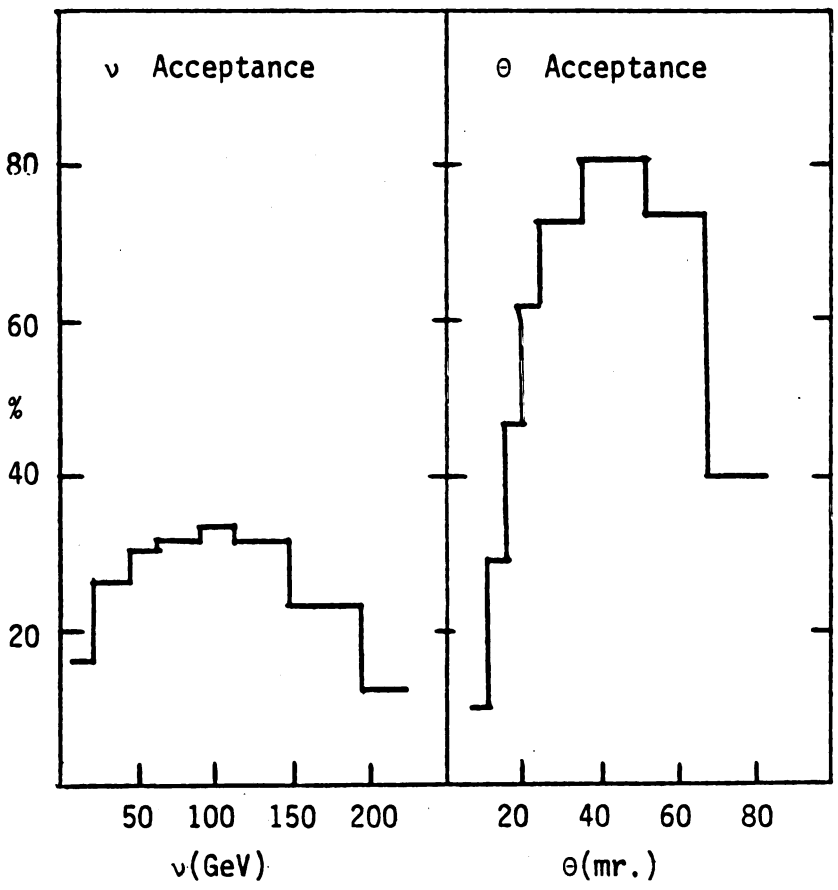

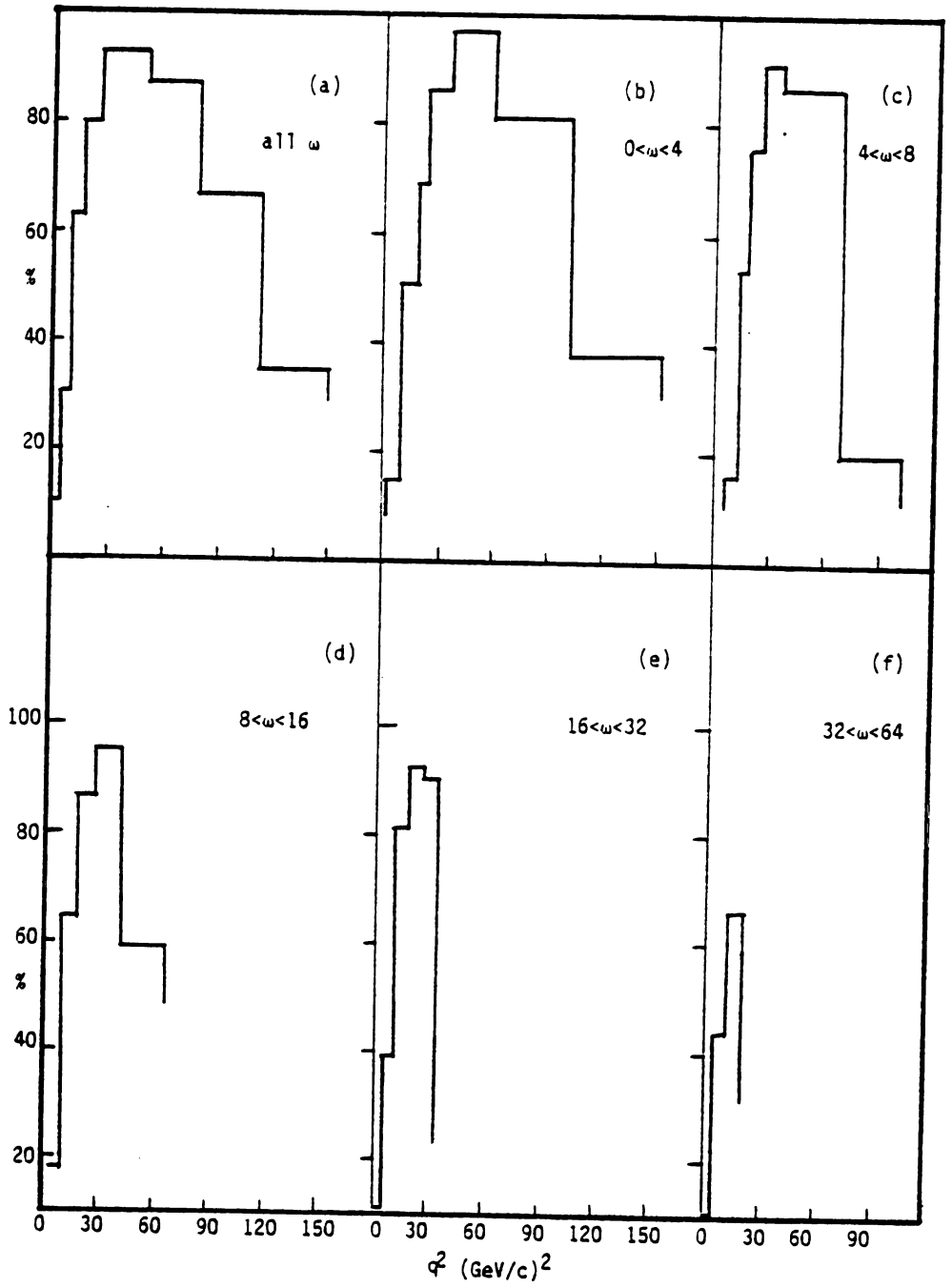

Figure 3.13 Acceptance in q^2

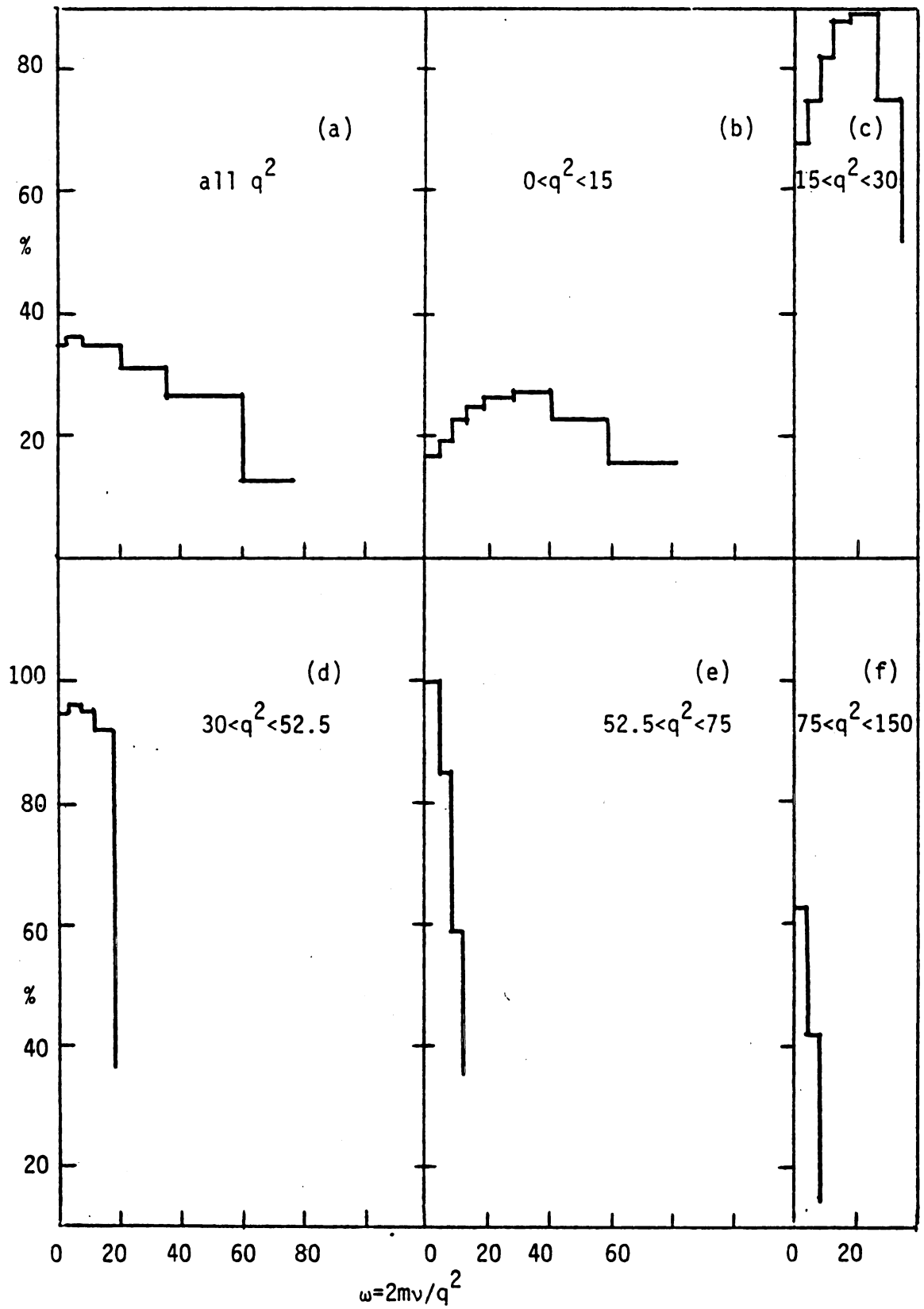

Figure 3.14 ω Acceptance

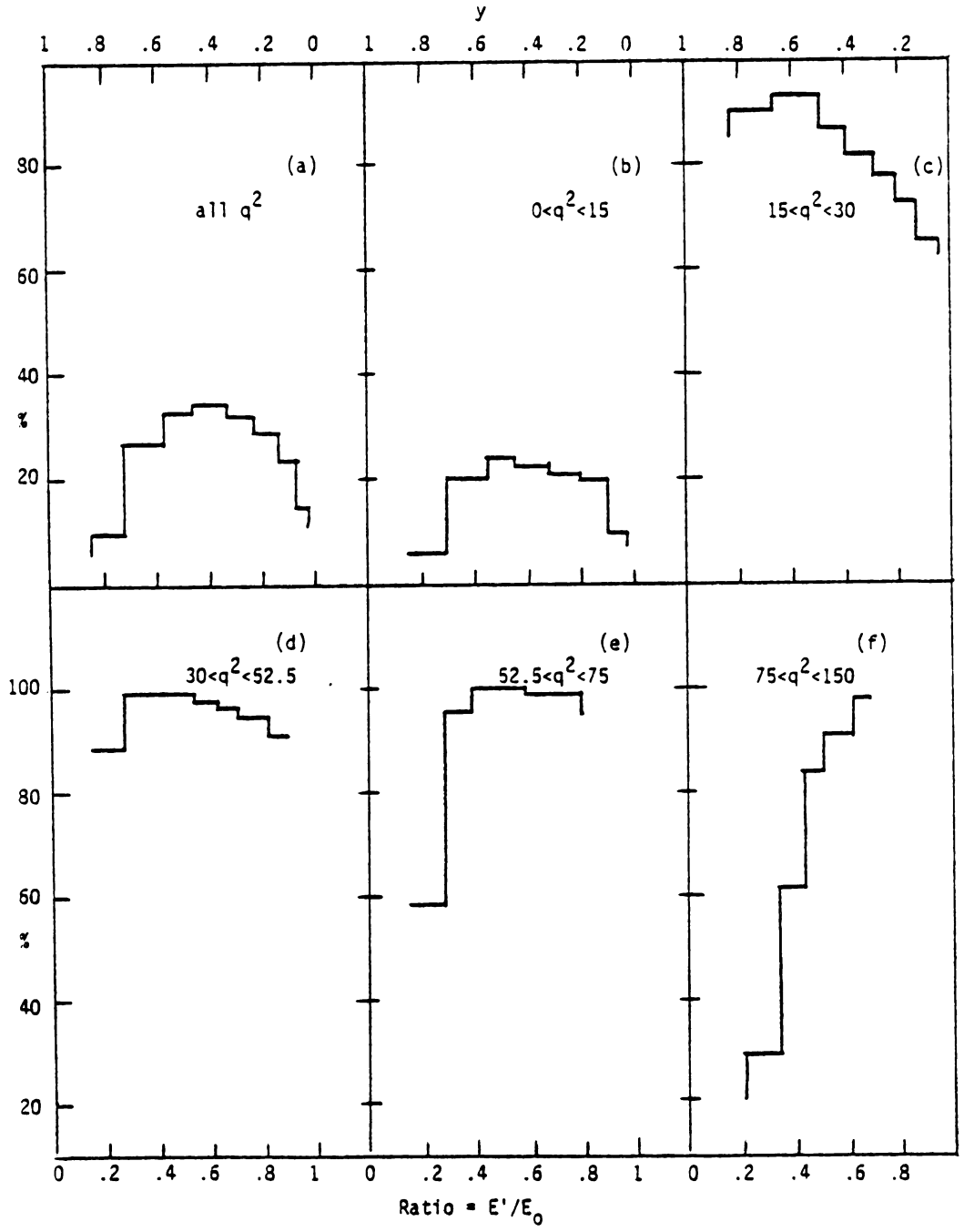

Figure 3.15 Acceptance in $y=\nu/E_0$ and $Ratio=E'/E_0$

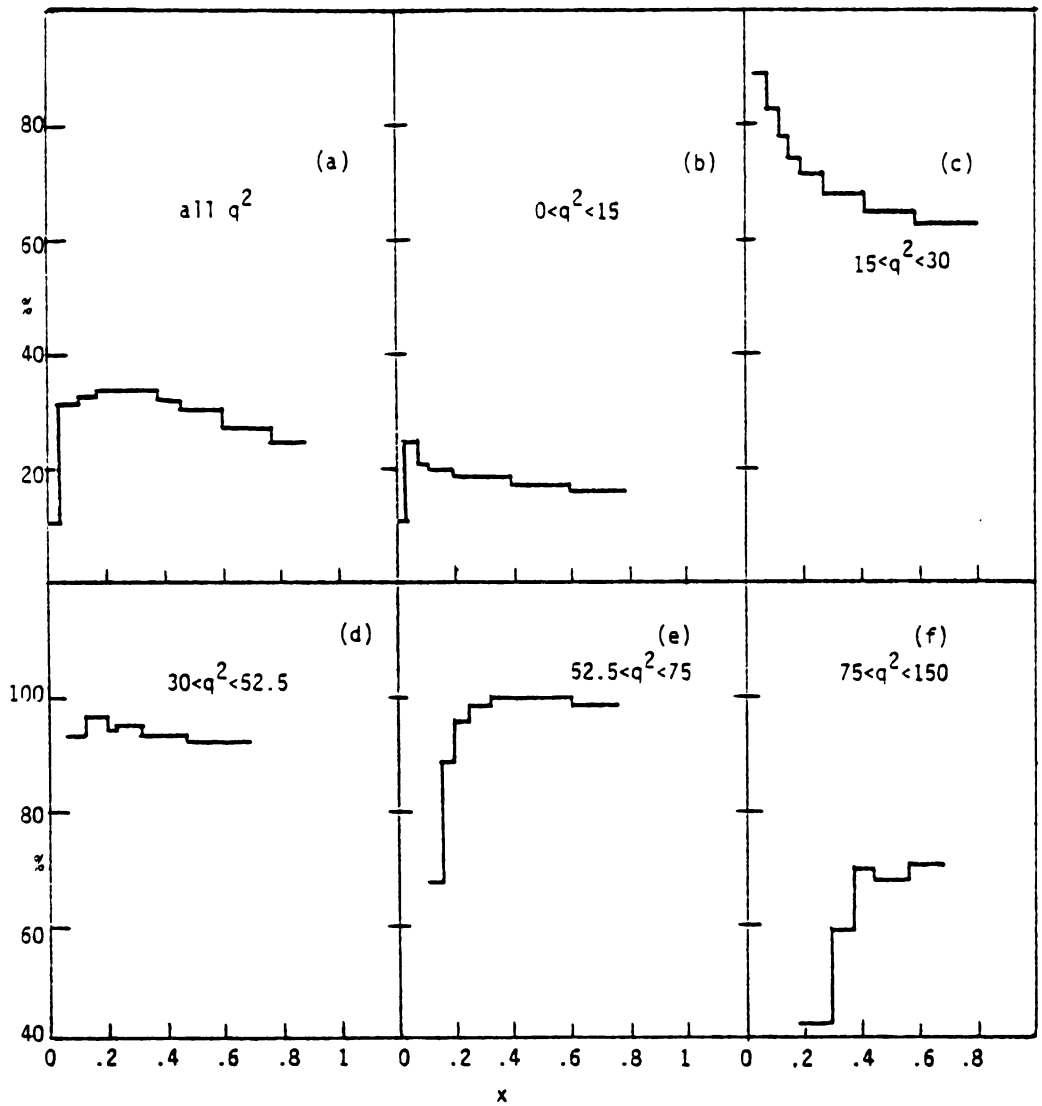

Figure 3.16 Acceptance in $x=q^2/2m\nu$

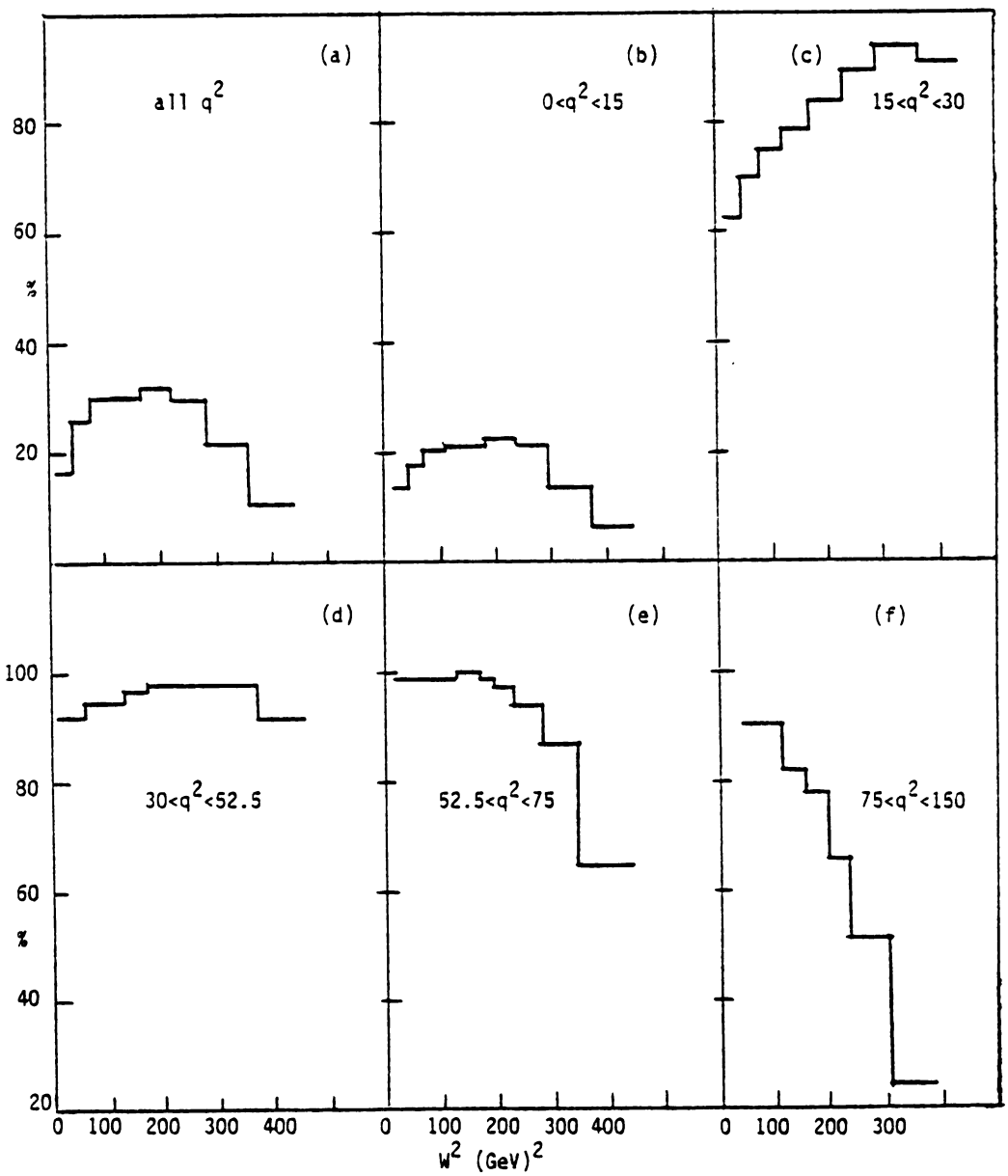

Figure 3.17 Acceptance in $W^2=2m\nu+m^2-q^2$

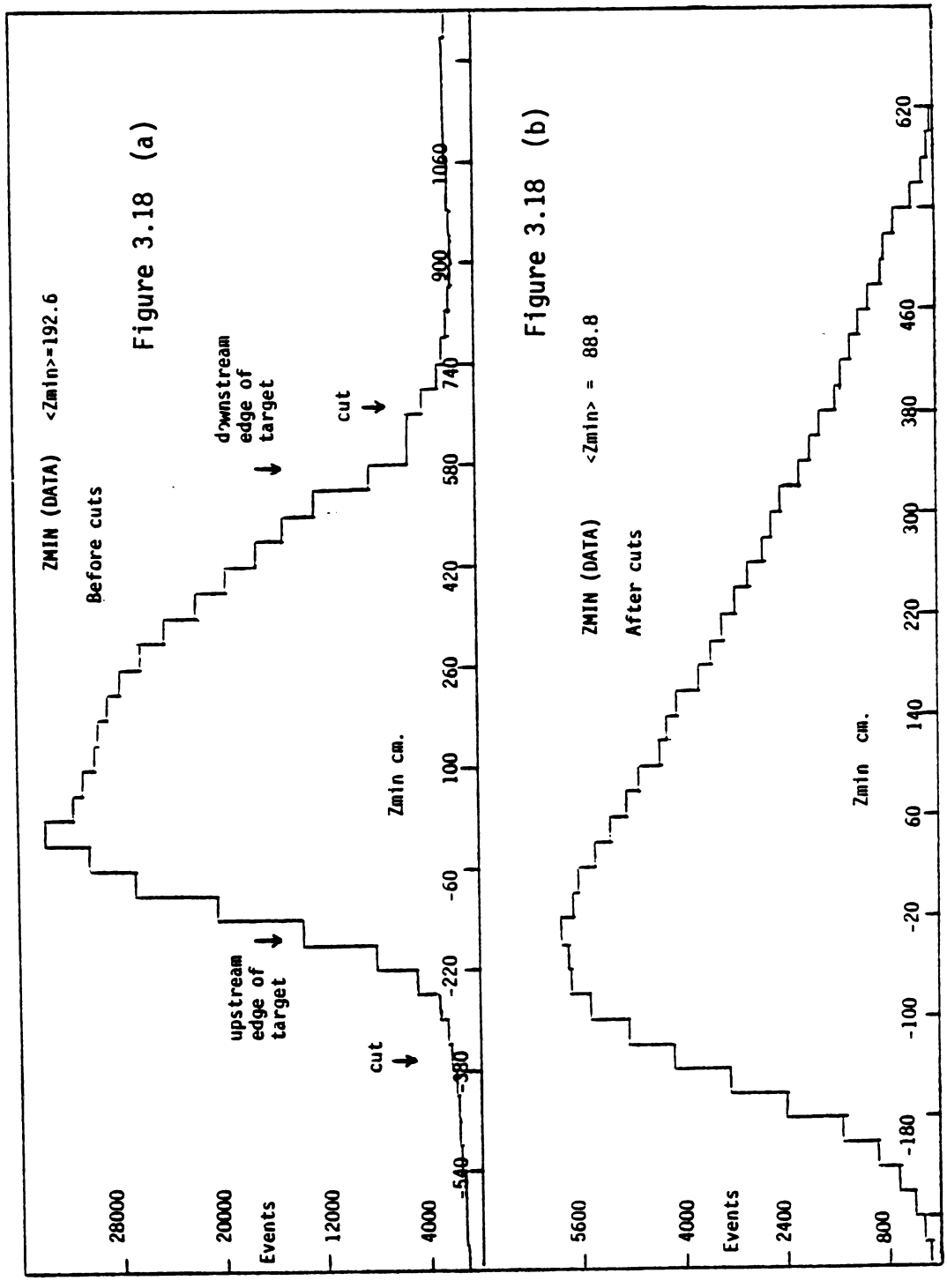
ZMIN (DATA) <Zmin>=192.6
Before cuts
Figure 3.18 (a)
upstream edge of target
downstream edge of target
cut
cut
Events
Zmin cm.
28000
20000
12000
4000
-540
-380
-220
-60
100
260
420
580
740
900
1060
ZMIN (DATA) <Zmin> = 88.8
After cuts
Figure 3.18 (b)
Events
Zmin cm.
5600
4000
2400
800
-180
-100
-20
60
140
220
300
380
460
620

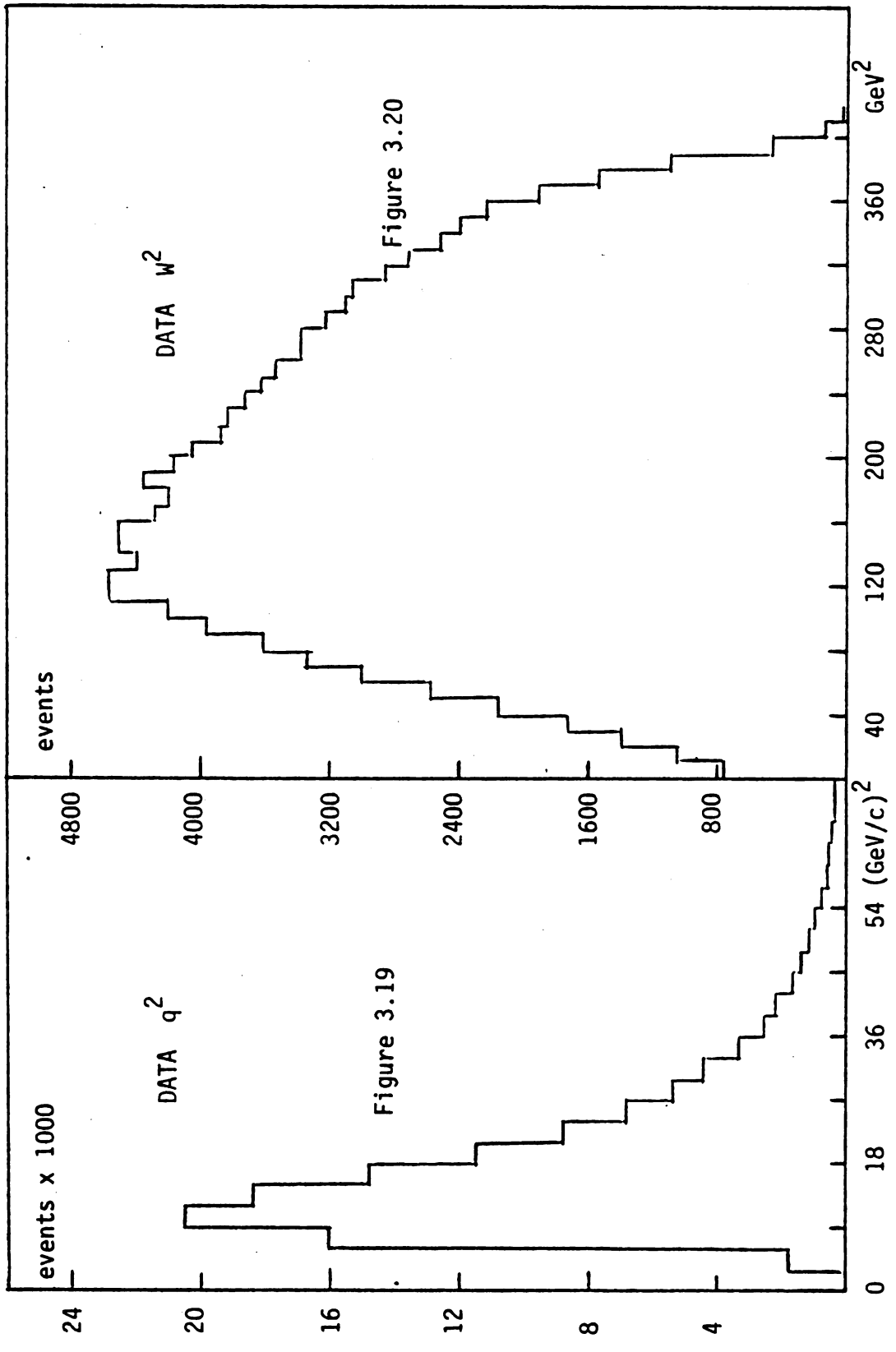

Figure 3.19

Figure 3.20

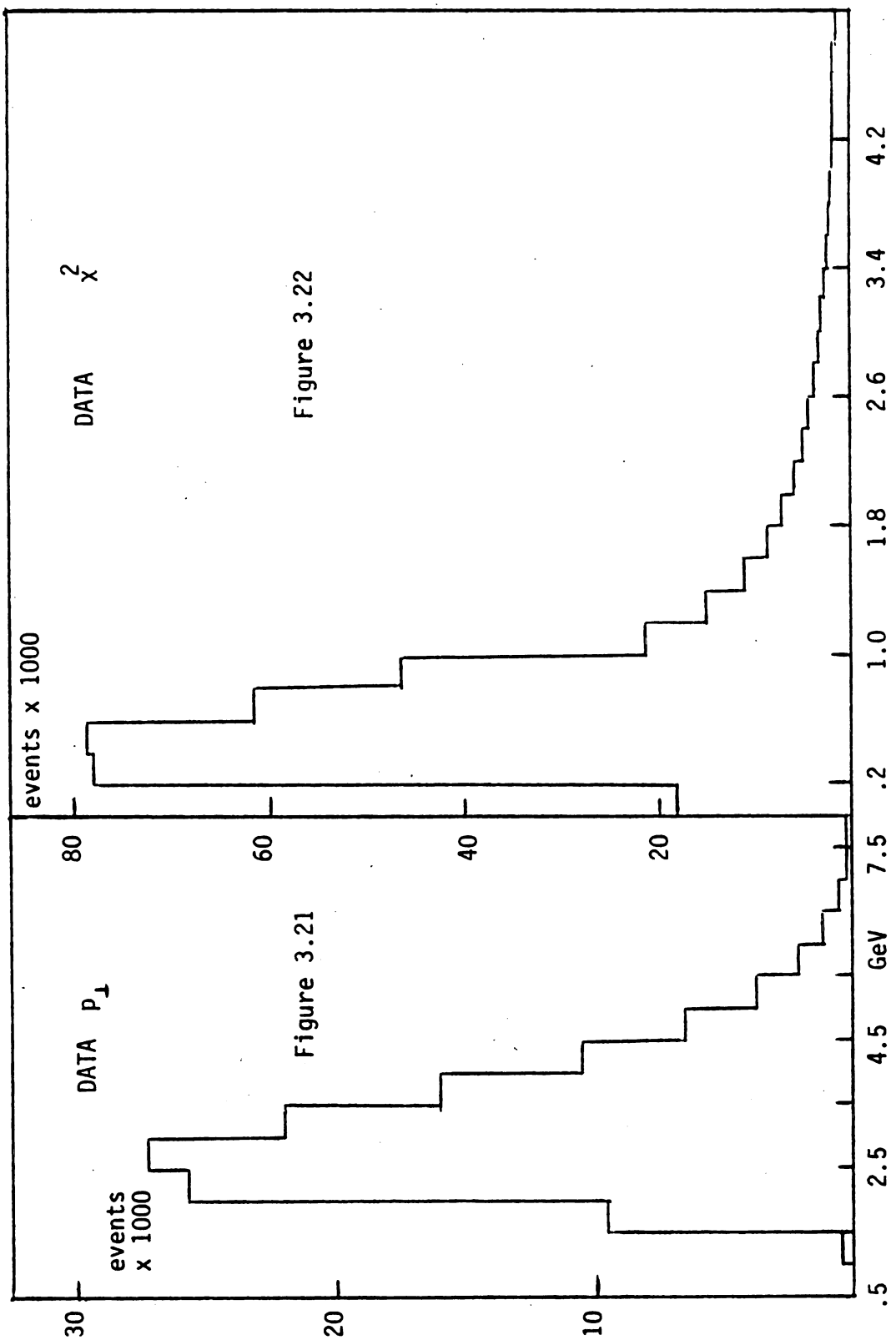

Figure 3.21

Figure 3.22

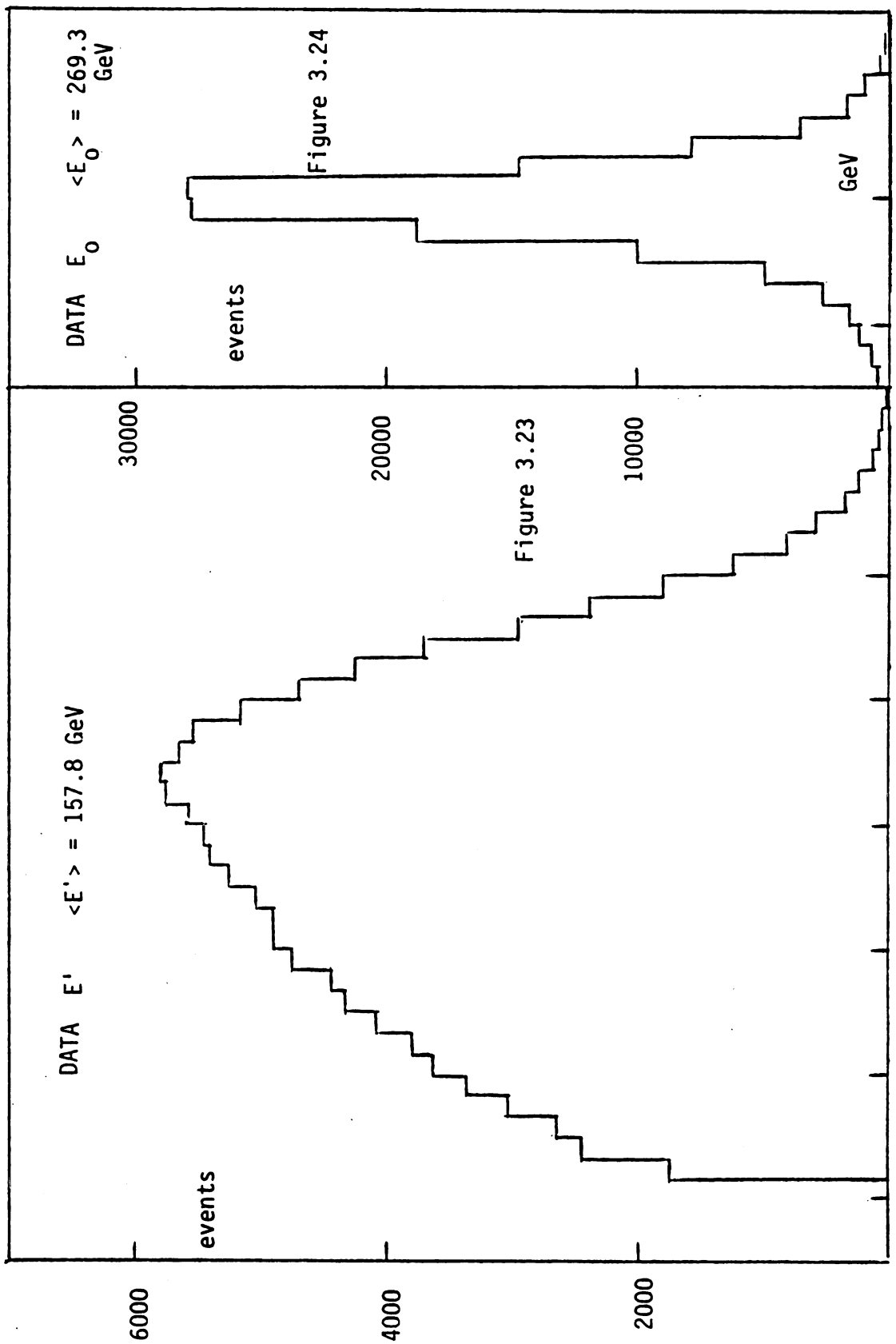
DATA E'
<E'> = 157.8 GeV
events
6000
4000
2000
42
84
126
168
210
252
GeV
Figure 3.23
DATA E_o
$<E_o>$ = 269.3 GeV
events
30000
20000
10000
258
270
282
GeV
Figure 3.24

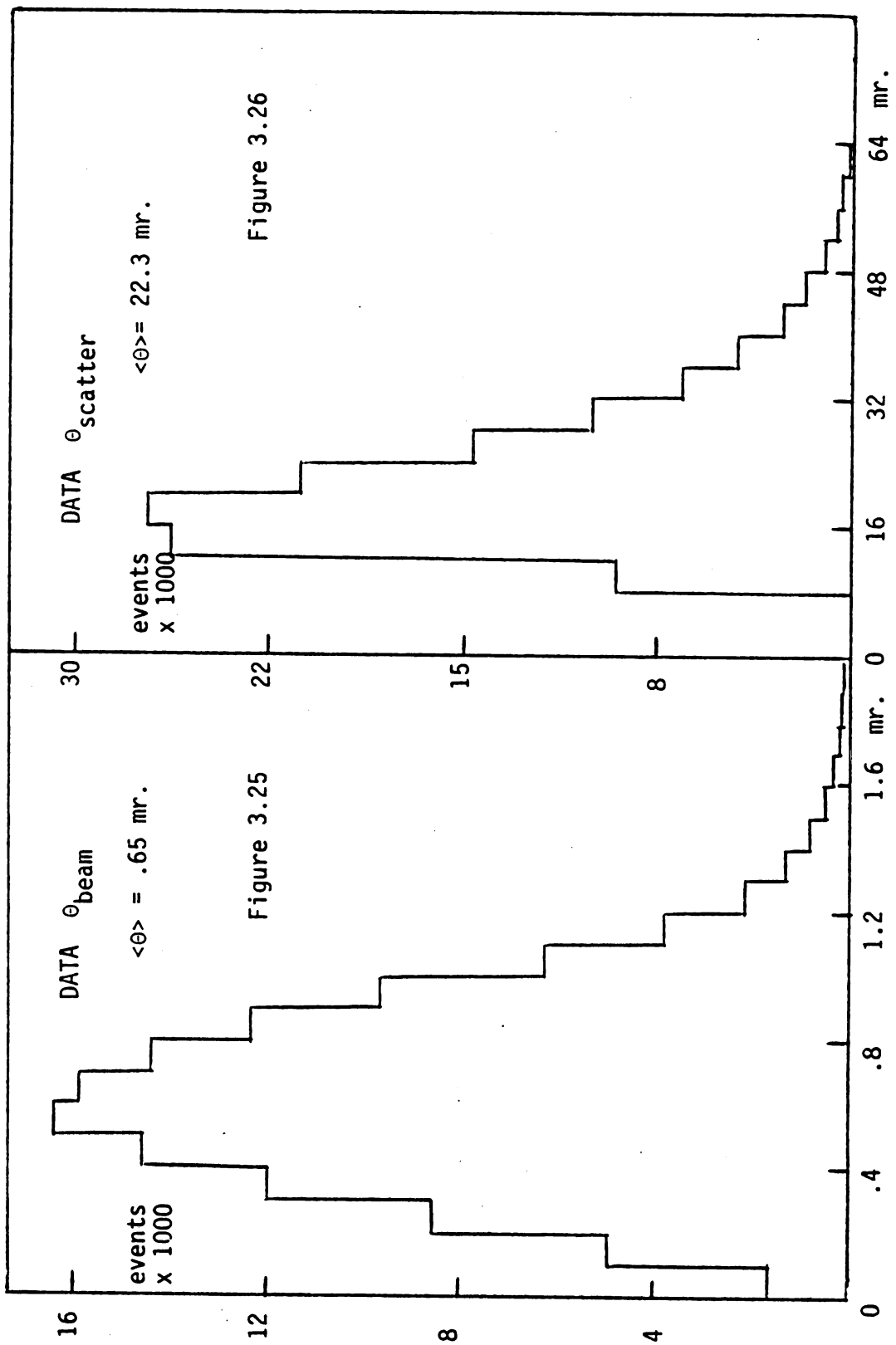

Figure 3.25

Figure 3.26

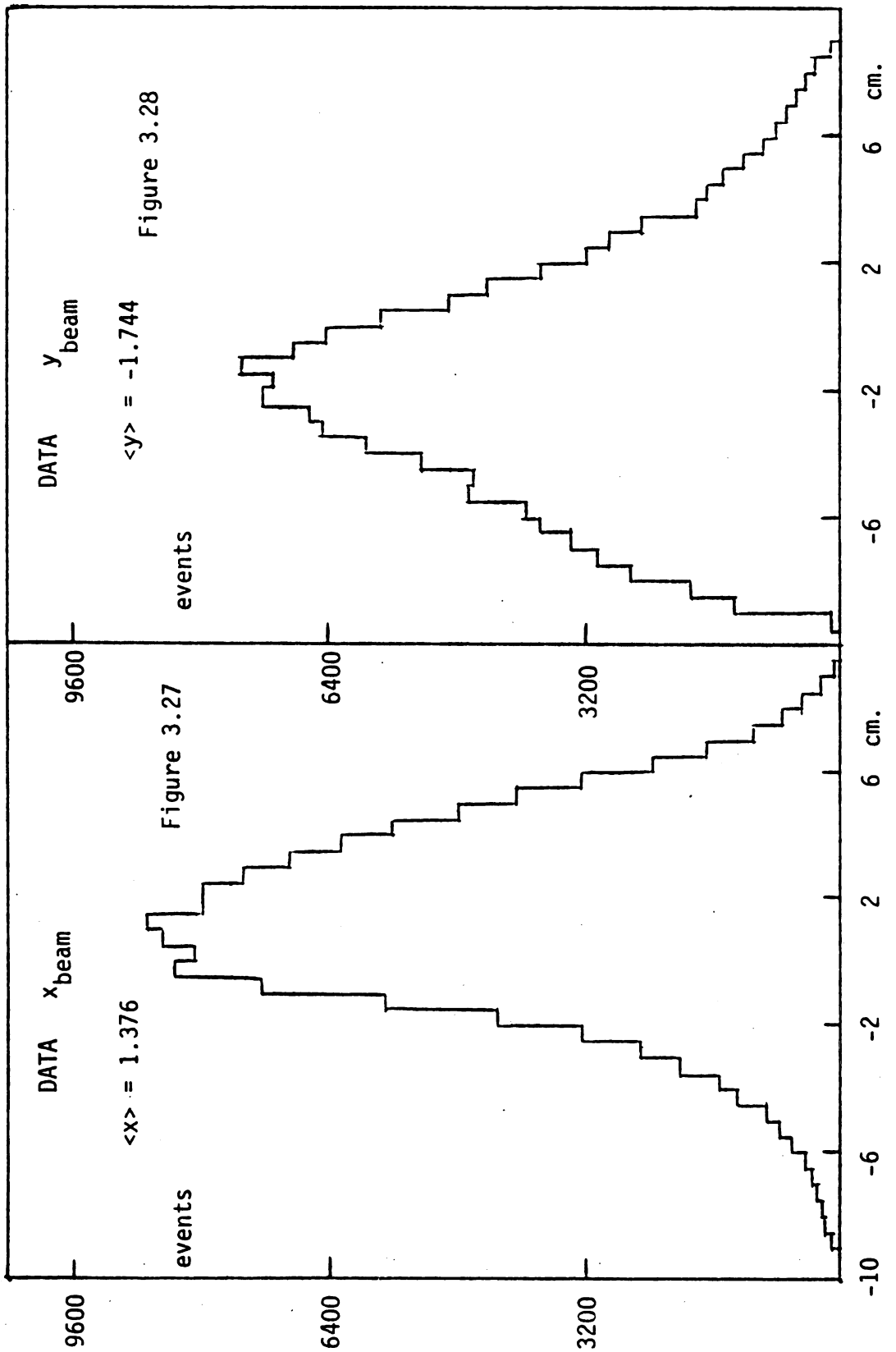

Figure 3.27

Figure 3.28

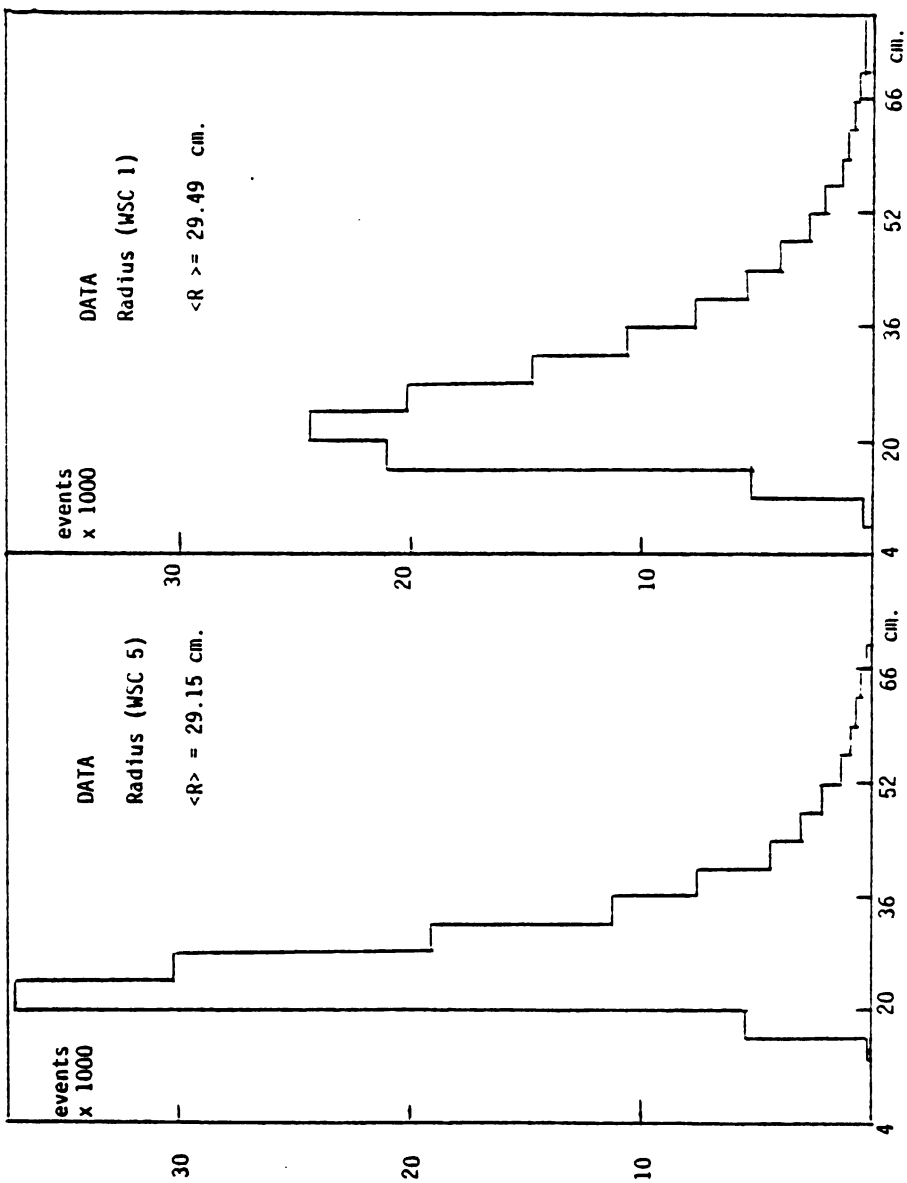

Figure 3.29

Figure 3.30

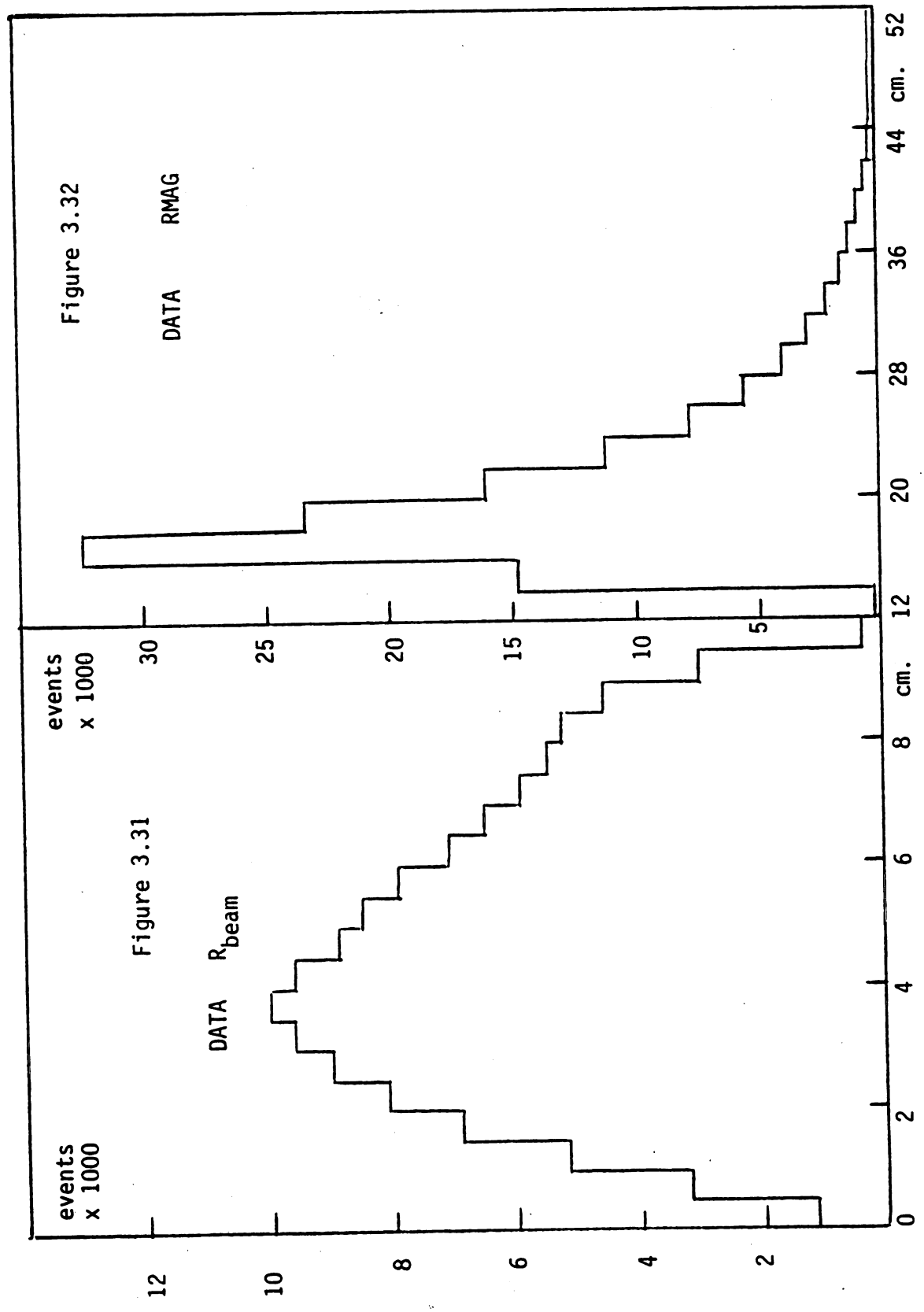
Figure 3.31
DATA R_{beam}
events x 1000
12
10
8
6
4
2
0
2
4
6
8 cm.
Figure 3.32
DATA RMAG
events x 1000
30
25
20
15
10
5
12
20
28
36
44 cm. 52

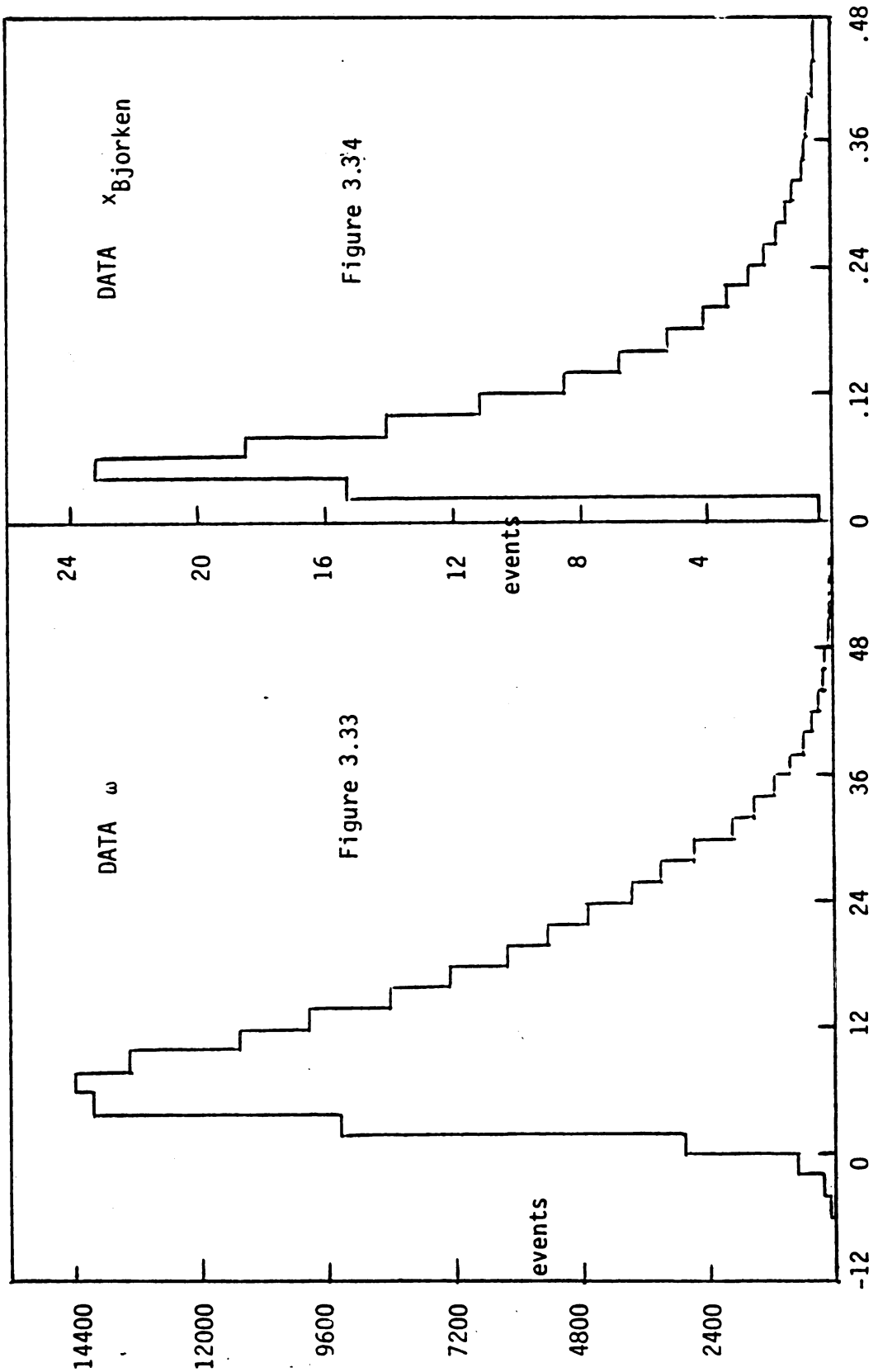

Figure 3.33

Figure 3.34

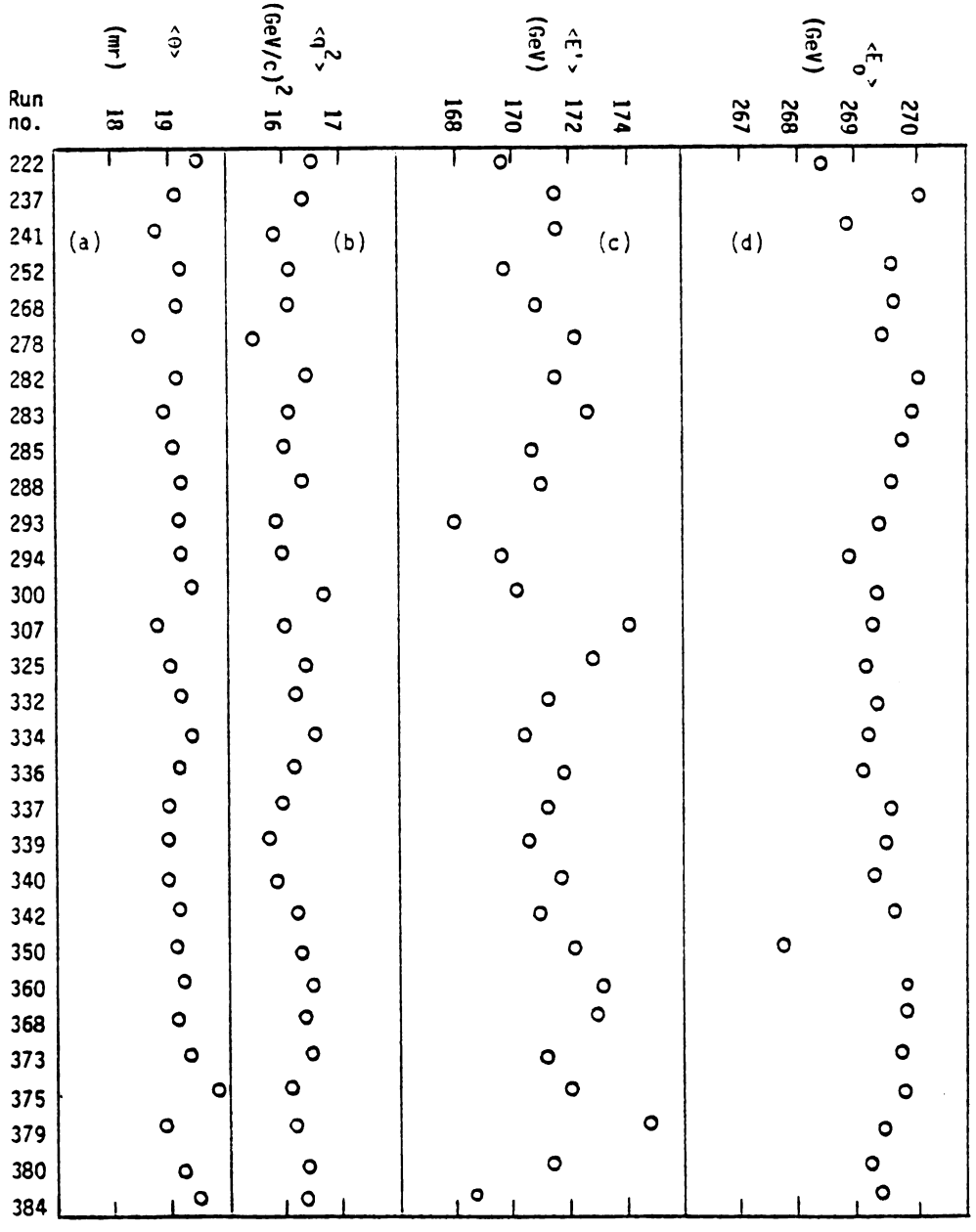

Figure 3.35 Consistency of several kinematic variables for randomly chosen runs

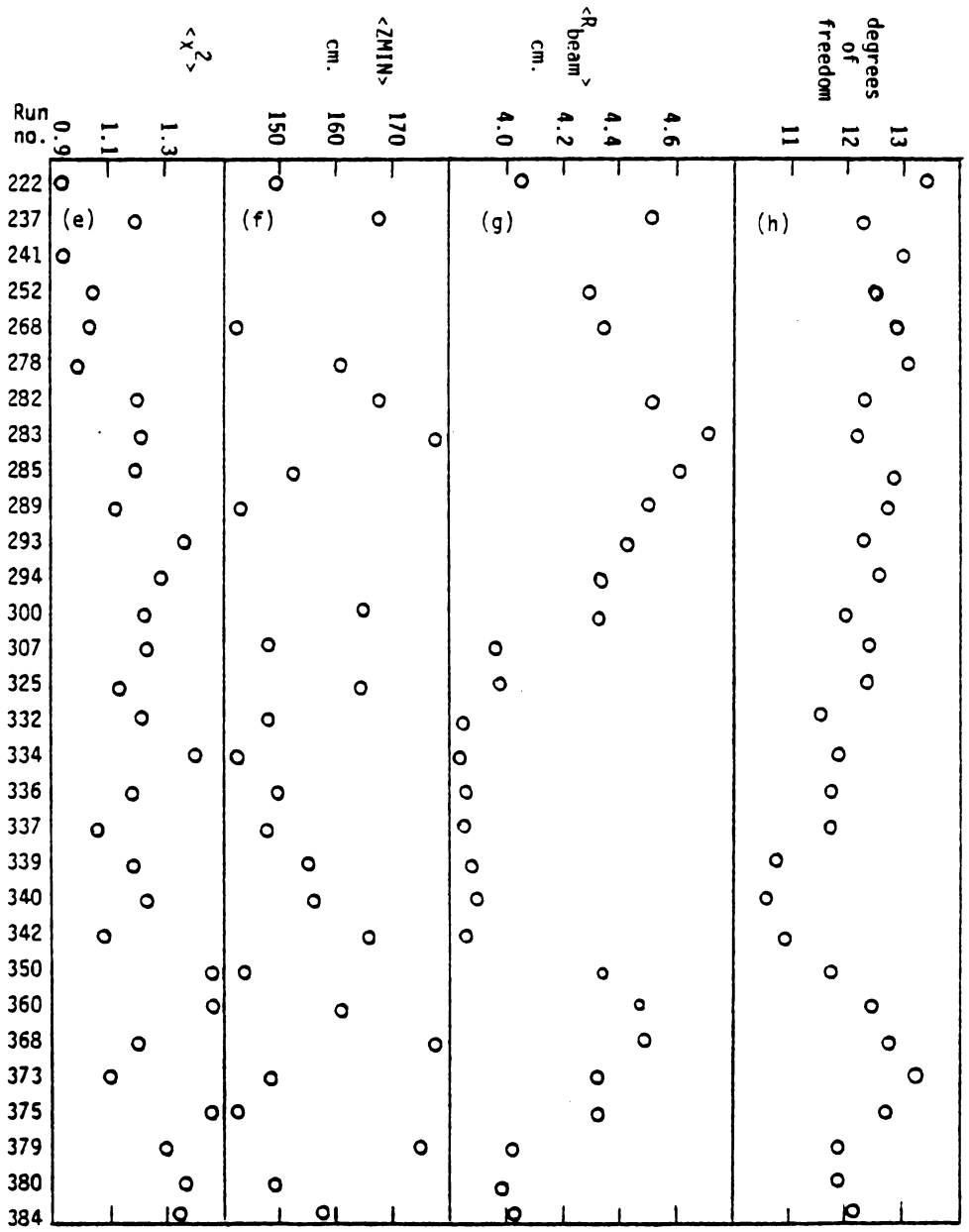

Figure 3.35 continued

CHAPTER IV

MONTE CARLO

4.1 Monte Carlo Philosophy

The central purpose of E319 was to measure the deep inelastic scattering of muons. In order to understand the results of these measurements, a monte carlo program (MCP) was designed for use in resolution, calibration, and acceptance studies of the apparatus. This was done by simulating the passage of a scattered muon through the target and spectrometer, taking into account energy loss, Coulomb multiple scattering, chamber inefficiencies, and other factors. Each event undergoes momentum reconstruction just like real data. Besides providing predictions for the behavior of the apparatus, the monte carlo simulation is useful for studying the experimental implications of certain theoretical models. The extraction of the deep inelastic structure function $\nu W_2(q^2,x)$ from the raw data is performed using a data-to-monte carlo comparison. In this chapter I shall explain which assumptions and which theoretical models are used in the construction of the monte carlo, and how νW_2 is obtained. The principal inputs to the monte carlo program are outlined briefly in Table 4.1.

Table 4.1 Summary of main monte carlo features

-beam track read from data tape

-interaction vertex thrown uniformly throughout the target

-Coulomb multiple scattering in the target and spectrometer

-event weight proportional to $\frac{d^2\sigma}{dE'd\Omega}$

-scale invariance assumed: $\nu W_2(x) = \sum_i a_i(1-x)^i$ i=3,4,5,6,7
(reference 10)

-radiative corrections applied: Mo and Tsai (reference 32)
"effective radiator"

-wide angle bremsstrahlung correction applied (reference 34)

-energy loss from ionization, pair production, nucleon scattering, and straggling (reference 33)

-Fermi motion of nucleon in nucleus simulated with a thermodynamic model

-the value of $R = \sigma_s/\sigma_t$ used throughout is a constant, $= .25 \pm .10$

-"sparks" recorded at each chamber; momentum can be reconstructed just like real data

-inefficiencies are randomly applied to the chambers mimicing real chamber performance

-a smeared value of E_{hadron} simulating the calorimeter will be added in the future

4.2 The Beam

In order to provide a statistically meaningful comparison, the number of monte carlo events generated should be approximately equal to, or greater than, the number of data events recorded. As mentioned above, the monte carlo sample can be used for studying resolution and acceptance. But the principal role is the direct comparison, for all possible regions of q^2 and x, of the experimentally observed sample of data events to a sample of hypothetical events generated on the basis of scale-invariant structure functions. In performing this comparison, the monte carlo program must mimic, as closely as possible, the conditions of actual data taking.

The first consideration in generating a typical monte carlo event is the passage of a beam muon into the target. Since the acceptance is extremely sensitive to the beam shape, the beam information (beam angle, position, and energy) from real data events, as recorded on magnetic tape for special "pulser" triggers, was used as the basis for monte carlo event generation. In order to simulate the uncertainties of the beam track measurement, the beam angle was smeared using a Gaussian function with a standard deviation of .01 mr., while the beam position at z=0 was smeared by 0.1 cm.

4.3 Interaction in the Target

The beam muon continues its hypothetical journey into the target/calorimeter where it suffers small energy losses and multiple scattering in the iron. After interacting it again loses energy and multiple scatters on its way out of the target.

The energy loss of muons in iron is computed in small intervals. Losses due to μ-e, μ-N, bremsstrahlung, μ pair production, and

straggling effects are taken into account, both in the target and in the spectrometer.

Coulomb multiple scattering of muons in iron is simulated by smearing the angles along the trajectory, $\theta_x \simeq dx/dz$ and $\theta_y \simeq dy/dz$, with a Gaussian function whose standard deviation is given by:

$$\sigma = \langle\theta^2\rangle^{1/2} = \frac{.015}{p}\sqrt{\frac{L}{1.77}} \tag{66}$$

where p is the momentum in GeV and L is the step size in meters. This is the familiar multiple scattering formula; single large-angle scatters were not included since this effect is small for lengths larger than about ten radiation lengths. The energy loss and multiple scattering simulation is carried at two uniformly spaced locations in the target leading up to the interaction vertex, and then again for two locations for the scattered muon as it leaves the target.

The interaction vertex is chosen randomly along the whole length of the target. The x and y coordinates of the vertex are established before hand by the beam tape information, subject to slight changes brought about by multiple scattering. The muon's momentum 4-vector is transformed into the nucleon rest system. This is necessary since most deep inelastic phenomena are described in a "lab" frame where the nucleon is at rest. In this frame, the outgoing energy E' and scattering angle θ are chosen randomly. The value of the target nucleon's "Fermi motion" is generated using a Fermi-gas model:

$$f(p) = \frac{p^2}{1 + \exp[(P^2 - P_f^2)/2MkT]}$$

where $P_f=P_{max}=.260$ GeV and kT=.008 GeV. This momentum is oriented randomly in spatial direction. From the simulated values of E', E_o, and θ, one can compute all the other useful kinematic quantities such as ν, q^2, ω, and x. The weight for each event is proportional to the differential cross section:

$$\frac{d^2\sigma}{dE'd\Omega} = \left(\frac{d\sigma}{d\Omega}\right)_{Mott} \frac{F_2(x)}{\nu} \left[1 + 2\tan^2\frac{\theta}{2}\left(\frac{1+\nu^2/q^2}{1+R}\right)\right] \tag{67}$$

Before running the monte carlo program, called MCP, a large look-up table was constructed containing cross section information necessary for assigning a weight to an event with a given E_o, E', and θ.

Several remarks should be made about expression (67). Firstly, $R=\sigma_S/\sigma_T=.25\pm.10$ represents the average of the SLAC results reported at the Hamburg Photon-Lepton Symposium.[34] Secondly, a scale-invariant form of $F_2=\nu W_2$ was used. This was done so that the contrast between a Bjorken scale invariant prediction, and our data (which was expected to show scale violating behavior), would be more evident. In particular, the following formulas were used to derive F_2 [10]:

$$F_2^{proton}(x') = 1.0621(1-x')^3 - 2.2594(1-x')^4 + 10.54(1-x')^5 - 15.8277(1-x')^6 + 6.7931(1-x')^7 \tag{68}$$

$$F_2^{neutron}(x') = F_2^{proton}\left[1.0172 - 1.2605x' + .73723x'^2 - .34044x'^3\right] \tag{69}$$

$$F_2^{iron}(x') = \frac{Z}{A} F_2^{proton} + \frac{N}{A} F_2^{neutron} \qquad (70)$$

where Z=26, N=30, A=55.85, and $1/x'=1/x+m^2/q^2$. This formulation of F_2 is a fit to the data in Figure 1.6 which shows little or no q^2 dependence for fixed x. As for the sensitivity of the cross section to the value of R which is used, Figure 4.1 shows the ratio of $d^2\sigma/dE'd\Omega$ computed for various R's, to that for R=.25. The average $y=\nu/E_0$ for E319 was about 0.4, although a value as high as 0.8 was kinematically possible.

Muon pair production and bremsstrahlung ("internal" bremsstrahlung) at the time of the deep inelastic collision are taken into account by using the "effective radiator" technique of Mo and Tsai.[32] This process corrects the cross section for the reaction shown in Figure 4.2(a) with terms corresponding to the reactions shown in Figures 4.2 (b)-(d). "External" bremsstrahlung, taking place long before or after the nuclear collision, is handled in the energy loss mechanism described earlier. The sum of all these effects can be treated, to good approximation, like the "external" bremsstrahlung correction. The internal bremsstrahlung is equivalent to external radiation in two "equivalent radiators," one before and one after the interaction, with thickness

$$t_r = b^{-1}(\frac{\alpha}{\pi})[\ell n(q^2/m^2) - 1] \qquad b\simeq 4/3 \qquad (71)$$

Figure 4.3 shows how the total radiative correction can be approximated by a single diagram (T is the length of the target scattering material). The effective length of the scattering material in which radiation of photons is important becomes $\frac{T}{2} + t_r$.

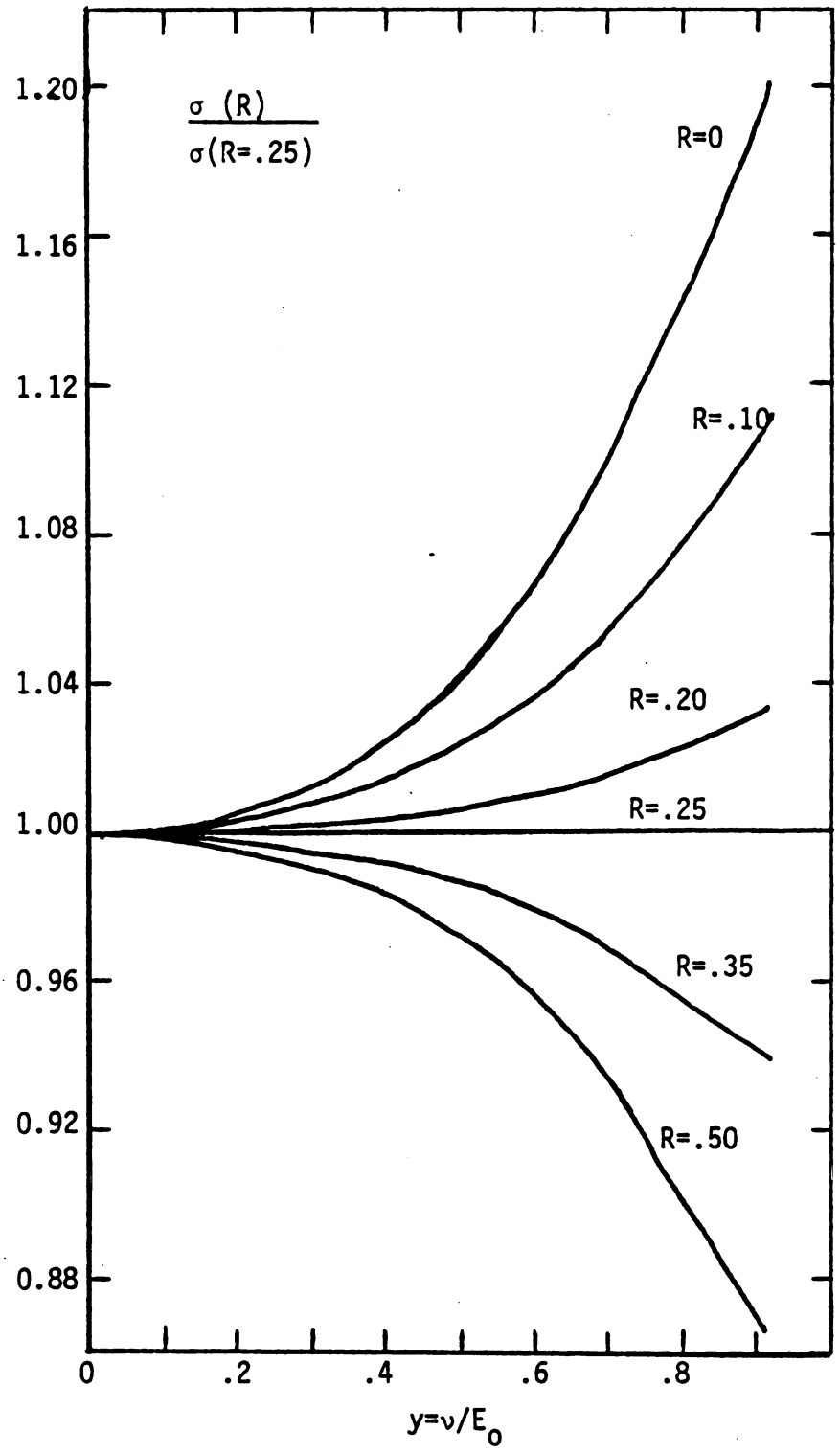

Figure 4.1 The effect of $R=\sigma_s/\sigma_t$ on the cross section

Figure 4.4 shows how radiative processes confuse the measurement of the cross section at a particular point in the (E_0,E') plane. Let point A represent a measured pair of E_0 and E'; that is, E_0 as measured before the incident muon enters the target, and E' as measured in the spectrometer. The actual scattering may have taken place at point B where $E_0=E'$: E_0 may have been degraded via bremsstrahlung as in Figure 4.2(b), with the effect of making an elastic interaction at B look like a deep inelastic interaction at A. Similarly, an elastic interaction with variables at point C could mimic a deep inelastic interaction. Other effects such as two-photon exchange, and a combination of bremsstrahlung with inelastic scattering may give contributions from any of the points in the ABC triangle. The weight for each event is multiplied by a factor RC representing the correction due to contributions from elastic and inelastic scattering:[32]

$$RC = \frac{\left(\frac{d^2\sigma}{dE'd\Omega}\right)_{\substack{\text{elastic}\\ \text{corrected}}} + \left(\frac{d^2\sigma}{dE'd\Omega}\right)_{\substack{\text{inelastic}\\ \text{corrected}}}}{\left(\frac{d^2\sigma}{dE'd\Omega}\right)_{\substack{\text{inelastic}\\ \text{uncorrected}}}} \tag{72}$$

The last correction to the scattering cross section to be made was that due to wide-angle bremsstrahlung, the emission of a photon at a much larger angle than in the usual case already studied. This multiplicative correction to the event weight is of the form:[35]

$$\begin{aligned} \text{correction} &= 1 + \frac{d\sigma(\text{wide angle bremsstrahlung})}{d\sigma(\text{deep inelastic scattering})} \\ &\cong 1 + \frac{Z^2\alpha^2}{\pi A}\,\frac{y^2}{1-y}\,\frac{G(\omega)}{F_2(x,q^2)} \end{aligned} \tag{73}$$

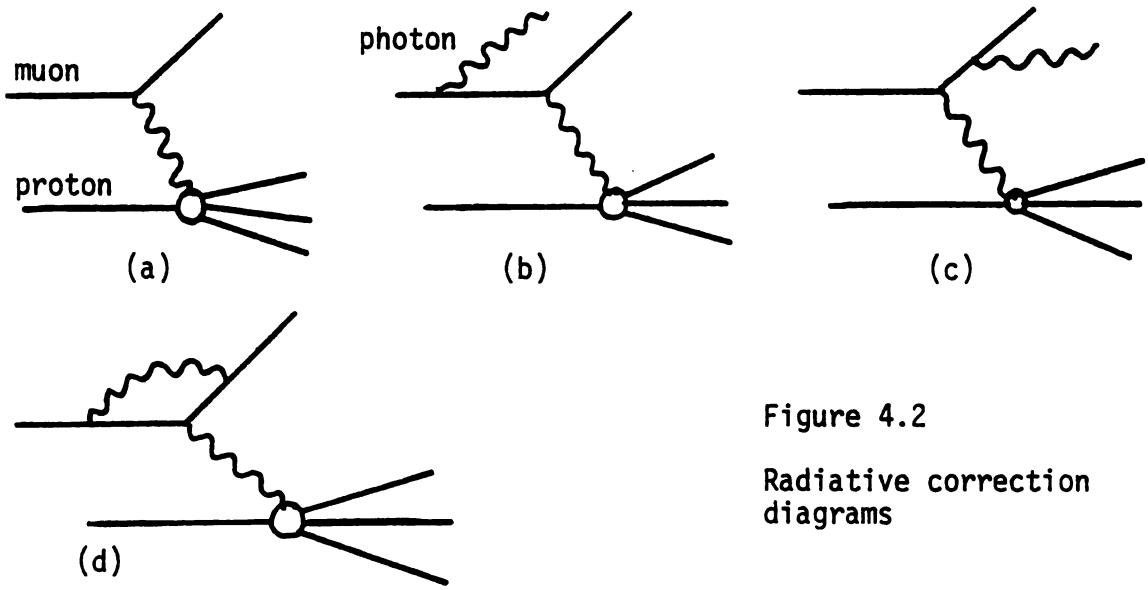

Figure 4.2

Radiative correction diagrams

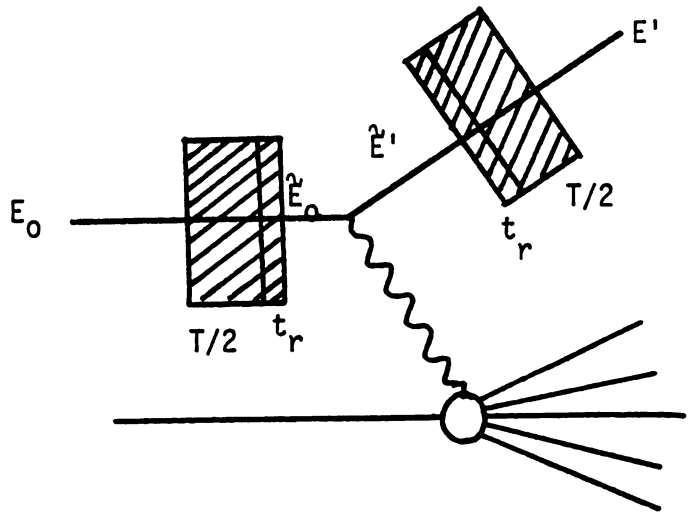

Figure 4.3

The "effective radiator" method

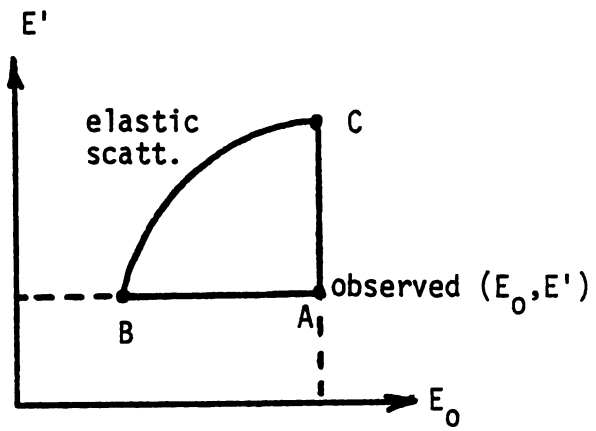

Figure 4.4

Contributions to the radiative corrections in the (E_o,E') plane

where $G(\omega) = -68.062/\omega^2 - 29.197/\omega + .70671 + .011969\omega - .49948\times10^{-4}\omega^2$ and $Z=26$, $A=55.85$, $y=\nu/E_0$, and $\omega=2m\nu/q^2$.

4.4 Ray Tracing

After interacting and leaving the target, the muon is made to enter the spectrometer. In each magnet the trajectory tracing is done in three steps. At each step the muon's path bends in the magnetic field, undergoes Coulomb multiple scattering, and suffers energy loss. Spark positions are recorded at each chamber and given a Gaussian smear (σ=0.1 cm.) to simulate measurement uncertainties. Later, in the momentum reconstruction phase, certain chambers will be randomly "turned off" for various events to simulate chamber inefficiencies.

4.5 MCP Distributions

Not all generated monte carlo events reach the end of the spectrometer. Like real data, some of the hypothetical muons pass into the holes in the toroid and fail to hit the trigger banks. Others exit out the side of the magnets. For those muons which successfully traverse the spectrometer, a record is written on tape using the same format as for real data, and its momentum and scattering angle are reconstructed. If the event passes all the standard analysis cuts (see section 5.2), it enters the sample of events to be used in the comparison to real data. Analogous to the data distribution of Figures 3.18-3.34, the corresponding monte carlo distributions are shown in Figures 4.5-4.21.

4.6 Data/MCP Comparison: Extracting $\nu W_2(x,q^2)$

A ratio can be formed in each region of the x-q^2 plane of the number of data events to the number of monte carlo events (corrected for incident flux):

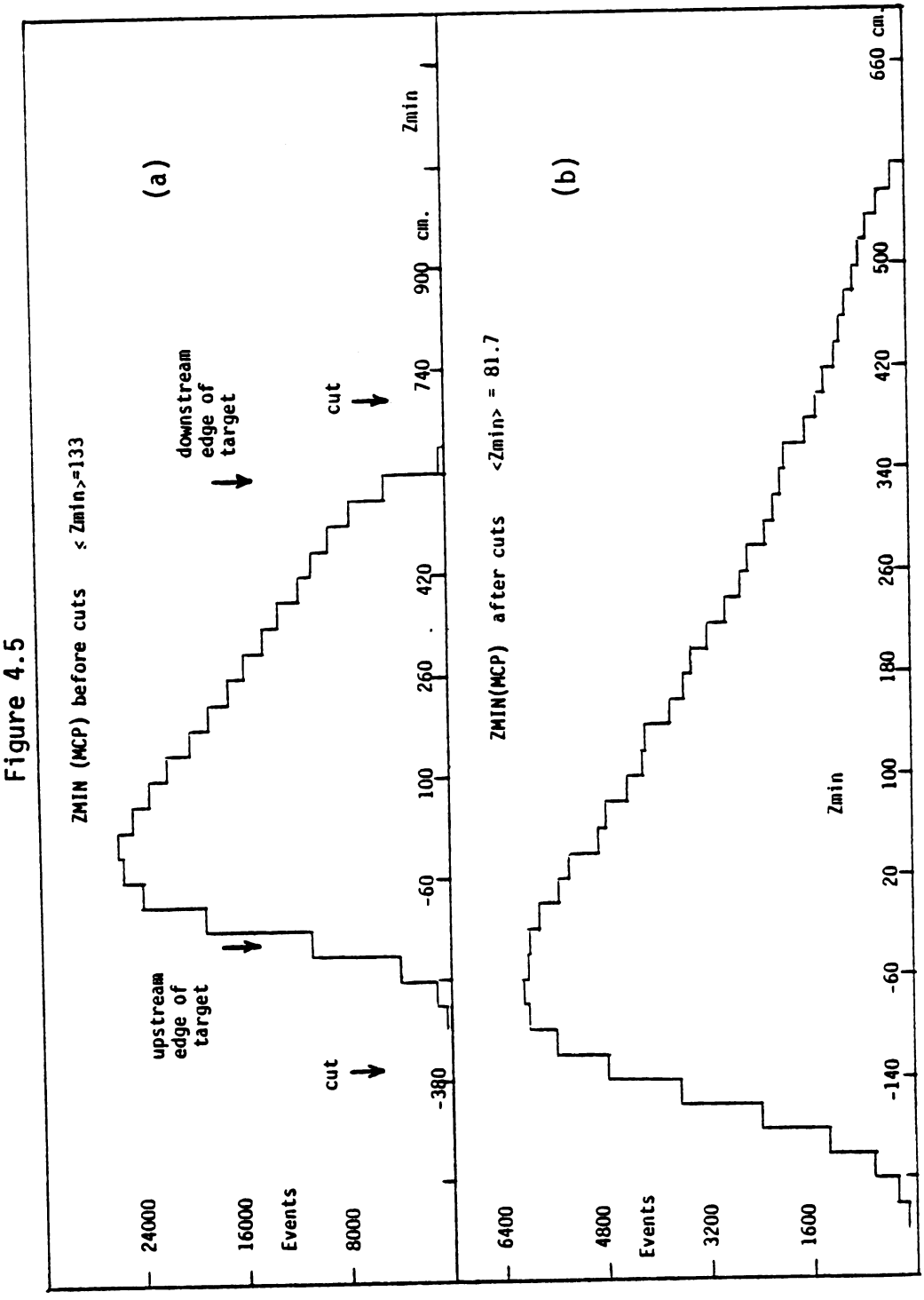
ZMIN (MCP) before cuts <Zmin>=133
(a)
upstream edge of target
downstream edge of target
cut
cut
Events
24000
16000
8000
-380
-60
100
260
420
740
900 cm.
Zmin
ZMIN(MCP) after cuts <Zmin> = 81.7
(b)
Events
6400
4800
3200
1600
-140
-60
20
100
180
260
340
420
500
660 cm.
Zmin

Figure 4.5

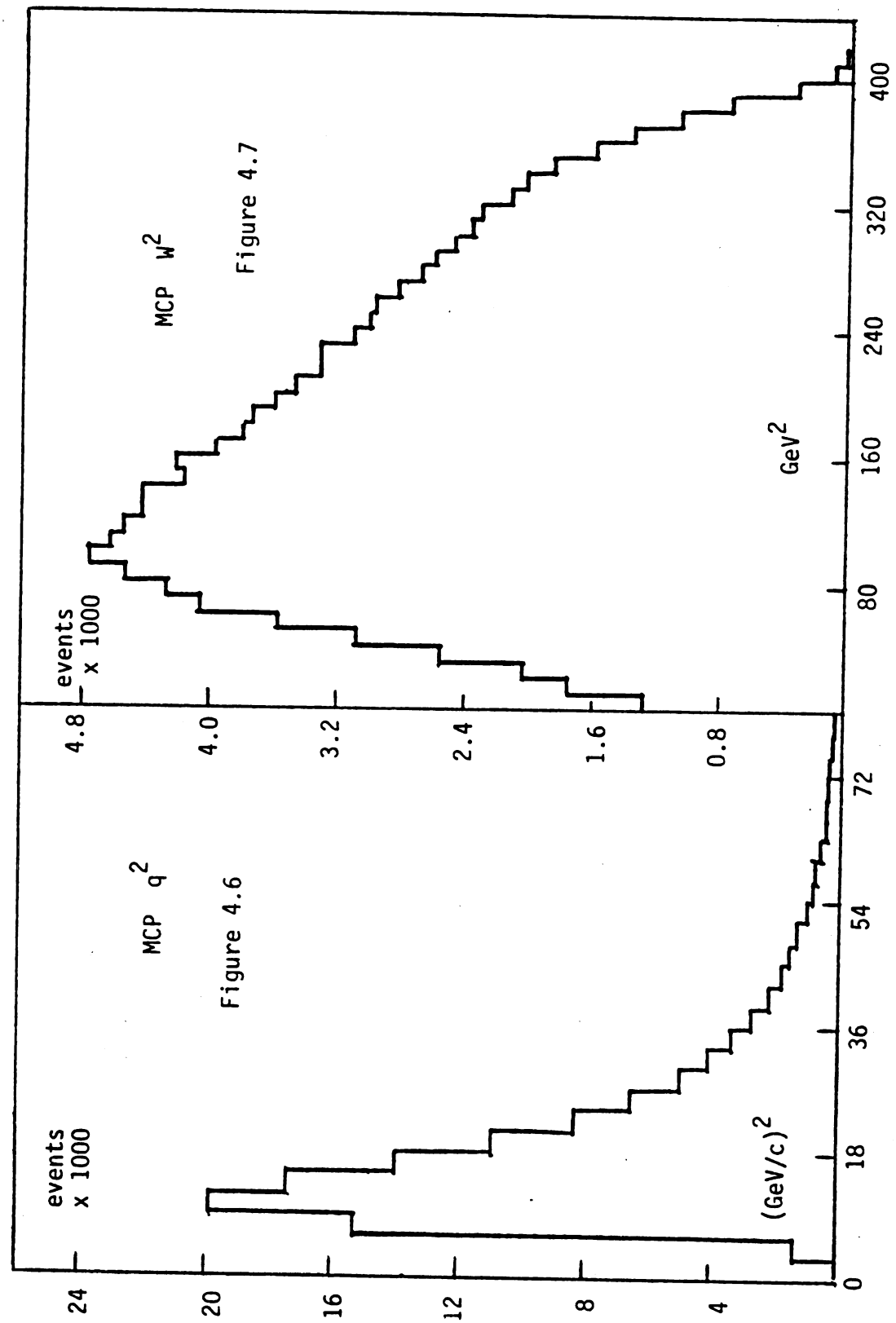

Figure 4.6

Figure 4.7

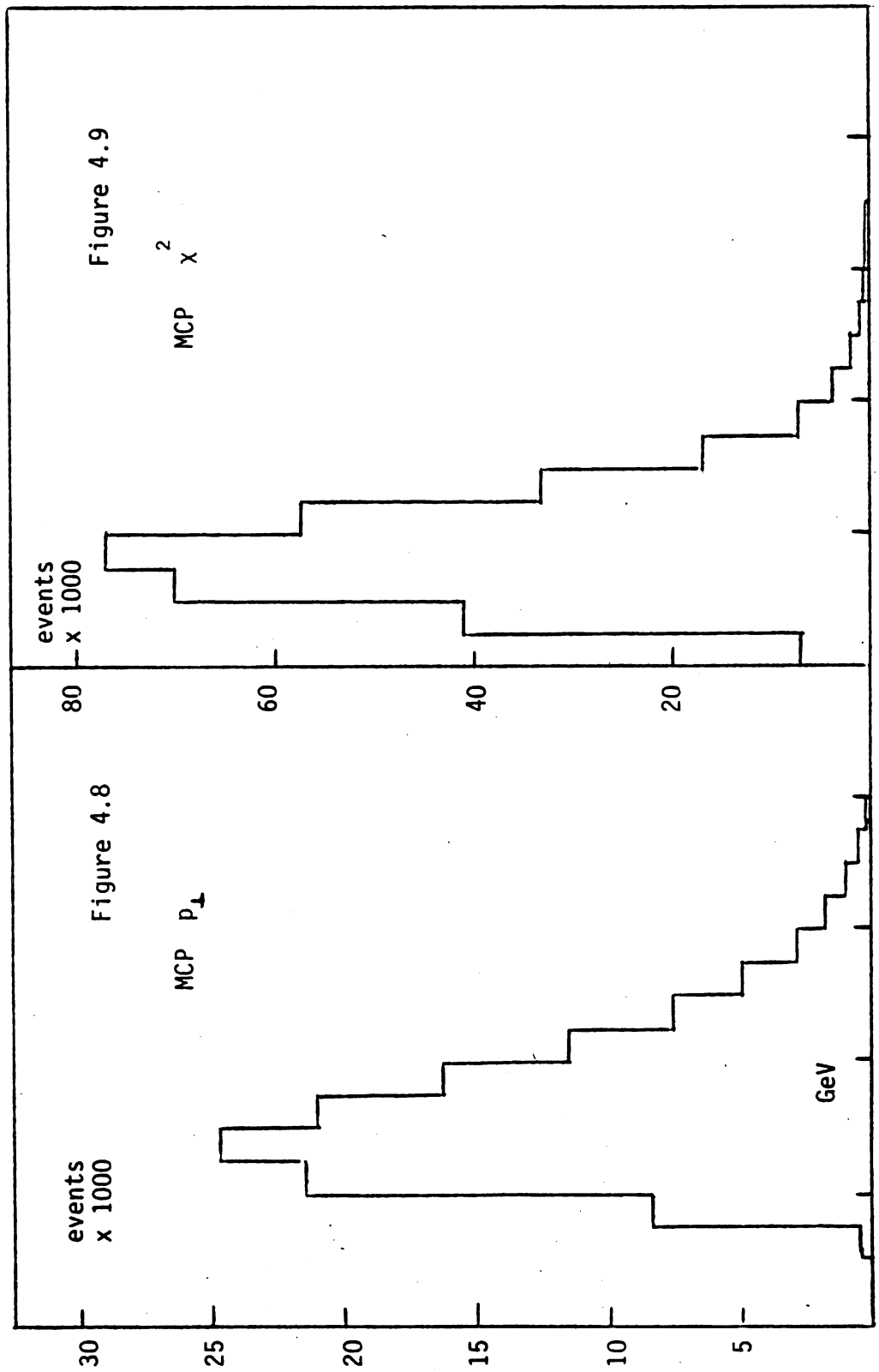
Figure 4.8
MCP $p_\perp$
events
x 1000
GeV
Figure 4.9
MCP χ^2
events
x 1000

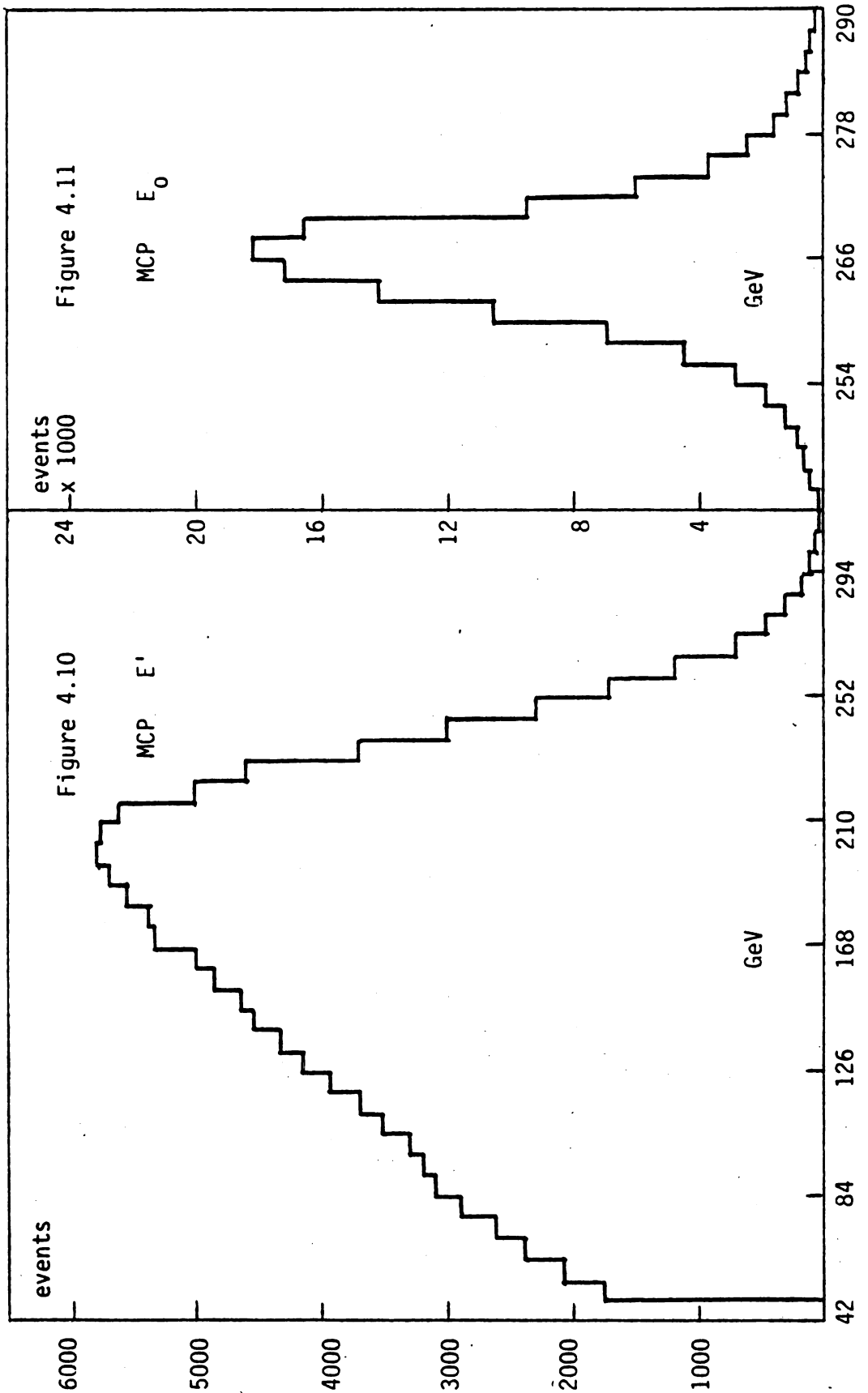
Figure 4.10
MCP E'
events
6000
5000
4000
3000
2000
1000
42
84
126
168
210
252
294
GeV
Figure 4.11
MCP E_o
events
x 1000
24
20
16
12
8
4
254
266
278
290
GeV

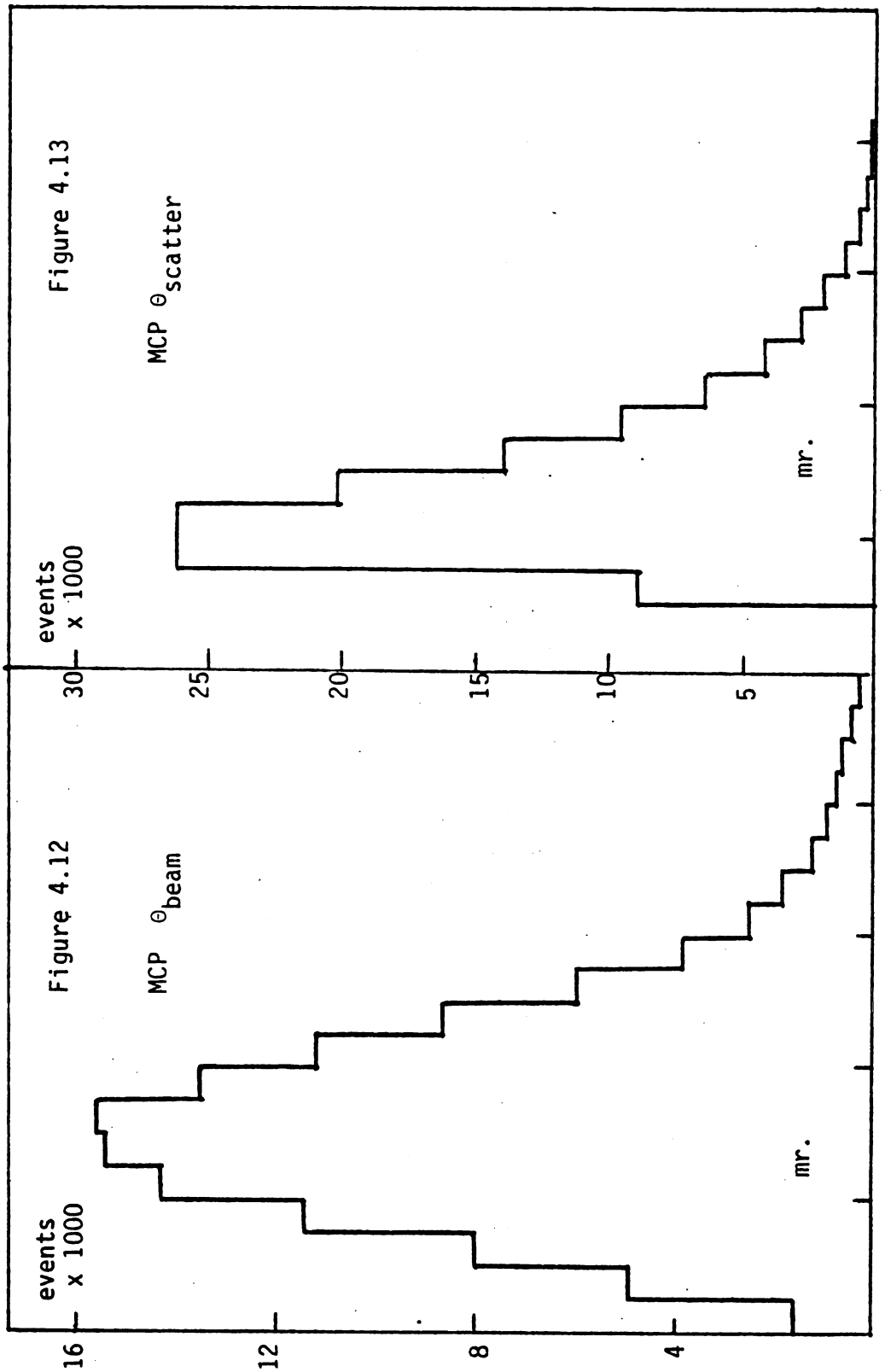
Figure 4.12
MCP Θ_{beam}
events x 1000
16
12
8
4
0
0
0.4
0.8
1.2
1.6
mr.
Figure 4.13
MCP $\Theta_{scatter}$
events x 1000
30
25
20
15
10
5
0
16
32
48
64
mr.

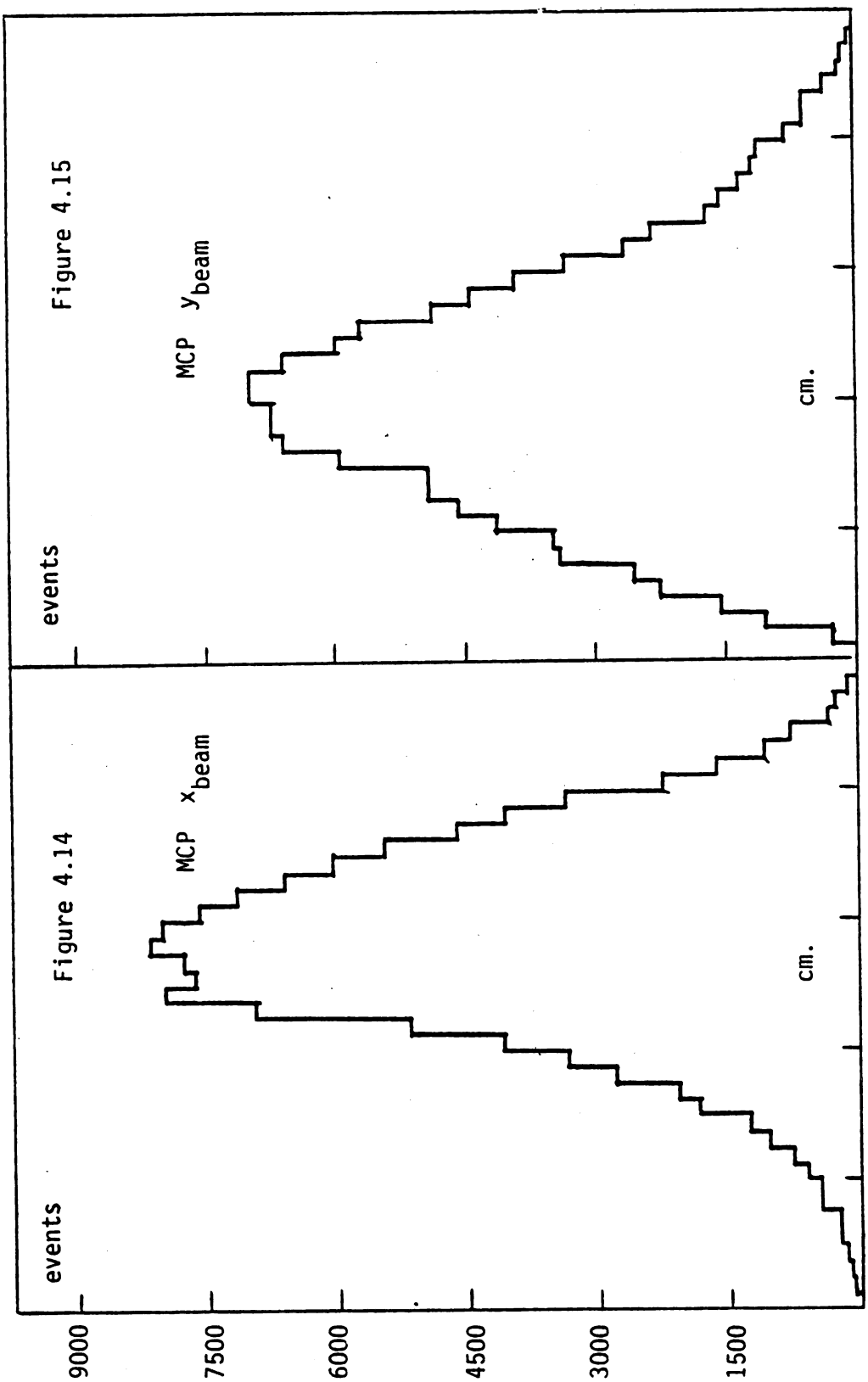
Figure 4.14
MCP x_{beam}
events
cm.
Figure 4.15
MCP y_{beam}
events
cm.
9000
7500
6000
4500
3000
1500
-10
-6
-2
2
6
-6
-2
2
6

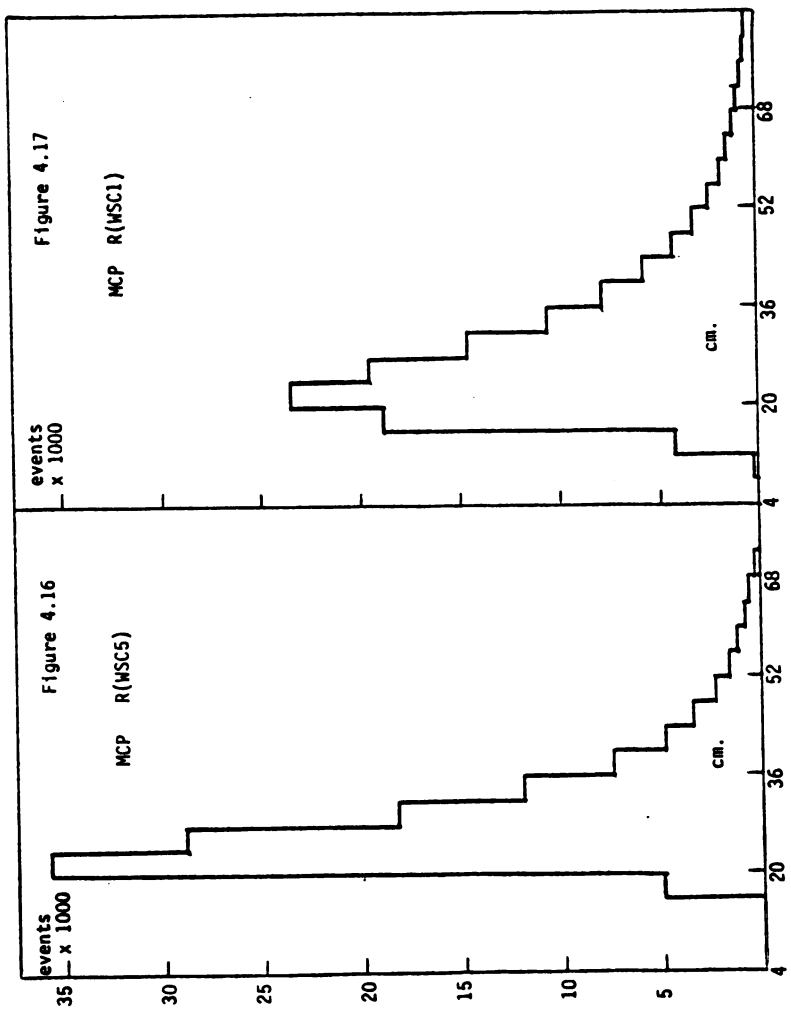
Figure 4.16
MCP R(WSC5)
events
x 1000
35
30
25
20
15
10
5
4
20
36
52
68
cm.
Figure 4.17
MCP R(WSC1)
events
x 1000
4
20
36
52
68
cm.

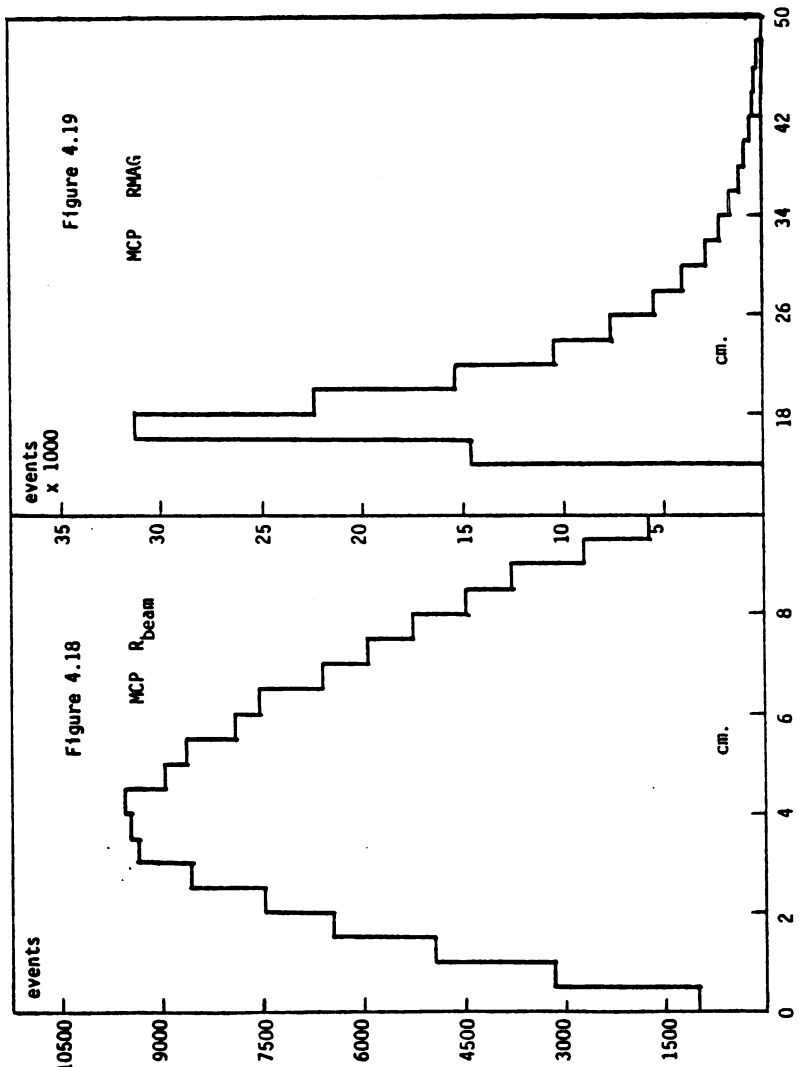
Figure 4.18
MCP R_{beam}
events
10500
9000
7500
6000
4500
3000
1500
0
2
4
6
8
cm.
Figure 4.19
MCP RMAG
events
x 1000
35
30
25
20
15
10
5
18
26
34
42
50
cm.

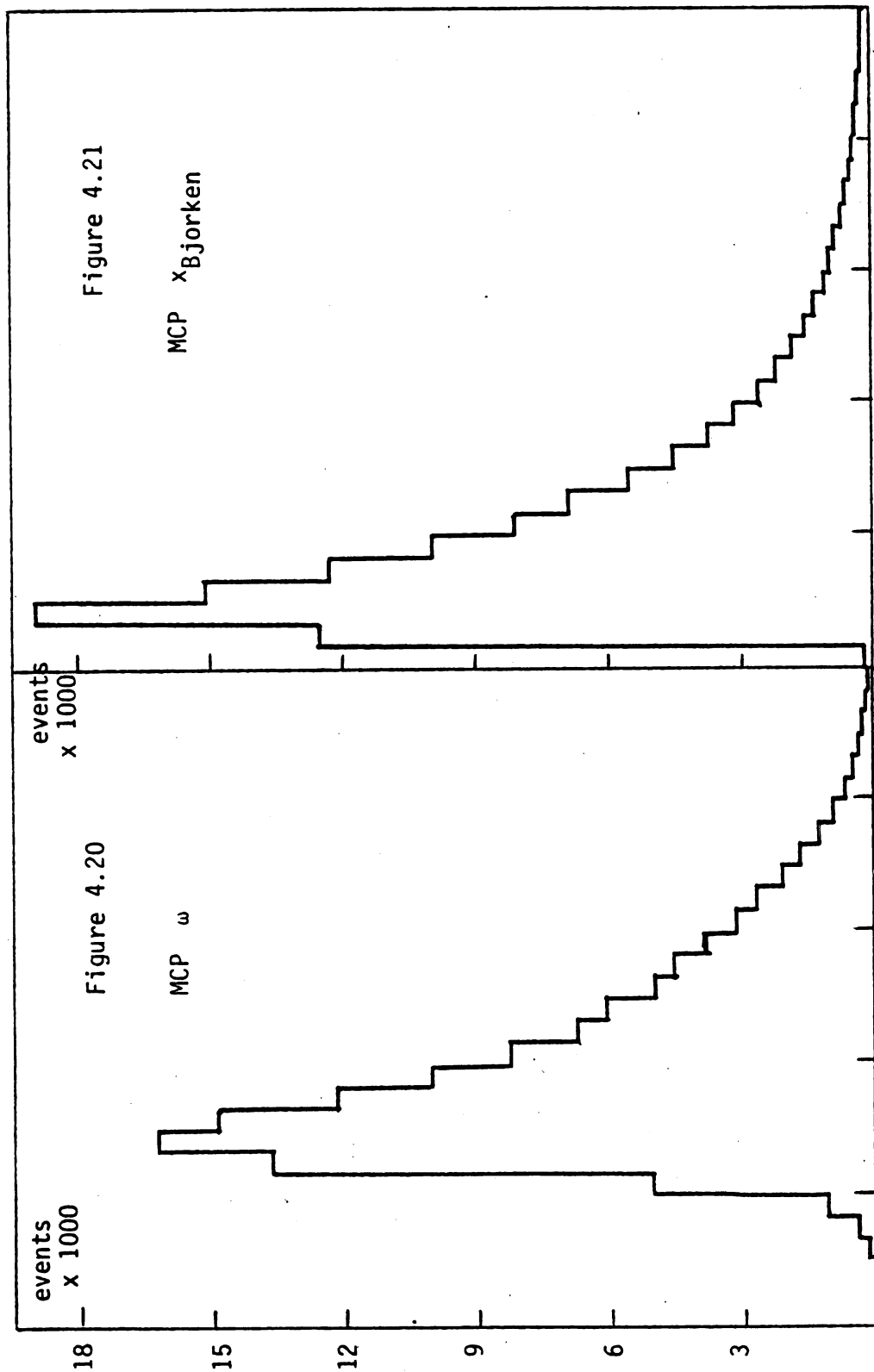
Figure 4.20
MCP ω
events
x 1000
18
15
12
9
6
3
-12
0
12
24
36
Figure 4.21
MCP $x_{Bjorken}$
events
x 1000
0
.12
.24
.36
.48

$$R(x,q^2) = \frac{\text{number of data events } (x,q^2)}{\text{number of monte carlo events } (x,q^2)} = \frac{DATA(x,q^2)}{MCP(x,q^2)}$$

The most important result of the single-muon analysis, the derivation of the structure function $F_2=\nu W_2$, is obtained using R:

$$F_2(x,q^2) = R(x,q^2) \cdot F_2^{STEIN}(x) \tag{74}$$

In this formula F_2^{STEIN} is the same function as in equation (70); the scale invariant structure function dependent only on x.[10] I shall now give the justification of this construction.

The expression given earlier for the differential cross section can be expressed in terms of experimentally observed quantities:

$$\frac{d^2\sigma}{dE'd\Omega} = \left(\frac{d\sigma}{d\Omega}\right)_{Mott} \frac{F_2(x,q^2)}{\nu} \left[1 + 2\tan^2\frac{\theta}{2}\left(\frac{1+\nu^2/q^2}{1+R}\right)\right]$$

$$= \frac{\text{event rate } (E',\Omega)}{\Delta E'\Delta\Omega} \cdot \frac{1}{\text{luminosity}} \cdot \frac{1}{\text{acceptance}} \tag{75}$$

where the luminosity is just the number of incident muons per time times the number of target nucleons per cm^2. We can solve equation (75) for F_2:

$$F_2(x,q^2) = data(E',\Omega)\left[\frac{\nu\{1 + 2\tan^2\frac{\theta}{2}\left(\frac{1+\nu^2/q^2}{1+R}\right)\}^{-1}}{\Delta E'\Delta\Omega \text{ luminosity} \cdot \text{acceptance}}\right] \tag{76}$$

The quantity inside the bracket is just the ratio $F_2^{STEIN}/MCP(x,q^2)$ if the following equation is true:

$$\langle \text{Acceptance}(x,q^2)\rangle\left\langle \frac{d^2\sigma}{dE'd\Omega}\right\rangle = \frac{1}{N_{acc}} \sum_{\substack{\text{accepted}\\ \text{events}}} \frac{d^2\sigma}{dE'd\sigma} \cdot \text{Acceptance} \quad (77)$$

The averaging and summation implied in equation (77) is over all monte carlo events within the (x,q^2) region in question. Figure 1.6 shows that F_2^{STEIN} is a slowly and smoothly varying function of x for x less than about 0.5. The regions of x and q^2, over which we compute $F_2(x,q^2)$, are small enough that equation (77) is a good approximation. Used in this way, the monte carlo simulation of real data can be thought of as a sophisticated acceptance routine. The dependence on a particular model, such as the use of F_2^{STEIN}, for finding the structure νW_2, is eliminated by using equation (74); F_2^{STEIN} in the numerator and denominator cancel out.

4.7 Systematic Errors in $F_2(x,q^2)$

A possible systematic error in $F_2(x,q^2)$ can arise from many sources. The greatest possibility for error comes from measurement uncertainties in E_o, E', and θ. From the calibration runs, we have estimated that the uncertainties in these variables are .4%, 1%, and .4% respectively. The effect on F_2 of these uncertainties is shown in Tables 4.2, 4.3, and 4.4; both in the q^2-y plane, and in the x-q^2 plane. The change in $F_2(x,q^2)$ due to an error in the measured E', for instance, can be calculated by tampering with the monte carlo:

Table 4.2

$$\frac{\text{Monte Carlo } (E_o + .4\%)}{\text{Monte Carlo } (E_o)} \times$$

(a)

q^2 (GeV/c)^2	0	21	43	64	86	107	128
.50	0.90	0.98	0.96	0.95	1.05	1.00	
.45	0.95	0.97	1.00	1.03	1.08	1.00	
.40	0.86	1.02	0.97	1.00	1.02		
.35	1.00	0.99	1.03	1.02	1.03		
.30	1.00	1.02	1.00	1.00	1.02		
.25	1.03	1.00	1.00	1.07			
.20	1.00	1.01	1.02	1.02			
.15	1.02	1.02	1.03				
.10	1.01	1.02	1.09				
.05	1.01	1.04					
0							

(b)

q^2 (GeV/c)^2	0	0.1	0.2	0.3	0.4	0.5	0.6	0.7	0.8	0.9
150						1.00				
128					1.19	1.19	1.00			
107			1.05	1.11	1.03	0.93	1.06			
86			0.97	1.01	1.02	1.04	1.02	1.03	1.07	
64		1.04	0.96	1.01	1.01	1.01	1.00	1.03	1.02	
43	0.87	1.00	1.01	1.01	1.01	1.01	1.02	1.00	1.02	
21	0.94	1.01	1.01	1.00	1.02	1.00	1.00	1.00	1.01	
0										

$y = \nu/E_o$

Table 4.3

(a)

$$\frac{\text{Monte Carlo}(E'+1\%)}{\text{Monte Carlo}(E')} \times$$

.50	1.19	1.10	1.00	1.01	0.96	
.45	1.18	1.08	1.11	1.07	1.10	1.01
.40	1.02	1.01	1.02	1.00	1.01	1.02
.35	1.02	0.99	0.99	0.99	1.02	
.30	0.88	1.04	1.06	1.02	0.98	
.25	0.99	0.98	0.97	1.03		
.20	0.95	0.97	1.00	1.04		
.15	0.95	0.98	1.00			
.10	0.96	0.99	0.99			
.05	0.96	0.87				
0	0	21	42	64	86	107	128

q^2 (GeV/c)^2

(b)

q^2 (GeV/c)^2

150					0.99	0.99			
128				1.08	0.98	1.19	1.00	1.00	
107			1.14	1.17	0.98	1.00	0.95	1.00	1.00
86			1.05	1.03	1.02	1.04	1.00	1.08	1.01
64		1.17	1.02	1.00	1.00	1.00	0.99	1.01	0.99
43		1.04	0.99	0.98	0.98	0.99	0.99	0.99	0.98
21	1.06	0.96	0.96	0.96	0.97	0.97	0.97	0.96	0.94
0	0	0.1	0.2	0.3	0.4	0.5	0.6	0.7	0.8	0.9

y=ν/E

Table 4.4

(a)

$$\frac{\text{Monte Carlo } (\theta+.4\%)}{\text{Monte Carlo } \theta} \times$$

.50						
.45	1.02	1.05	1.03	1.03	0.98	
.40	1.01	1.01	1.03	1.06	1.01	1.01
.35	0.99	1.04	1.01	1.01	1.03	1.10
.30	1.01	1.00	0.97	1.02	1.00	
.25	0.98	1.01	1.04	1.00	1.04	
.20	1.01	1.01	1.00	1.05		
.15	1.00	1.01	1.02	1.05		
.10	0.99	1.00	1.02			
.05	0.99	1.01	1.03			
0	0.98	0.93				
	0	21	43	64	86	107	128

q^2 (GeV/c)^2

(b)

q^2 (GeV/c)^2									
150						1.00			
128				0.99	1.07	1.00			
107			1.04	1.10	1.03	0.97	1.03	1.00	
86			1.00	1.03	1.04	1.04	1.02	1.05	1.11
64		1.02	1.01	1.02	1.01	1.01	1.01	1.03	1.00
43	1.04	1.02	1.01	1.01	1.00	1.00	1.01	1.00	1.01
21	1.00	0.99	0.99	0.99	1.00	1.00	0.99	0.99	0.98
0	0	0.1	0.2	0.3	0.4	0.5	0.6	0.7	0.8	0.9

$y=\nu/E_0$

$$\frac{\Delta F_2}{F_2} = \frac{F_2(E') - F_2(E'+\Delta E')}{F_2(E')} \qquad \Delta E' = \text{error in } E' \tag{78}$$

$$= \frac{\frac{DATA}{MCP(E')} F_2^{STEIN} - \frac{DATA}{MCP(E'+\Delta E')} F_2^{STEIN}}{\frac{DATA}{MCP(E')} F_2^{STEIN}} \tag{79}$$

$$= 1 - \frac{MCP(E')}{MCP(E'+\Delta E')} \tag{80}$$

The effect of switching on or off the radiative corrections or the wide angle bremsstrahlung are shown in Tables 4.5 and 4.6. The effect of changing $R=\sigma_S/\sigma_T=.25$ to $R=0$ is shown in Table 4.7. Figure 4.22 shows contours of constant systematic error (the errors due to E_o, E', and θ in quadrature) in the q^2-x plane.

In the kinematic region where the data exists, the possible systematic errors are everywhere less than a few percent, except for $x<0.1$ where they may be as large as 10%. In the last chapter I will discuss $F_2(x,q^2)$ itself and also other possible systematic errors which can not be simulated by monte carlo, namely normalization errors due to the uncertainty in the muon flux, and errors due to analysis inefficiencies.

Table 4.5

$$\frac{\text{Radiative Corrections Off}}{\text{Radiative Corrections On}} \times$$

(a)

.50	1.05	1.06	1.07	1.06	1.06	1.05
.45	1.04	1.06	1.06	1.05	1.05	1.03
.40	1.04	1.05	1.05	1.04	1.03	1.02
.35	1.03	1.04	1.03	1.02	1.01	
.30	1.03	1.03	1.02	1.00	0.98	
.25	1.02	1.01	0.99	0.97		
.20	1.01	0.99	0.96	0.93		
.15	0.99	0.95	0.91	0.88		
.10	0.95	0.89	0.84			
.05	0.89	0.80				
0	0	21	43	64	85	107	128

q^2 (GeV/c)^2

(b)

150						1.06			
128				1.09	1.05	1.02	0.98		
107			1.09	1.06	1.04	1.01	0.99	0.95	
85			1.08	1.05	1.02	0.99	0.97	0.93	0.89
64		1.08	1.05	1.02	0.99	0.97	0.94	0.91	0.86
43	1.07	1.05	1.02	0.99	0.97	0.94	0.91	0.87	0.82
21	1.03	1.01	0.98	0.96	0.93	0.91	0.88	0.84	0.79
0	0	0.1	0.2	0.3	0.4	0.5	0.6	0.7	0.8	0.9

q^2 (GeV/c)^2

$y=\nu/E_o$

Table 4.6

(a)

$$\frac{\text{Wide-Angle Bremsstrahlung Off}}{\text{Wide-Angle Bremsstrahlung On}} \times$$

.50						
	1.00	1.00	1.00	1.00	0.99	0.98
.45	1.00	1.00	1.00	0.99	0.99	0.99
.40	1.00	1.00	1.00	0.99	0.99	0.98
.35	1.00	1.00	1.00	0.99	1.00	
.30	1.00	1.00	1.00	0.99	0.99	
.25	1.00	1.00	1.00	1.00		
.20	1.00	1.00	1.00	1.02		
.15	1.00	1.00	1.03			
.10	1.00	1.02	1.07			
.05	0.95	1.01				
0	0	21	43	64	86	107	128

q^2 (GeV/c)^2

(b)

q^2 (GeV/c)^2

150									
						0.98			
128				0.99	0.99	0.98	0.95	1.00	
107			1.00	0.99	0.99	0.99	1.00	1.03	1.08
85			1.00	0.99	0.99	0.99	1.00	1.02	1.05
64		1.00	1.00	1.00	1.00	1.00	1.01	1.03	1.08
43	1.00	1.00	1.00	1.00	1.00	1.00	1.01	1.02	1.03
21	1.00	1.00	1.00	1.00	0.99	0.98	0.95	0.91	0.85
0	0	0.1	0.2	0.3	0.4	0.5	0.6	0.7	0.8	0.9

$y = \nu/E_o$

Table 4.7

$$\frac{\text{Monte Carlo } (R=0)}{\text{Monte Carlo } (R=.25)} \quad x \quad (a)$$

.50	1.00	1.00	1.01	1.01	1.03	1.03
.45	1.00	1.00	1.01	1.02	1.03	1.06
.40	1.00	1.00	1.01	1.02	1.04	1.05
.35	1.00	1.00	1.01	1.03	1.06	
.30	1.00	1.01	1.02	1.05	1.08	
.25	1.00	1.01	1.04	1.07		
.20	1.00	1.02	1.06	1.11		
.15	1.01	1.04	1.11			
.10	1.03	1.09	1.14			
.05	1.06	1.15				
0	0	21	43	64	86	107 128

q^2 (GeV/c)^2

(b)

q^2 (GeV/c)^2									
150					1.03	1.05			
128				1.02	1.03	1.05			
107			1.01	1.02	1.03	1.05	1.08		
86			1.01	1.02	1.03	1.05	1.08	1.12	1.15
64		1.00	1.01	1.02	1.03	1.05	1.08	1.12	1.16
43	1.00	1.00	1.01	1.02	1.03	1.05	1.08	1.12	1.16
21	1.00	1.00	1.01	1.02	1.03	1.05	1.08	1.12	1.15
0	0	0.1	0.2	0.3	0.4	0.5	0.6	0.7	0.8 0.9

$y=\nu/E_o$

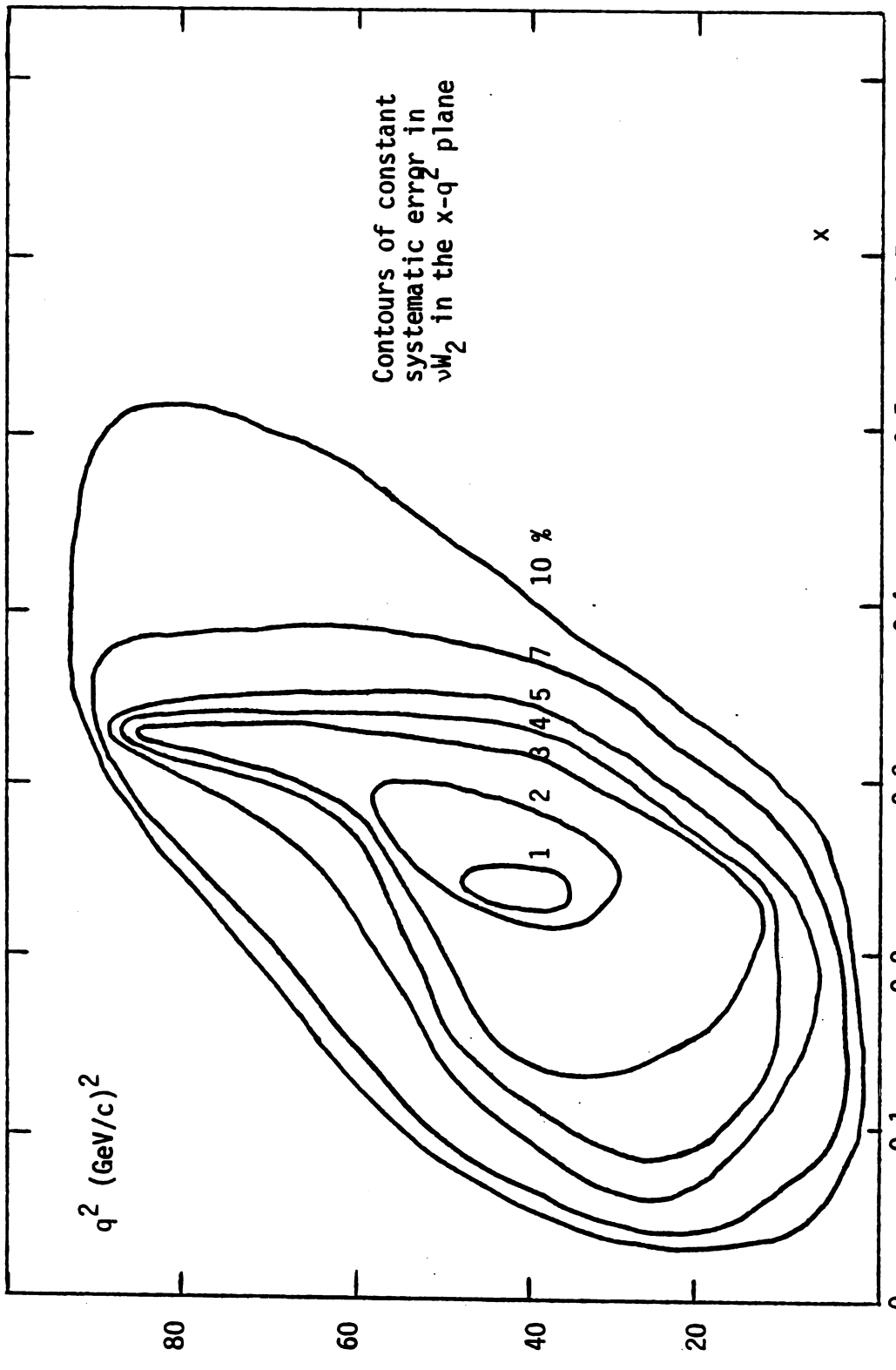
Contours of constant systematic error in νW_2 in the x-q^2 plane
q^2 (GeV/c)^2
x
1
2
3
4
5
7
10 %
0
0.1
0.2
0.3
0.4
0.5
0.7
0.8
20
40
60
80

Figure 4.22

CHAPTER V

RESULTS AND CONCLUSIONS

5.1 Summary of the Data Sample

The data reported in this dissertation represents about 90% of the 270 GeV μ^+ data. When the 270 GeV μ^- data (about 30% of the μ^+) is fully analyzed, it will be added to the μ^+ sample; certain differences in the beam shape for the two data samples have to be studied first.

The sample of monte carlo events was generated (with program MCP) in such a way that the effective flux would roughly match that of the real data sample. The monte carlo events were momentum analyzed just like the data and subjected to the same analysis cuts. These cuts are shown in Table 5.1. Before corrections were applied, the number of accepted monte carlo events was approximately equal to the number of data events. The fraction of triggers recorded on primary data tapes which are reconstructed and can pass all analysis cuts is about 12%.

Table 5.2 shows a direct comparison of kinematic averages and other statistics for the two samples. Correcting only for flux (but not for other factors such as will be described in the next section), the number of accepted events past cuts is almost identical. Discrepancies between average values for data and monte carlo kinematic variables can be chiefly attributed to inefficiencies in the track finding program VOREP, and the divergence of the data from a monte

Table 5.1 Single-muon analysis cuts

1. -366 cm < ZMIN < 672 cm. interaction vertex

2. DMIN <5.0 cm. distance of closest approach of beam and spectrometer tracks

3. χ^2/DOF < 10 chi-squared per degree of freedom of the momentum reconstruction fit in the spectrometer

4. 0< Θ_{beam} < 2 mr. beam angle relative to the beam axis

5. 0 < R_{beam} < 10 cm. beam radius relative to the beam axis

6. minumum radius of muon track at WSC 2 and WSC 3 = 16.51 cm. this cut is applied to actual sparks

7. minumum radius of muon track at WSC 4,5,6 = 16.51 cm. this cut is applied to fitted spark positions

8. maximum radius of muon track at WSC 3,4,5,6,7 = 83.82 this cut is applied to fitted spark positions

9. 10 mr. < Θ < 1 radian scattering angle

10. 50 GeV < E'< 350 GeV scattered muon energy

11. 1 $(GeV/c)^2$ < q^2 < 500 $(GeV/c)^2$

12. radius at the front of the first magnet 15.24 cm < RMAG < 83.82 cm. (the radius of the muon trajectory is extrapolated to this point)

13. halo cut using P(the fully reconstructed muon momentum in the spectometer) and PBACK(the reconstructed momentum using only the last 5 spark chambers):
$$(PBACK - P)/P < 0.5$$

14. cut on events with tracks inside the field-free region of the toroid magnets and which also cross the beam axis

15. one and only one beam track (the effective incident flux is corrected by the proportion of triggers lost by this cut)

Table 5.2 Data/Monte Carlo comparison results

Kinematic average	DATA	MCP
E'	157.8	164.8 GeV
E_o	269.3	265.9 GeV
θ	22.30	22.32 mr.
$x_{Bjorken}$	.1205	.1429
W^2	193.5	174.6 $(GeV/c)^2$
$P_\perp$	3.201	3.355 GeV/c
ω	13.53	12.11
ZMIN	88.8	81.7 cm.
χ^2/DOF	1.181	.7286
DMIN	.6872	.4650 cm.
RMAG	21.06	21.28 cm.
R_{beam}	4.709	4.729 cm.
θ_{beam}	.6521	.6738 mr.
flux	9.31693×10^9	9.08646×10^9 μ's
runs	117	122
accepted events	125,944	122,641

this sample is 90% of the 270 GeV μ^+ data

it is 60% of all 270 GeV data

total luminosity = $1.47224 \times 10^{10} \times 2.56 \times 10^{27} cm^{-2} = 3.77 \times 10^{37} cm^{-2}$ of 270 GeV data

carlo sample based on the assumption of Bjorken scale invariance. The study of these two areas is the subject of this chapter.

5.2 Normalization of νW_2

Inefficiencies in the analysis program VOREP were checked with a completely independent program, MULTIMU, which was developed in conjunction with the analysis of multi-muon final states, but which was adapted for use in single-muon analysis as well. Using comparable statistics, these two programs were checked for reconstruction and track finding consistency as a function of x and q^2. Corrections were made to the VOREP sample of found events when MULTIMU did a better job. By this method the overall sample of events was increased by about 11%. VOREP seems to be relatively inefficient at low q^2 and low x. This is a result of VOREP's difficulty at finding tracks (the correct track, anyway) for events with small scattering angle and high E'. This class of events consists of muons which are just barely within the magnetized regions of the toroid magnets. It is often difficult to properly reconstruct such events since the "true" sparks are often situated amidst the extra sparks which arise from penetrating hadron shower particles. This problem is more crucial in the front chambers; it is here that MULTIMU does a much better job than VOREP in detecting the correct sparks corresponding to the scattered muon. In fact, it is contemplated that all future analysis will be performed with MULTIMU which traces tracks from the front to the back of the spectrometer rather than VOREP which does the reverse.

To arrive at an absolute normalization for the data, we studied the yield for each run (accepted triggers past cuts divided by flux), and also the method for calculating the effective incident flux.

These studies were particularly important since our data appeared to be about 10% lower than the very precise data taken by the SLAC-MIT experiment[15], in the kinematic region for which the two experiments overlapped. Figure 5.1 shows the "corrected" yield versus average incident muon flux per spill (the data points correspond to individual runs with a statistical error of about 5%). The beam shape for the μ^- sample was wider than for the μ^+. This resulted in more low-q^2 triggers, many of which are cut during analysis, thus depreciating the average μ^- yield. Since we generated the monte carlo events on the basis of beam tapes corresponding to each data run, taking the ratio of data to monte carlo should remove all dependence on the beam shape. In this way the yields for μ^+ and μ^-, as a function of incident flux, could be compared directly. Figure 5.1 shows that there is a flux dependence; the yield for the μ^- runs which were taken at lower flux is higher than for the μ^+ runs. A spline fit to this data is rather flat in the vicinity of the μ^- runs, despite the wide scatter of data points. Supposing this constant plateau yield to be the "ideal" or "true" yield, the average μ^+ yield was found to be 14% low; the μ^+ was therefore normalized upwards accordingly. At the level of the experimental apparatus, this flux dependence is not yet understood.

The normalization procedure can be summarized in the following expression for the structure function:

$$\nu W_2 = F_2(x,q^2) = \frac{\text{Data events}(x,q^2)}{\text{MCP events}(x,q^2)} \cdot F_2^{\text{STEIN}}(x,q_0^2)\cdot N_1(x,q^2)\cdot N_2 \qquad (81)$$

where $N_1(x,q^2)$ is the inefficiency correction function from the

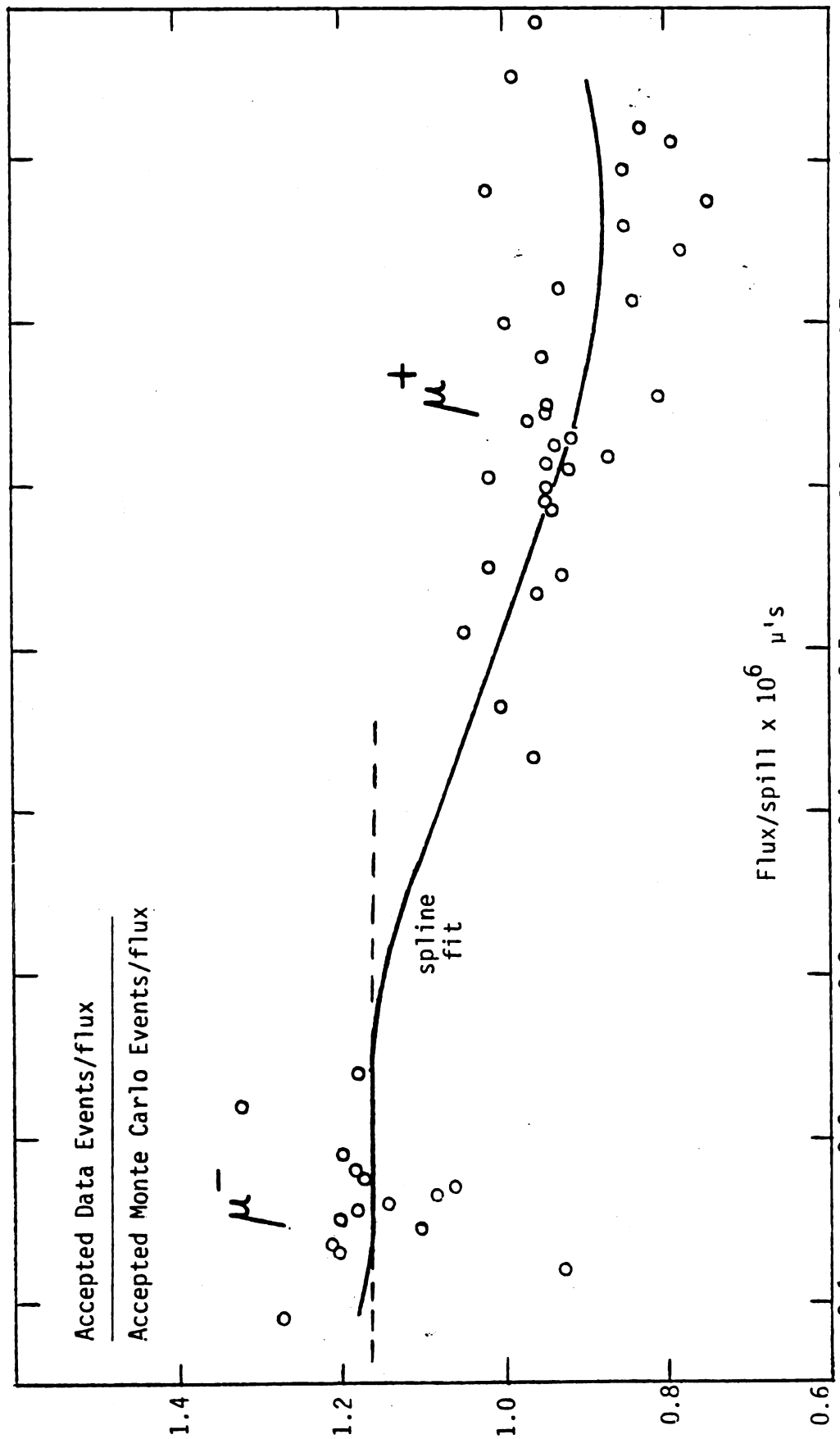

Figure 5.1 Corrected yield vs. flux

MULTIMU-to-VOREP comparison, and N_2 is the overall normalization factor (14%) representing the flux rate effects. There may, of course, be a class of events which is inefficiently reconstructed by both VOREP and MULTIMU. We estimate that the uncertainty in $N_1(x,q^2)$ may be as high as 5%. The systematic error in N_2 is also believed to be about 5%. These errors, along with the errors in E_o, E', and θ discussed in the last chapter, can be added in quadrature to give a total systematic error for νW_2 of about 7-10%. This total may decrease somewhat as the calculation and correction of inefficiences become better understood.

5.3 Parameterizing Scale Breaking

One way of showing how the structure function F_2 breaks scale invariance is to fit the data to a curve with an explicit q^2 dependent term. It was first thought[19] that such a term would be of the form $N/(1+q^2/\Lambda^2)^2$. But this did not allow for a positive increase in F_2 for increasing q^2. It became convenient to parameterize scaling violations in the following way:

$$F_2(x,q^2) = F_2(x,q_o^2)\left(\frac{q^2}{q_o^2}\right)^{b(x)} \tag{82}$$

$$b(x) = \frac{\partial \ell n F_2}{\partial \ell n q^2} = \frac{\Delta F_2/F_2}{\Delta q^2/q^2} \tag{83}$$

$b(x)$ is the fractional change in F_2 for a given fractional change in q^2. Recent data for $b(x)$ are shown in Figure 5.2.[34] $F_2(x,q_o^2)$ is the value of F_2 at some reference q_o^2; for our purposes, we used $F_2^{STEIN}(x)$,[10] and set $q_o^2=3(GeV/c)^2$. Table 5.3 shows several different fits to the data

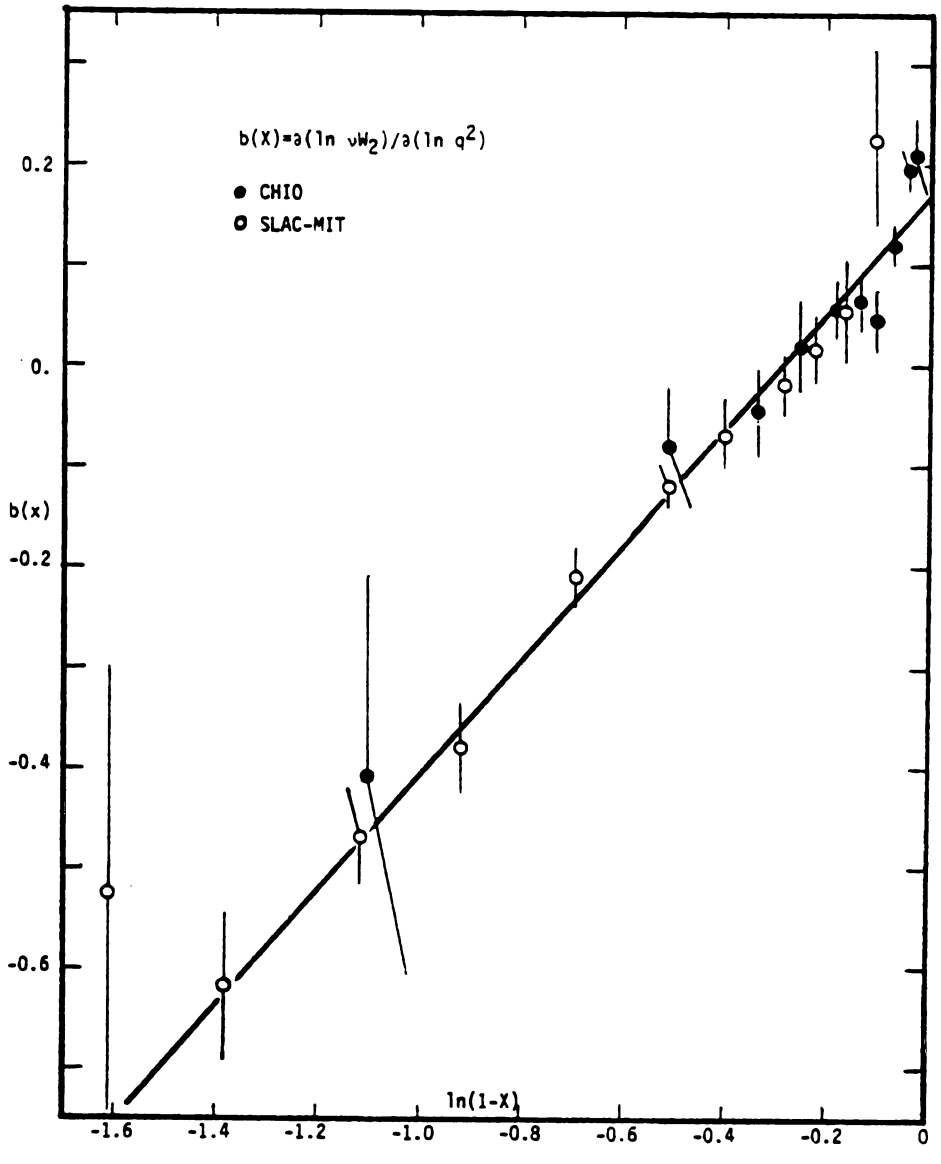

Figure 5.2 The scale-violating parameter b(x)

Table 5.3 Various fits to the combined b(x) data

$b = C_1 + C_2x$	proton:	$C_1 = .18497 \pm .0115$
		$C_2 = .83179 \pm .040$
		$\chi^2/DOF = 1.18$
	iron:	$C_1 = .18929 \pm .0098$
		$C_2 = .8787 \pm .037$
		$\chi^2/DOF = 1.22$
$b = C_1 \ln(1/6x)$	proton:	$C_1 = .11555 \pm .0063$
		$\chi^2/DOF = 4.45$
	iron:	$C_1 = .11462 \pm .0054$
		$\chi^2/DOF = 5.05$
$b = C_1 \ln(1/C_2x)$	proton:	$C_1 = .11844 \pm .0064$
		$C_2 = 7.2189 \pm .446$
		$\chi^2/DOF = 4.16$
	iron:	$C_1 = .12227 \pm .0057$
		$C_2 = 7.6334 \pm .4208$
		$\chi^2/DOF = 4.46$
$b = C_1 + C_2 \ln(1-x)$	iron:	$C_1 = .16895 \pm .00987$
		$C_2 = .5777 \pm .0252$
		$\chi^2/DOF = 1.062$

in Figure 5.2. The best results occurred for a fit of the type $b(x)=C_1 + C_2\ \ell n(1-x)$. This is the form we adopted when using the b(x)-type scale breaking factor. One additional note: by expanding the expression for $F_2(x,q^2)$ in equation (82), one arrives at a formula reminiscent of QCD:

$$F_2(x,q^2) \simeq F_2(x,q_0^2)\ [1 + b(x)\ \ell n(q^2/q_0^2) + \ldots] \qquad (84)$$

5.4 νW_2 Versus x

Figure 5.3 shows plots of the structure function νW_2, measured in E319, versus x, for several regions of q^2. The background curves are those given by equation (82), that is, by a scale-breaking cross section governed by the b(x) parameter. The few open circle points at high x are from reference [15]. The agreement between the data and the curve is good at high x but progressively worse at smaller x. One interesting possibility to consider is whether or not a threshold in W^2 (missing mass squared) could account for the rise above the reference curve. For constant q^2 one can calculate a value for W^2 at each x since $W^2=q^2(1/x - 1) + m^2$. What this implies is that above a certain final state mass, say M=10 GeV/c^2 (W^2=100), the cross section would rise above what is ordinarily expected from a $(q^2/q_0^2)^b$ scale breaking behavior due to the creation of some new physical state. The small arrows in Figure 5.3 mark the value of x at which W^2=100. Since the experimental resolution in W^2 is 20-30%, one would not expect that the apparent rise above the reference curve would coincide with the arrows in each plot. As it is, the agreement is not too bad.

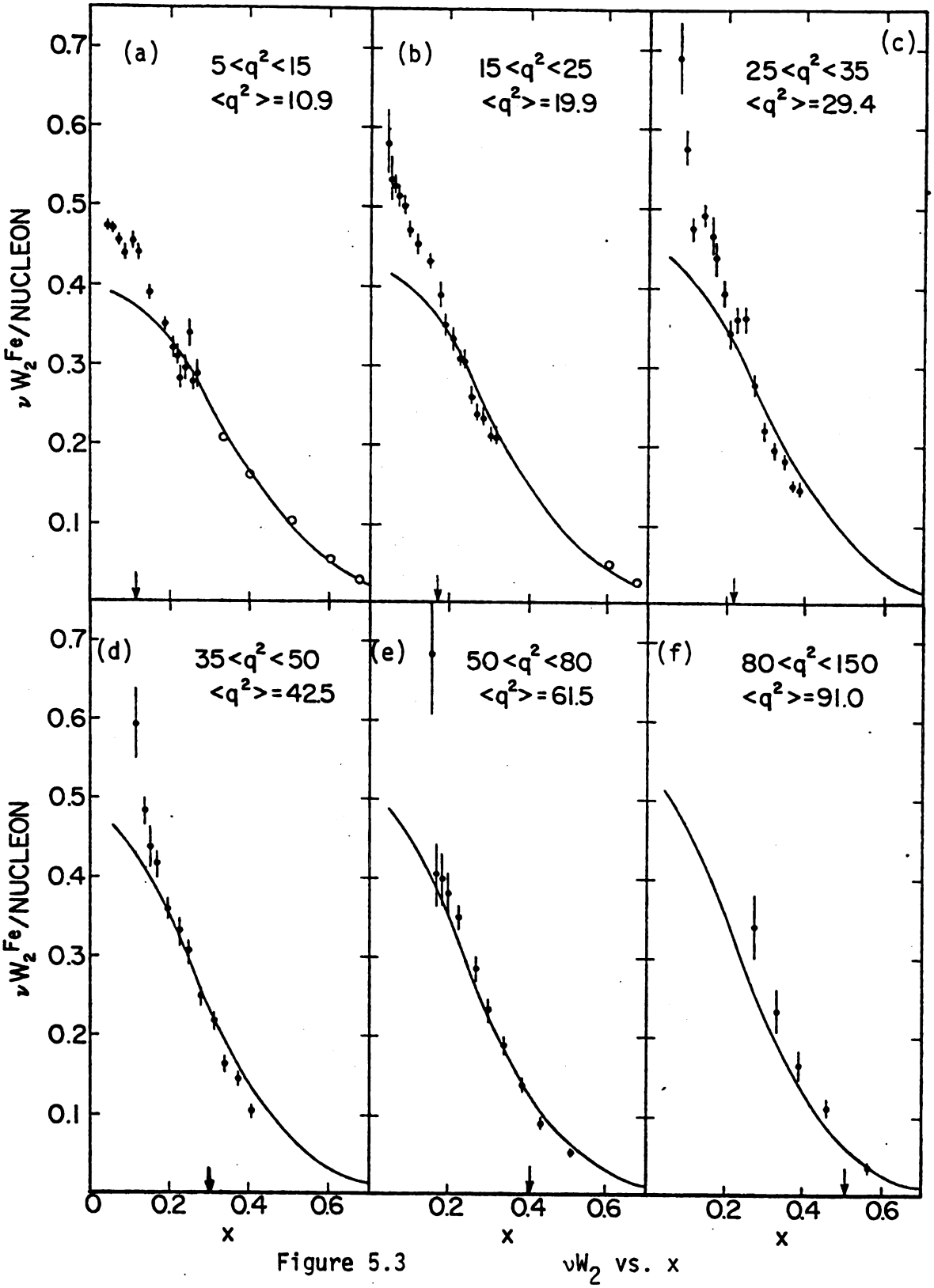

Figure 5.3 νW_2 vs. x

As a preliminary check of the threshold hypothesis, $b(x)=\partial \ell n F_2/\partial \ell n q^2$ was calculated using all E319 data, and then again using only data for which $W^2 \leq 100 \pm 20$ $(GeV/c^2)^2$. The results are shown in Figure 5.4 along with the straight line fit to all the previous b(x) data, as in Figure 5.2. Except for the points at high x (small $\ell n(1-x)$), the values of b(x) below the $W^2=100$ "threshold" agree well with previous measurements, while b(x) calculated using, in addition, data above the threshold shows an unmistakable rise above the fitted line.

A few words should be said about the points which appear far below the line. The value of b(x) as a function of x is essentially the slope of a straight line fit to a plot of $\ell n F_2$ versus $\ell n q^2$ for a finite region of $\omega(=1/x)$. In this case these points corresponded to the range $2<\omega<3$; with $<\omega>=2.87$. Each data point within the ω region has its own average ω, ranging from a low of 2.42 up to a high of 2.80. As in no other ω region, the data points arrayed themselves in such a way that the points with largest average ω (and lowest average x) were at lower values of $\ell n q^2$, while points with small average ω were consistently at larger values of $\ell n q^2$. Since the cross section grows with smaller x, no matter what the value of q^2, the plot was higher at low $\ell n q^2$ than it should have been, and the value of b(x) is therefore more negative than it should have been. The values of b(x) for all data and for data $W^2<100$ is given in Table 5.4.

5.5 QCD Predictions

Since QCD only makes predictions for the moments of F_2, and not for F_2 itself, some kind of inversion has to be performed. This involves a formula of the type:

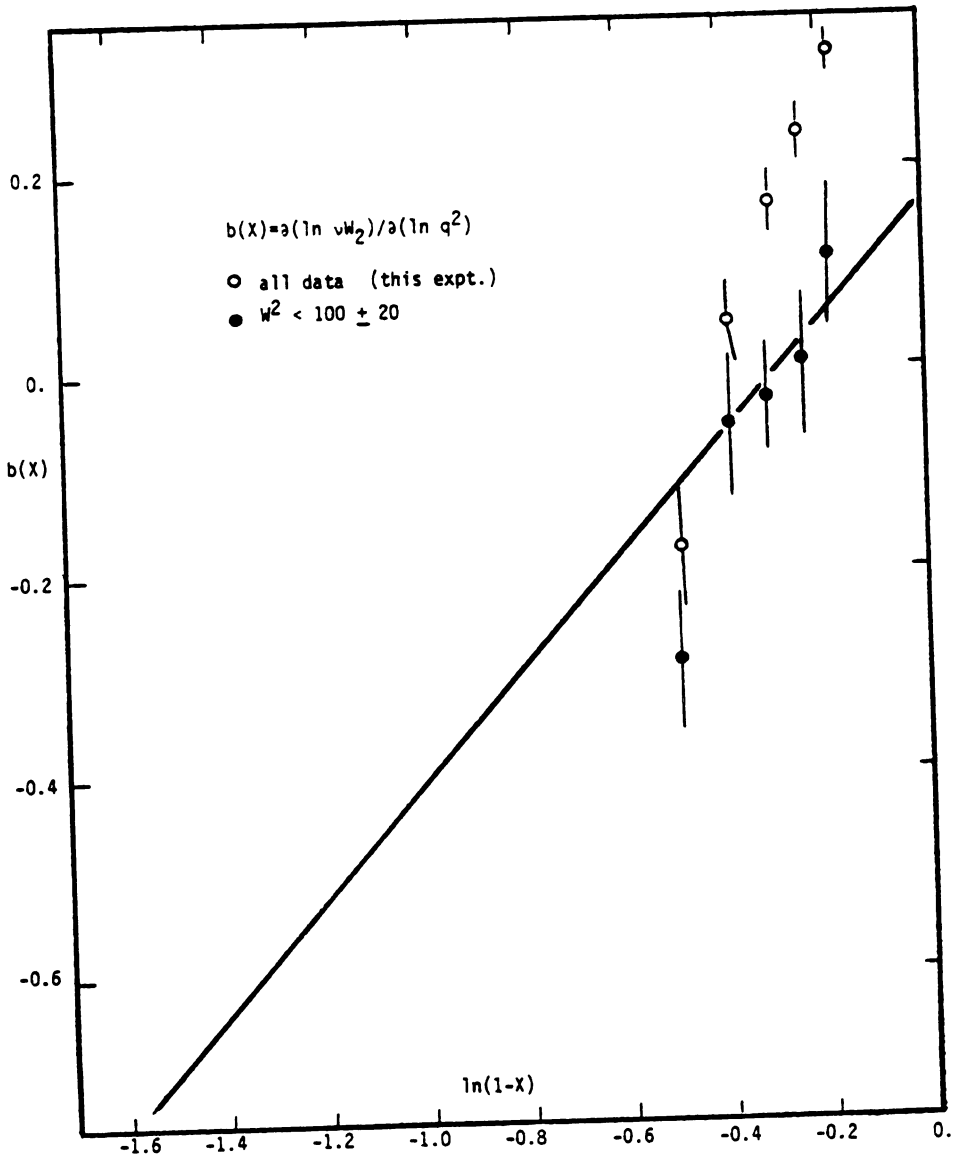

Figure 5.4 E319 b(x)

Table 5.4 E319 values for $b(x)=\partial \ln F_2/\partial \ln q^2$

x	ln(1-x)	b(x) all data	χ^2/DOF	b(x) $W^2<100+20$	χ^2/DOF	
.386	-.49	-.174±.063	2.38	-.287±.072	.789	
.315	-.38	.0576±.039	.666	-.0577±.074	.080	
.265	-.308	.166±.028	3.56	-.0279±.050	1.84	
.217	-.245	.236±.021	3.86	.0114±.070	.821	
.165	-.180	.314±.020	3.86	.117±.090		only two points in each region
.111	-.12	.221±.020	1.16	-.0534±.173		
.058	-.06	.182±.024	9.20	-.463±.253		
.035	-.04	-.536±.125	2.72	-.716±.306		

$$F_2(x,q^2) = \frac{1}{2\pi i}\int \frac{dn}{x^{n-1}}\ M(n,q^2) \tag{85}$$

Since the n dependence of $M(n,q^2)$ is complicated, the integration can only be performed numerically. Using measured values of F_2 at some $q^2=q_0^2$ from deep inelastic scattering (from which $M(n,q_0^2)$ can be computed), and inventing a particular expression for the gluon distribution within the nucleon, several authors have constructed numerical estimates of the q^2 and x behavior of F_2 and of the individual quark densities.[36,37] These studies develop the q^2 dependence of F_2 using QCD methods and the basic x dependence assumed in the simple parton model.[38] The QCD model which will be discussed presently is that of Buras and Gaemers.[39] By making certain assumptions about the n dependence of the moments M they are able to derive analytic expressions for the quark densities and for F_2 as a function of x and q^2.

They define two valence quark densities:

$$\begin{aligned} V_8(x,q^2) &= u_v(x,q^2) + d_v(x,q^2) \\ V_3(x,q^2) &= u_v(x,q^2) - d_v(x,q^2) \end{aligned} \tag{86}$$

They also derive densities for the gluons (G), for the charmed sea (C), and for the non-charmed sea (S). Since G, S, and C are steeply falling functions of x, there is little contribution to the higher moments at large x. Therefore Buras and Gaemers use only the first two moments (n=2,3) in the inversion process and are able to derive analytic

expressions for G, S, and C in terms of x and the variable

$\bar{s} = \ell n \left(\frac{\ell n q^2/\Lambda^2}{\ell n q^2/q_o^2}\right)$:

$$xS(x,\bar{s}) = A_S(\bar{s})\ (1-x)^{\eta_S(\bar{s})}$$

$$xC(x,\bar{s}) = A_C(\bar{s})\ (1-x)^{\eta_C(\bar{s})} \qquad (87)$$

$$xG(x,\bar{s}) = A_G(\bar{s})\ (1-x)^{\eta_G(\bar{s})}$$

where, for example, $A_G(\bar{s}) = M_G(2,q^2)\left(\frac{M_G(2,q^2)}{M_G(3,q^2)} - 1\right)$

$$\eta_G(\bar{s}) = \frac{M_G(2,q^2)}{M_G(3,q^2)} - 2$$

In order to formulate the valence quark densities, which have a larger effect at big x, the first 12 moments were utilized:

$$xV_3(x,\bar{s}) = A_3(\bar{s})\ x^{\eta_1^3(\bar{s})}(1-x)^{\eta_2^3(\bar{s})}$$

$$(88)$$

$$xV_8(x,\bar{s}) = A_8(\bar{s})\ x^{\eta_1^8(\bar{s})}(1-x)^{\eta_2^8(\bar{s})}$$

Those parameters which are not given by the theory are gotten by fitting the experimentally observed moments of F_2, which in this case

are those for ep[15] and μp[17] inelastic scattering. The complete structure function is constructed from the quark densities, as in the parton model:

$$\nu W_2^{(p,n)}(x,q^2) = x[\tfrac{5}{18}V_8(x,q^2)\pm\tfrac{1}{6}V_3(x,q^2)+\tfrac{2}{9}S(x,q^2)+\tfrac{4}{9}C(x,q^2)] \qquad (89)$$

The quark densities and $F_2(x,q^2)$ calculated by these methods is shown in Figure 5.5 for $q^2=22.5$ (GeV/c)^2.

5.6 $F_2^{E319}(x,q^2)$ Compared to QCD

Using some of the newer μp data[40] and our μ-Fe data, Buras has derived this particular parameterization for his model at $q^2=q_o^2=2$:[41]

$$\Lambda = 0.4 \text{ GeV}$$

$$xG = 2.41\ (1-x)^5$$

$$xS = (1-x)^8$$

$$xv = \frac{3}{B(0.7,3.6)}\, x^{0.7}(1-x)^{2.6} \qquad (90)$$

$$xd_v = \frac{1}{B(.85,4.35)}\, x^{0.85}(1-x)^{3.35}$$

$$xC = 0$$

The curves generated by these formulas and the measured values of $F_2(x,q^2)$ are plotted in Figures 5.6 (a)-(f) versus x for fixed q^2 regions (the binning is slightly different than in Figure 5.3). For the sake of comparison, the QCD prediction and the CHIO (E398: Chicago-

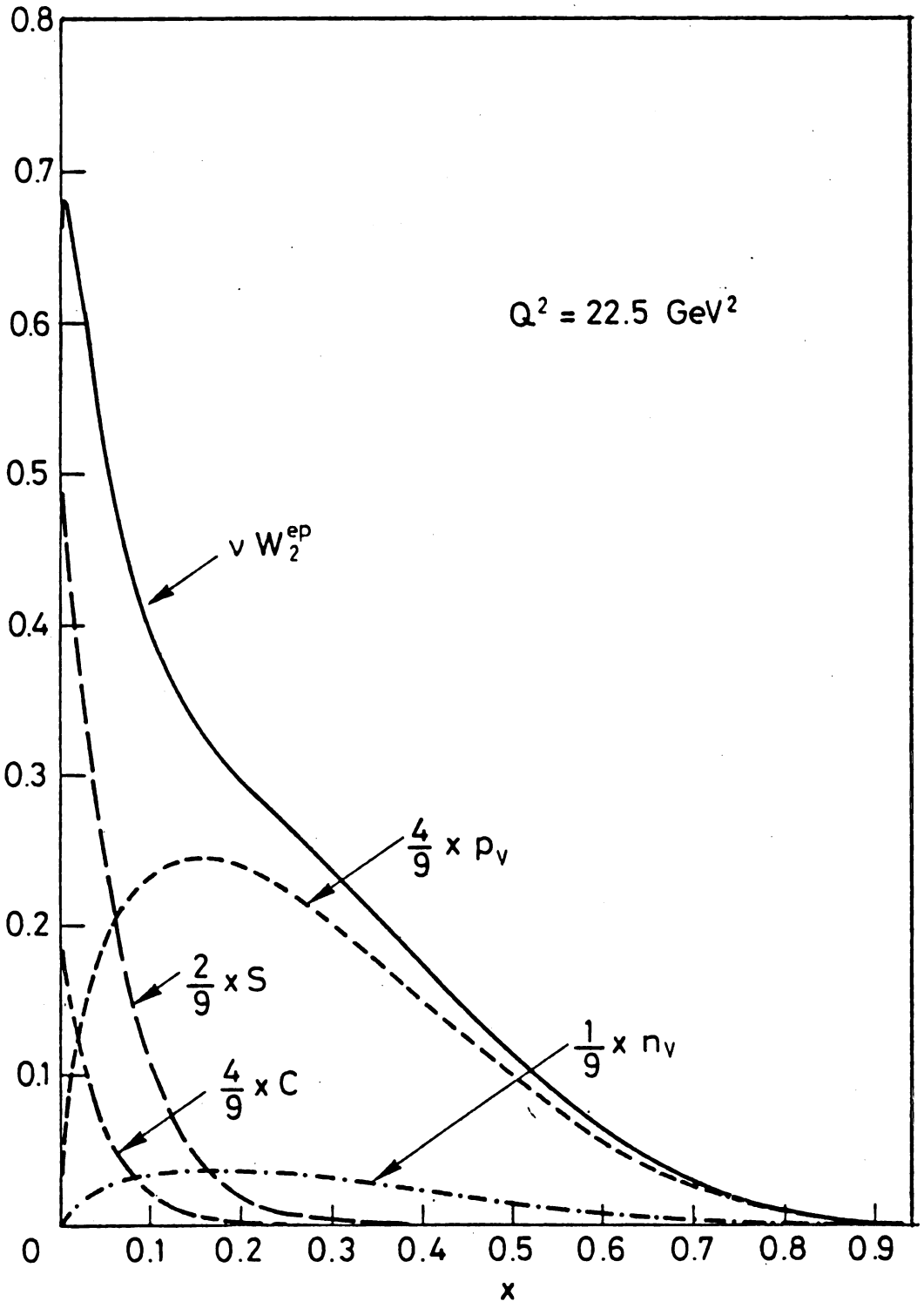

Figure 5.5 QCD predictions for F_2 and for quark densities

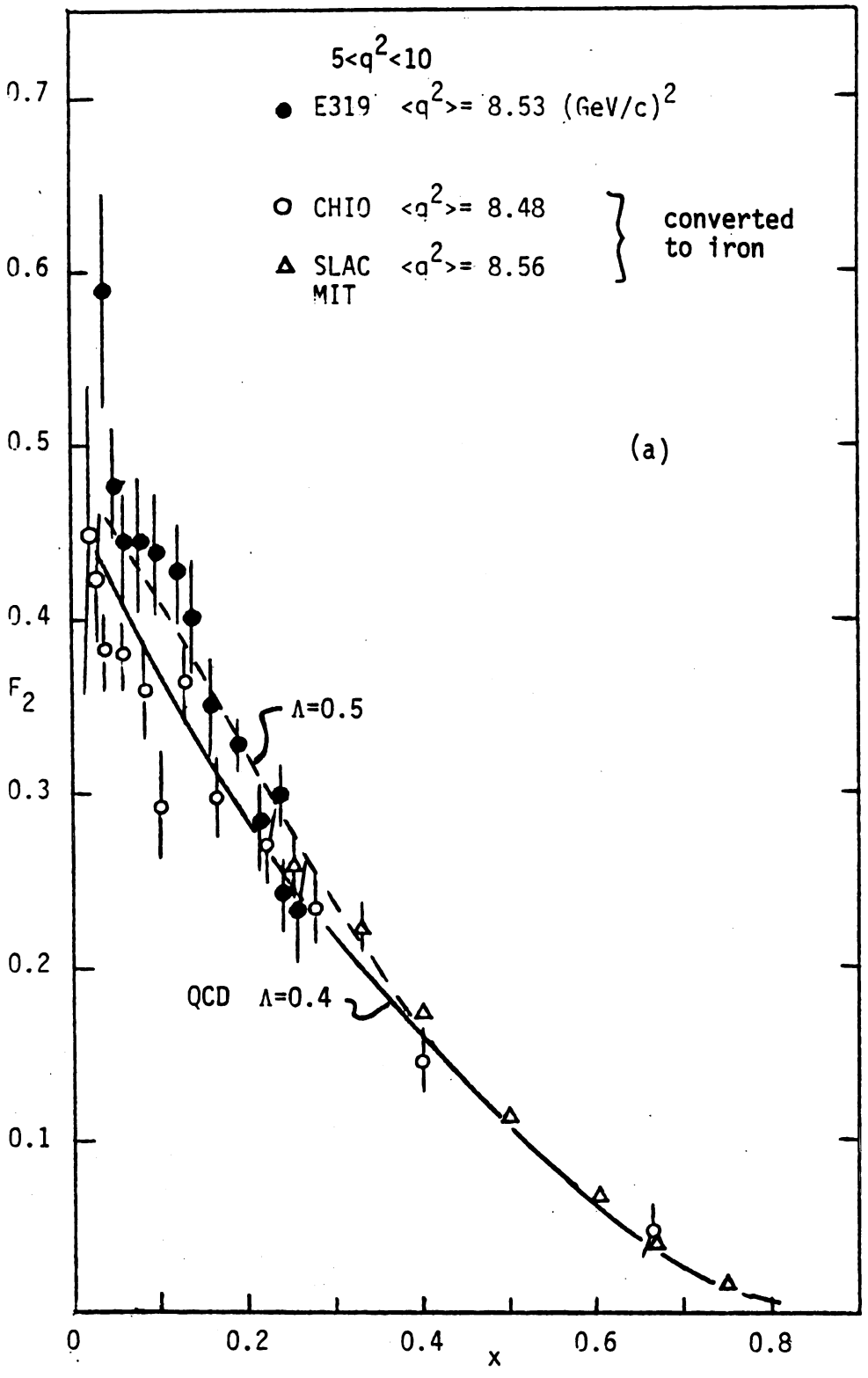

Figure 5.6 Measured F_2 versus x for fixed q^2

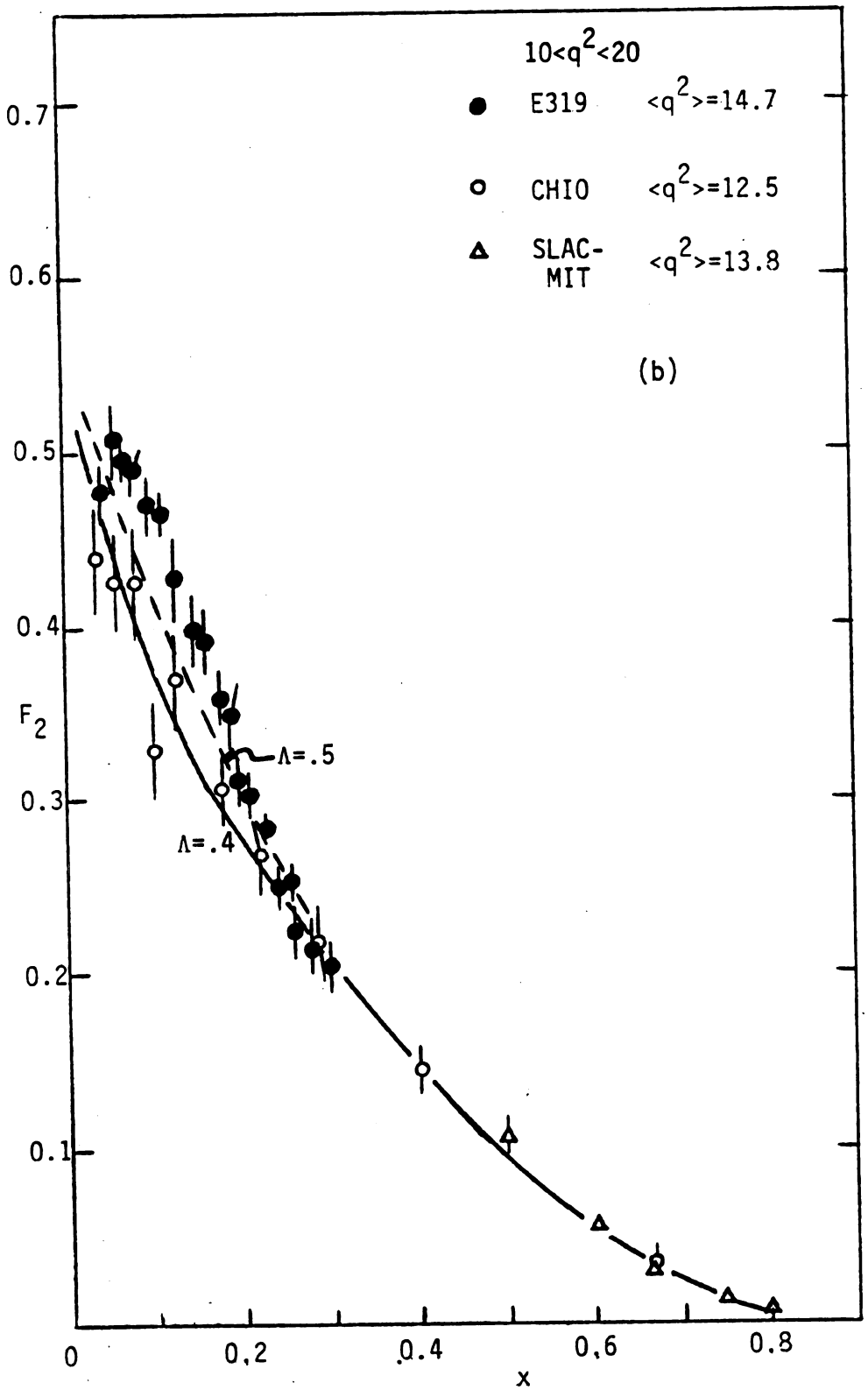

Figure 5.6 continued

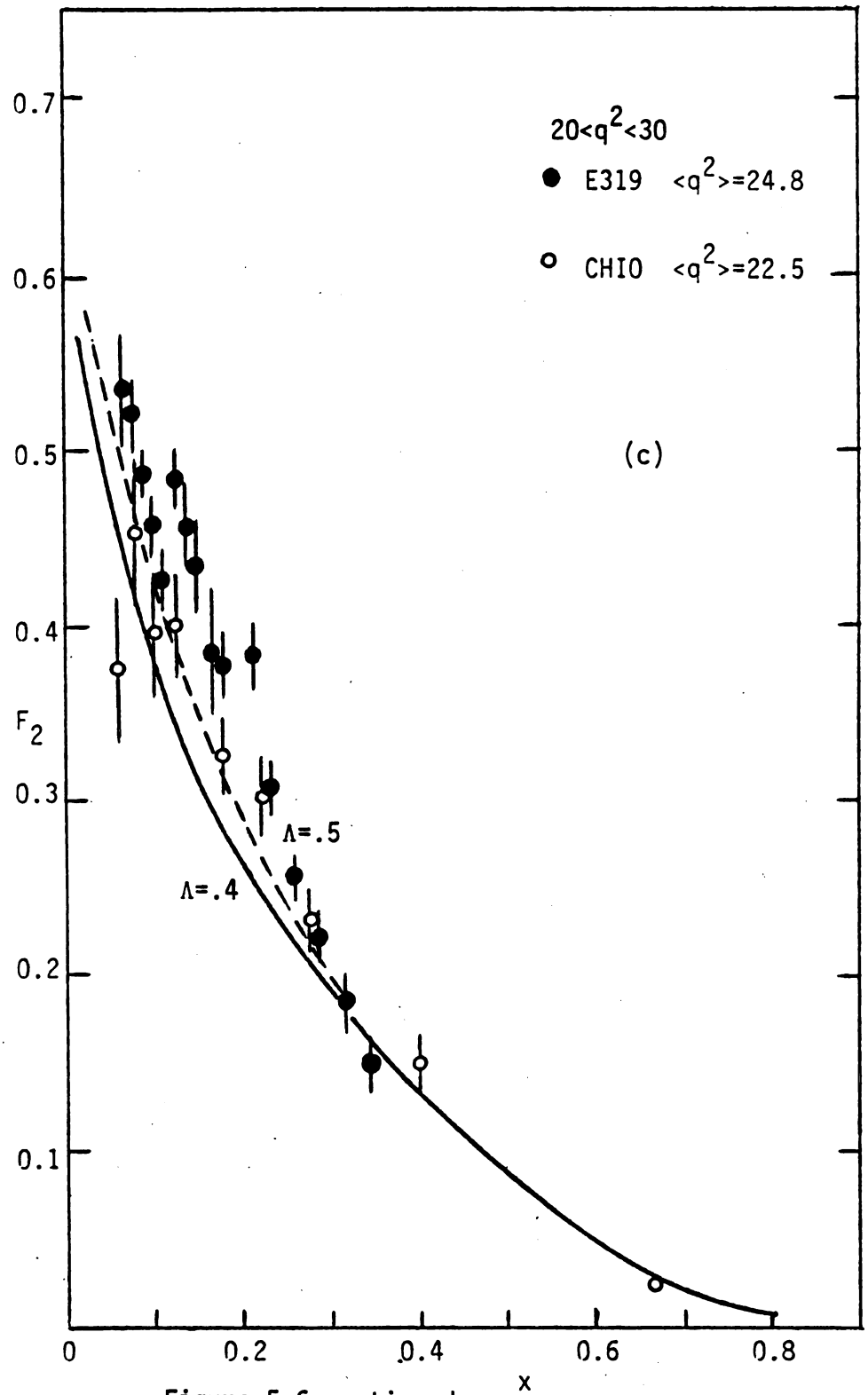

Figure 5.6 continued

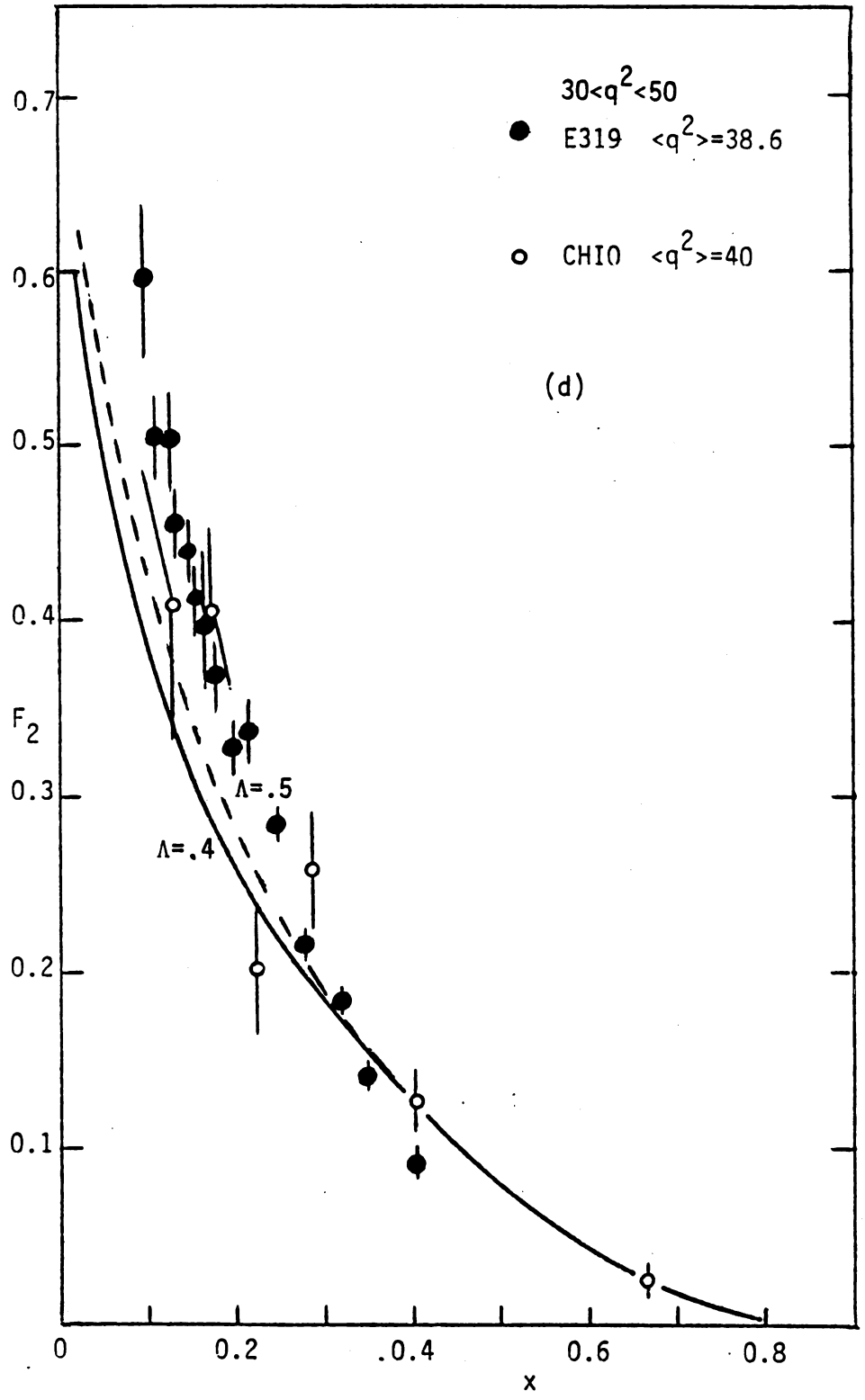

Figure 5.6 continued

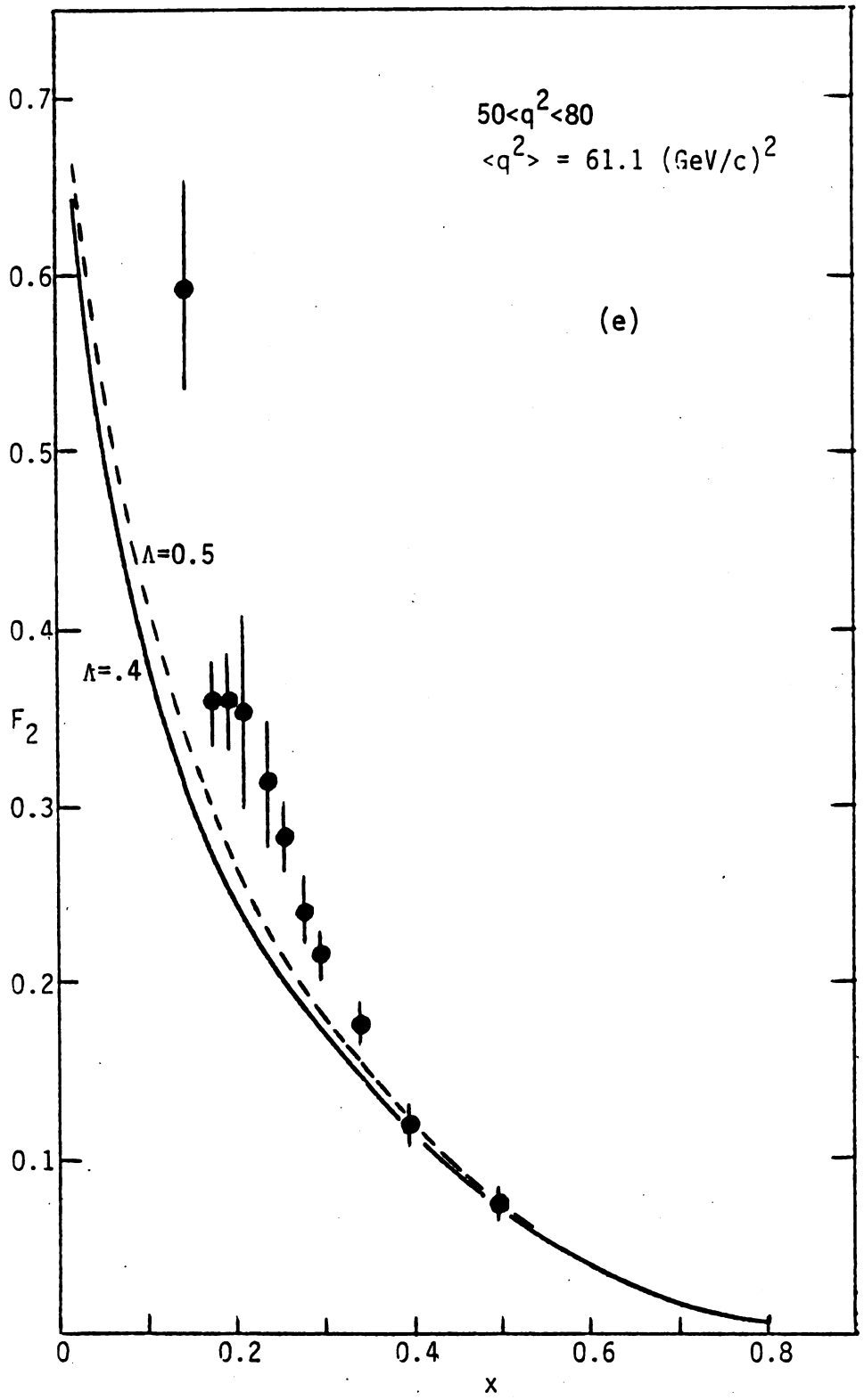

Figure 5.6 continued

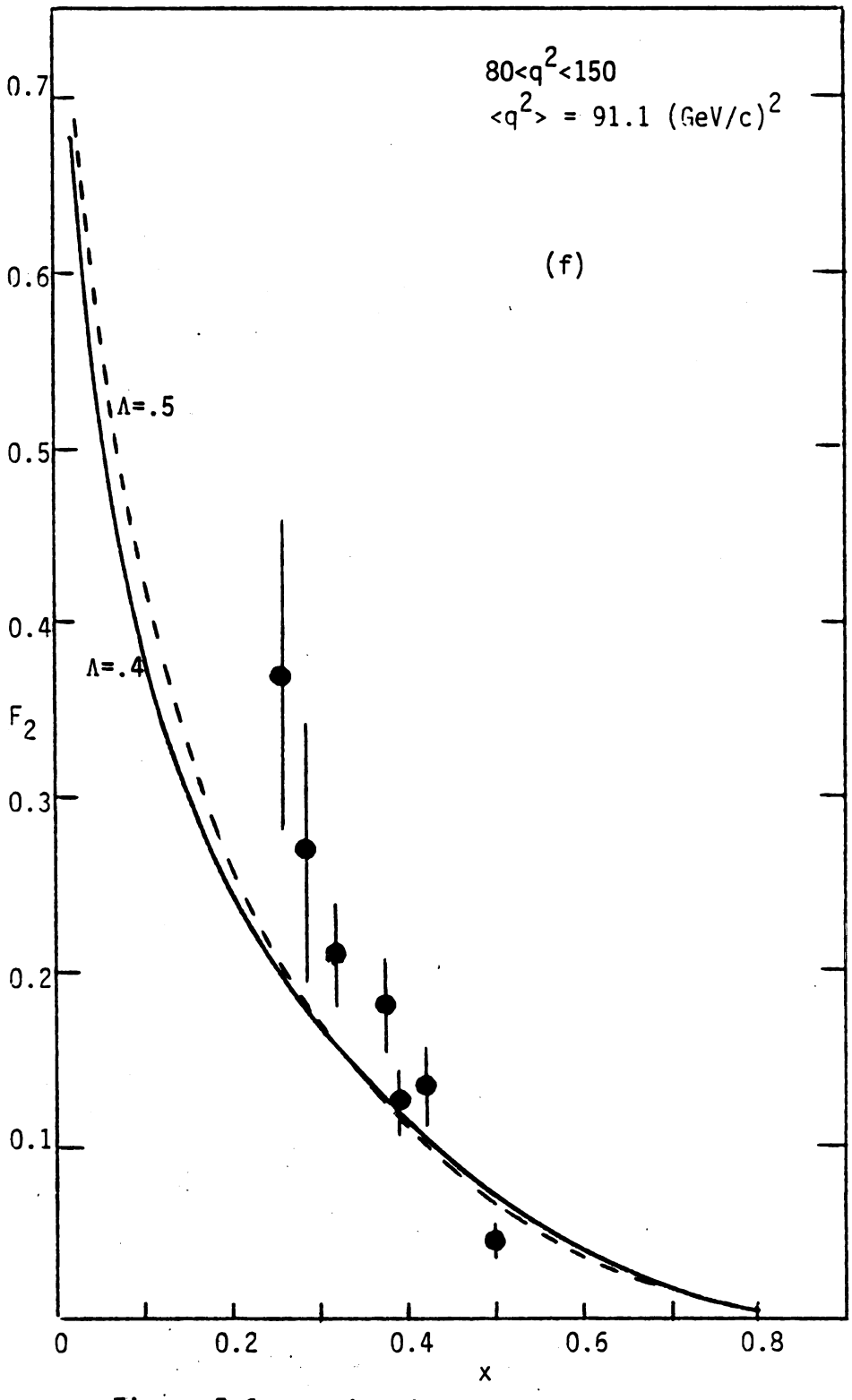

Figure 5.6 continued

Harvard-Illinois-Oxford) structure functions[40] have been converted to μ-Fe scattering using equation (70). There are even a few SLAC-MIT points[15] at high x for the lowest two q^2 regions. Also shown in these plots is a second curve representing QCD with Λ=0.5 and the following changes for the formulas in (90):

$$xS = .9(1-x)^5$$
$$xG = 2.1(1-x)^4 \qquad (91)$$

These modifications were suggested by Buras[41] to see if QCD could be made to agree with the data. The Λ=.4 curve is systematically below our data for small x; like Figure 5.3, the data rises above the curve below a certain value of x, as if some threshold had been reached. The Λ=.5 curve is much closer to the E319 data, but is systematically above the CHIO data. The threshold-like behavior is not as evident in the low q^2 regions but does persist in the higher q^2 regions where the Λ=.4 and Λ=.5 curves are similar. That it is possible to get better agreement in the lower q^2 regions just by cranking up the sea quark distribution and changing Λ to 0.5, shows that such a formulation of QCD is still very tentative.

This is demonstrated again in Figures 5.7 (a)-(g) where $F_2(x,q^2)$ is plotted versus q^2 for fixed x (or ω). The average ω for each plot is given along with the highest and lowest values of ω for any of the points used in that region. The two QCD curves drawn for each plot correspond to these high and low values of ω for each region. Only curves for Λ=.4 are shown since the curves for Λ=.5 are not much different. The SLAC-MIT data[15] is also shown, and lies mostly at low q^2.

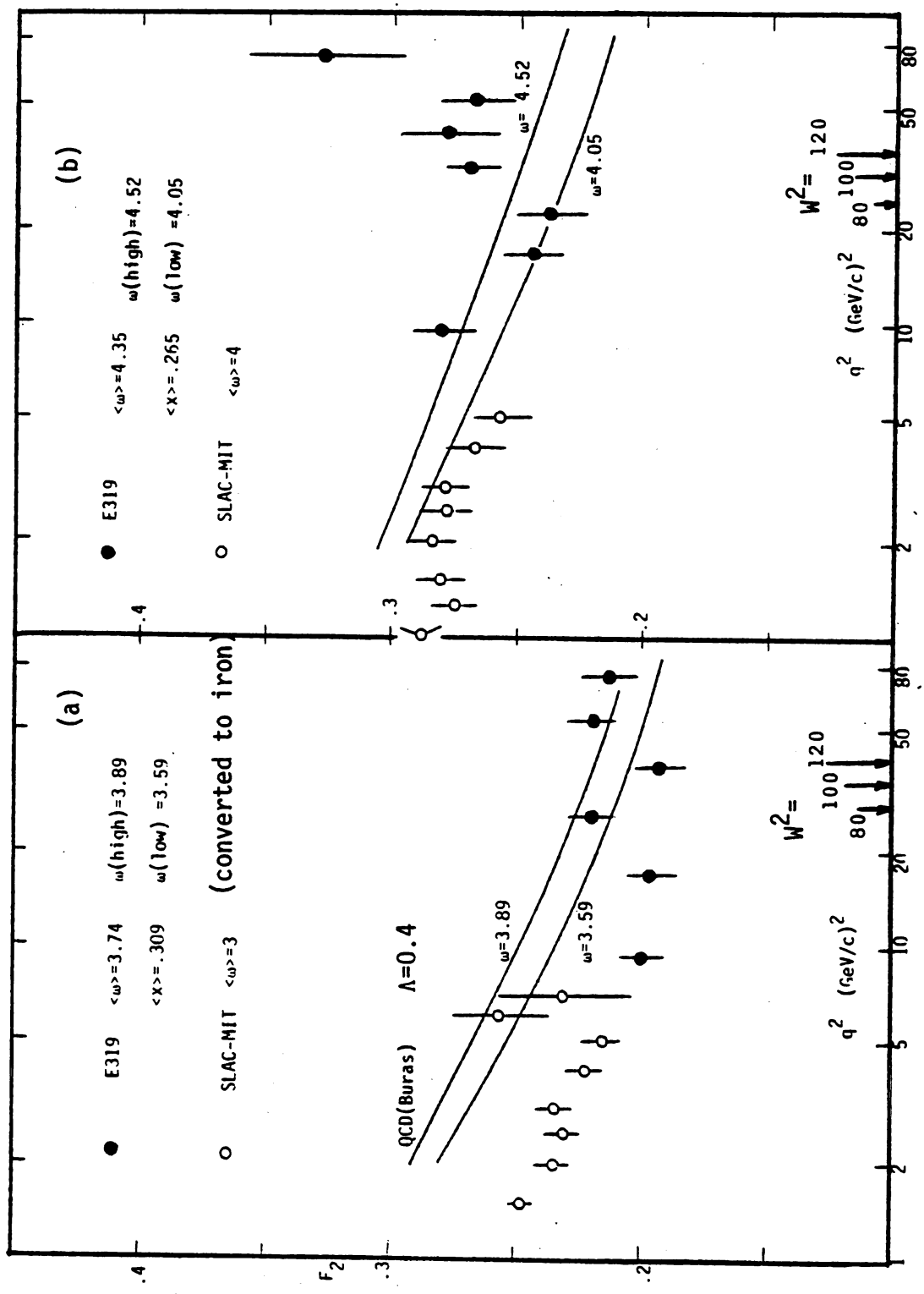

Figure 5.7 Measured F_2 versus q^2 for fixed ω (=1/x)

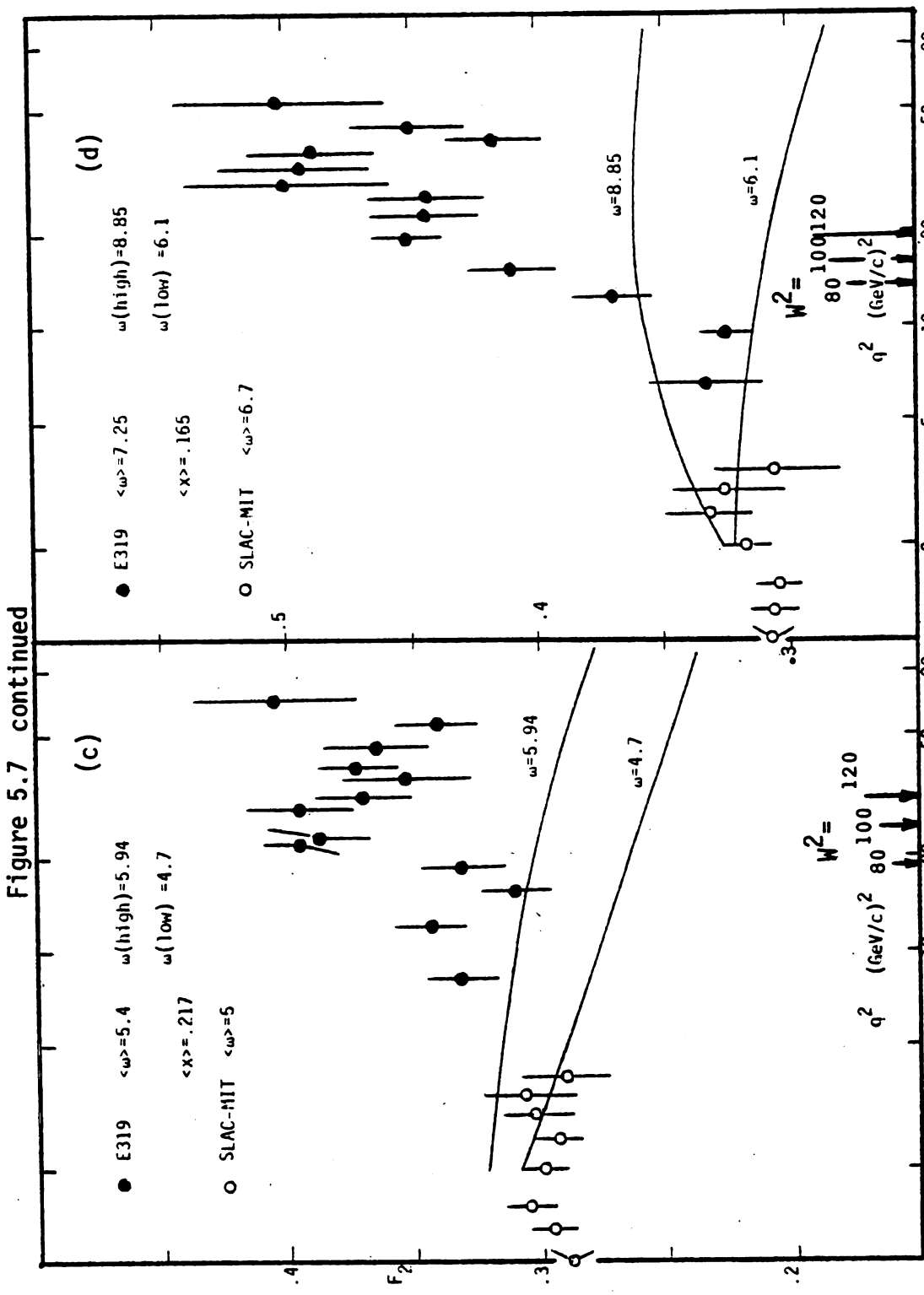

Figure 5.7 continued

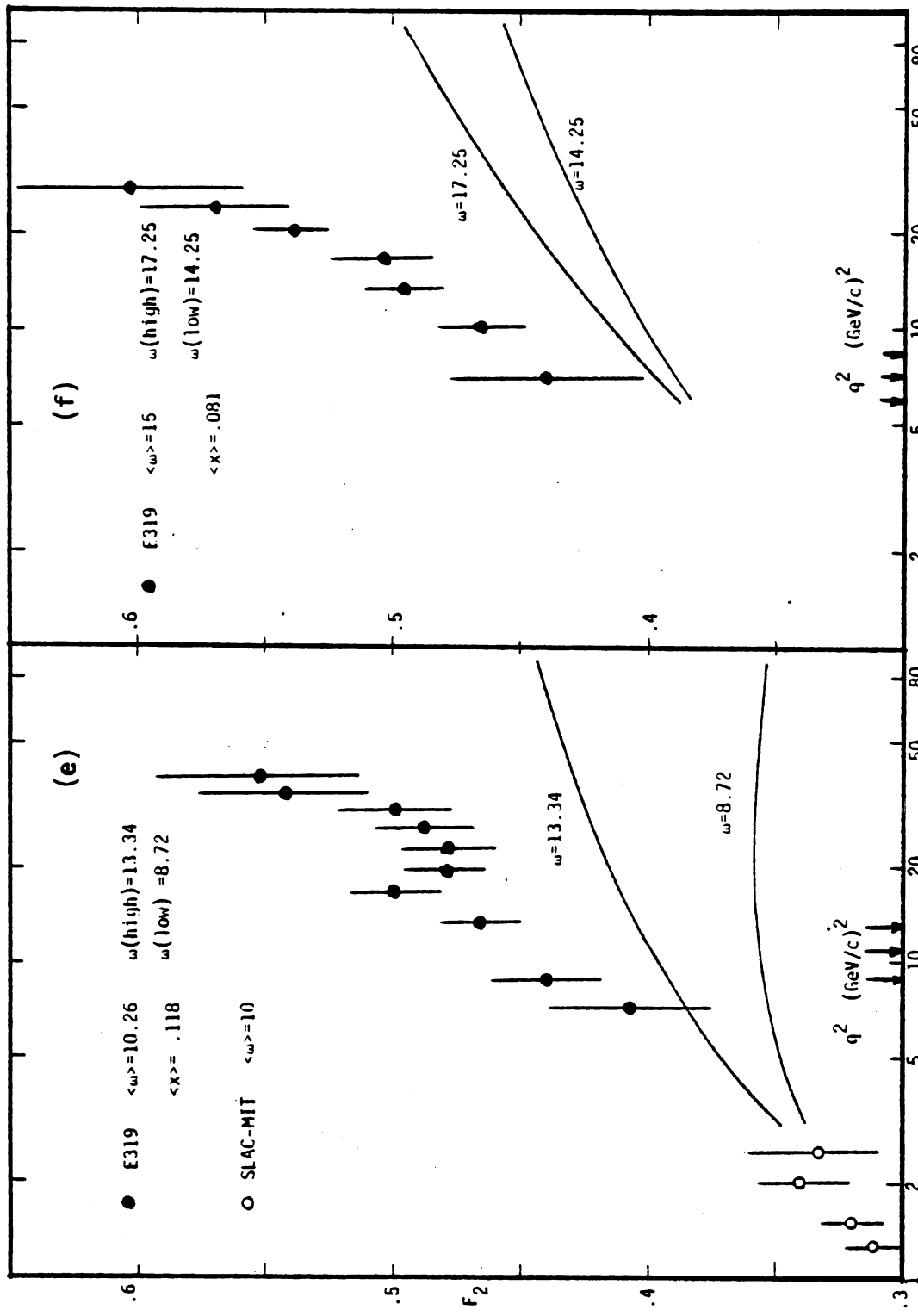

Figure 5.7 continued

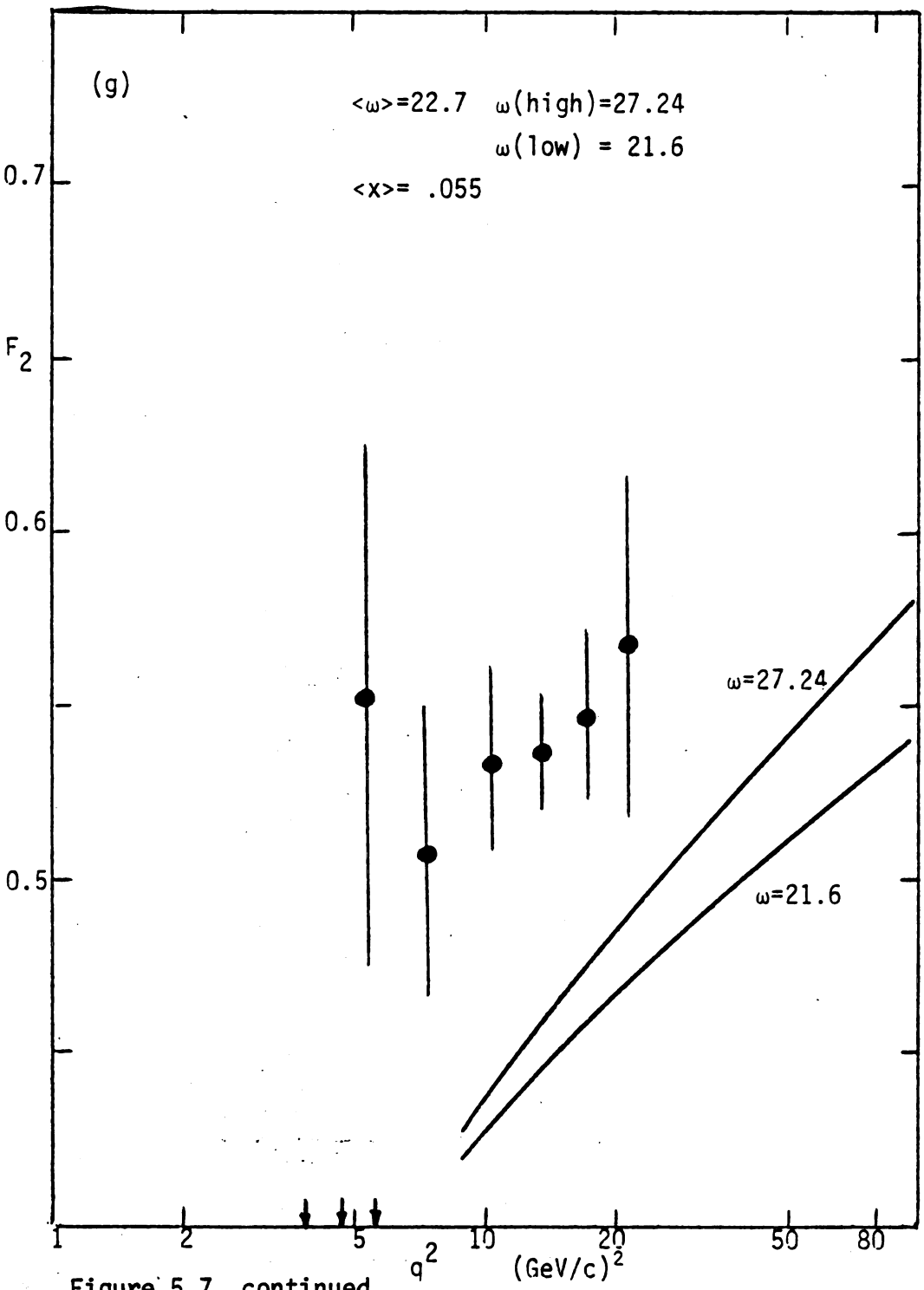

Figure 5.7 continued

An interesting feature in Figure 5.7 is the rather large rise in F_2 above the QCD curves for increasing q^2. This trend sets in as early as Figure 5.7(b) where $\langle\omega\rangle$=4.35. Even in 5.7(a), for $\langle\omega\rangle$=3.74, the data is not decreasing with increasing q^2. What this may suggest, again, is a threshold-like behavior in W^2. On each plot, three arrows have been drawn to indicate that value of q^2 for which W^2=80, 100, and 120 $(GeV/c^2)^2$. As in Figure 5.3, the evidence for a rise in F_2 in the vicinity of the arrows is not perfect, but is reasonably good. It will be very difficult to vary the quark density function, or Λ, in order to get the QCD curves to approach the data at high q^2; none of the curves shown was able to rise with q^2 after having fallen at lower q^2.

5.7 Moments

Figure 5.8 shows the first moment of F_2:

$$M(2,q^2) = \int_0^1 F_2(x,q^2)dx \qquad (92)$$

for μ-Fe scattering (E319) as well as μ-p and μ-d scattering.[42] Also shown is the moment computed for the QCD structure function used in Figure 5.6 (Λ=.4), and the moment of the structure function employing the b(x) parameter (used in Figure 5.3), $F_2(b)=F_2(x,q_0^2)(q^2/q_0^2)^b$. The moments at each value of q^2 are given in Table 5.5, along with the n=3 and n=4 moments of the E319 data.

The experimentally measured moments (n=2) in E319 rise with increasing q^2. The moment of $F_2(b)$ rises only slightly with q^2, while the QCD curve falls. The proton and deuterium data do not extend far enough to tell what happens at high q^2. In the parton model the n=2 moment of the structure function F_2 is proportional to the mean parton

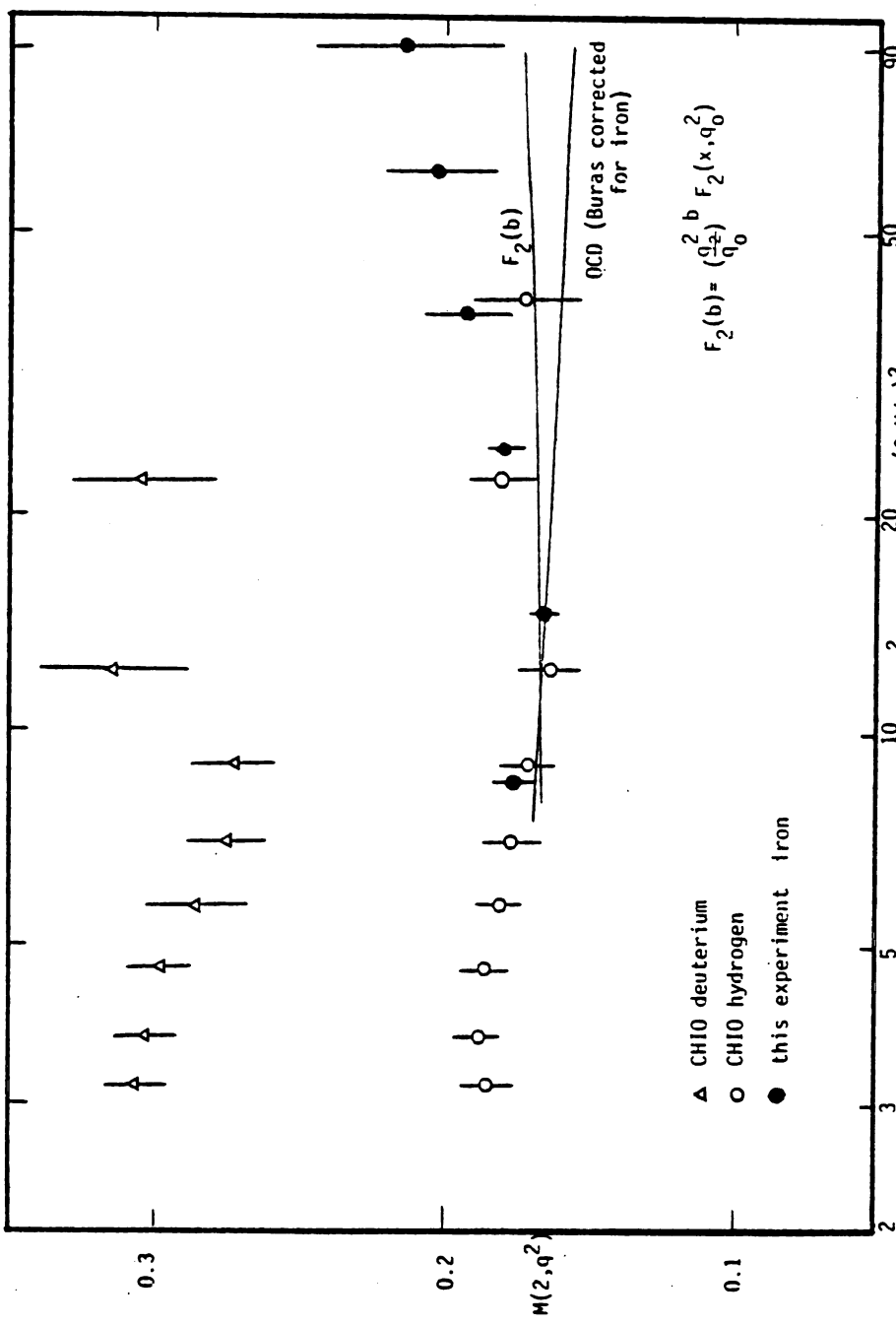

Figure 5.8 First moment of F_2 for μ-p, μ-d, and μ-Fe scattering

charge squared.[5] One interpretation of a falling moment with increasing q^2 is that neutral partons, such as gluons, could be more important at high q^2; either there are more of them or they assume a larger share of the nucleon's momentum. In contrast, the increase in the moments, observed in E319, is related to the other aspects of the data; namely the rise of F_2 above a reference curve (QCD, or $F_2(b)$), and the twofold behavior of b(x) computed with and without the data above $W^2=100\pm20$.

A few words should be said about how the moments are computed. First of all, x was used as the "scaling" variable rather than the more proper Nachtman variable (equation (40)) which takes into account various mass effects; this was permissible since our lowest q^2 region was 8.5 $(GeV/c)^2$, well above $q_o^2=2$. Secondly, the x axis was divided into three regions. In region II, where data for F_2 exists, the moment was found by Simpson's rule; just finding the area underneath the data points. For x below x_{min} (the lowest value of x for which there is data) the area computed was that for a trapezoid, the upper edge of which was a straight line given by the derivative of the power law fit to the data computed at x_{min}. The coefficients for these fits to the data in Figure 5.6 are given in Table 5.6. In region III, where x is above x_{max} (the highest x for which there is data), the function $F_2(b)=F_2(x,q_o^2)(q^2/q_o^2)^b$ was used, making sure that $F_2(b)$ was adjusted to agree with the data point at x_{max}.

5.8 Fits to the Data

The data in $F_2(x,q^2)$ plotted against x for fixed q^2 lends itself to a power law fit in x. For F_2 versus q^2 for fixed ω, several fits were attempted. Fit type III was a single parameter fit to the "standard" scale breaking curve $F_2(b)=F_2(x,q_o^2)(q^2/q_o^2)^b$ times a normalization

Table 5.5 Moments

q^2	E319 n=2	E319 n=3	E319 n=4	QCD n=2	$(\frac{q^2}{q_o^2})^b F_2(x,q_o^2)$ n=2
8.53	.1740±.006	.0428±.0006	.0299±.0006	.1694	.1691
14.7	.1739±.005	.0437±.0004	.0291±.0004	.1657	.0176
24.8	.1800±.008	.0455±.0006	.0284±.0004	.1627	.1680
38.6	.1932±.015	.0468±.0009	.0271±.0004	.1604	.1691
61.1	.2036±.022	.0507±.0021	.0267±.0005	.1582	.1713
91.1	.2136±.034	.0605±.0063	.0277±.0016	.1564	.1735

Table 5.6 Power law fit to $F_2(x,q^2)$ in various q^2 regions

$$F_2(x,q^2) = \sum_{i=3}^{5} a_i (1-x)^i$$

q^2	a_1	a_2	a_3	χ^2/DOF
8.53	-2.835±1.355	8.243±3.14	-4.931±1.81	1.358
14.7	-3.320±.559	9.355±1.325	-5.524±.779	1.819
24.8	-3.243±.633	9.551±1.588	-5.801±.986	2.57
38.6	-1.046±.506	3.473±1.366	-1.669±.911	1.163
61.1	-1.255±.770	4.305±2.261	-2.310±1.637	1.74
91.1	-1.752±1.817	6.012±6.201	-3.482±5.195	1.229

constant N. Fit type II was of the form

$$F_2 = NF_2(b) + A\,\Theta(W^2 - 100) \qquad (93)$$

where the second parameter A is the "strength" of a step-function which equals one for $W^2>100$ and is zero for $W^2<100$. Use was made of a step function to simulate a hypothetical threshold in W^2 at 100 $(GeV/c^2)^2$. A step function is a bit severe though: due to a shortage of data points, and our finite resolution, no such sharp rise in the data is visible. Therefore, for fit type I, the step function was replaced by a linear rise in q^2 for the region between a W^2 of 80 and 120 (20 on either side of $W^2=100$). This ought to represent the uncertainty in the location of the would-be W^2 threshold. The results of all these fits, for the various ω regions, are shown in Table 5.7. Included there is χ^2 per degree of freedom for each fit. A particular fitted curve (type I) for the $\langle\omega\rangle=7.25$ region is shown in Figure 5.9. The curve follows the rise in the data for $80<W^2<120$ (marked by the dashed lines) but misses the dip at higher q^2. It is just possible there might be a second threshold at higher W^2; the data in several of the ω regions shows a dip at high q^2.

5.9 Speculations on Scaling Violations

QCD predicts violations of exact Bjorken scale invariance of the form $\ell n(q^2/q_0^2)$. It also predicts a violation term of the form $(m^2/q^2)^n$ which is important only at small q^2 (m is the mass of a typical quark $\simeq$ 500 MeV).[24] The predictions for QCD do not agree that well with the measured structure function for μ-Fe scattering reported above. The data also does not agree very well with the function derived from

Table 5.7 Fits to F_2

$\langle\omega\rangle$	I $F_2=N\ F_2(b)$ $W^2<80$ $F_2=N\ F_2(b)+A+Bq^2$ $80<W^2<120$ $F_2=N\ F_2(b)+A+B\frac{120\ x}{(1-x)}$ $120<W^2$	II $F_2=N\ F_2(b)+A\theta(W^2-100)$	III $F_2=F_2(b)$ $=F_2(x,q_o^2):\left(\frac{q^2}{q_o^2}\right)^b$
3.74	N=.769 A=-.18 B=.0045 χ^2=2.00	N=.9353 A=.0289 χ^2=.133	N=.9749 χ^2=1.454
4.35	N=.8334 A=-.058 B=.0023 χ^2=4.355	N=.873 A=.063 χ^2=2.17	N=.935 χ^2=6.088
5.4	N=.9653 A=.046 B=-.0012 χ^2=3.89	N=.902 A=.075 χ^2=4.32	N=.994 χ^2=12.62
7.25	N=.9133 A=-.1011 B=.0103 χ^2=2.01	N=.955 A=.092 χ^2=7.78	N=1.05 χ^2=20.6
10.26	N=1.14 A=-.0212 B=.004 χ^2=1.109	N=1.057 A=.045 χ^2=2.00	N=1.132 χ^2=4.07
15	N=2.157 A=-.276 B=-.0107 χ^2=.611		
22.7	N=.7801 A=.997 B=-.139 χ^2=.228	N=1.537 A=-.106 χ^2=6.72	N=1.275 χ^2=7.6

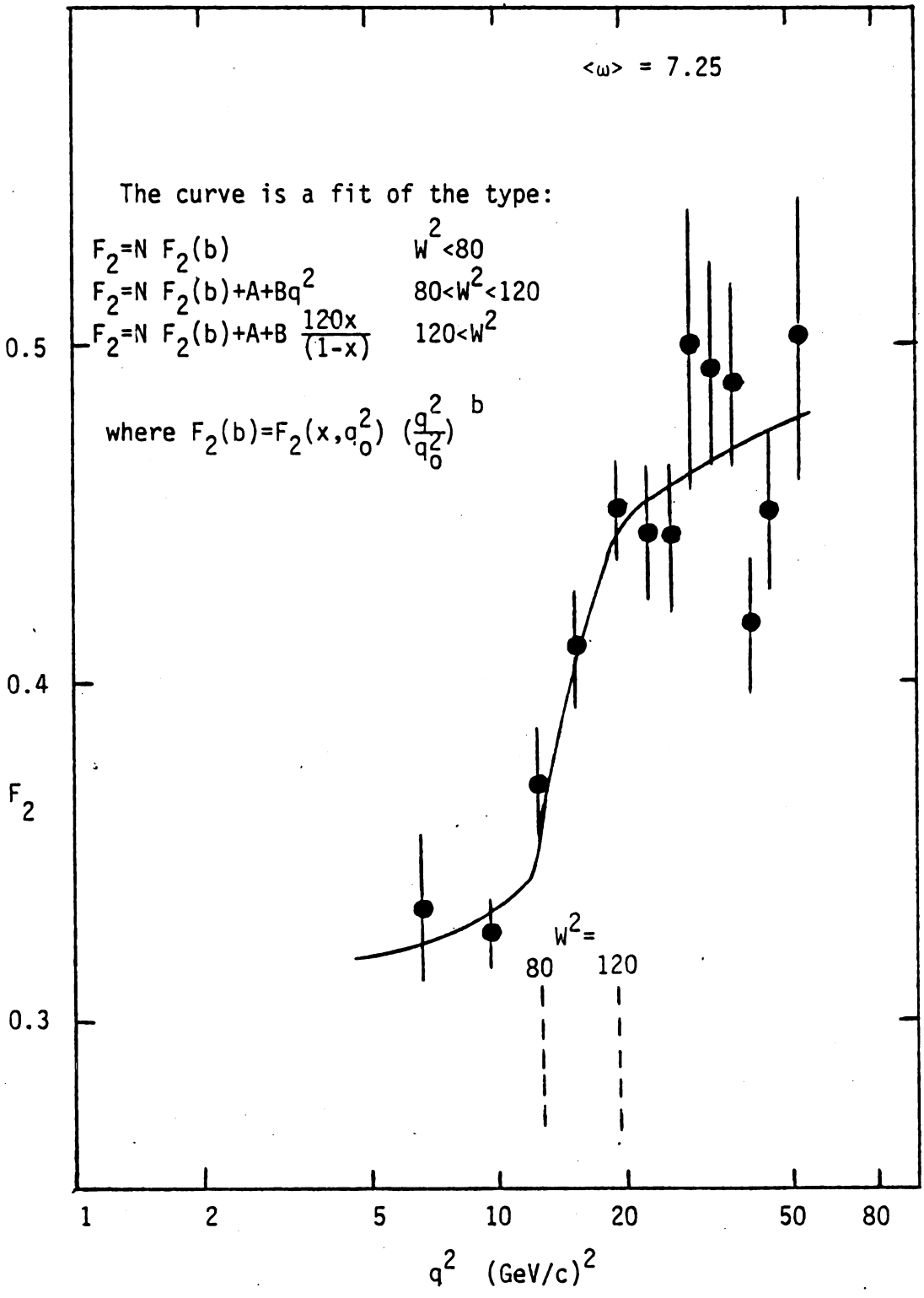

Figure 5.9 A fit to F_2 using a linear rise above W^2=80.

previous deep inelastic scale-violation data, $F_2(b)=F_2(x,q_0^2)(q^2/q_0^2)^b$. What other formulations of scale violations have been hypothesized?

The behavior of F_2 in Figure 5.7 suggests a possible threshold around $W^2=100\pm20$. Is this a threshold for producing a new quark? At small x, the production of charmed quarks (or bottom quarks) along with other sea quarks is possible, as in Figure 1.8(c). But the threshold for producing charmed quarks ($2m_D\cong3.7$ GeV/c^2) has been surpassed in many experiments and it is unlikely that $c\bar{c}$ production,[43] much less $b\bar{b}$ pair production, is responsible for the relatively large rise in F_2 with increasing q^2 (at fixed x) observed in E319; this rise persists to rather large x, a region where pair production of sea quarks is expected to be small. We are currently studying a sample of dimuons produced in this experiment, which may tell us something about charm cross sections.

Several authors[44] have attempted to relate the observed scale violations to the generalized vector dominance model (GVDM). Predictions are made for F_2 using GVDM and they agree pretty well with early inelastic data. But the kinematic region studied is at relatively low q^2 (less than 10-20 $(GeV/c)^2$) and it is uncertain whether the theory will still be applicable up to $q^2=100$. A related model[45] identifies scattering at small x (from sea quarks) with Pomeron exchange, while scattering from valence quarks at higher x is equivalent to Regge exchange. Again, the q^2 considered in these studies is no more than about 10 $(GeV/c)^2$.

A more exotic possibility for explaining the observed behavior of F_2 is "color thaw." A central problem in QCD, as well as any theory of the strong interaction, is the confinement of quarks; why should it be so hard, if not impossible, to observe free quarks in the laboratory?

A related question is why all observed physical particles are "colorless" while their supposed constituents, the quarks, possess color. In the theory of Salam,[46] where quarks have integral charges, the hadrons observed in the lab would still be colorless, but could be converted from color singlets to color octets. To use an isospin analogy, the observable color in the lab would still be zero ($I^z_{color}=0$), but the "color isospin" itself might be nonzero ($I_{color}\neq 0$). The energy necessary to reorient the color spin vectors of the quarks could perhaps be provided by the incoming virtual photon in deep inelastic scattering. The exitation of this new color state just might be related to a threshold in W^2.

One futher explanation for a large violation of scaling might be the existence of excited quarks or the hypothesis of non-pointlike quarks. Tajima and Matumoto[47] have made this assumption and arrive at two important conclusions. First, being extended objects with a finite size, quarks would have electromagnetic and weak form factors which would dampen the deep inelastic cross section (at q^2 large enough to resolve the size of the quark). This type of scale violation leads to a negative contribution with increasing q^2 (for fixed x); it would appear in the form of the old "propagator" term, $N/(1+Q^2/\Lambda^2)^2$, once used to measure deviations from perfect scaling.[19] Their second conclusion is that a positive contribution to scaling violations will be realized if the thresholds for certain quark excited states are reached. This would occur at $q^2 = \frac{W^2_{threshold}}{(\omega-1)}$.

There have been several generations of constituent theories of matter. Decades ago, the scattering of electrons from atoms revealed the atomic structure; the constituents in this case were electrons and

a heavy nucleus. Some of these constituents could be liberated from the atom if the incoming electron carried enough energy. Then the nucleus was found to have constituents, some of which could be ejected in the form of nucleons (protons, neutrons). Later, in the 1960's, evidence for the existence of nucleon constituents, namely partons, was exhibited in the deep inelastic ep scattering experiments at SLAC. If partons themselves had constituents, what would be the experimental implications?

Using the parton model and the hypothesis of Bjorken scaling, one can imagine exploring the next layer of matter inside the parton. For $q^2 \gtrsim m^2_{proton}$, the lepton-quark interaction is elastic, the effect of gluons is relatively small, and the structure function for μ-p deep inelastic scattering scales. When q^2 is increased further, the size of the quark can eventually be resolved. At this point, the muon-quark interaction can be inelastic and the μp structure function no longer scales. In this sense, the "precocious scaling" of F_2 for relatively low q^2, in the SLAC-MIT experiments, would not indicate asymptotic behavior, but only pre-asymptotic behavior,[48] only to be followed by scale violations at higher q^2. At even higher q^2, the sub quarks (if they existed) might be probed. If the incoherent scattering of muons from these individual sub-quarks were elastic, a form of scale invariance would be reinstituted. What we have here is a lepton "microscope": as q^2 is increased, the wavelength of the virtual photon probe is decreased, and we explore ever smaller structure within the hadronic "specimen."

Kogut and Susskind synthesize from this hierarchy of systems and subsystems a "scale-invariant parton model."[27] In this model systems of type N contain constituents of type N+1. Eventually, for large

enough N, the rules which govern the break-up of systems of type N would also govern systems of type N+1. The main reason for believing that we may have come to the natural end of this hierarchy of systems is that free quarks have not yet been discovered. A system of recursive constituents such as QCD, where quarks and gluons are to be found inside other quarks and gluons, may be the answer.

5.10 Summary and Conclusions

A large violation of Bjorken scale invariance has been observed out to q^2=150 $(GeV/c)^2$, extending previous deep inelastic results.[14-18] Except for low q^2, the measured values of $F_2(x,q^2)$ are higher than a particular QCD prediction[39], and show a possible threshold-like behavior in $W^2=q^2(\omega-1)+m^2$. The parameter $b(x)=\partial \ell n F_2/\partial \ell n q^2$ may not be so useful in describing scale violations since it appears to depend on W^2. Another area of disagreement between the data and QCD is the first moment of F_2; the data shows an increase in the moment above $q^2\simeq 15$ $(GeV/c)^2$ whereas QCD (as formulated in reference [39]) predicts a falling moment with increasing q^2.

The possibility of thresholds in W^2, and other explanations of the rise in $F_2(x,q^2)$, will be studied in greater detail in the thesis of R. C. Ball.[49] The μ^- data sample will be added to the μ^+. Also, the hadron energy, as measured directly in the calorimeter, will be available shortly. This will improve resolution in ν and x, and will facilitate a check on the present data.

Other deep inelastic muon experiments are being conducted at Fermilab and at CERN. These results, with large statistics and higher q^2, will contribute even further to the study of hadronic matter at small distances.

APPENDIX A

$F_2(x,q^2)$ for various values of x and q^2

Two recent developments in the data analysis have served to change the data somewhat: (i) the overall normalization correction described on p. 157 has changed from 14% down to 10%; (ii) an adjustment in the way $\omega=2m\nu/q^2$ is calculated in the nucleon rest system for the monte carlo program has resulted in higher values of $F_2(x,q^2)$ for large values of $x=1/\omega$. The latest data for F_2 versus q^2 (for constant x) and F_2 versus x (for constant q^2) incorporating all new corrections is given in Tables A.1 and A.2 respectively.

Although the new binning of the data is not the same as in Figures 5.6 and 5.7, some qualitative changes can be described. In Figure 5.6, the data will be everywhere lower by about 4% except for some of the points at large x which will actually rise somewhat. This latter effect tends to bring the points as large x into better agreement with the QCD curves in that region. Similar adjustments occur in the plot of F_2 versus q^2 in Figure 5.7. It should be emphasized that these adjustments do not alter the threshold-like behavior discussed in chapter five. The values of b(x) in Figure 5.4 do not change very much; the dichotomy between data above and below $W^2=100$ remains. The moments plotted in Figure 5.8 also do not change very much; the increase at large q^2 continues.

Table A.1 $F_2(x,q^2)$ versus q^2 for fixed x $(x=1/\omega)$

$\langle\omega\rangle$	q^2	F_2	ΔF_2
2.87	25.77	.1548	.010
	30.58	.1531	.011
	35.36	.1417	.011
	40.64	.1431	.012
	48.28	.1206	.008
	58.06	.1279	.009
	74.79	.1283	.008
	100.1	.1897	.019
3.56	16.40	.2114	.011
	21.67	.2135	.011
	26.55	.2132	.012
	32.10	.1902	.011
	36.91	.1805	.011
	42.75	.1987	.013
	47.33	.2090	.015
	52.89	.2119	.016
	60.54	.1837	.011
	77.85	.1802	.010
4.36	7.92	.2097	.015
	11.99	.2287	.011
	17.04	.2157	.010
	22.05	.2141	.010

Table A.1 continued

$\langle\omega\rangle$	q^2	F_2	ΔF_2
4.36	27.43	.2333	.011
	32.87	.2303	.012
	37.93	.2541	.015
	43.86	.2765	.017
	48.68	.2435	.017
	53.71	.2494	.019
	62.20	.2912	.019
	75.41	.2380	.017
5.4	8.06	.2529	.011
	12.28	.2624	.008
	17.53	.2515	.007
	22.84	.3144	.009
	28.22	.3422	.011
	33.56	.3279	.012
	38.52	.3204	.013
	44.30	.3447	.016
	49.45	.3193	.016
	55.22	.2827	.017
	59.87	.2799	.020
	68.24	.3483	.026
7.26	8.22	.2890	.009
	12.72	.3048	.007
	17.98	.3743	.008
	23.35	.3967	.010
	28.67	.4300	.012
	34.06	.4385	.014
	39.92	.3826	.015
	45.24	.3730	.018
	50.84	.3809	.026
	56.01	.4688	.051

Table A.1 continued

$\langle\omega\rangle$	q^2	F_2	ΔF_2
11.0	7.24	.3605	.011
	9.18	.3677	.010
	11.27	.4005	.010
	13.55	.4251	.011
	15.58	.4626	.012
	17.84	.4401	.012
	19.94	.4439	.013
	22.35	.4629	.015
	24.17	.4554	.015
	25.90	.4465	.022
	29.04	.4715	.013
	34.49	.4905	.021
22.3	6.02	.5153	.025
	7.36	.4907	.011
	9.37	.4816	.008
	11.5	.4878	.008
	13.53	.4789	.009
	15.66	.5258	.012
	17.92	.5134	.014
	20.16	.5396	.019
	22.40	.5236	.025
	25.28	.6590	.041

Table A.2 $F_2(x,q^2)$ versus x for fixed q^2 regions

q^2	<x>	F_2	ΔF_2
10.9	.043	.4763	.008
	.053	.4622	.007
	.071	.4329	.007
	.085	.4163	.010
	.102	.4445	.010
	.122	.4212	.009
	.148	.3827	.008
	.184	.370	.007
	.206	.266	.012
	.214	.259	.012
	.222	.239	.011
	.232	.2591	.012
	.246	.2919	.015
	.256	.2396	.009
	.266	.2534	.015
19.9	.046	.5924	.043
	.050	.5363	.027
	.060	.5073	.012
	.070	.4923	.013
	.081	.4812	.012
	.094	.4520	.010
	.116	.4390	.010
	.148	.3998	.008
	.172	.3634	.015
	.188	.3139	.012
	.205	.3049	.012
	.221	.2876	.012
	.236	.2877	.012
	.252	.2489	.011
	.267	.2307	.010
	.283	.2321	.011
	.300	.2144	.011
	.317	.2185	.012

Table A.2 continued

q^2	<x>	F_2	ΔF_2
29.4	.076	.6364	.042
	.090	.5298	.020
	.106	.4361	.013
	.132	.456	.012
	.152	.4381	.023
	.167	.4161	.021
	.182	.3753	.019
	.198	.3331	.016
	.216	.3349	.017
	.235	.3600	.017
	.260	.2834	.014
	.284	.2276	.012
	.309	.2051	.011
	.333	.1906	.011
	.353	.1608	.010
	.373	.1525	.011

Table A.2 continued

q^2	<x>	F_2	ΔF_2
42.5	.113	.4993	.038
	.131	.4211	.016
	.148	.3913	.024
	.163	.3829	.015
	.190	.3403	.013
	.221	.3252	.017
	.248	.3082	.016
	.275	.2531	.013
	.306	.2268	.012
	.337	.01760	.010
	.370	.1590	.010
	.402	.1169	.009
61.5	.152	.5601	.060
	.166	.3349	.034
	.180	.3329	.028
	.193	.3498	.023
	.224	.2979	.013
	.265	.2442	.014
	.299	.2063	.011
	.336	.1675	.009
	.381	.1378	.008
	.430	.1131	.008
	.506	.1240	.009

Table A.2 continued

q^2	<x>	F_2	ΔF_2
91.1	.268	.2373	.029
	.325	.2066	.025
	.380	.1628	.018
	.450	.1431	.015
	.552	.0606	.006

REFERENCES

1. D.H. Perkins, Introduction to High Energy Physics (Addison-Wesley, Reading, Mass., 1972).
2. R.P. Feynman, Photon-Hadron Interactions (Benjamin, New York, 1972).
3. J.I. Friedman and H.W. Kendall, Annual Rev. of Nucl. Science 22, 203 (1972).
4. S.D. Drell, T.M. Yan, and D.J. Levy, Phys. Rev. 187, 2159 (1969).
5. J.D. Bjorken and E.A. Paschos, Phys. Rev. 185, 1975 (1969).
6. F.E. Close, "Quarks and Partons," Proceedings of the 1976 CERN School of Physics, Geneva (1976).
7. J. Kuti and V.F. Weisskopf, Phys. Rev. D4, 3418 (1971).
8. C.H.Llewellyn Smith, "Neutrino Interactions," Proceedings of the 1977 CERN-JINR School of Physics, Geneva (1977).
9. P.M. Fishbane and R.L. Kingsley, Phys. Rev. D8, 3074 (1973).
10. S. Stein et al., Phys. Rev. D12, 1884 (1975).
11. S.D. Drell and M.S. Chanowitz, Phys. Rev. Letters 30, 807 (1973).
12. H.D. Politzer, Harvard preprint HUTP-77/A038; talk presented at Fermilab (1977).
13. G. Altarelli, Ninth Ecole d'Eté de Physique de Particles, GIF-SUR-YVETTE (1977).
14. C. Chang et al., Phys. Rev. Letters 35, 901 (1975).
    Y. Watanabe et al., Phys. Rev. Letters 35, 898 (1975).
15. E.M. Riordan et al.,SLAC-PUB-1634, Aug. (1975).

16. H. Anderson et al., Phys. Rev. Letters 37, 4 (1976).

17. H. Anderson et al., Phys. Rev. Letters 38, 1450 (1977).

18. D.H. Perkins, P. Schreiner, and W.G. Scott, Phys. Letters 67B, 347 (1977).

19. F.J. Gilman, SLAC-PUB-1455 (1974).

20. H.D. Politzer, Physics Reports 17C, 129 (1974).

21. K. Wilson, "Products of Currents," Proceedings of the 1971 International Symposium on Electron and Photon Interactions at High Energies, Cornell (1971).

22. Wu-ki Tung, Phys. Rev. D17, 739 (1978).

23. O. Nachtmann, "Deep Inelastic Lepton Scattering," Proceedings of the 1977 International Symposium on Lepton and Photon Interactions at High Energies, Hamburg (1977).

24. A. DeRujula, H.Georgi, and H.D. Politzer, Ann. Phys. 103, 315 (77).

25. S.D. Drell and T.M. Yan, Ann. Phys. 66, 578 (1971).

26. G. Parisi, "An Introduction to Scaling Violations," Proceedings of the Eleventh Recontre de Moriond on Weak Interactions and Neutrino Physics, 1976.

27. J. Kogut and L. Susskind, Phys. Rev. D9, 697 (1974).

28. D. Bauer, Ph.D. Thesis, Michigan State University, in preparation.

29. Y. Watanabe, Ph.D. Thesis, Cornell (1975), unpublished.

30. C. Chang, Ph.D. Thesis, Michigan State University (1975), unpublished.

31. S. Herb, Ph.D. Thesis, Cornell (1975), unpublished.

32. L.W. Mo and Y.S. Tsai, Rev. Mod. Phys. 41, 205 (1969).

33. C. Richard-Serre, CERN 71-18 report, Sept.,1971.

34. L. Hand, Proceedings of the 1977 International Symposium on Lepton and Photon Interactions at High Energies, Hamburg (1977).

35. R.H. Siemann et. al., Phys. Rev. Letters 22, 421 (1969).
M. Strovink, E26 internal memo, 1974.

36. M. Glück and E. Reya, Phys. Rev. D14, 3034 (1976).

37. I. Hinchliffe and C.H. Llwellyn Smith, Nucl. Phys. B128,93 (1977).

38. V. Barger and R.J.N. Phillips, Nucl. Phys. B73, 269 (1974).
R.D. Field and R.P. Feynman, CALT-68-565 (1976).

39. A.J. Buras and K.J.F. Gaemers, Nucl. Phys. B132, 249 (1978) and Nucl. Phys. B125, 125 (1977).

40. W. Francis, private communicatiaon: new μ-p (E398) data to be published in Phys. Rev. Letters.

41. A.J. Buras, private communication.

42. H.L. Anderson et. al., Phys. Rev. Letters 40, 1061 (1978).

43. F. Falzen and D.M. Scott, "Scaling Violations in Deep Inelastic Lepton Scattering: How Important is Charm?" Wisconsin preprint, 1978.

44. F.E. Close et. al., Nucl. Phys. B117, 134 (1976).
R. Devenish and D. Schildknecht, Phys. Rev. D14, 93 (1976).

45. P.H. Frampton and J.J. Sakurai, Phys. Rev. D16, 572 (1977).
J.J. Sakurai and D.Schildknecht, Phys. Letters 41B, 489 (1972).

46. A. Salam, Proc. Royal Soc. London A355, 515 (1977).

47. T. Tajima and K.I. Matumoto, Phys. Rev. D14, 97 (1976).
K.I. Matumoto, T. Muta, and T. Tajima: "Models of Bjorken Scaling Violations," to appear in Prog. Theoretical Phys., No. 63 (1978).

48. M.S. Chanowitz and S.D. Drell, Phys. Rev. D9, 2078 (1974).

49. R.C. Ball, Michigan State Ph.D. thesis in preparation.